

Simulating Systems of Flexible Fibers

by

Leonard H. Switzer III

A dissertation submitted in partial fulfillment
of the requirements for the degree of

Doctor of Philosophy
(Chemical Engineering)

at the

UNIVERSITY OF WISCONSIN–MADISON

2002

In memory of Leonard and Marian Switzer, Sr.

Abstract

The characteristics of non-Brownian fiber suspensions depend on the properties of the fibers, the suspending fluid, and fiber interactions. This thesis describes the development and application of a fiber-level simulation technique to probe these relationships. Fibers are modelled as chains of rigid spherocylinders connected by ball and socket joints, including such features as fiber flexibility, non-straight equilibrium shapes, and interfiber friction. The model and simulation technique were employed to probe the effect of these fiber features on floc formation, floc dispersion, and the rheological properties of fiber suspensions in shear flow, as well as to study the formation and mechanical properties of planar fiber networks.

Simulations demonstrate that flexible fibers that interact via interfiber friction will flocculate in simple shear flow, even in the absence of attractive forces between fibers. The degree of flocculation depends on the fiber equilibrium shape, fiber stiffness, and coefficient of friction. The results are consistent with the elastic fiber interlocking mechanism of floc coherency.

Flocs formed in simple shear flow were observed to disperse when isolated in various unbounded linear flow fields (i.e., simple shear, uniaxial extension, and planar extension). Shear flow completely disperses flocs at a rate that increases with decreasing fiber stiffness and coefficient of friction. Flocs in extensional flows initially disperse much faster than flocs in shear flow at similar deformation rates. However,

the dispersion in extensional flow is incomplete, as smaller secondary flocs remain intact.

Simulated fiber suspensions exhibited non-Newtonian behavior, including shear thinning, which depends on the fiber aspect ratio and shape. When flocs form in sheared suspensions, this shear thinning regime persists to lower shear rates than that observed for homogeneous suspensions. Fiber equilibrium shape significantly influences the suspension rheology. The suspension viscosity and first normal stress difference increase as the equilibrium fiber shape deviates more from perfectly straight.

The model and simulation technique were modified to simulate the formation of planar fiber networks. The networks were then elongated in the plane of the network, in order to investigate their mechanical properties. The predicted mechanical response agrees qualitatively with that observed experimentally. The tensile strength increases as the fiber stiffness, coefficient of friction, and fiber aspect ratio increase.

Acknowledgments

The research presented in this thesis was supported in part by the USDA NRI Competitive Grants Program (award no. 2001-35103-09933). I would like to express my sincere thanks and gratitude to my advisor, Daniel J. Klingenberg, for his support and guidance during my time at the University of Wisconsin.

I would like to thank the faculty and staff of the Department of Chemical Engineering and Tim Scott of the U.S.D.A Forest Products Laboratory, for their support throughout my studies. The knowledge you have imparted to me has helped to shape my future.

I wish to thank fellow members of the Klingenberg research group, both past and present: Chris Schmid, Stefan Zauscher, Peter Rankin, Prakorn Kittipoomwong, Karl von Pfeil, Martin Heine, Heiko Bette, and Emilio Tozzi, the people who started their studies with me in the Fall of 1997, and the newcomers that have arrived since, for sharing their time here with me, and making the quest for knowledge that much more enjoyable.

Finally, I could not have accomplished this without the support of my family: grandparents Robert and Evelyn Turnquist, siblings Stephen, Sara, and Eric, parents Leonard and Susan Switzer, God-mother Mary Pekkala, in-laws John, Eunice, and Richard Gustavson, and my dog Britt. Your encouragement has been the backbone of all of my successes.

Most importantly, I must thank my wife Debra. You are my inspiration and strength. This is for you.

LEONARD H. SWITZER III

University of Wisconsin–Madison

September 2002

Contents

Abstract	ii
Acknowledgments	iv
List of Figures	xi
List of Tables	xix
Chapter 1 Introduction	1
1.1 Motivation and project overview	1
1.2 Single particle motion	4
1.2.1 Rigid fibers	6
1.2.2 Flexible fibers	8
1.3 Fiber suspensions	10
1.3.1 Flocculation of fibers	10
1.3.2 Fiber suspension rheology	17
1.3.3 Determining fiber suspension structure	22
Chapter 2 Simulation method	30
2.1 Equations of motion	30
2.2 Hydrodynamic forces and torques	32
2.3 External forces	33

2.4	Contact forces	34
2.5	Constraint forces	38
2.5.1	Inextensibility constraint	38
2.5.2	Friction constraint	39
2.6	Restoring torque	40
2.6.1	Frames of reference	41
2.6.2	Restoring torques in terms of bending and twisting	43
2.6.3	Anisotropic bending	46
2.7	Scaling of the equations of motion	48
2.8	Generalized coordinates: Euler parameters	50
2.8.1	Relation of Euler parameters to the body rotation matrix	51
2.8.2	Relation between Euler parameters and the angular velocity	53
2.9	Solution methods	55
2.9.1	Direct integration	57
2.9.2	Approximate method of direct integration	62
2.10	The computational algorithm	67
2.10.1	Initialization	68
2.10.2	Constraint evaluation and integration	69
2.10.3	Post-processing	70
2.11	Planar fiber networks	72
2.11.1	Network formation	72
2.11.2	Elongation of planar networks	74
Chapter 3 Flocculation in sheared fiber suspensions		77
3.1	Introduction	77

3.2	Simulation method	82
3.3	Results and discussion	87
3.3.1	Illustration of flocculation via friction	87
3.3.2	Effects of friction and fiber stiffness	89
3.3.3	Effects of fiber shape	95
3.3.4	Effects of kinetic friction	96
3.3.5	Effects of weak attractive forces	99
3.3.6	Effects of anisotropic bending	101
3.4	Conclusions	103
Chapter 4 Fiber floc dispersion		105
4.1	Introduction	105
4.2	Simulation method	108
4.2.1	Creating flocs	112
4.3	Results and discussion	114
4.3.1	Simple shear flow	114
4.3.2	Extensional flows	118
4.4	Conclusions	124
Chapter 5 Rheology of flexible fiber suspensions via simulations		126
5.1	Introduction	126
5.2	Simulation method	133
5.3	Results and discussion	138
5.3.1	Effects of fiber shape and friction	138
5.3.2	Effects of aspect ratio and stiffness	144
5.3.3	Yield stress	147

5.3.4	Rheology in flocculated suspensions	150
5.4	Conclusions	153
Chapter 6 Handsheet formation and mechanical testing via fiber-level simulations		155
6.1	Introduction	155
6.2	Methods	159
6.2.1	Fiber model and simulations	159
6.2.2	Experiments	165
6.3	Results and discussion	166
6.3.1	Experiments on small fiber sheets	166
6.3.2	Simulations: effect of fiber equilibrium shape, length, flexibility, and friction	168
6.4	Discussion	177
6.5	Conclusions	180
Chapter 7 Conclusions and recommendations		181
7.1	Summary	181
7.2	Recommendations for future Research	183
7.2.1	Experimental research	183
7.2.2	Simulations	185
Appendix A Stress in a suspension of interacting fibers		187
A.1	Generalized particle stress contribution	187
A.2	Particle stress for a flexible fiber suspension	190
Appendix B Fiber bending		192

B.1	Radius of curvature for a U-shaped model fiber	192
B.2	Fiber flexibility	193
Appendix C Details of the friction constraints		197
Appendix D Simulation codes		200
D.1	Flexible fiber code	200
D.1.1	Definition of variables	201
D.2	Code to calculate the average particle stress	231
D.3	Planar network elongation code	236
D.4	Example simulation: The star test floc	245
Bibliography		256

List of Figures

1.1	Suspension of softwood pulp fibers in water, in which heterogenous structures (flocs) are observed.	2
1.2	(a) Euler angles for a fiber and (b) path of the end point of a spheroid with $r_p = 10$ for different orbit constants, C	7
1.3	Classification of flexible fibers orbits based on fiber flexibility [31]	9
1.4	Examples of fiber interactions in a suspension.	14
2.1	Model fiber made up of N_{seg} rigid sphero-cylinders connected by ball and socket joints.	31
2.2	Forces and torques acting on fiber segment i in contact with segment j	32
2.3	Three possible scenarios for interactions between fiber segments i and j , (a) side-side, (b) end-side, or (c) end-end interactions.	35
2.4	The inextensibility constraint causes the end-points of adjacent fibers to coincide.	38
2.5	The frictional force at a contact is constrained to a plane perpendicular to the normal between the segment centers at the contact point, \mathbf{n}_{ij} . The plane of contact contains the orthogonal unit vectors, \mathbf{e}_{ij}^1 and \mathbf{e}_{ij}^2	40
2.6	Relationship between the three types of coordinate frames related to segment i : inertial frame, body i frame, and equilibrium body i frame.	41

2.7	Construction of the equilibrium rotation matrix is accomplished by two rotations: (1) ϕ_i^{eq} about \mathbf{p}_{i-1} and (2) θ_i^{eq} about $\hat{\mathbf{y}}'$	43
2.8	The effect of θ_i^{eq} and ϕ_i^{eq} (measured in degrees) on equilibrium shape of symmetric fibers ($\theta_2^{\text{eq}} = \theta_3^{\text{eq}} = \dots = \theta_{N_{\text{seg}}}^{\text{eq}}$ and $\phi_2^{\text{eq}} = \phi_3^{\text{eq}} = \dots = \phi_{N_{\text{seg}}}^{\text{eq}}$).	44
2.9	SEM image of a softwood pulp fibers	47
2.10	Fibers with a non-circular cross section have a preferred bending direction, for example, with respect to the \hat{y} -axis.	48
2.11	The vector \mathbf{w} in the inertial frame ($\hat{\mathbf{e}}_x, \hat{\mathbf{e}}_y, \hat{\mathbf{e}}_z$) is transformed to \mathbf{w}' in the body frame ($\hat{\mathbf{x}}_i, \hat{\mathbf{y}}_i, \hat{\mathbf{z}}_i$) by a rotation of the inertial frame by an angle χ about the vector \mathbf{u} , which has the same coordinates in both frames.	51
2.12	Scenarios for contacts among any three segments i , j , and m , where the main contact of interest is between i and j	65
2.13	Formation of a planar fiber network is accomplished by squeezing a randomly oriented fiber suspension between two plates.	73
2.14	Example of fiber that intersects the end plane of the planar network.	74
3.1	Schematic diagram of a model fiber composed of rigid spherocylinders linked by ball and socket joints. Here, segment i is in contact with segment k from another fiber.	83
3.2	Schematic illustration of an anisotropic fiber with a preferred bending axis \hat{y} . In simulations with anisotropic fibers reported here, the fiber cross-section remains circular.	85

3.3	Simulation snapshots after shearing to a strain of $\gamma = 1500$, with parameters $nL^3 = 20$, $r_p = 75$, $N_{\text{seg}} = 5$, and (a) $\mu^{\text{stat}} = 20$, $S^{\text{eff}} = 0.05$, $\theta^{\text{eq}} = 0.8$, $\phi^{\text{eq}} = 0.7$ (flocculated suspension); (b) same as (a) except $\theta^{\text{eq}} = \phi^{\text{eq}} = 0$; (c) same as (a) except $\mu^{\text{stat}} = 0$; and (d) same as (a) except $S^{\text{eff}} = 0.0005$	88
3.4	(a) Pair distribution function, and (b) average number of contacts per fiber versus strain for the runs depicted in Figure 3.3.	90
3.5	Critical coefficient of friction as a function of the effective stiffness for the star test floc in simple shear flow, $(N_{\text{seg}}, r_p, \theta^{\text{eq}}, \phi^{\text{eq}}) = (7, 56, 0, 0)$	93
3.6	Threshold concentration to produce flocs as a function of the inverse of the effective stiffness, $1/S^{\text{eff}} \propto \eta_o$; $(N_{\text{seg}}, r_p, \theta^{\text{eq}}, \phi^{\text{eq}}, \mu^{\text{stat}}) = (5, 75, 0.6, 0, 20)$	94
3.7	(a) Suspension homogeneity (at $\gamma = 1500$) mapped as a function of curvature (b/R_U) and concentration [$(N_{\text{seg}}, r_p, S^{\text{eff}}, \mu^{\text{stat}}) = (5, 75, 0.05, 20)$]; (b) Average number of contacts per fiber at steady state ($\langle n_c \rangle_{\text{ss}}$) as a function of b/R_U for suspensions at $nL^3 = 20$ after shearing for $\gamma = 1500$ [$(N_{\text{seg}}, r_p, S^{\text{eff}}, \mu^{\text{stat}}) = (5, 75, 0.05, 20)$].	97
3.8	Pair distribution function for the fiber centers-of-mass of suspensions in simple shear flow at steady state $\gamma > 1000$, for various values of the coefficients of static and kinetic friction $(N_{\text{seg}}, r_p, nL^3, S^{\text{eff}}, \theta^{\text{eq}}, \phi^{\text{eq}}) = (5, 75, 20, 0.05, 0.6, 0)$	98
3.9	Pair distribution function for the fiber centers-of-mass of suspensions in simple shear flow at steady state $\gamma > 1000$, with and without attractive potentials $(N_{\text{seg}}, r_p, nL^3, S^{\text{eff}}, \theta^{\text{eq}}, \phi^{\text{eq}}) = (5, 75, 20, 0.05, 0.8, 0.7)$	100

3.10	Pair distribution function for the centers-of-mass of fibers with isotropic ($S^{\text{eff}} = 0.05$, $\mu^{\text{stat}} = 20$) and anisotropic bending [(A) $(S^{\text{eff}})_{\text{easy}} = 0.05$, $\mu^{\text{stat}} = 20$; (B) $(S^{\text{eff}})_{\text{easy}} = 0.05$, $\mu^{\text{stat}} \rightarrow \infty$; and (C) $(S^{\text{eff}})_{\text{easy}} = 0.01$, $\mu^{\text{stat}} = 20$] using pin joints after shearing for $\gamma = 1500$ with $(N_{\text{seg}}, r_p, nL^3, \theta^{\text{eq}}, \phi^{\text{eq}}, \mu^{\text{kin}}) = (5, 75, 20, 0.6, 0, 0)$	103
4.1	Schematic diagram of a model fiber composed of rigid spherocylinders linked by ball and socket joints. Here, segment i is in contact with segment k from another fiber.	109
4.2	Examples of equilibrium shapes for U-shaped fibers $(\theta^{\text{eq}}, \phi^{\text{eq}}) = (0.6, 0)$ and helical fibers $(\theta^{\text{eq}}, \phi^{\text{eq}}) = (0.8, 0.7)$ from two perspectives.	113
4.3	Flocs are created in a suspension with periodic boundary conditions and the largest floc is extracted to an unbounded linear flow to observe disruption.	113
4.4	Snapshots of the largest fragment of a floc in a simple shear flow field at various strains ($N_{\text{fib}}^0 = 69$, $r_p = 75$, $S^{\text{eff}} = 0.05$, $\theta^{\text{eq}} = 0.6$, $\phi^{\text{eq}} = 0$, $\mu^{\text{stat}} = 20$).	115
4.5	Fraction of the initial number of fibers (U-shaped) remaining in the largest floc fragment as a function of strain for various values of (a) S^{eff} (with $\mu^{\text{stat}} = 20$) and (b) μ^{stat} (with $S^{\text{eff}} = 0.05$) in unbounded simple shear flow ($N_{\text{fib}}^0 = 69$, $\theta^{\text{eq}} = 0.6$, $\phi^{\text{eq}} = 0$).	116
4.6	Fraction of the initial number of fibers (helical) remaining in the largest floc fragment as a function of strain for various values of (a) S^{eff} (with $\mu^{\text{stat}} = 20$) and (b) μ^{stat} (with $S^{\text{eff}} = 0.05$) in unbounded simple shear flow ($N_{\text{fib}}^0 = 114$, $\theta^{\text{eq}} = 0.8$, $\phi^{\text{eq}} = 0.7$).	117

4.7	Snapshots of fiber floc structures in uniaxial extensional flow with (a) $S^{\text{eff}} = 0.005$ and (b) $S^{\text{eff}} = 0.5$ at various strains ($\theta^{\text{eq}} = 0.8$, $\phi^{\text{eq}} = 0.7$, $\mu^{\text{stat}} = 20$).	119
4.8	Fraction of the initial number of fibers (helical) in the largest floc fragment as a function of strain for dispersion in uniaxial extensional flow for various values of S^{eff} , compared to that for shear flow with $S^{\text{eff}} = 0.05$ ($N_{\text{fib}}^0 = 114$, $\theta^{\text{eq}} = 0.8$, $\phi^{\text{eq}} = 0.7$, $\mu^{\text{stat}} = 20$).	121
4.9	Fraction of the initial number of fibers (U-shaped) in the largest floc fragment as a function of strain in uniaxial extensional flow for various values of S^{eff} , compared to that for simple shear flow with $S^{\text{eff}} = 0.05$ ($N_{\text{fib}}^0 = 106$, $\theta^{\text{eq}} = 0.6$, $\phi^{\text{eq}} = 0$, $\mu^{\text{stat}} = 20$).	122
4.10	Fraction of the initial number of fibers (U-shaped) in the largest floc fragment as a function of strain for dispersion in planar and uniaxial extensional flows for various values of S^{eff} ; ($N_{\text{fib}}^0 = 106$, $\theta^{\text{eq}} = 0.6$, $\phi^{\text{eq}} = 0$, $\mu^{\text{stat}} = 20$).	123
4.11	Critical values of S^{eff} and μ^{stat} in uniaxial extensional flow in which flocs remain coherent ($N_{\text{fib}}^0 = 106$, $\theta^{\text{eq}} = 0.6$, $\phi^{\text{eq}} = 0$).	124
5.1	Model fiber of rigid spherocylinders linked by ball and socket joints that experience mechanical contacts with other fibers in the suspension.	134
5.2	Example of the starting configuration of fibers randomly placed in a periodic simulation cell.	137
5.3	Examples of U-shaped fibers ($\phi^{\text{eq}} = 0$, $r_p = 75$) for various values of θ^{eq} .	138
5.4	Steady-state specific viscosity as a function of concentration for suspensions with fibers of different shapes and coefficients of friction.	139

5.5	Specific viscosity as a function of equilibrium shape of U-shaped fibers after shearing for $\gamma = 1500$ ($N_{\text{seg}}, r_p, nL^3, S^{\text{eff}}, \phi^{\text{eq}}, \mu^{\text{stat}} = (5, 75, 20, 0.05, 0, 20)$).	142
5.6	The specific viscosity as a function of the static coefficient of friction for suspensions of fibers that are U-shaped ($\theta^{\text{eq}} = 0.1, \phi^{\text{eq}} = 0$) and helical ($\theta^{\text{eq}} = 0.8, \phi^{\text{eq}} = 0.7$) after shearing for $\gamma = 1500$ with all other parameter constant ($N_{\text{seg}}, nL^3, r_p, S^{\text{rmeff}} = (5, 20, 75, 0.05)$).	144
5.7	(a) Specific viscosity and (b) normalized first normal stress difference N_1/E_Y as a function of the dimensionless shear rate $\eta_o \dot{\gamma}/E_Y$ for fibers of various aspect ratios suspension and constant stiffness ($E_Y I$) after shearing for $\gamma = 1500$ ($N_{\text{seg}}, r_p, \Phi, \theta^{\text{eq}}, \phi^{\text{eq}}, \mu^{\text{stat}} = (5, 75, 0.003, 0.1, 0, 20)$).	146
5.8	Specific viscosity as a function of concentration for shorter fiber suspensions ($r_p = 35$), using rigid fibers ($N_{\text{seg}}, S^{\text{eff}}, \mu^{\text{stat}} = (1, \infty, 20)$), straight flexible fibers ($N_{\text{seg}}, S^{\text{eff}}, \theta^{\text{eq}}, \phi^{\text{eq}}, \mu^{\text{stat}} = (5, 0.7, 0, 0, 20)$), and slightly deformed flexible fibers ($N_{\text{seg}}, S^{\text{eff}}, \theta^{\text{eq}}, \phi^{\text{eq}}, \mu^{\text{stat}} = (5, 0.7, 0.1, 0, 20)$) compared with the experimental data of Chaouche and Koch [18]. . .	147
5.9	(a) Shear stress (σ_{xz}) as a function of shear rate for simulations of fiber suspensions at different volume fractions, and (b) the extrapolated apparent yield stress (σ_0) from (a) as a function of volume fraction; ($N_{\text{seg}}, r_p, \theta^{\text{eq}}, \phi^{\text{eq}}, \mu^{\text{stat}} = (5, 75, 0.1, 0, 20)$).	150
5.10	Pair distribution function for the fiber centers-of-mass for a flocculated suspension ($\mu^{\text{stat}} = 20$) and a homogeneous suspension ($\mu^{\text{stat}} = 1$) after shearing for $\gamma = 1500$; ($N_{\text{seg}}, r_p, nL^3, S^{\text{eff}}, \theta^{\text{eq}}, \phi^{\text{eq}} = (5, 75, 15, 0.05, 0.1, 0)$).	151

5.11	Specific viscosity versus the reciprocal of the effective stiffness for suspensions of equivalent concentration ($nL^3 = 15$) and aspect ratio ($r_p = 75$) in which (A) flocculates and (B) and (C) remain homogeneous: (A) $(\theta^{\text{eq}}, \phi^{\text{eq}}, \mu^{\text{stat}}) = (0.8, 0.7, 20)$; (B) $(\theta^{\text{eq}}, \phi^{\text{eq}}, \mu^{\text{stat}}) = (0.8, 0.7, 1)$; (C) $(\theta^{\text{eq}}, \phi^{\text{eq}}, \mu^{\text{stat}}) = (0.1, 0, 20)$	152
6.1	Schematic diagram of a model fiber composed of rigid spherocylinders linked by ball and socket joints. Here, segment i is in contact with segment k from another fiber.	160
6.2	Schematic diagram illustrating the simulation cell after the formation of the planar network, and the location of the planes containing the fibers that experience external forces to simulate elongation.	163
6.3	Schematic diagram of the tensile apparatus developed to test small planar fiber networks.	166
6.4	Tensile force as a function of deformation for a typical handsheet as described in the text.	167
6.5	Snapshots of the structure of a typical fiber network subjected to elongation at various deformations.	168
6.6	Dimensionless tensile force $T/\eta_o u_p L$ versus deformation $\Delta x/L$ for the simulation run shown in Fig. 6.5	170
6.7	(a) Softwood fibers in water, and (b) examples of U-shaped fibers ($\phi^{\text{eq}} = 0$) for various values of θ^{eq}	171
6.8	Dimensionless tensile force $T/\eta_o u_p L$ as a function of the deformation $\Delta x/L$ for fiber networks of different shapes, and configuration snapshots at $\Delta x/L = 1$	173

6.9	(a) Dimensionless tensile force $T/E_Y b^2$ as a function of deformation $\Delta x/L$ for fibers of different aspect ratios, and (b) the dimensionless maximum tensile strength $T_u/E_Y b^2$ and elastic modulus of the fiber networks E_{xx}/E_Y as a function of fiber aspect ratio	175
6.10	Dimensionless tensile force $T/\eta_o u_p L$ as a function of deformation $\Delta x/L$ for planar fiber networks at various effective stiffness values.	176
6.11	Dimensionless tensile force $T/\eta_o u_p L$ as a function of deformation $\Delta x/L$ for planar fiber networks in which the coefficient of friction is varied.	177
B.1	Two methods to describe the radius of curvature R_U for a U-shaped fiber	193
B.2	Continuous fiber subjected to an external torque and deformed slightly from its equilibrium configuration.	194
B.3	Fiber restoring torques at each joint are modelled as a virtual spring.	196
C.1	Example contact group consisting of 4 segments (highlighted) and 3 contacts.	198
D.1	Star configuration used in example files.	245

List of Tables

2.1	Evaluation of s_{ij} and s_{ji} for interacting segments i and j by side-side, end-side, or end-end interactions based on the original values found with Eqs. (2.11)-(2.12).	37
2.2	Summary of the interaction tensor for the off-diagonal components of \mathcal{R}_F for contact between segments i and j ($i < j$) in which an indirect contact occurs with segment m (see also Fig. 2.12).	64
2.3	Input parameter for fiber simulations	69

Chapter 1

Introduction

1.1 Motivation and project overview

Particulate suspensions appear in a wide variety of applications, including mineral processing, pulp and paper production, and biological processes. The particles may be spherical, flakes, fibers, or more complicated geometries with characteristic particle lengths ranging from nanometers to centimeters, and may be suspended in either Newtonian or non-Newtonian fluids. The work presented here focuses on suspensions of non-Brownian fibers like those found in wood pulp suspensions and fiber-reinforced composites. Fibers in suspensions assume a variety of conformations. For example, rigid fibers rotate with a prescribed period in a simple shear flow, and interact with other fibers. Real fibers take on a variety of equilibrium shapes (i.e., fibers are not generally straight), and also tend to deform when subjected to hydrodynamic forces. All of these factors affect the suspension microstructure. The overall goal of this work is to gain an understanding of how fiber characteristics affect the microstructure and rheology of fiber suspensions and networks.

In many applications involving fiber suspensions, one desires to control the microstructure (i.e., fiber positions and orientations). For example, a homogeneous

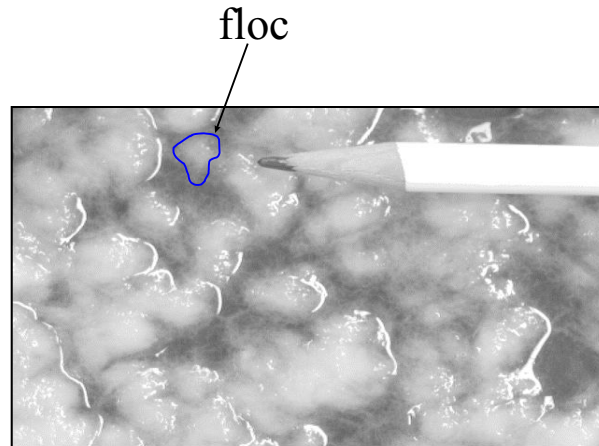


Figure 1.1: Suspension of softwood pulp fibers in water, in which heterogeneous structures (flocs) are observed.

suspension of wood pulp is desired in the headbox of a paper machine. Heterogeneous structures, known as *flocs* (illustrated in Fig. 1.1), can lead to product non-uniformities. Other applications may require fibers to align in a given direction or form flocculated structures. Thus, understanding the factors that control the suspension microstructure is crucial.

In the remaining sections of this chapter, a review of fiber systems is presented. We start by discussing single particle dynamics and behavior of elongated particles. Previous studies on the flocculation of fiber suspensions, floc dispersion, rheology of fiber suspensions, and modelling aspects are also discussed.

In Chapter 2 we present our particle-level simulation technique for probing the relationship between fiber characteristics and the properties of fiber suspensions. Fibers are modelled as rigid cylinders with hemispherical end-caps, connected by ball and socket joints that allow the fibers to bend and twist. The fibers may interact through mechanical contact forces. By knowing all of the forces and torques that act on the fibers, we can solve the equations of motion of the fibers and determine the suspension microstructure. Using the model, we have been able to study the fiber

characteristics that affect flocculation, floc dispersion, suspension rheology, and the mechanical strength of planar fiber networks.

Chapters 3-6 contain the results of simulations of fiber systems. Each chapter is self-contained, including a discussion of the relevant background material, and a brief description of the model, along with a discussion of the simulation results. Thus, each chapter may be read independently.

Results of simulations probing flocculation of fiber suspensions in simple shear flow are presented in Chapter 3. We find that when model fibers are flexible, have deformed equilibrium shapes, and interact through static friction forces, fiber suspensions can form heterogeneous structures, or flocs. Adding kinetic friction and weak attractive forces as features to the model fiber have little effect on the flocculation behavior of suspensions, while anisotropic fiber bending tends to shift the onset of flocculation to higher coefficients of friction.

Simulations of the dispersion of isolated flocs in various linear flow fields are presented in Chapter 4. The flocs are subjected to unbounded simple shear and extensional flow fields. Flocs in simple shear flow disperse more quickly as the fiber stiffness and coefficient of friction are decreased. Extensional flows tend to initially break up flocs faster than in simple shear, but often leave coherent secondary flocs of substantial size.

Rheological properties of simulated fiber suspensions in simple shear flow are presented in Chapter 5. The suspension viscosity is strongly influenced by the fiber shape, stiffness, and coefficient of friction. The yield stress of fiber suspensions scales with volume fraction in the same manner as that observed experimentally. Flocculation impacts the suspension viscosity by extending shear thinning regimes to lower shear rates than that observed for homogeneous fiber suspensions.

Extensions of the model to simulate the formation and mechanical testing of planar fiber networks are presented in Chapter 6. Fiber “sheets” are formed by squeezing a suspension between parallel plates. The resulting planar networks are then elongated at a constant strain rate, and the required tensile force is calculated. As in previous chapters, we find that the fiber shape, stiffness, length, and coefficient of friction impact the tensile strength of these simulated fiber networks.

The main conclusions from this research are summarized in Chapter 7. Also presented in this chapter are recommendations for future work.

1.2 Single particle motion

The motion of particles in a suspension is influenced strongly by hydrodynamic forces exerted by the suspending fluid. The suspending fluid velocity \mathbf{u} is governed by the equations of continuity and motion,

$$\frac{\partial \rho}{\partial t} + \nabla \cdot (\rho \mathbf{u}) = 0 \quad (1.1)$$

$$\rho \left(\frac{\partial \mathbf{u}}{\partial t} + \mathbf{u} \cdot \nabla \mathbf{u} \right) = \nabla \cdot \boldsymbol{\sigma} + \rho \mathbf{f}, \quad (1.2)$$

where ρ is the fluid density, $\boldsymbol{\sigma}$ is the stress in the fluid, and \mathbf{f} represents external body forces. The Reynolds number Re_p of interest is defined based on the length scale of a particle,

$$Re_p = \frac{d\rho U}{\eta_o}, \quad (1.3)$$

where d is the characteristic particle dimension, η_o is the fluid viscosity, and U is a characteristic particle velocity. For typical suspensions of small particles in viscous liquids, $Re_p \ll 1$, which implies that inertia can be neglected in the equation of motion [49]. Suspending fluids are commonly incompressible and Newtonian, resulting in the

simplified equations of continuity and motion,

$$\nabla \cdot \mathbf{u} = 0, \quad (1.4)$$

$$\eta_o \nabla^2 \mathbf{u} - \nabla p = \mathbf{0}, \quad (1.5)$$

in which Eq. (1.5) is known as the *Stokes equation*.

The velocity field described by the Stokes equation for flow past a rigid particle can be represented by a distribution of point forces exerted on the fluid, distributed about the particle surface. The velocity at a point \mathbf{x} in the fluid becomes [49],

$$\mathbf{u}(\mathbf{x}) = \mathbf{U}^\infty(\mathbf{x}) - \oint_S [\boldsymbol{\sigma}(\boldsymbol{\xi}) \cdot \mathbf{n}] \cdot \boldsymbol{\mathcal{G}}(\mathbf{x} - \boldsymbol{\xi}) dS(\boldsymbol{\xi}), \quad (1.6)$$

where \mathbf{U}^∞ is the ambient fluid velocity, \mathbf{n} the unit outward normal to the particle surface, dS is a surface area element on the particle surface, and $\boldsymbol{\mathcal{G}}$ is known as the Oseen tensor,

$$\boldsymbol{\mathcal{G}}(\mathbf{x}) = \frac{1}{8\pi\eta_o} \left[\frac{1}{r} \boldsymbol{\delta} + \frac{1}{r^3} \mathbf{x}\mathbf{x} \right], \quad (1.7)$$

with $r = (\mathbf{x} \cdot \mathbf{x})^{1/2}$. The velocity field far from the particle can be approximated by expanding $\boldsymbol{\mathcal{G}}(\mathbf{x} - \boldsymbol{\xi})$ in a Taylor series around $\boldsymbol{\xi} = \mathbf{0}$ and substituting the expansion into Eq. (1.6). This form of the velocity field is known as the *multipole expansion* and the first two terms may be expressed as

$$\begin{aligned} \mathbf{u}(\mathbf{x}) - \mathbf{U}^\infty(\mathbf{x}) = & - \underbrace{\left[\oint_S \boldsymbol{\sigma} \cdot \mathbf{n} dS \right]}_{\mathbf{F}} \cdot \boldsymbol{\mathcal{G}}(\mathbf{x}) + \\ & \frac{1}{2} \boldsymbol{\epsilon} : \left\{ \underbrace{\left[\oint_S (\boldsymbol{\sigma} \cdot \mathbf{n}) \times \boldsymbol{\xi} dS \right]}_{\mathbf{T}} \cdot \nabla \boldsymbol{\mathcal{G}} \right\} + \\ & \underbrace{\left[\frac{1}{2} \oint_S [(\boldsymbol{\sigma} \cdot \mathbf{n}) \boldsymbol{\xi} + \boldsymbol{\xi} (\boldsymbol{\sigma} \cdot \mathbf{n})] dS - \frac{1}{3} \boldsymbol{\delta} \oint_S (\boldsymbol{\sigma} \cdot \mathbf{n}) \cdot \boldsymbol{\xi} dS \right]}_{\mathbf{S}} \cdot \nabla \boldsymbol{\mathcal{G}} + \dots, \end{aligned} \quad (1.8)$$

where the bracketed terms are the hydrodynamic force (\mathbf{F}), torque (\mathbf{T}), and stresslet (\mathbf{S}) on the particle.

The linearity of the Stokes equation allows \mathbf{F} , \mathbf{T} , and \mathbf{S} to be related to the particle translational velocity $\dot{\mathbf{r}}$, particle angular velocity $\boldsymbol{\omega}$, and ambient rate of strain tensor \mathbf{E}^∞ as

$$\begin{pmatrix} \mathbf{F} \\ \mathbf{T} \\ \mathbf{S} \end{pmatrix} = \begin{bmatrix} \mathbf{A} & \tilde{\mathbf{B}} & \tilde{\mathbf{G}} \\ \mathbf{B} & \mathbf{C} & \tilde{\mathbf{H}} \\ \mathbf{G} & \mathbf{H} & \mathbf{M} \end{bmatrix} \begin{pmatrix} \mathbf{U}^\infty - \dot{\mathbf{r}} \\ \boldsymbol{\Omega}^\infty - \boldsymbol{\omega} \\ \mathbf{E}^\infty \end{pmatrix}, \quad (1.9)$$

where \mathbf{A} , \mathbf{B} , and \mathbf{C} are second-rank resistance tensors, \mathbf{G} and \mathbf{H} are third-rank resistance tensors, and \mathbf{M} is a fourth rank resistance tensor, all of which are only functions of the particle geometry. The *tilde* terms indicate symmetries with the corresponding tensors (e.g., $H_{ijk} = \tilde{H}_{kij}$) [49]. The ambient angular velocity and rate of strain tensor are

$$\boldsymbol{\Omega}^\infty = \frac{1}{2} [\nabla \times \mathbf{U}^\infty] \quad (1.10)$$

$$\mathbf{E}^\infty = \frac{1}{2} [\nabla \mathbf{U}^\infty + (\nabla \mathbf{U}^\infty)^\dagger]. \quad (1.11)$$

The form of Eq. (1.9) is known as the *resistance* problem, in which unknown forces and torques are to be determined for known translational and angular velocities. Alternatively, the *mobility* form is the inverse problem in which the unknown translational and angular velocities are to be found for known forces and torques.

1.2.1 Rigid fibers

Jeffery [41] described the motion of an ellipsoidal particle in a Newtonian fluid with a velocity field $\mathbf{U}^\infty = (\dot{\gamma}y, 0, 0)$, where $\dot{\gamma}$ is the shear rate. A prolate spheroid (an elongated ellipsoid of revolution with a circular cross section) rotates with a constant period that depends on the aspect ratio of the particle, $r_p \equiv \ell/b$, where ℓ is the

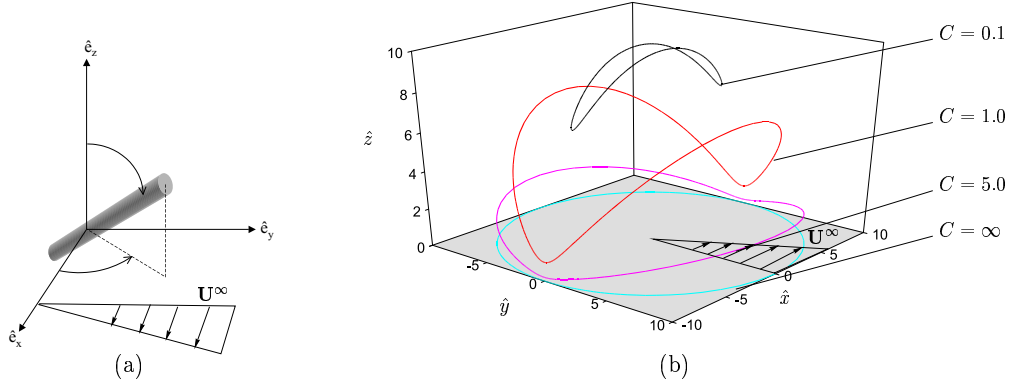


Figure 1.2: (a) Euler angles for a fiber and (b) path of the end point of a spheroid with $r_p = 10$ for different orbit constants, C .

half length of the major axis and b is the half length of the minor axis. The spheroid remains on its initial streamline and periodically repeats the same orbit in the absence of external forces (i.e., contacts, body forces, etc.). In spherical coordinates [see Figure 1.2(a)], the angular motion of an isolated prolate spheroid is written as

$$\tan \theta = \frac{Cr_p}{[r_p^2 \cos^2 \phi + \sin^2 \phi]^{1/2}}, \quad (1.12)$$

$$\tan \phi = r_p \tan \left(\frac{\dot{\gamma} t}{r_p + \frac{1}{r_p}} \right), \quad (1.13)$$

where C is a constant of integration, called the orbit constant. The orbit period is $T = 2\pi(r_p + r_p^{-1})/\dot{\gamma}$. Figure 1.2(b) shows paths of an end point of a spheroid centered at the origin for various values of C . The orbit constant can vary from $0 \leq C < \infty$. An orbit constant of $C \rightarrow \infty$ corresponds to the spheroid tumbling in the plane of shear, and an orbit constant of $C = 0$ corresponds to a “log rolling” motion where the spheroid spins in the vorticity direction. An isolated spheroid with a large aspect ratio spends most of the time roughly aligned in the direction of flow and quickly flips every half period.

Prolate spheroids are an idealization of a rigid fiber. In reality, many fibers have rod-like shapes that are best described as cylindrical. Bretherton [16] showed

that any axisymmetric body with fore-aft symmetry in a linear flow field will have a closed orbit and will not drift across streamlines. In addition, the dynamics of the axisymmetric body are identical to that of a prolate spheroid with an “equivalent aspect ratio”, $r_e = \lambda r_p$, where λ is the ratio of the equivalent and real aspect ratios. Trevalyan and Mason [89] demonstrated this experimentally by measuring the orbit periods of glass fibers in a Couette shearing device at low shear rates. The cylindrical particles rotated in Jeffery orbits, but the periods of rotation were shorter for the cylindrical particles than predicted for prolate spheroids with the same aspect ratio. The ratio of the equivalent aspect ratio to the measured aspect ratio ranged from $\lambda = 0.57$ - 0.72 for $r_p = 17.8$ - 132 , in which λ decreased as r_p increased.

1.2.2 Flexible fibers

Elongated particles are not perfectly rigid and can deform during flow. The straining motion in the flow field can produce sufficiently large axial forces to cause the fiber to buckle during rotation. Burgers [32] found the critical stress required to buckle a fiber to be

$$(\dot{\gamma}\eta_o)_{\text{crit}} \simeq \frac{E_b (\ln 2r_p - 1.75)}{2r_p^4}, \quad (1.14)$$

in which the bending modulus of the rod is $E_b \approx 2E_Y$, where E_Y is the Young’s modulus of the fiber.

A flexible fiber in a flowing fluid can assume a variety of shapes as it rotates. Forgacs and Mason [31, 32] performed experiments on different types of flexible fibers to examine fiber motion. Dilute suspensions of fibers were observed between rotating concentric cylinders. Stiff fibers tended to rotate with periodic closed orbits as predicted by Jeffery [41]. The effective flexibility of fibers was varied by adjusting the fluid viscosity, the shear rate, and by using fibers of different aspect ratios. As the

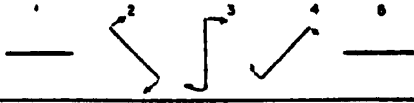
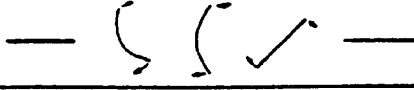
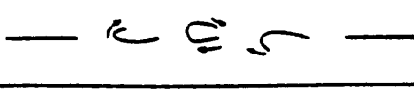
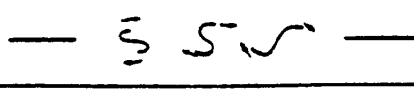
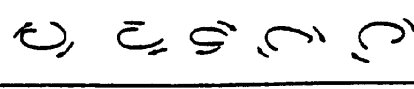
	ORBIT CLASS	HALF ROTATION
	I RIGID	
	II SPRINGY	
	III 'SNAKE TURN'	
	'S-TURN'	
	IV COMPLEX	

Figure 1.3: Classification of flexible fibers orbits based on fiber flexibility [31]

fluid viscosity and shear rate increase, the viscous forces acting on a fiber increase to cause it to appear more flexible. Longer fibers exhibit lower critical stresses necessary for buckling [see Eq. (1.14)], and thus are effectively more flexible.

By changing η_o , $\dot{\gamma}$, and r_p , the effective flexibility of the fibers was increased such that the stress in the fiber exceeded $(\eta_o \dot{\gamma})_{\text{crit}}$, and the fibers were said to rotate with *springy orbits*. In this case, the motion was similar to that predicted for a rigid fiber when the fibers were nearly aligned in the direction of flow. As the orientation angle ϕ approached $\pi/4$ (the angle of maximum compression), the fibers slightly buckled, then snapped back to nearly straight as they realigned with the flow direction. As the fibers became even more flexible, they exhibited more complex rotations classified as *flexible orbits*. Examples of the various conformations of flexible fibers observed are summarized in Figure 1.3.

1.3 Fiber suspensions

Fibers suspended in a liquid medium change the macroscopic properties of the liquid, which are determined by the distribution of positions and orientations of fibers in the suspension. Depending on the application, a homogeneous fiber distribution may be desired, such as in paper making, or aligned fibers may be required, such as in certain polymer composites processing. In principle, if the suspension microstructure is known, then the macroscopic properties may be calculated.

One manner in which fiber suspensions are characterized is by concentration, employing terminology similar to that used for polymer solutions [98]. A fiber suspension is said to be *dilute* if less than one fiber on average is found in a spherical volume of diameter equal to the fiber length; i.e., $nL^3 < 1$, where n is the number of fibers per unit volume and L is the fiber length. The *semi-dilute* regime is characterized by $1 < nL^3 < r_p$, in which fibers are significantly hindered during rotation due to interactions with other fibers. Above $nL^3 > r_p$, the suspension is said to be *concentrated*, and every fiber is assumed to be interacting with other fibers to form a network.

1.3.1 Flocculation of fibers

In applications such as paper making and the processing of some fiber-filled composites, a homogenous dispersion of fibers is desired in order to yield a uniform product. Wood pulp fibers in particular tend to aggregate in a process known as flocculation, which produces spatially heterogeneous structures. The term flocculation is defined as the *state* of unevenness in a fiber suspension, or as the *process* by which fiber flocs form.

Flocculation only occurs if fibers interact. Most commercially relevant fibers are too large to be brought into contact by Brownian motion, and therefore they must be mechanically agitated (i.e., subjected to external forces) to cause them to interact. Mason [56] reasoned that the externally forced motion of fibers is a major factor in determining suspension structure and flocculation behavior. Experiments have demonstrated that numerous factors affect flocculation including concentration, fiber size, fiber shape, surface characteristics, solution characteristics (i.e., ion type and concentration, fillers, viscosity, etc.), shear rate, and turbulence.

Mason [55] studied the motion of fibers by shearing pulp suspensions between two concentric glass cylinders. He observed the formation of flocs at low shear rates, and the dispersion of the flocs as the shear rate increased. Mason described flocculation as a “dynamic equilibrium” process in which fibers are constantly moving in and out of flocs, breaking and reforming contacts. Fiber suspension structure has also been studied using flow loops. In these types of experiments, the fiber suspension flows through a section of tubing through which light is passed. The intensity of the transmitted light is measured to assess the homogeneity of the suspension. Using this method, Robertson and Mason [70] and Takeuchi et al. [85] found that flocs tend to form as the velocity is decreased. They also determined that the tendency to form flocs increases with concentration. Beghello [11] developed an image analysis technique for determining floc size of wood pulp suspensions in a flow loop. He found that as the concentration and fiber aspect ratio increased, the floc size increased as well. The size of flocs decreased if the suspending fluid viscosity increased, the fiber surface was charged by carboxymethylation, or a low molecular weight polymer (carboxymethylcellulose) was added to the suspension. These observations suggest that fiber interactions are important in determining suspension structure.

Processing of suspensions of pulp fibers often occurs in turbulent flow. Increasing the flow velocity to the point of turbulence can cause flocs to disperse into a homogeneous suspension. However, in areas of decaying turbulence, Andersson [4] observed that flocs reformed in his flow loop. Kerekes and Schell [45] investigated the formation of flocs in decaying turbulence by moving a plunger with a 2-dimensional grid attached to a stationary channel and observing the fiber suspensions upon cessation of the plunger motion. They found that as the concentration increased, the suspension formed flocs with greater coherency in the decaying turbulence. Zhao and Kerekes [101] used the same apparatus to examine the effect of the suspending liquid viscosity on flocculation. Lower viscosity suspending fluids tended to produce flocculation more readily in the decaying turbulence. Kerekes [44] hypothesized that the reason flocs form in decaying turbulence is that the decelerating flow tends to crowd fibers together. Soszynski and Kerekes [81, 82] further investigated this mechanism by examining the behavior of nylon fibers in a rotating, half-filled, horizontal cylinder. The recirculating flow patterns that resulted possessed regions of acceleration and deceleration. Flocs were observed to form above a threshold concentration in the regions of decelerating flow. As the circulation continued, flocs densified and developed significant mechanical strength.

The character of fiber interactions can be described in terms of the concentration. Mason [56] defined a critical concentration Φ_{crit} , as one fiber on average in the spherical volume with a diameter equal to the fiber length, $\Phi_{\text{crit}} = 3/2r_p^2$. Above this concentration, fibers can no longer rotate without interacting with other fibers. The number of fibers any given fiber may interact with as it rotates is called the *crowding factor* N_{crowd} [47],

$$N_{\text{crowd}} = \frac{2}{3}\Phi r_p^2 \approx 5C_m \frac{L^2}{w}, \quad (1.15)$$

where Φ is the volume fraction, C_m is the mass fraction of fibers (consistency), and w is the linear density (coarseness) of the fiber. The crowding factor can also be related to the number of contacts per fiber n_c , by employing the fiber network model of Meyer and Wahren [58],

$$N_{\text{crowd}} \approx \frac{4}{3} \frac{\pi n_c^3}{n_c - 1}. \quad (1.16)$$

Kerekes and Schell [45] observed that increasing N_{crowd} resulted in stronger flocs for both nylon and wood pulp fibers in cyclic flows of decaying turbulence. Coherent flocs tended to form for $N_{\text{crowd}} \gtrsim 60$ for longer fibers ($r_p \geq 68$), which corresponds to approximately three contacts per fiber—the minimum number of contacts necessary to lock fibers into a network [58]. Shorter nylon and wood pulp fibers ($r_p \leq 46$), however, would not flocculate even at very large values of N_{crowd} . Zhao and Kerekes [101] found that increasing the suspending fluid viscosity increased the critical crowding factor, defined as the value of N_{crowd} at which coherent flocs begin to form. Flocs formed at very high crowding factors can also be dispersed by adding water soluble polymers into concentrated pulp suspensions [100]. These results suggest flocculation is not determined solely by the value of N_{crowd} , since other parameters such as fiber flexibility, suspending fluid properties, and fiber interactions appear to be important.

The mechanisms that produce fiber networks and coherent flocs are related to fiber-fiber contacts. The phenomena that contribute to fiber contacts may be divided into four categories [47]: colloidal forces, surface tension effects, mechanical surface linkages, and elastic fiber interlocking. Figure 1.4 illustrates examples of these phenomena.

Colloidal forces between fibers occur due to the chemical characteristics of the fibers and the suspending fluid. These include electrostatic interactions, van der Waals forces, hydrogen bonding, etc. Colloidal forces are challenging to quantify for

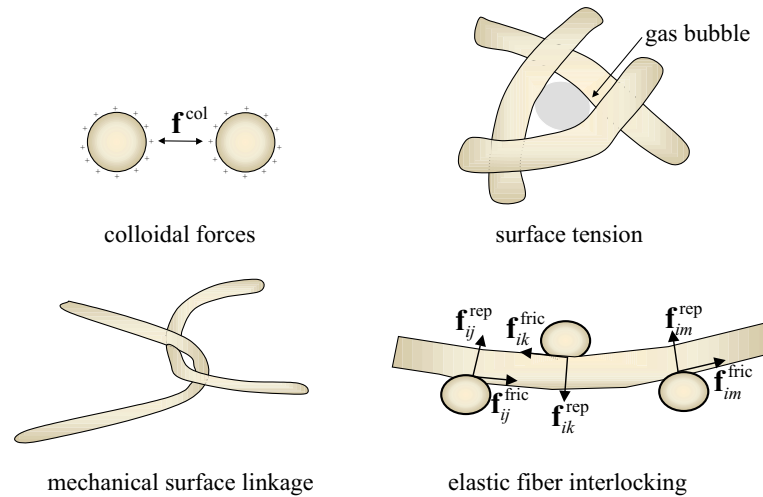


Figure 1.4: Examples of fiber interactions in a suspension.

chemically heterogeneous particles with rough surfaces, such as wood fibers.

Surface tension effects are due to entrained gas within a fiber suspension. Bubbles of gas may appear in fiber suspensions due to mixing or other processing. The bubbles lodge in particle interstices and create an effective attractive force between particles, which may affect or even cause flocculation.

Mechanical surface linkages form due to contacts involving irregularly shaped fibers and fibers with surface protrusions. Fibers like those found in pulp suspensions are naturally deformed at equilibrium and may become entangled by “hooking” or intertwining (see Fig. 1.4). In addition, fibers may be fibrillated—that is, small fibrous entities (fibrils) of the fiber may extend out from the fiber surface. In this case, the fibrils of contacting fiber surfaces may become mechanically entangled.

Elastic fiber interlocking occurs when flexible fibers form an elastic network. Flowing fiber suspensions may experience sufficient viscous forces to cause fibers to elastically deform from an equilibrium configuration. As the fibers attempt to relax, they can become locked in elastically strained configurations due to contacts with

other fibers. The fiber surfaces experience friction forces which are proportional to the normal force between fibers, and the normal force is a function of the fiber flexibility. Flocs formed through this fiber interlocking mechanism store elastic energy and have mechanical strength.

For many fiber suspensions, mechanical and elastic effects are the dominant mechanisms that determine structure and network strength [33, 47, 56]. Meyer and Wahren [58] developed a simple network theory to explain the elastic behavior observed in concentrated fiber suspensions. They assumed that fibers behave like elastic bodies that form networks in which fibers are locked in position due to interfiber contacts. Meyer and Wahren derived an expression for the network shear modulus based on the number of contacts per fiber, the fiber aspect ratio, and the fiber Young's modulus. Farnood et al. [29] used this simple network theory to develop expressions for the shear and tensile strengths of a floc. The mechanism of elastic fiber interlocking is consistent with experimental results, such as the observation that increasing the suspending fluid viscosity leads to a lower shear modulus (decrease in elastic energy storage) [83] and a less flocculated state [11, 101].

Soszynski and Kerekes [81, 82] produced experimental evidence that fiber interlocking via elastic bending exists in suspensions of nylon fibers. This was accomplished by removing coherent flocs from a suspension, heating them above the glass transition temperature of nylon to relax the bending stresses, and upon cooling, agitating the flocs to try to disperse them. The heat-treated flocs dispersed upon light agitation whereas the never-heated flocs dispersed only under strong agitation, suggesting that cohesion was caused by interlocking of elastically bent fibers. In other words, fibers need to be stiff enough to store sufficient elastic energy when deformed, and remain in strained configurations in order to form flocs or fiber networks.

Floc dispersion

Flocs are usually dispersed by applying sufficient mechanical stress to the suspension in order to break the fiber contacts and pull the flocs apart. This is often accomplished by subjecting the suspension to turbulent flow. Andersson [4] observed the motion of pulp fiber suspensions in turbulent flow. He noted that floc destruction dominated over floc formation in the turbulence zone; however, flocs were seen to form in decaying turbulence. Andersson developed an expression for the probability of floc rupture in turbulent flow using the tensile stress exerted on the fiber network. Takeuchi et al. [85] studied the destruction of flocs in a turbulent flow in various channels. The rate of destruction increased with increasing flow velocity, and the destruction time depended on the type of fiber (i.e., hardwood or softwood). In both of these studies, however, it was difficult to determine a mechanism that caused floc rupture.

Mechanisms of pulp floc rupture were qualitatively investigated by Lee and Brodkey [52], in which the break up of individual flocs was observed in turbulent flow between two oppositely moving belts. They characterized floc dispersion by two major processes, global scale disruption and small scale surface erosion. Global disruptions were distinguished by major changes to the floc shape, including breaking into secondary flocs, stretching into string-like structures, and floc disintegration. Surface erosion occurs over the surface of the floc and accounts for the loss of individual fibers from the floc. Lee and Brodkey also used the term shedding to distinguish a type of dispersion somewhere between global and surface erosion, in which flocs occasionally lose small clumps of fibers from the main body of the floc. Global scale disruptions were most prevalent at high stress levels. However, global disruption of flocs only occurred if the stress was applied for a significant time. At low stress levels in which the turbulent length scale is much larger than the floc size, flocs followed

the motion of the flow and tended to lose fibers by surface erosion and shedding mechanisms.

The fact that flocs tend to get pulled apart or form string-like structures suggests that the extensional character of the flows is important. Kerekes [43] studied the behavior of pulp flocs upon entry into constrictions, which approximate extensional flow. Kerekes observed that flocs first stretched upon entering the constriction, and then ruptured if the stress was high enough. He characterized the rupture as tensile failure after substantial elongation of the floc. Flocs did not always rupture, which was attributed to insufficient hydrodynamic stresses, and that sometimes the flocs simply did not spend enough time in the flow field to be deformed to the rupture point.

1.3.2 Fiber suspension rheology

Experimental data on fiber suspension rheology

Fiber suspensions can exhibit non-Newtonian fluid characteristics similar to polymer melts and solutions. Suspension rheological properties depend on the properties of the fluid, fibers, fiber interactions, and the flow field. Suspensions of long fibers ($r_p > 150$) in Newtonian liquids have been observed to exhibit the Weissenberg effect (i.e., rod-climbing) which becomes more pronounced as the aspect ratio and fiber concentration increase [57, 61]. Busse [17] found that Teflon fibers in some polymer melts demonstrated increased die swelling compared to the neat polymer melt. Fiber-filled polymer melts extruded through circular dies exhibited dramatic surface irregularities at low shear rates that were not attributed to polymer melt fracture [10, 48]. Measurement of the rheological properties of fiber suspensions is difficult because of the

numerous suspension parameters, as well as issues with the experimental apparatus (i.e., wall-fiber interactions).

Some suspensions of fibers exhibit visco-elastic behavior. Wahren [91] attributed this type of behavior to the formation of elastic fiber networks. He performed creep and stress relaxation measurements on pulp suspensions which demonstrated behavior similar to solid viscoelastic materials. The simple network theory of Meyer and Wahren [58] described previously performed well for predicting the shear modulus of suspensions measured experimentally [87]. Shear thinning behavior and positive first normal stress differences were observed in suspensions of long glass, nylon and vinylon fibers, which became stronger as the aspect ratio, flexibility, and concentration increased [34, 50, 51].

At lower aspect ratios ($r_p \lesssim 50$), fiber suspensions still exhibit elastic behavior [18, 64], but not as pronounced as that for longer fibers. Chaouche and Koch [18] observed that shear thinning of short nylon fibers in a viscous Newtonian fluid occurred at lower shear rates than that observed for suspensions of longer fibers. Since fibers at these conditions are quite stiff, Chaouche and Koch attributed the shear thinning behavior to adhesive forces between fibers.

At low shear rates and sufficiently high concentrations (semi-dilute), fiber suspensions require a minimum applied stress (i.e., a yield stress) to make the suspension flow. The yield stress of various wood pulp and nylon fiber suspensions in low viscosity liquids was measured by Bennington et al. [12] using a rotary shearing device. They found that the yield stress (σ_0) scaled with the volume fraction as $\sigma_0 \sim \Phi^\beta$, where the exponent β varied from 2.5-3.5, consistent with simple fiber network theory [58] which gives $\beta = 3$. The network theory also suggests that the yield stress should scale linearly with the fiber Young's modulus; however Bennington et al. did not observe

this scaling in their experiments. Kitano and Kataoka [50] measured the dynamic yield stress of vinylon fiber suspensions in a viscous silicone oil by extrapolating the shear stress data to zero shear rate. They found approximately the same dependence on volume fraction as Bennington et al. for shorter fibers ($r_p \approx 45$). Suspensions of higher aspect ratio fibers showed a substantial decrease in β , which was attributed to fiber interactions, increased effective flexibility, and wall effects.

The rheology of planar fiber networks is important in determining wet-web strength when making paper and determining the strength of formed sheets of paper. Planar fiber networks subjected to mechanical extension show viscoelastic behavior at small strains, then experience plastic deformation before the network ruptures [62]. The limiting factors in the overall strength of a fiber network is the type of contacts between fibers (i.e., friction, hydrogen bonds, etc.) and the strength of the fibers themselves [24]. Numerous other parameters affect the network strength, a summary of which has been compiled by Niskanen [62].

Mohlin et al. [60] examined the effect of shape on the tensile strength of soft-wood fiber handsheets. They measured the fiber deformation in terms of curl, which is related to the ratio of the end-to-end distance and the contour length, and by counting the number of defects (i.e., kinks, twists, microcompressions, etc.) per fiber under a microscope. Mohlin et al. observed that the network tensile strength increased as the fibers became straighter or contained fewer defects. Seth [77] observed that as fiber length increased and coarseness (mass per length of fiber) decreased, the tensile strength also increased in wet webs. This was attributed to the fact that longer fibers experience more contacts per fiber, and it is the contacts that give the network strength. Fibers that are less coarse have thinner walls which allow them to collapse and experience larger bonding areas.

The fiber shape, length, and coarseness are all affected by refining which decreases the freeness, or drainability, of the fiber network. Fibers with a high freeness tend to be deformed and have large values for the coarseness. In general, refining leads to fiber shortening, increased external fibrillation, equilibrium shape changes, and fiber collapse [53]. Thus, networks formed from refined fibers have greater tensile strengths than those formed from unrefined fibers [53, 62]. Forgacs et al. [33] also observed that the tensile strength of wet webs increased with decreasing freeness, which they attributed to the importance of friction forces between contacting fibers.

Predicting rheological behavior

Rheological properties of fiber suspensions, such as the stress, may be calculated from knowledge of the structure, i.e., the positions and orientations of the fibers. In general, the bulk average stress $\langle \boldsymbol{\sigma} \rangle$ in a particulate suspension is

$$\langle \boldsymbol{\sigma} \rangle = -P\boldsymbol{\delta} + 2\eta_o\mathbf{E}^\infty + \boldsymbol{\sigma}^p, \quad (1.17)$$

where P is the bulk pressure and $\boldsymbol{\sigma}^p$ is the particle contribution to the bulk stress. The particle contribution to the stress in a suspension of volume V is [7, 49]

$$\boldsymbol{\sigma}^p = \frac{1}{V} \sum \oint_{S_0} \{[\boldsymbol{\sigma} \cdot \mathbf{n}]\mathbf{x} - \eta_o[\mathbf{un} + \mathbf{nu}]\} dS, \quad (1.18)$$

where S_0 is the surface of a particle, \mathbf{n} is the unit outward normal to the particle surface pointing into the suspension, and the summation is over all particles in the suspension. For rigid particles, the integral over $\mathbf{un} + \mathbf{nu}$ is zero. Since the stress is symmetric [49], Eq. (1.18) simplifies to

$$\boldsymbol{\sigma}^p = \frac{1}{2V} \sum \oint_{S_0} \{[\boldsymbol{\sigma} \cdot \mathbf{n}]\mathbf{x} + \mathbf{x}[\boldsymbol{\sigma} \cdot \mathbf{n}]\} dS. \quad (1.19)$$

In order to utilize Eq. (1.19) for fibers, it is commonly assumed that the fibers are long and slender ($r_p \ll 1$), and thus $\boldsymbol{\sigma} \cdot \mathbf{n}$ may be approximated using slender-body theory [6, 23, 88]. The basic idea of slender-body theory is that the disturbance to the flow field containing a long slender body can be approximated as the disturbance due to a line distribution of point forces along the body [6]. The slender-body theory approximation for the particle contribution to the stress for long fibers that only interact via hydrodynamic interactions is given by [54]

$$\boldsymbol{\sigma}^p \simeq \frac{n}{2} \left\langle \int_{-\ell}^{\ell} \left[s\mathbf{F}(s)\mathbf{p} + s\mathbf{p}\mathbf{F}(s) - \frac{2}{3}(s\mathbf{F}(s) \cdot \mathbf{p})\boldsymbol{\delta} \right] ds \right\rangle, \quad (1.20)$$

where \mathbf{p} is the orientation vector of the fiber, $\mathbf{F}(s)$ is the point force per unit length exerted at the axial position s on the fiber, ℓ is the fiber half-length, and the angled brackets indicate the average over all fibers in the suspension. Batchelor [8] used the slender-body theory to derive an expression for $\boldsymbol{\sigma}^p$ for a dilute suspension of non-interacting rigid fibers,

$$\boldsymbol{\sigma}^p = \eta^{\text{fib}} \left[\langle \mathbf{p}\mathbf{p}\mathbf{p}\mathbf{p} \rangle : \mathbf{E}^\infty - \frac{2}{3}(\langle \mathbf{p}\mathbf{p} \rangle : \mathbf{E}^\infty)\boldsymbol{\delta} \right], \quad (1.21)$$

where $\eta^{\text{fib}} = n\pi L^3 \eta_o / 6 \ln(2r_p)$, as a first approximation for fibers with a circular cross-section.

As the concentration increases into the semi-dilute regime, fiber interactions affect the suspensions stress. Batchelor [8] developed an alternative expression for η^{fib} for semi-dilute suspensions of aligned fibers in a pure straining flow, and Shaqfeh and Fredrickson [78] generalized this for isotropically orientated fiber suspensions. Mackaplow and Shaqfeh [54] numerically calculated $\mathbf{F}(s)$ and the velocity field for a variety of fiber configurations, and used the simulated data to find the bulk stress in the suspension. They found that the simulated data corresponded well with experimental results at lower concentrations, but started to deviate as the concentration

increased. This was attributed to slender-body theory underpredicting the effects of close fiber-fiber interactions.

If fibers experience a net hydrodynamic force, Eq. (1.20) can be modified to calculate the particle stress. A net hydrodynamic force may occur due to mechanical contacts between fibers or the presence of an external force or moment. The particle contribution to the stress becomes (see Appendix A)

$$\begin{aligned} \boldsymbol{\sigma}^p \simeq & \frac{n}{2} \left\langle \int_{-\ell}^{\ell} \left[s\mathbf{F}(s)\mathbf{p} + s\mathbf{p}\mathbf{F}(s) - \frac{2}{3}(s\mathbf{F}(s) \cdot \mathbf{p})\boldsymbol{\delta} \right] ds \right. \\ & \left. + \mathbf{F}^{\text{hyd}}\mathbf{r} + \mathbf{r}\mathbf{F}^{\text{hyd}} - \frac{2}{3}(\mathbf{F}^{\text{hyd}} \cdot \mathbf{r})\boldsymbol{\delta} \right\rangle, \end{aligned} \quad (1.22)$$

where \mathbf{F}^{hyd} is the net hydrodynamic force on the fiber and \mathbf{r} is the fiber center-of-mass. Using the leading order slender-body theory approximation, the hydrodynamic force per unit length $\mathbf{F}(s)$, and the net hydrodynamic force \mathbf{F}^{hyd} are

$$\mathbf{F}(s) = \frac{8\pi\eta_o}{\ln(2r_p)} \left[\boldsymbol{\delta} - \frac{1}{2}\mathbf{p}\mathbf{p} \right] \cdot (\mathbf{U}^\infty(\mathbf{r}) - \dot{\mathbf{r}} - s\dot{\mathbf{p}}), \quad (1.23)$$

$$\mathbf{F}^{\text{hyd}} = \frac{8\pi\eta_o\ell}{\ln(2r_p)} \left[\boldsymbol{\delta} - \frac{1}{2}\mathbf{p}\mathbf{p} \right] \cdot (\mathbf{U}^\infty(\mathbf{r}) - \dot{\mathbf{r}}). \quad (1.24)$$

1.3.3 Determining fiber suspension structure

Ideally, we would like to be able to predict flocculation behavior and calculate rheological quantities *a priori*. The difficulty lies in obtaining the structure of the suspension, which is necessary for calculating the average stress in Eq. (1.22). Two methods are commonly employed for determining the structure of fiber suspensions: obtaining distribution functions from the solution of conservative equations, and direct particle-level simulations.

Distribution functions of fiber structure

Structure of fiber suspensions can be described statistically by distribution functions of the positions and orientations. The probability density of finding a fiber with center at \mathbf{r} and orientation of \mathbf{p} at time t is represented by the distribution function $\Psi(\mathbf{r}, \mathbf{p}, t)$, which can be factored as [25]

$$\Psi(\mathbf{r}, \mathbf{p}, t) = n(\mathbf{r}, t)\psi(\mathbf{p}, t), \quad (1.25)$$

where n is the position-dependent number density, and ψ is the orientation distribution function. For a spatially uniform distribution of fibers, n is a constant.

The orientation distribution function ψ can be used to calculate average orientation moments of the suspension (i.e., $\langle \mathbf{p}\mathbf{p} \rangle$, $\langle \mathbf{p}\mathbf{p}\mathbf{p}\mathbf{p} \rangle$, ...) which are typically needed for finding the suspension stress. The averages of the odd moments of \mathbf{p} are zero and the averages of the even moments such as $\langle \mathbf{p}\mathbf{p}\mathbf{p}\mathbf{p} \rangle$ are obtained via

$$\langle \mathbf{p}\mathbf{p}\mathbf{p}\mathbf{p} \rangle = \int \mathbf{p}\mathbf{p}\mathbf{p}\mathbf{p}\psi \, d\mathbf{p}. \quad (1.26)$$

The evolution of the orientational distribution function is described by the equation of continuity for ψ ,

$$\frac{D\psi}{Dt} = - \left(\frac{\partial}{\partial \mathbf{p}} \cdot \dot{\mathbf{p}}\psi \right), \quad (1.27)$$

where D/Dt is the substantial derivative operator. To solve Eq. (1.27) for ψ , a constitutive relation for the time rate of change of the fiber orientation vector $\dot{\mathbf{p}}$ is needed. Dinh and Armstrong [25] approximated $\dot{\mathbf{p}}$ with the motion of a prolate spheroid using Jeffery's equations [41], which assumes no particle interactions. Folgar and Tucker [30] added a correction term to $\dot{\mathbf{p}}$ to account for interactions,

$$\dot{\mathbf{p}} = \boldsymbol{\Omega}^\infty \times \mathbf{p} + \frac{Y^H}{Y^C} [\mathbf{E}^\infty \cdot \mathbf{p} - \mathbf{E}^\infty : \mathbf{p}\mathbf{p}\mathbf{p}] - C_I \dot{\gamma} \frac{1}{\psi} \frac{\partial \psi}{\partial \mathbf{p}}, \quad (1.28)$$

where the last term describes the rotary diffusion of a fiber, characterized by an empirical constant C_I called the interaction coefficient. Numerous researchers have used this method to estimate macroscopic flow properties of fiber suspensions [25, 30, 40, 68, 69, 90]. Fan et al. [27] assumed that rotary diffusion was effectively a random process, and replaced the rotary diffusion term in Eq. (1.28) with a Brownian noise term. These methods can be used to predict suspension averaged properties by assuming a form of the particle stress that depends on the moments \mathbf{p} , but they cannot predict the evolution of heterogeneous distributions of particle mass, as is required to describe flocculation.

Direct simulation techniques

Direct particle-level simulation techniques are used to calculate the position and orientation history of a system of particles in a fluid by numerically solving Newton's equations of motion (conservation of linear and angular momentum) for each particle i ,

$$m_i \ddot{\mathbf{r}}_i = \sum \mathbf{F}_i, \quad (1.29)$$

$$\mathbf{J}_i \cdot \dot{\boldsymbol{\omega}}_i = \sum \mathbf{T}_i, \quad (1.30)$$

where m_i is the particle mass, \mathbf{J}_i is the moment of inertia tensor, and \mathbf{F}_i and \mathbf{T}_i are the forces and torques on particle i . The forces and torques acting on the particle may include contributions due to hydrodynamic drag, hydrodynamic interactions, external fields, Brownian motion, direct mechanical interactions, and any additional kinematic constraints to the particle motion. Particle inertia is often neglected as well, which reduces the equations of motion to simple force and torque balances on the particles.

If the particle Reynolds number [Eq. (1.3)] is much less than one, the velocity disturbances caused by the particles are described by the Stokes equation, which results in a linear relationship between all of the particle velocities, angular velocities, and rate of strain tensors [$\mathbf{U} = (\mathbf{U}^\infty - \dot{\mathbf{r}}, \boldsymbol{\Omega}^\infty - \boldsymbol{\omega}, \mathbf{E}^\infty)$] and the hydrodynamic forces, torques, and stresslets [$\mathbf{F} = (\mathbf{F}, \mathbf{T}, \mathbf{S})$] on the particles [26],

$$\mathbf{U} = \mathbf{R}^{-1}\mathbf{F}. \quad (1.31)$$

The matrix \mathbf{R} is called the *grand resistance* matrix, which depends only on the positions and orientations of the particles. Determining the grand resistance matrix exactly requires the solution of the many-body Stokes equation. Approximate solution methods employing appropriate summations of far-field and near-field (lubrication) pairwise hydrodynamic interactions are commonly employed [26, 49].

The term *Stokesian Dynamics* is used to describe the solution of Eqs. (1.29)-(1.30) for hydrodynamically interacting particles and was originally used to solve for the motion of suspensions of spherical particles [14]. The method was generalized by Claeys and Brady [20] to describe suspensions of fibers modelled as prolate spheroids (ellipses of revolution). The attraction of using prolate spheroids is that the local surfaces are continuous, and that exact expressions for pair resistance functions can be obtained [20, 49]. Inter-particle separations may be calculated for arbitrarily orientated particle pairs in a straightforward manner, and thus interactions between fiber surfaces can be obtained. Claeys and Brady calculated macroscopic suspension properties with this simulation technique, including the translational diffusivity, the rotational diffusivity, the permeability in fibrous packing, and the suspension viscosity [20, 21, 22]. The disadvantages of this method are the difficulty in building the grand resistance matrix and the computational expense of finding inter-particle separations as the spheroid aspect ratio increases.

Fibers in real suspensions typically resemble cylinders more closely than prolate spheroids. Yamane et al. [98] simulated suspensions of non-Brownian cylinders subjected to simple shear flow in the semi-dilute concentration regime ($nL^3 > 1$). They assumed that the fiber motion could be approximated as that of an isolated fiber in a Jeffery orbit plus a small perturbation due to near-field hydrodynamic interactions (i.e., lubrication forces). Lubrication forces between interacting particles are proportional to the rate of change of the separation distance between fibers. Fan et al. [28] improved upon this model by taking into account long range hydrodynamic interactions via slender body theory. While this method gave better results for the Folgar-Tucker constant at higher concentrations compared to that reported by Yamane et al., it was significantly more computationally demanding and did not qualitatively change the suspension property predictions. Both methods showed quantitative agreement with experimental data for the viscosity at lower concentrations, but the viscosity deviated as the concentration increased.

As discussed in Section 1.3.1, one of the major causes of structural changes in fiber suspensions (i.e., flocculation) is mechanical contacts. Sundararajakumar and Koch [84] developed a fiber simulation method that included direct mechanical contacts, while neglecting hydrodynamic interactions. They explicitly calculated the normal force required to keep contacting fibers from passing through each other by using the constraint of no relative motion in the normal direction between contacting fibers. The results for the suspension viscosity and first normal stress difference as a function of concentration showed good agreement with some experimental results. Their argument for neglecting hydrodynamic interactions is based on how they affect fiber flipping, and thus the orientation distribution, compared to that resulting from mechanical contacts. By using the results of Rahnema et al. [67] for the orientation

distributions of hydrodynamically interacting fibers, Sundararajakumar and Koch found that for fibers with moderate aspect ratios ($r_p < 60$), mechanical contacts are the main cause of orientational dispersion. As the aspect ratio increases, they argued that hydrodynamic interactions become more important relative to mechanical contacts. However, at concentrations large enough such that each fiber experiences multiple contacts, mechanical contacts will again dominate over hydrodynamic interactions in determining the suspension dynamics. Evidence for the importance of hydrodynamic interactions is further supported by the work of Harlen et al. [35] for simulations of falling ball rheometry of fiber suspensions. They found only modest differences in the drag coefficient by including hydrodynamic interactions with mechanical contacts compared to simulations with only mechanical contacts, with smaller differences as the concentration increased. Simulations of fibers with mechanical contacts also showed positive first normal stress differences, while fibers that only interact via hydrodynamic interactions do not exhibit a first normal stress difference [66].

Simulation techniques have recently been developed to investigate flexible fiber suspensions as well. Yamamoto and Matsuoka [93, 94, 95, 96, 97] developed a model for fibers consisting of linked spheres. The joints between spheres allowed for bending, twisting, and stretching such that the fibers could assume arbitrary conformations. The forces and torques on the spheres included: hydrodynamic interactions among spheres in a single fiber, stretching forces between adjacent spheres in a fiber, bending and twisting torques between adjacent spheres in a fiber, tangential frictional forces and moments between adjacent spheres in a fiber, and lubrication forces between spheres on different fibers. The attraction of modelling flexible fibers in this way is that calculating the motion of hydrodynamically interacting spheres is well under-

stood through the use of Stokesian dynamics [14]. Yamamoto and Matsuoka used this model to predict the viscosity, normal stresses, and structure of fiber suspensions [94, 96, 97]. They also examined fiber fracture in linear flow fields [95]. The main disadvantage of this method is the computational cost. For fibers of moderate aspect ratio, many spheres are required to describe a suspension in the semi-dilute regime. The model requires that one solve a $6N \times 6N$ linear system of equations where N is the number of spheres in a fiber, as well as satisfy a set of constraint equations at every time step.

Ross and Klingenberg [71] constructed a simulation model where each fiber is represented by N_{seg} rigid prolate spheroids connected end-to-end in order to represent fibers of larger aspect ratios. The prolate spheroids are connected by ball and socket joints, which allow for bending and twisting. This hinge constraint replaces Yamamoto and Matsuoka's friction constraint, and the force necessary to hold fiber segments together is calculated directly. Hydrodynamic interactions were neglected, and a short-range repulsive force was employed to prevent spheroids from overlapping significantly. The model correctly predicted single fiber dynamics, including flexible orbits like those seen experimentally [31, 32, 89], and orbit drift due to fiber flexibility [80]. They were also able to calculate the relative viscosity of fiber suspensions, which compared reasonably well with experimental data. A disadvantage of this approach is the difficulty of finding interfiber separations among spheroids (which requires an iterative method).

In order to simplify the calculation of interfiber separations, Schmid et al. [75] modelled flexible fibers as chains of circular cylinders with hemispherical end-caps connected by ball and socket joints. The fibers interact with mechanical contacts via short-range repulsive forces as well as static friction forces. The inclusion of friction

forces, flexibility, and deformed equilibrium shape—in the absence of attractive forces between fibers—resulted in the formation of heterogeneous structures (i.e., flocs).

The work presented in this thesis is an extension of the model of Schmid et al., in which flexible fibers are modelled as linked rigid bodies. We investigate the effects of fiber characteristics such as flexibility, equilibrium shape, and mechanical interactions on the structure of semi-dilute fiber suspensions. The simulation results illustrate the parameters that are important for predicting flocculation behavior and the rheological properties (i.e., stress and viscosity) of fiber suspensions. The model is also used to examine floc break-up in various linear flow fields, as well as the tensile strength of planar fiber networks.

Chapter 2

Simulation method

We have developed a particle-level simulation technique to model systems of flexible fibers. The model incorporates realistic fiber features such as deformed equilibrium shapes, fiber flexibility, and mechanical contacts (e.g., friction). Each fiber is modelled as a series of N_{seg} linked rigid cylinders, with hemispherical end-caps connected by ball and socket joints. Figure 2.1 illustrates the segments of a fiber, where the center-of-mass of each segment i is represented by \mathbf{r}_i , and the orientation vector is \mathbf{p}_i . Fiber joints are numbered starting with a virtual joint at the free end of the first segment. Each segment has a length 2ℓ measured with respect to the center of the hemisphere end-caps, and a diameter of $2b$ which results in a fiber segment aspect ratio of $r_{ps} \equiv \ell/b$. The overall fiber aspect ratio is $r_p = L/2b$ where $L = 2\ell N_{\text{seg}}$.

2.1 Equations of motion

The motion of fibers is described by Newton's equations of motion [Eqs. (1.29)-(1.30)]. Particle inertia is neglected which simplifies the equations of motion to simple force and torque balances on each segment i of a fiber. The forces that act on a fiber segment i include hydrodynamic forces ($\mathbf{F}_i^{\text{hyd}}$), external force fields ($\mathbf{F}_i^{\text{ext}}$), mechanical

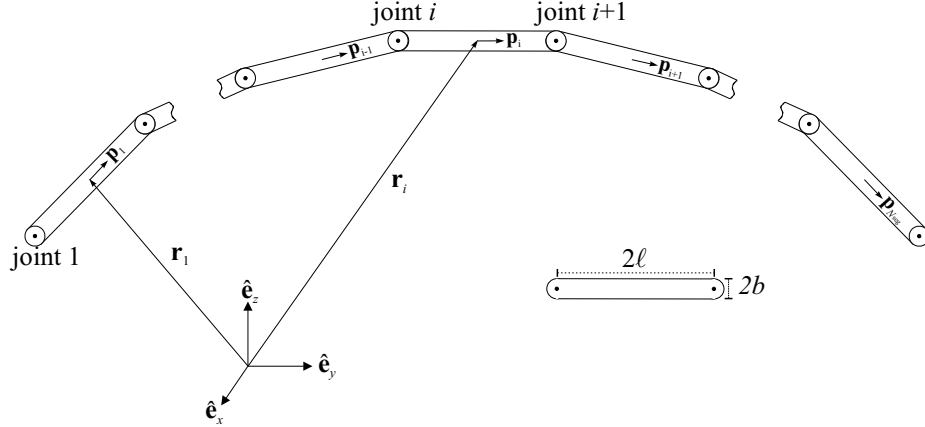


Figure 2.1: Model fiber made up of N_{seg} rigid sphero-cylinders connected by ball and socket joints.

contact forces with segments j ($\mathbf{F}_{ij}^{\text{con}}$), and forces at each joint that keep the fiber at a constant length (\mathbf{X}_i),

$$\mathbf{F}_i^{\text{hyd}} + \mathbf{F}_i^{\text{ext}} + \sum_j^{N_{C_i}} \mathbf{F}_{ij}^{\text{con}} + \mathbf{X}_{i+1} - \mathbf{X}_i = \mathbf{0}, \quad (2.1)$$

where N_{C_i} is the number of contacts on fiber segment i . The torque balance on fiber segment i includes similar contributions with the addition of a restoring torque at each joint (\mathbf{Y}_i),

$$\mathbf{T}_i^{\text{hyd}} + \mathbf{T}_i^{\text{ext}} + \sum_j^{N_{C_i}} [\mathbf{G}_{ij} \times \mathbf{F}_{ij}^{\text{con}}] + \ell \mathbf{p}_i \times [\mathbf{X}_{i+1} + \mathbf{X}_i] + \mathbf{Y}_{i+1} - \mathbf{Y}_i = \mathbf{0}, \quad (2.2)$$

where $\mathbf{T}_i^{\text{hyd}}$ is the hydrodynamic torque and $\mathbf{T}_i^{\text{ext}}$ is an external moment exerted on the suspension. The vector \mathbf{G}_{ij} is the vector from the segment center to the point of contact with segment j ,

$$\mathbf{G}_{ij} = s_{ij} \mathbf{p}_i + \frac{g_{ij}}{2} \mathbf{n}_{ij},$$

where s_{ij} is the distance from segment center i to the point of contact with segment j directed along the segment axis with respect to direction of \mathbf{p}_i ; g_{ij} is the minimum centerline separation distance between fiber segments; and \mathbf{n}_{ij} is the normal vector

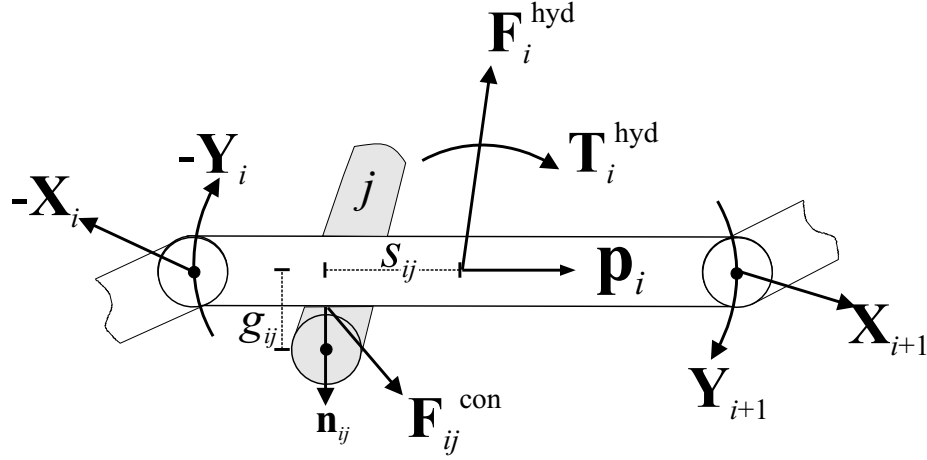


Figure 2.2: Forces and torques acting on fiber segment i in contact with segment j .

at the point of minimum separation directed for segment i to j . Fig. 2.2 illustrates the forces and torques on segment i .

2.2 Hydrodynamic forces and torques

Hydrodynamic interactions are neglected based on simulations performed by Sundararajakumar and Koch, and Harlen et al. [35, 84] as explained in Section 1.3.3. The hydrodynamic drag force and torque are approximated with the expressions for an isolated prolate spheroid with an equivalent aspect ratio r_e . The value of r_e is chosen so that the model fiber has approximately the same period of rotation as that measured experimentally for cylindrical fibers [89]. The ratio r_e/r_p in general depends weakly on the fiber aspect ratio [73], and we choose the average value $r_e/r_p = 0.7$ for our simulations. The expressions for the hydrodynamic force and torque on each fiber segment are [49]

$$\mathbf{F}_i^{\text{hyd}} = 6\pi\eta_o\ell\mathbf{A}_i \cdot (\mathbf{U}_i^\infty - \dot{\mathbf{r}}_i), \quad (2.3)$$

$$\mathbf{T}_i^{\text{hyd}} = 8\pi\eta_o\ell^3 \left[\mathbf{C}_i \cdot (\boldsymbol{\Omega}^\infty - \boldsymbol{\omega}_i) + \tilde{\mathbf{H}}_i : \mathbf{E}^\infty \right], \quad (2.4)$$

where η_o is the suspending fluid viscosity, $\dot{\mathbf{r}}_i$ is the segment translational velocity, and $\boldsymbol{\omega}_i$ is the segment angular velocity. The hydrodynamic resistance tensors \mathbf{A}_i , \mathbf{C}_i , and $\tilde{\mathbf{H}}_i$ are

$$\begin{aligned}\mathbf{A}_i &= Y^A \boldsymbol{\delta} + (X^A - Y^A) \mathbf{p}_i \mathbf{p}_i, \\ \mathbf{C}_i &= Y^C \boldsymbol{\delta} + (X^C - Y^C) \mathbf{p}_i \mathbf{p}_i, \\ \tilde{\mathbf{H}}_i &= -Y^H \boldsymbol{\epsilon} \cdot \mathbf{p}_i \mathbf{p}_i.\end{aligned}$$

where $\boldsymbol{\epsilon}$ is the alternating unit tensor. The scalar resistance functions X^A , Y^A , X^C , Y^C , and Y^H depend only on the segment eccentricity, $e \equiv (1 - 1/r_{e_s}^2)^{1/2}$, and are given by

$$\begin{aligned}X^A &= \frac{8}{3}e^3 [-2e + (1 + e^2)D]^{-1}, \\ Y^A &= \frac{16}{3}e^3 [2e + (3e^2 - 1)D]^{-1}, \\ X^C &= \frac{4}{3}e^3(1 - e^2) [2e - (1 - e^2)D]^{-1}, \\ Y^C &= \frac{4}{3}e^3(2 - e^2) [-2e + (1 + e^2)D]^{-1}, \\ Y^H &= \frac{4}{3}e^5 [-2e + (1 + e^2)D]^{-1},\end{aligned}\tag{2.5}$$

in which $D = \ln(1 + e/1 - e)$.

2.3 External forces

The external forces and torques ($\mathbf{F}_i^{\text{ext}}$ and $\mathbf{T}_i^{\text{ext}}$) are due to any external fields such as gravity, electric fields, magnetic fields, etc. For the work reported here, the fibers are assumed to be neutrally buoyant and no other external fields are applied (i.e., $\mathbf{F}_i^{\text{ext}} = \mathbf{T}_i^{\text{ext}} = \mathbf{0}$).

2.4 Contact forces

Fibers experience mechanical contacts with other fibers in the suspension. The force that results from each contact is decomposed into two components,

$$\mathbf{F}_{ij}^{\text{con}} = \mathbf{F}_{ij}^{\text{N}} + \mathbf{F}_{ij}^{\text{fric}}, \quad (2.6)$$

where $\mathbf{F}_{ij}^{\text{N}}$ is the force in the normal direction of the contact and $\mathbf{F}_{ij}^{\text{fric}}$ is the frictional force in the plane of the contact. The friction force will be describe in more detail in Section 2.5.2.

The purely repulsive normal force exerted on segment i by segment k is modelled

$$\mathbf{F}_{ij}^{\text{N}} = -6\pi\eta_0\ell F \exp[-ah_{ij}]\mathbf{n}_{ij}, \quad (2.7)$$

where the separation between the surfaces of segments i and j is h_{ij} , F is the magnitude of the normal force, and a is related to the decay distance of the normal force. The simulations presented here use the values $F = 150b\dot{\gamma}$ and $a = 20/b$, where $\dot{\gamma}$ is the ambient deformation rate.

To find the minimum separation distance between spherocylinder segments (i.e., circular cylinders with hemispherical end-caps), we must consider three possible scenarios: side-side interactions, end-side interactions, and end-end interactions. Fig 2.3 illustrates these types of interactions.

The separation distance is found by first calculating the minimum separation between two lines that lie along the axes of the two fiber segments of interest. Consider two segments i and j in which the separation between the lines through the axes relative to arbitrary points on the segment axes is

$$g(s'_{ij}, s'_{ji}) = |\mathbf{r}_j + s'_{ji}\mathbf{p}_j - \mathbf{r}_i - s'_{ij}\mathbf{p}_i|, \quad (2.8)$$

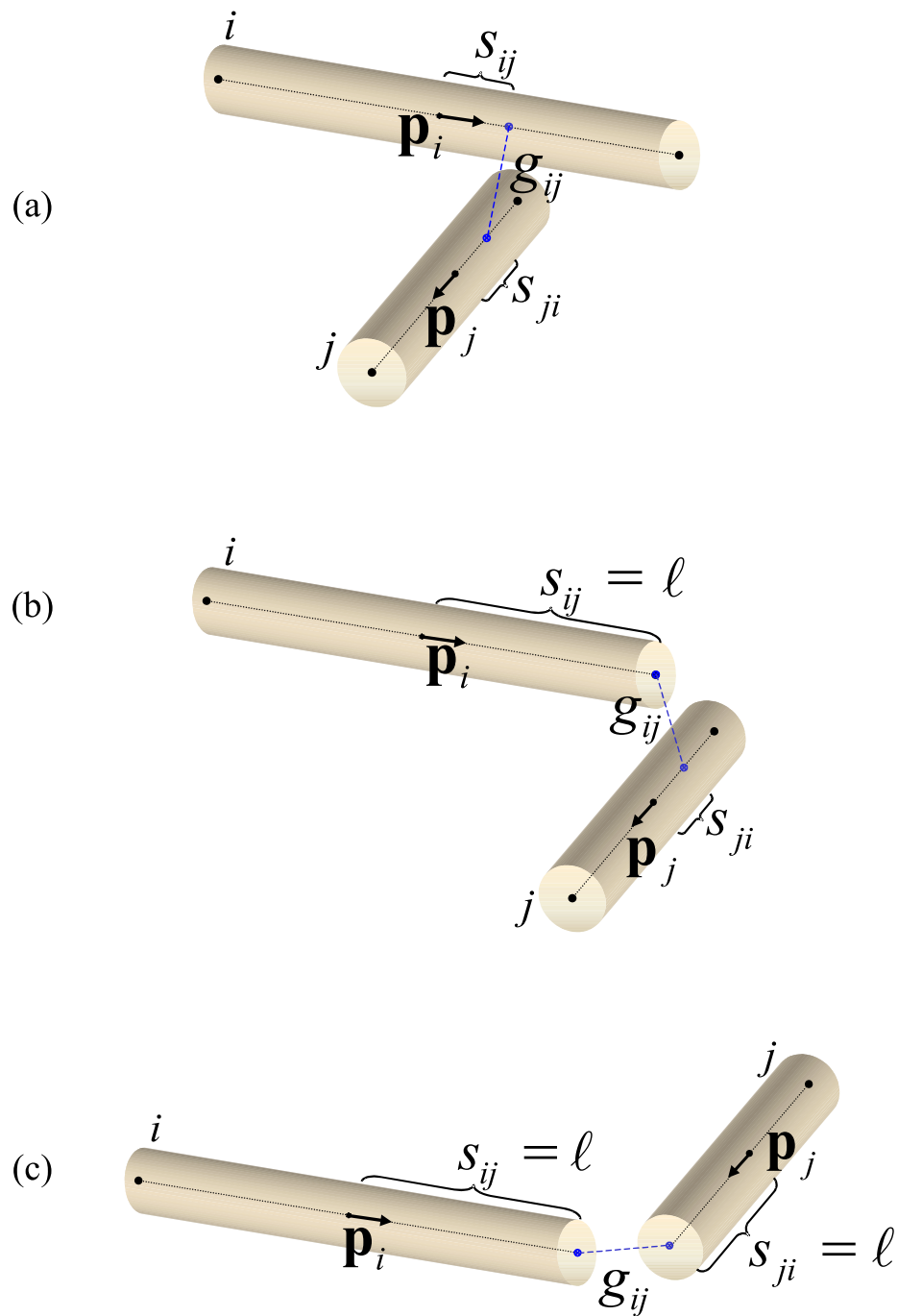


Figure 2.3: Three possible scenarios for interactions between fiber segments i and j , (a) side-side, (b) end-side, or (c) end-end interactions.

where s'_{ij} and s'_{ji} are the distances along the axes from the center of the segments in the directions \mathbf{p}_i and \mathbf{p}_j , respectively. The minimum distance between these lines is found by solving the system of equations,

$$\frac{\partial g}{\partial s'_{ij}} = 0, \quad (2.9)$$

$$\frac{\partial g}{\partial s'_{ji}} = 0, \quad (2.10)$$

for s'_{ij} and s'_{ji} . The values for s'_{ij} and s'_{ji} which result in the minimum separation between the lines are

$$s'_{ij} = s_{ij} = \frac{[(\mathbf{r}_i - \mathbf{r}_j) \cdot \mathbf{p}_j](\mathbf{p}_i \cdot \mathbf{p}_j) - (\mathbf{r}_i - \mathbf{r}_j) \cdot \mathbf{p}_i}{1 - (\mathbf{p}_i \cdot \mathbf{p}_j)^2}, \quad (2.11)$$

$$s'_{ji} = s_{ji} = \frac{[(\mathbf{r}_j - \mathbf{r}_i) \cdot \mathbf{p}_i](\mathbf{p}_i \cdot \mathbf{p}_j) - (\mathbf{r}_j - \mathbf{r}_i) \cdot \mathbf{p}_j}{1 - (\mathbf{p}_i \cdot \mathbf{p}_j)^2}. \quad (2.12)$$

Once s_{ij} and s_{ji} are known, the type of interaction is evaluated. If both $|s_{ij}|$ and $|s_{ji}|$ are less than the fiber half length ℓ , then a side-side interaction occurs [Fig. 2.3(a)]. An end-side interaction occurs, for example, when a hemispherical end of segment i interacts with the side of segment j as in Fig. 2.3(b), corresponding to $|s_{ij}| > \ell$ and $|s_{ji}| < \ell$. The minimum separation is now the minimum distance from the end of fiber i to the axis of segment j , and is found by setting $s_{ij} = \pm\ell$ and $s_{ji} = \mathbf{p}_j \cdot (\mathbf{r}_i \pm \ell\mathbf{p}_i - \mathbf{r}_j)$, where the sign depends on which end of the fiber is involved. When both $|s_{ij}| > \ell$ and $|s_{ji}| > \ell$ as determined by Eqs. (2.11) and (2.12), an end-end interaction occurs as shown in Fig. 2.3(c). The positions on the segment axes where the minimum separation is measured becomes $s_{ij} = \pm\ell$ and $s_{ji} = \pm\ell$. Table 2.1 summarizes the nine possible interaction scenarios and how to evaluate s_{ij} and s_{ji} .

Once the proper values of s_{ij} and s_{ji} are found, the separation distance g_{ij} between fiber segment axes is calculated via

$$g_{ij} = |\mathbf{r}_j + s_{ji}\mathbf{p}_j - \mathbf{r}_i - s_{ij}\mathbf{p}_i|, \quad (2.13)$$

Table 2.1: Evaluation of s_{ij} and s_{ji} for interacting segments i and j by side-side, end-side, or end-end interactions based on the original values found with Eqs. (2.11)-(2.12).

Original Result of Eqs. (2.11)-(2.12)		Type	s_{ij}	s_{ji}
$s_{ij} < \ell$	$s_{ji} < \ell$	side-side	Eq. (2.11)	Eq. (2.12)
$s_{ij} < \ell$	$s_{ji} > \ell$	end-side	$\mathbf{p}_i \cdot (\mathbf{r}_j + \ell \mathbf{p}_j - \mathbf{r}_i)$	ℓ
$s_{ij} < \ell$	$s_{ji} < -\ell$	end-side	$\mathbf{p}_i \cdot (\mathbf{r}_j - \ell \mathbf{p}_j - \mathbf{r}_i)$	$-\ell$
$s_{ij} > \ell$	$s_{ji} < \ell$	end-side	ℓ	$\mathbf{p}_j \cdot (\mathbf{r}_i + \ell \mathbf{p}_i - \mathbf{r}_j)$
$s_{ij} < -\ell$	$s_{ji} < \ell$	end-side	$-\ell$	$\mathbf{p}_j \cdot (\mathbf{r}_i - \ell \mathbf{p}_i - \mathbf{r}_j)$
$s_{ij} > \ell$	$s_{ji} > \ell$	end-end	ℓ	ℓ
$s_{ij} > \ell$	$s_{ji} < -\ell$	end-end	ℓ	$-\ell$
$s_{ij} < -\ell$	$s_{ji} > \ell$	end-end	$-\ell$	ℓ
$s_{ij} < -\ell$	$s_{ji} < -\ell$	end-end	$-\ell$	$-\ell$

and the surface separation is simply $h_{ij} = g_{ij} - 2b$. The normal unit vector between segments at the point of minimum separation directed from i to j is

$$\mathbf{n}_{ij} = \frac{\mathbf{r}_j + s_{ji} \mathbf{p}_j - \mathbf{r}_i - s_{ij} \mathbf{p}_i}{g_{ij}}. \quad (2.14)$$

If $h_{ij} \leq h_{\text{lim}}$ where h_{lim} is the maximum interaction distance, then the fiber segments interact with a normal force given by Eq. (2.7). In addition, if $h_{ij} \leq h_{\text{cut}}$ where h_{cut} is the contact cutoff distance ($h_{\text{cut}} \leq h_{\text{lim}}$), then the fiber segments are said to be in contact and interact with a friction force in the plane of contact as well as the normal force.

Fibers that experience contacts are sorted into groups, in order to facilitate the solution of the equations of motion (described below). As interactions are encountered, the sorting algorithm groups the fibers based on four criteria: (1) if neither fiber is contained in a group yet, a new group is formed; (2) if one of the fibers has been previously sorted into a group, the new interacting fiber is added; (3) if both fibers have been previously counted in different groups, both groups are combined into the group containing the fiber with the lower index; and (4) if both fibers are already in the same group, the number of fibers in the group is not affected and

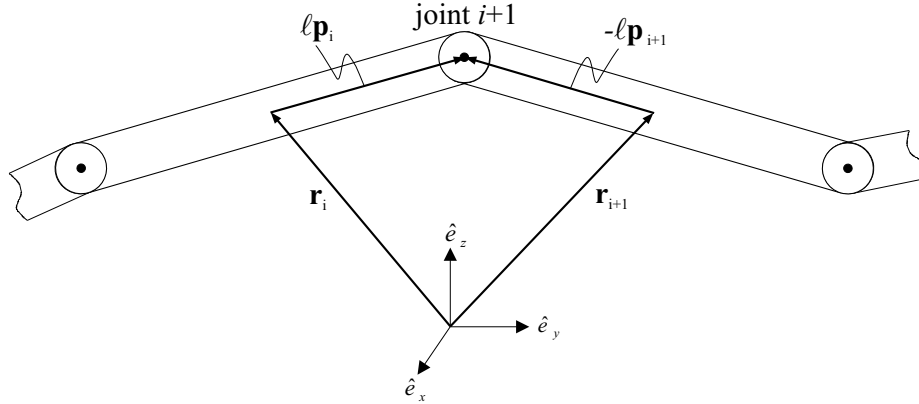


Figure 2.4: The inextensibility constraint causes the end-points of adjacent fibers to coincide.

an additional contact is counted. Contacts that occur at hinges are counted as one contact in the sorting algorithm, in which the lower indexed segment is chosen as the contacting body.

2.5 Constraint forces

2.5.1 Inextensibility constraint

A force \mathbf{X}_i is applied at each joint to keep the fiber at a constant length L . The value of \mathbf{X}_i is found by applying a holonomic constraint, which is only a function of positions and orientations of the connected segments. The constraint for joint $i + 1$ is

$$\Psi_i(\mathbf{r}, \mathbf{p}) = \mathbf{r}_i + \ell \mathbf{p}_i - (\mathbf{r}_{i+1} - \ell \mathbf{p}_{i+1}) = \mathbf{0}, \quad (2.15)$$

and is illustrated in Fig. 2.4. The constraint demands that the end points of fiber segments that share a joint coincide. The force applied at the virtual joint is always $\mathbf{X}_1 = 0$.

2.5.2 Friction constraint

Segments i and j that are in contact ($h_{ij} \leq h_{\text{cut}}$) may experience a friction force at the contact. A constraint that allows for no relative motion between segments i and j in the plane of the contact is needed to find the friction force $\mathbf{F}_{ij}^{\text{fric}}$,

$$\Xi_{ij}(\mathbf{r}, \mathbf{p}, \dot{\mathbf{r}}, \dot{\mathbf{p}}, \mathbf{F}_{ij}^{\text{fric}}) = \begin{pmatrix} \Delta \mathbf{u}_{ij} \cdot \mathbf{e}_{ij}^1 \\ \Delta \mathbf{u}_{ij} \cdot \mathbf{e}_{ij}^2 \\ \mathbf{F}_{ij}^{\text{fric}} \cdot \mathbf{n}_{ij} \end{pmatrix} = \mathbf{0}, \quad (2.16)$$

where the orthonormal unit vectors \mathbf{e}_{ij}^1 and \mathbf{e}_{ij}^2 define the plane of contact as shown in Fig. 2.5,

$$\mathbf{e}_{ij}^1 = \frac{[\boldsymbol{\delta} - \mathbf{n}_{ij} \mathbf{n}_{ij}] \cdot \hat{\mathbf{e}}_x}{|[\boldsymbol{\delta} - \mathbf{n}_{ij} \mathbf{n}_{ij}] \cdot \hat{\mathbf{e}}_x|}, \quad (2.17)$$

$$\mathbf{e}_{ij}^2 = \frac{\mathbf{n}_{ij} \times \mathbf{e}_{ij}^1}{|\mathbf{n}_{ij} \times \mathbf{e}_{ij}^1|}. \quad (2.18)$$

The velocity difference $\Delta \mathbf{u}_{ij}$ between fibers i and j at the contact point is,

$$\Delta \mathbf{u}_{ij} = \frac{d}{dt} \left[\left(\mathbf{r}_i + s_{ij} \mathbf{p}_i + \frac{g_{ij}}{2} \mathbf{n}_{ij} \right) - \left(\mathbf{r}_j + s_{ji} \mathbf{p}_j - \frac{g_{ij}}{2} \mathbf{n}_{ij} \right) \right] = \mathbf{0}. \quad (2.19)$$

Substituting $\dot{\mathbf{p}}_i = \boldsymbol{\omega}_i \times \mathbf{p}_i$ and $\dot{\mathbf{n}}_{ij} = \boldsymbol{\omega}_i \times \mathbf{n}_{ij}$ yields

$$\Delta \mathbf{u}_{ij} = \dot{\mathbf{r}}_i - \dot{\mathbf{r}}_j + \boldsymbol{\omega}_i \times \mathbf{G}_{ij} - \boldsymbol{\omega}_j \times \mathbf{G}_{ji}. \quad (2.20)$$

Combining the friction constraint with the equations of motion [Eqs. (2.1)-(2.2)] and the inextensibility constraint [Eq. (2.15)] allows for the solution of the friction forces $\mathbf{F}_{ij}^{\text{fric}}$ for all contacting segments. The friction forces are subjected to a Coulombic friction law,

$$\begin{aligned} |\mathbf{F}_{ij}^{\text{fric}}| &\leq \mu^{\text{stat}} |\mathbf{F}_{ij}^{\text{N}}| \Rightarrow \text{contact remains intact} \\ &> \mu^{\text{stat}} |\mathbf{F}_{ij}^{\text{N}}| \Rightarrow \mathbf{F}_{ij}^{\text{fric}} = \mu^{\text{kin}} |\mathbf{F}_{ij}^{\text{N}}| \frac{\Delta \mathbf{u}_{ij}}{|\Delta \mathbf{u}_{ij}|}, \end{aligned} \quad (2.21)$$

where μ^{stat} and μ^{kin} are the static and kinetic coefficients of friction, respectively.

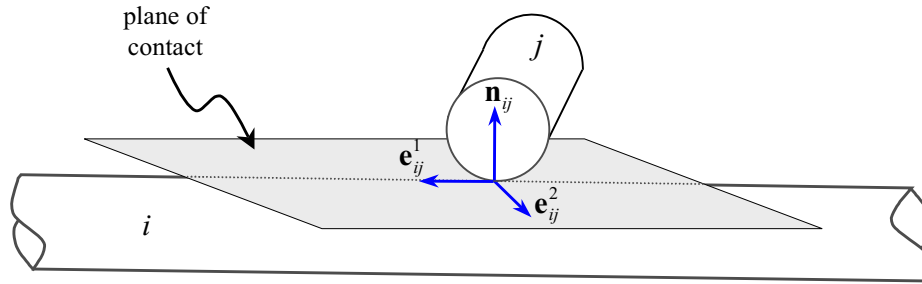


Figure 2.5: The frictional force at a contact is constrained to a plane perpendicular to the normal between the segment centers at the contact point, \mathbf{n}_{ij} . The plane of contact contains the orthogonal unit vectors, \mathbf{e}_{ij}^1 and \mathbf{e}_{ij}^2 .

2.6 Restoring torque

In the model, restoring torques \mathbf{Y}_i are prescribed at the joints to resist deformation. Like the inextensibility constraint forces, the restoring torque at the first joint is $\mathbf{Y}_1 = \mathbf{0}$ since it is a virtual joint. The restoring torque in joint i is decomposed into bending and twisting contributions, $\mathbf{Y}_i = \mathbf{Y}_i^b + \mathbf{Y}_i^t$. The individual components \mathbf{Y}_i^b and \mathbf{Y}_i^t are approximated from beam theory for small deformations. Each moment is proportional to the difference between the angle at the joint formed by connected segments and its equilibrium value,

$$\mathbf{Y}_i^b = -\kappa_b (\theta_i - \theta_i^{\text{eq}}) \mathbf{e}_i^b, \quad (2.22)$$

$$\mathbf{Y}_i^t = -\kappa_t (\phi_i - \phi_i^{\text{eq}}) \mathbf{e}_i^t, \quad (2.23)$$

where θ_i and ϕ_i are the bending and twisting angles and θ_i^{eq} and ϕ_i^{eq} are the equilibrium values (measured in radians throughout this document except where noted); \mathbf{e}_i^b and \mathbf{e}_i^t are the unit vectors in the directions of the bending and twisting torques; and κ_b and κ_t are the bending and twisting constants. The bending constant is approximated as that of an elastic cylinder subject to small deformations, $2\ell\kappa_b = E_Y I$, where E_Y is the Young's modulus of the fiber and I is the area moment of the fiber cross-section

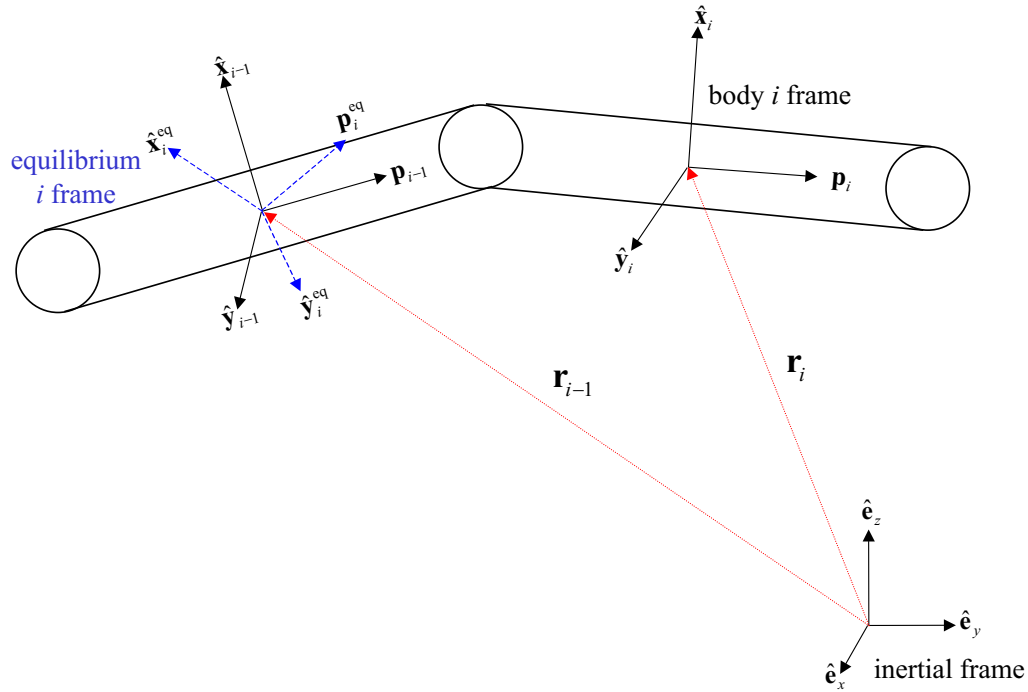


Figure 2.6: Relationship between the three types of coordinate frames related to segment i : inertial frame, body i frame, and equilibrium body i frame.

(see Appendix B for the derivation of κ_b). The twisting constant is approximated with $\kappa_t/\kappa_b = 0.67$, which is equivalent to an elastic cylinder with a Poisson's ratio of 0.5.

2.6.1 Frames of reference

Three frames of reference are considered in order to describe the orientation of a fiber segment: the inertial (laboratory) frame, the segment i body frame, and the equilibrium i body frame. The inertial frame is a frame of reference that remains fixed in space and time. The equations of motion are evolved with respect to the inertial frame. The body and equilibrium frame coordinate systems evolve with the dynamics of the segment to which they are attached. Fig. 2.6 illustrates the relationship between the three frames of reference.

Each segment i has a body coordinate frame associated with it which is defined with respect to the orientation vector \mathbf{p}_i , and two arbitrary unit vectors $\hat{\mathbf{x}}_i$ and $\hat{\mathbf{y}}_i$ that form an orthonormal coordinate system $(\hat{\mathbf{x}}_i, \hat{\mathbf{y}}_i, \mathbf{p}_i)$. This frame remains fixed to segment i as it translates with velocity $\dot{\mathbf{r}}_i$ and rotates with angular velocity $\boldsymbol{\omega}_i$. Once the body frame is chosen, the coordinates of an arbitrary vector \mathbf{w}_i in the inertial frame can be transformed into the body frame coordinates, \mathbf{w}'_i , by a linear transformation of the form $\mathbf{w}'_i = \mathcal{R}_i \cdot \mathbf{w}_i$. The rotation matrix \mathcal{R}_i is orthogonal ($\mathcal{R}_i^{-1} = \mathcal{R}_i^\dagger$) and the components are the direction cosines:

$$\mathcal{R}_i = \begin{pmatrix} \hat{\mathbf{x}}_i \cdot \hat{\mathbf{e}}_x & \hat{\mathbf{x}}_i \cdot \hat{\mathbf{e}}_y & \hat{\mathbf{x}}_i \cdot \hat{\mathbf{e}}_z \\ \hat{\mathbf{y}}_i \cdot \hat{\mathbf{e}}_x & \hat{\mathbf{y}}_i \cdot \hat{\mathbf{e}}_y & \hat{\mathbf{y}}_i \cdot \hat{\mathbf{e}}_z \\ \mathbf{p}_{xi} & \mathbf{p}_{yi} & \mathbf{p}_{zi} \end{pmatrix}. \quad (2.24)$$

The inertial frame is in Cartesian coordinates, which makes the base vectors $\hat{\mathbf{e}}_x = (1, 0, 0)$, $\hat{\mathbf{e}}_y = (0, 1, 0)$, and $\hat{\mathbf{e}}_z = (0, 0, 1)$.

The equilibrium body i frame $(\hat{\mathbf{x}}_i^{\text{eq}}, \hat{\mathbf{y}}_i^{\text{eq}}, \mathbf{p}_i^{\text{eq}})$ is fixed to the preceding segment $i - 1$ (i.e., the equilibrium i frame translates and rotates with segment $i - 1$). The equilibrium frame is compared to the body frame of segment i to determine the change in configuration of a segment from equilibrium—the body frame and equilibrium body frame coincide at equilibrium ($\mathbf{Y}_i = \mathbf{0}$). The coordinates of the equilibrium body frame are related to the coordinates in the body frame of segment $i - 1$ by the linear transformation $\hat{\mathbf{e}}_i^{\text{eq}} = \mathcal{R}_i^{\text{eq}} \cdot \hat{\mathbf{e}}_{i-1}^{\text{body}}$. The equilibrium rotation matrix $\mathcal{R}_i^{\text{eq}}$ is constructed by two rotations of the $i - 1$ body frame as seen in Fig. 2.7: (1) rotation (twist) by an angle ϕ_i^{eq} around \mathbf{p}_{i-1} into the primed frame, and (2) rotation (bend) by an angle θ_i^{eq} about $\hat{\mathbf{y}}'$ to form the equilibrium frame.

Each joint of a fiber has two equilibrium angles, θ_i^{eq} and ϕ_i^{eq} , associated with it that describe the shape of the fiber when no forces or torques are acting on it. By adjusting these two parameters, the fiber equilibrium shape may be straight, U-

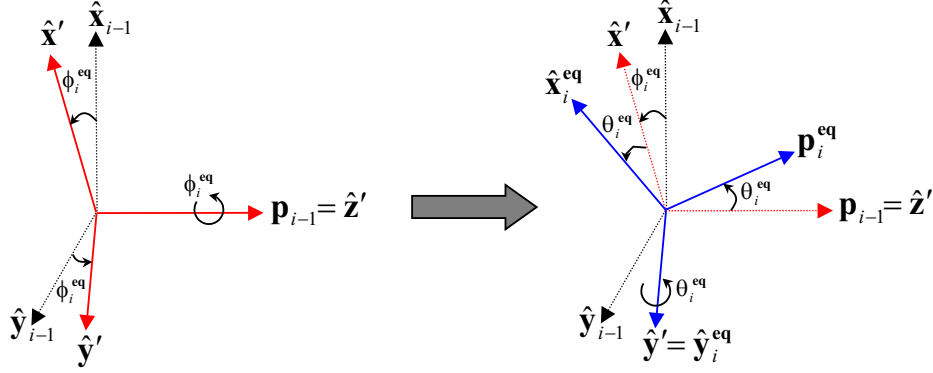


Figure 2.7: Construction of the equilibrium rotation matrix is accomplished by two rotations: (1) ϕ_i^{eq} about \mathbf{p}_{i-1} and (2) θ_i^{eq} about $\hat{\mathbf{y}}'$.

shaped, helical, or of an arbitrary configuration at equilibrium. For example, if θ_i^{eq} is constant at every joint and $\phi_i^{\text{eq}} = 0$, the fiber will assume a U-shape; if θ_i^{eq} and ϕ_i^{eq} are both non-zero constants at every joint, the fiber has a helical shape. Examples of different fiber equilibrium shapes for different values of θ_i^{eq} and ϕ_i^{eq} are found in Fig. 2.8.

2.6.2 Restoring torques in terms of bending and twisting

The bending at each joint is defined by relating the orientation vectors of the equilibrium i frame \mathbf{p}_i^{eq} , and the body i frame \mathbf{p}_i . The difference between the bending angle θ_i and its equilibrium value θ_i^{eq} is

$$\theta_i - \theta_i^{\text{eq}} = \cos^{-1}(\mathbf{p}_i \cdot \mathbf{p}_i^{\text{eq}}). \quad (2.25)$$

The vector \mathbf{p}_i^{eq} is transformed from the equilibrium i frame coordinates into the $i-1$ body frame, and then transformed into inertial coordinates,

$$\mathbf{p}_i^{\text{eq}} = \mathcal{R}_{i-1}^\dagger \cdot (\mathcal{R}_i^{\text{eq}})^\dagger \cdot \mathbf{p}_{i[\text{eq } i]}, \quad (2.26)$$

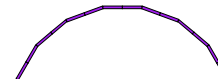
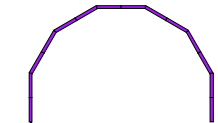
$\theta^{\text{eq}} (^\circ)$	$\phi^{\text{eq}} (^\circ)$	Side View	Front View
5	0		
10	0		
20	0		
20	20		
30	0		
30	10		
30	20		

Figure 2.8: The effect of θ_i^{eq} and ϕ_i^{eq} (measured in degrees) on equilibrium shape of symmetric fibers ($\theta_2^{\text{eq}} = \theta_3^{\text{eq}} = \dots = \theta_{N_{\text{seg}}}^{\text{eq}}$ and $\phi_2^{\text{eq}} = \phi_3^{\text{eq}} = \dots = \phi_{N_{\text{seg}}}^{\text{eq}}$).

where $\mathbf{p}_{i[\text{eq } i]}^{\text{eq}} = (0, 0, 1)$. The direction of the bending torque is perpendicular to both \mathbf{p}_i and \mathbf{p}_i^{eq} ,

$$\mathbf{e}_i^b = \frac{\mathbf{p}_i \times \mathbf{p}_i^{\text{eq}}}{|\mathbf{p}_i \times \mathbf{p}_i^{\text{eq}}|}. \quad (2.27)$$

The amount of twisting may be found in a similar fashion. A vector perpendicular to \mathbf{p}_i is chosen to determine the amount of twisting at a joint. The body frame direction, $\hat{\mathbf{y}}_i$ is compared to its counterpart, $\hat{\mathbf{y}}_i^{\text{eq}}$, in the equilibrium frame. This vector is found in a manner analogous to that used to obtain \mathbf{p}_i^{eq} ,

$$\hat{\mathbf{y}}_i^{\text{eq}} = \mathcal{R}_{i-1}^\dagger \cdot (\mathcal{R}_i^{\text{eq}})^\dagger \cdot \hat{\mathbf{y}}_{i; [\text{eq } i]}^{\text{eq}}. \quad (2.28)$$

The angle between $\hat{\mathbf{y}}_i$ and $\hat{\mathbf{y}}_i^{\text{eq}}$ cannot be compared directly, but rather the projection of the perpendicular components along the direction $\mathbf{c}_i \equiv (\mathbf{r}_i - \mathbf{r}_{i-1})/(|\mathbf{r}_i - \mathbf{r}_{i-1}|)$ are compared. Therefore, the amount of twist at the i^{th} joint is the angle between the vectors $\hat{\mathbf{y}}_i^\perp$ and $\hat{\mathbf{y}}_i^{\text{eq}\perp}$,

$$\phi_i - \phi_i^{\text{eq}} = \cos^{-1} \left(\hat{\mathbf{y}}_i^\perp \cdot \hat{\mathbf{y}}_i^{\text{eq}\perp} \right), \quad (2.29)$$

where $\hat{\mathbf{y}}_i^\perp$ and $\hat{\mathbf{y}}_i^{\text{eq}\perp}$ are defined as

$$\hat{\mathbf{y}}_i^\perp = \frac{(\boldsymbol{\delta} - \mathbf{c}_i \mathbf{c}_i) \cdot \hat{\mathbf{y}}_i}{|(\boldsymbol{\delta} - \mathbf{c}_i \mathbf{c}_i) \cdot \hat{\mathbf{y}}_i|}, \quad (2.30)$$

$$\hat{\mathbf{y}}_i^{\text{eq}\perp} = \frac{(\boldsymbol{\delta} - \mathbf{c}_i \mathbf{c}_i) \cdot \hat{\mathbf{y}}_i^{\text{eq}}}{|(\boldsymbol{\delta} - \mathbf{c}_i \mathbf{c}_i) \cdot \hat{\mathbf{y}}_i^{\text{eq}}|}. \quad (2.31)$$

The direction of the twisting torque is normal to these two projections,

$$\mathbf{e}_i^t = \frac{\hat{\mathbf{y}}_i^\perp \times \hat{\mathbf{y}}_i^{\text{eq}\perp}}{|\hat{\mathbf{y}}_i^\perp \times \hat{\mathbf{y}}_i^{\text{eq}\perp}|}. \quad (2.32)$$

The overall restoring torque is the sum of the bending and twisting contributions,

$$\mathbf{Y}_i = -\kappa_b [(\theta_i - \theta_i^{\text{eq}}) \mathbf{e}_i^b + 0.67 (\phi_i - \phi_i^{\text{eq}}) \mathbf{e}_i^t]. \quad (2.33)$$

The amount of elastic energy stored by a fiber can be calculated by integrating the magnitude of Eq. (2.33) with respect to the change in the bending and twisting angles, and summing the contribution over the entire fiber. This results in the elastic energy E^{elas} of a single fiber,

$$E^{\text{elas}} = \frac{\kappa_b}{2} \sum_{i=2}^{N_{\text{seg}}} [(\theta_i - \theta_i^{\text{eq}})^2 + 0.67(\phi_i - \phi_i^{\text{eq}})^2]. \quad (2.34)$$

2.6.3 Anisotropic bending

Thus far, we have assumed that the model fibers bend isotropically (i.e., no preferential bending direction). Natural fibers do not typically have circular cross sections, and thus have preferential directions of deformation. An SEM image of softwood fibers is presented in Fig. 2.9. The wood fibers are ribbon-like and tend to bend more easily in the direction with the shortest dimension.

Anisotropic bending may be modelled by defining two orthogonal bending directions with bending constants $(\kappa_b)_{\text{hard}} = E_Y I_{\text{hard}}/2\ell$ and $(\kappa_b)_{\text{easy}} = E_Y I_{\text{easy}}/2\ell < (\kappa_b)_{\text{hard}}$, as illustrated in Fig 2.10. The bending directions are set to the equilibrium body frame vectors, $\hat{\mathbf{x}}_i^{\text{eq}}$ and $\hat{\mathbf{y}}_i^{\text{eq}}$ for the hard and easy directions, respectively. The contributions to the bending component of the restoring torque $\mathbf{Y}_i^b = (\mathbf{Y}_i^b)_{\text{hard}} + (\mathbf{Y}_i^b)_{\text{easy}}$ are

$$(\mathbf{Y}_i^b)_{\text{hard}} = (\kappa_b)_{\text{hard}} (\Delta\theta_i)_{\text{hard}} \hat{\mathbf{x}}_i^{\text{eq}} \quad (2.35)$$

$$(\mathbf{Y}_i^b)_{\text{easy}} = (\kappa_b)_{\text{easy}} (\Delta\theta_i)_{\text{easy}} \hat{\mathbf{y}}_i^{\text{eq}}. \quad (2.36)$$

The angle differences relative to equilibrium are $(\Delta\theta_i)_{\text{hard}}$ and $(\Delta\theta_i)_{\text{easy}}$,

$$(\Delta\theta_i)_{\text{hard}} = \tan^{-1} \left(\frac{\mathbf{p}_i^{\text{eq}} \cdot \hat{\mathbf{x}}_i}{\mathbf{p}_i^{\text{eq}} \cdot \hat{\mathbf{z}}_i} \right), \quad (2.37)$$

$$(\Delta\theta_i)_{\text{easy}} = \tan^{-1} \left(\frac{\mathbf{p}_i^{\text{eq}} \cdot \hat{\mathbf{y}}_i}{\mathbf{p}_i^{\text{eq}} \cdot \hat{\mathbf{z}}_i} \right), \quad (2.38)$$

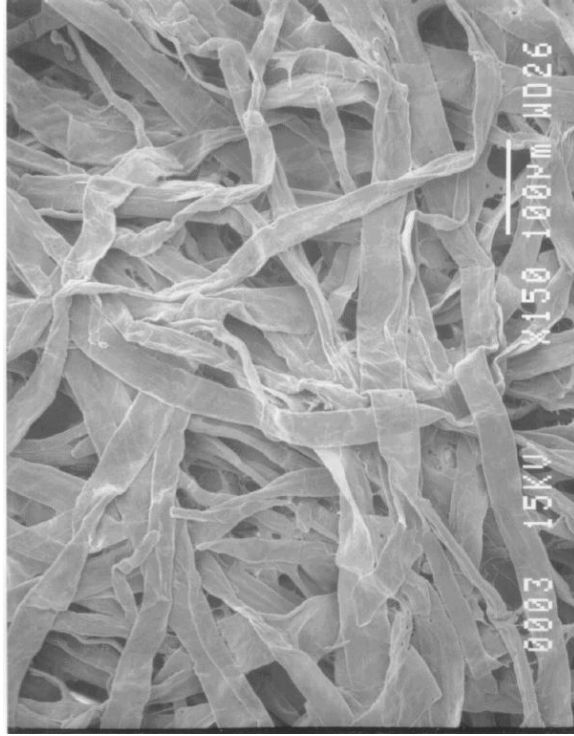


Figure 2.9: SEM image of a softwood pulp fibers

where \mathbf{p}_i^{eq} is defined by Eq. (2.26).

A limiting case of interest is when the fiber becomes infinitely stiff in one direction, $(\kappa_b)_{\text{hard}} \rightarrow \infty$. In this case, the joint may be modelled as a pin joint, resulting in an additional constraint that restricts bending at a joint to that about a preferred axis, $\boldsymbol{\vartheta}_i$. The restoring torque at a joint is

$$\mathbf{Y}_i = \mathbf{Y}_i^b + \mathbf{Y}_i^t + Y_i^{\text{an}} \mathbf{e}_i^{\text{an}}, \quad (2.39)$$

where Y_i^{an} is the magnitude constraint torque directed along \mathbf{e}_i^{an} , that forces a fiber to only bend about $\boldsymbol{\vartheta}_i$. The direction of the pin joint can be arbitrarily chosen, and evolves with body i frame. For the work reported here, the direction of the hinge was chosen to coincide with one of the body frame coordinate vectors, $\boldsymbol{\vartheta} = \hat{\mathbf{y}}_i$. The

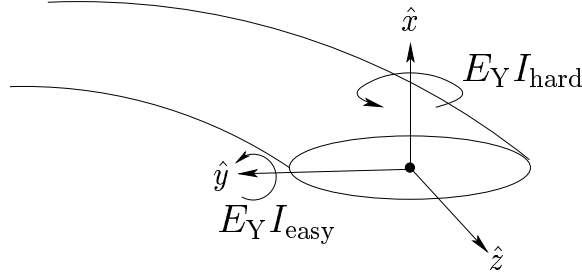


Figure 2.10: Fibers with a non-circular cross section have a preferred bending direction, for example, with respect to the \hat{y} -axis.

direction of the constraint torque is

$$\mathbf{e}_i^{\text{an}} = \frac{\boldsymbol{\vartheta}_i \times \mathbf{p}_{i+1}}{|\boldsymbol{\vartheta}_i \times \mathbf{p}_{i+1}|}. \quad (2.40)$$

The value of Y_i^{an} is found by including the constraint equation,

$$\boldsymbol{\vartheta}_i \cdot \mathbf{p}_{i+1} = \cos \theta', \quad (2.41)$$

where θ' is a constant. This equation constrains the relative motion of adjoining segments to a plane, perpendicular to $\boldsymbol{\vartheta}_i$.

2.7 Scaling of the equations of motion

The equations of motion are scaled in order to reduce the number of parameters in the system. Distance is scaled with the fiber diameter b , and the time is made dimensionless with the inverse of the shear rate, $\dot{\gamma}^{-1}$. The forces are scaled with the quantity $6\pi\eta_o\ell b\dot{\gamma}$ and the torques with $8\pi\eta_o\ell^3\dot{\gamma}$. The dimensionless quantities of interest are (denoted with superscripted asterisks):

$$\begin{aligned} \mathbf{F}_i^{\text{N}*} &= \frac{\mathbf{F}_i^{\text{N}}}{6\pi\mu\ell b\dot{\gamma}}, & \mathbf{F}_i^{\text{fric}*} &= \frac{\mathbf{F}_i^{\text{fric}}}{6\pi\mu\ell b\dot{\gamma}}, & \mathbf{X}_i^* &= \frac{\mathbf{X}_i}{6\pi\mu\ell b\dot{\gamma}}, \\ \mathbf{Y}_i^* &= \frac{\mathbf{Y}_i}{8\pi\mu\ell^3\dot{\gamma}}, & \mathbf{G}_{ij}^* &= \frac{\mathbf{G}_{ij}}{b}, \\ \dot{\mathbf{r}}_i^* &= \frac{\dot{\mathbf{r}}_i}{b\dot{\gamma}}, & \mathbf{U}_i^{\infty*} &= \frac{\mathbf{U}_i^{\infty}}{b\dot{\gamma}}, \\ \boldsymbol{\omega}_i^* &= \frac{\boldsymbol{\omega}_i}{\dot{\gamma}}, & \boldsymbol{\Omega}_i^{\infty*} &= \frac{\boldsymbol{\Omega}_i^{\infty}}{\dot{\gamma}}. \end{aligned} \quad (2.42)$$

The terms above are substituted into Eqs. (2.1)-(2.2) to obtain the dimensionless fiber segment translational velocity $\dot{\mathbf{r}}_i^*$ and angular velocity $\boldsymbol{\omega}_i^*$,

$$\dot{\mathbf{r}}_i^* = \mathbf{a}_i^* + \mathbf{A}_i^{-1} \cdot \left[\sum_j^{N_{C_i}} \mathbf{F}_{ij}^{\text{fric}*} + \mathbf{X}_{i+1}^* - \mathbf{X}_i^* \right] \quad (2.43)$$

$$\boldsymbol{\omega}_i^* = \mathbf{b}_i^* + \mathbf{C}_i^{-1} \cdot \left[\frac{3}{4r_{ps}^2} \sum_j^{N_{C_i}} \tilde{\mathbf{G}}_{ij}^* \cdot \mathbf{F}_{ij}^{\text{fric}*} + \frac{3}{4r_{ps}} \tilde{\mathbf{p}}_i \cdot [\mathbf{X}_{i+1}^* + \mathbf{X}_i^*] \right], \quad (2.44)$$

where \mathbf{a}_i^* and \mathbf{b}_i^* are given by

$$\begin{aligned} \mathbf{a}_i^* &= \mathbf{U}_i^{\infty*} + \mathbf{A}_i^{-1} \cdot \sum_j^{N_{R_i}} \mathbf{F}_{ij}^{\text{N}*}, \\ \mathbf{b}_i^* &= \boldsymbol{\Omega}_i^{\infty*} - \frac{Y^H}{Y^C} [\mathbf{E}^{\infty*} \cdot \mathbf{p}_i] \times \mathbf{p}_i + \mathbf{C}_i^{-1} \cdot \left[\frac{3}{4r_{ps}^2} \sum_j^{N_{R_i}} \tilde{\mathbf{G}}_{ij}^* \cdot \mathbf{F}_{ij}^{\text{N}*} + \mathbf{Y}_{i+1}^* - \mathbf{Y}_i^* \right]. \end{aligned}$$

The terms $\tilde{\mathbf{G}}_{ij}^*$ and $\tilde{\mathbf{p}}_i$, are the matrix representations of cross-products. For example, $\tilde{\mathbf{p}}$ is defined

$$\tilde{\mathbf{p}} = \begin{bmatrix} 0 & -p_z & p_y \\ p_z & 0 & -p_x \\ -p_y & p_x & 0 \end{bmatrix}, \quad (2.45)$$

and thus $\mathbf{p} \times \mathbf{u} = \tilde{\mathbf{p}} \cdot \mathbf{u}$, where \mathbf{u} is an arbitrary vector.

For the majority of this work, the ambient flow field is simple shear flow in the x direction with the velocity gradient in the z direction. The dimensionless expressions for $\mathbf{U}^{\infty*}$, $\boldsymbol{\Omega}^{\infty*}$, and $\mathbf{E}^{\infty*}$ are

$$\begin{aligned} \mathbf{U}_i^{\infty*} &= (r_{z_i}^*, 0, 0), \\ \boldsymbol{\Omega}_i^{\infty*} &= \frac{1}{2} \boldsymbol{\nabla} \times \mathbf{U}_i^{\infty*} = (0, 0.5, 0), \\ \mathbf{E}_i^{\infty*} &= \frac{1}{2} [\boldsymbol{\nabla} \mathbf{U}_i^{\infty*} + (\boldsymbol{\nabla} \mathbf{U}_i^{\infty*})^\dagger] = \begin{bmatrix} 0 & 0 & 0.5 \\ 0 & 0 & 0 \\ 0.5 & 0 & 0 \end{bmatrix}. \end{aligned}$$

Two dimensionless parameters result from the given scaling of the equations of motion: the aspect ratio of a segment, r_{ps} , and the dimensionless bending constant,

κ_b^* . The dimensionless bending constant is defined

$$\kappa_b^* = \frac{\kappa_b}{8\pi\eta_o\dot{\gamma}\ell^3}, \quad (2.46)$$

or equivalently defined by substituting $\kappa_b = E_Y I/2\ell$,

$$\kappa_b^* = \frac{N_{\text{seg}}^4}{\pi} \underbrace{\left[\frac{E_Y I}{\eta_o \dot{\gamma} L^4} \right]}_{S^{\text{eff}}}. \quad (2.47)$$

The term in brackets is called the *effective stiffness* and given the symbol S^{eff} . The effective stiffness characterizes the ratio of the bending moment within the fiber to the viscous torque exerted by the fluid on the fiber. Throughout this work, S^{eff} will be used to describe the relative flexibility of fibers in a suspension.

2.8 Generalized coordinates: Euler parameters

The dynamics of the fiber segments is found by integrating the equations of motion to obtain the positions and orientations as a function of time. However, the expression for the angular velocity $\boldsymbol{\omega}_i^*$ [Eq. (2.44)] is not integrable, and therefore, it must be transformed into time derivatives of the generalized coordinates for the orientation of the fiber segment. One option is to use Euler angles, but this can lead to special cases in which the transformation to the time derivatives of the Euler angles from $\boldsymbol{\omega}_i^*$ has a singular result [92]. An alternative set of generalized coordinates that avoids this problem are *Euler parameters*.

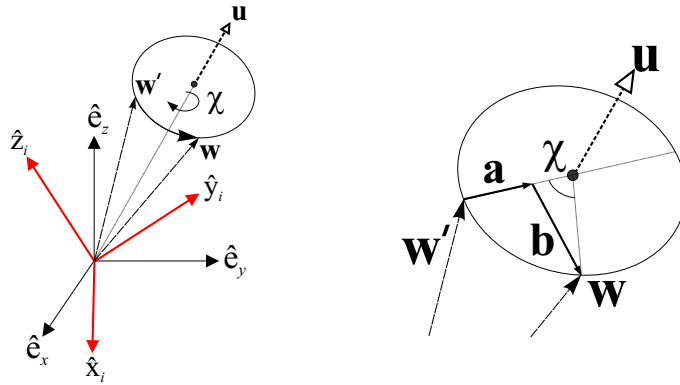


Figure 2.11: The vector \mathbf{w} in the inertial frame $(\hat{\mathbf{e}}_x, \hat{\mathbf{e}}_y, \hat{\mathbf{e}}_z)$ is transformed to \mathbf{w}' in the body frame $(\hat{\mathbf{x}}_i, \hat{\mathbf{y}}_i, \hat{\mathbf{z}}_i)$ by a rotation of the inertial frame by an angle χ about the vector \mathbf{u} , which has the same coordinates in both frames.

2.8.1 Relation of Euler parameters to the body rotation matrix

Euler's theorem states that two arbitrary orthonormal reference frames with a common origin share at least one unit vector \mathbf{u} that has the same coordinates in each reference frame [36, 92]. This implies that the two frames can be made to coincide by rotating one of the frames about the vector \mathbf{u} by an angle χ , as shown in Fig. 2.11.

Consider an arbitrary vector \mathbf{w} with coordinates in the inertial frame defined by the base vectors $(\hat{\mathbf{e}}_x, \hat{\mathbf{e}}_y, \hat{\mathbf{e}}_z)$. We want to know the linear transformation of \mathbf{w} into body frame coordinates

$$\mathbf{w}' = \mathcal{R} \cdot \mathbf{w}, \quad (2.48)$$

in which the body frame base vectors $(\hat{\mathbf{x}}_i, \hat{\mathbf{y}}_i, \hat{\mathbf{z}}_i)$ have been translated to share a common origin with the inertial frame. The end of the vectors \mathbf{w} and \mathbf{w}' both lie on a circle with the center defined by the vector \mathbf{u} . We define two additional vectors \mathbf{a} and \mathbf{b} as shown in Fig 2.11 to help us relate \mathbf{w} and \mathbf{w}' as

$$\mathbf{w} = \mathbf{w}' + \mathbf{a} + \mathbf{b}. \quad (2.49)$$

The vectors \mathbf{a} and \mathbf{b} are defined as

$$\mathbf{a} = (1 - \cos \chi) [\mathbf{u} \times (\mathbf{u} \times \mathbf{w}')] , \quad (2.50)$$

$$\mathbf{b} = \sin \chi [\mathbf{u} \times \mathbf{w}'] . \quad (2.51)$$

We make use of two trigonometric identities,

$$1 - \cos \chi = 2 \sin^2(\chi/2),$$

$$\sin \chi = 2 \sin(\chi/2) \cos(\chi/2),$$

and the values of \mathbf{a} and \mathbf{b} above, to substitute into Eq. (2.49) to obtain

$$\mathbf{w} = \mathbf{w}' + 2 \{ \mathbf{u} \sin(\chi/2) \times [\mathbf{u} \sin(\chi/2) \times \mathbf{w}'] \} + 2 \cos(\chi/2) [\mathbf{u} \sin(\chi/2) \times \mathbf{w}'] \quad (2.52)$$

We introduce the new quantities

$$q_0 = \cos(\chi/2),$$

$$\mathbf{q} = \mathbf{u} \sin(\chi/2),$$

where the coordinates of \mathbf{q} are q_1 , q_2 , and q_3 , which have the same values in either reference frame because of the properties of \mathbf{u} . These four coordinates (q_0, q_1, q_2, q_3) are called *Euler parameters* (also called Caley-Klein parameters), and can be used to represent the orientation of a rigid body in space. The definition of (q_0, \mathbf{q}) leads to the identity,

$$q_0^2 + q_1^2 + q_2^2 + q_3^2 = 1. \quad (2.53)$$

Substitution of q_0 and \mathbf{q} into Eq. (2.52) results in a relation between the vectors \mathbf{w} and \mathbf{w}' of the form

$$\mathbf{w} = \underbrace{[\delta + 2\tilde{\mathbf{q}}\tilde{\mathbf{q}} + 2q_0\tilde{\mathbf{q}}]}_{\mathcal{R}^\dagger} \mathbf{w}', \quad (2.54)$$

where $\tilde{\mathbf{q}}$ is the matrix representation of a cross-product vector,

$$\tilde{\mathbf{q}} = \begin{bmatrix} 0 & -q_3 & q_2 \\ q_3 & 0 & -q_1 \\ -q_2 & q_1 & 0 \end{bmatrix}. \quad (2.55)$$

The term in brackets in Eq. (2.54) is simply the transpose of the body rotation matrix which was defined in Section 2.6.1. In terms of Euler parameters, \mathcal{R} becomes

$$\mathcal{R} = \begin{pmatrix} 2(q_0^2 + q_1^2) - 1 & 2(q_1q_2 + q_0q_3) & 2(q_1q_3 - q_0q_2) \\ 2(q_1q_2 - q_0q_3) & 2(q_0^2 + q_2^2) - 1 & 2(q_2q_3 + q_0q_1) \\ 2(q_1q_3 + q_0q_2) & 2(q_2q_3 - q_0q_1) & 2(q_0^2 + q_3^2) - 1 \end{pmatrix}, \quad (2.56)$$

or if the body rotation matrix is known initially, the Euler parameters are found by

$$\begin{aligned} q_0 &= \frac{1}{2} \sqrt{1 + \mathcal{R}_{11} + \mathcal{R}_{22} + \mathcal{R}_{33}}, \\ q_1 &= \frac{1}{2} \frac{\mathcal{R}_{23} - \mathcal{R}_{32}}{\sqrt{1 + \mathcal{R}_{11} + \mathcal{R}_{22} + \mathcal{R}_{33}}}, \\ q_2 &= \frac{1}{2} \frac{\mathcal{R}_{31} - \mathcal{R}_{13}}{\sqrt{1 + \mathcal{R}_{11} + \mathcal{R}_{22} + \mathcal{R}_{33}}}, \\ q_3 &= \frac{1}{2} \frac{\mathcal{R}_{12} - \mathcal{R}_{21}}{\sqrt{1 + \mathcal{R}_{11} + \mathcal{R}_{22} + \mathcal{R}_{33}}}. \end{aligned} \quad (2.57)$$

2.8.2 Relation between Euler parameters and the angular velocity

The relation between (q_0, \mathbf{q}) and the angular velocity is derived using Poisson's equations [92]. Poisson's equations relate the angular velocity of a body frame coordinate system to the rotation matrix by,

$$\tilde{\boldsymbol{\omega}}' = -\dot{\mathcal{R}} \cdot \mathcal{R}^\dagger, \quad (2.58)$$

where $\dot{\mathcal{R}}$ is the time derivative of the body rotation matrix and $\tilde{\boldsymbol{\omega}}'$ is the matrix representation of the cross-product vector of $\boldsymbol{\omega}$ in body frame coordinates. Substituting Eq. (2.56) into Poisson's equation relates the angular velocity to the Euler

parameters,

$$\tilde{\boldsymbol{\omega}}' = -2 \left[(\tilde{\mathbf{q}} \cdot \dot{\tilde{\mathbf{q}}}) + \dot{q}_0 \tilde{\mathbf{q}} - q_0 \dot{\tilde{\mathbf{q}}} \right], \quad (2.59)$$

or as a vector,

$$\boldsymbol{\omega}' = -2 [\tilde{\mathbf{q}} \cdot \dot{\tilde{\mathbf{q}}} + \dot{q}_0 \mathbf{q} - q_0 \dot{\mathbf{q}}]. \quad (2.60)$$

Eq. (2.60) shows that the angular velocity in body frame coordinates is a linear combination of the Euler parameters and their time derivatives. This can be represented in matrix notation as,

$$\boldsymbol{\omega}' = 2 \underbrace{\begin{bmatrix} -q_1 & q_0 & q_3 & -q_2 \\ -q_2 & -q_3 & q_0 & q_1 \\ -q_3 & q_2 & -q_1 & q_0 \end{bmatrix}}_{\mathbf{\Gamma}} \begin{pmatrix} \dot{q}_0 \\ \dot{q}_1 \\ \dot{q}_2 \\ \dot{q}_3 \end{pmatrix}, \quad (2.61)$$

where the matrix $\mathbf{\Gamma}$ is orthogonal. In general, we will refer to the Euler parameters of fiber segment i as $\mathbf{q}_i \equiv (q_0, \mathbf{q})_i$, and the inverse of Eq. (2.61) is therefore

$$\dot{\mathbf{q}}_i = \frac{1}{2} \mathbf{\Gamma}^\dagger \cdot \boldsymbol{\omega}'. \quad (2.62)$$

The time derivatives of the Euler parameters can be expressed in terms of the inertial frame coordinates of the angular velocity $\boldsymbol{\omega}$, by the transformation $\boldsymbol{\omega}' = \mathbf{R} \cdot \boldsymbol{\omega}$. Substitution into Eq. (2.62) yields

$$\dot{\mathbf{q}}_i = \frac{1}{2} \mathbf{\Gamma}^\dagger \cdot \mathbf{R} \cdot \boldsymbol{\omega} = \frac{1}{2} \check{\mathbf{\Gamma}}^\dagger \cdot \boldsymbol{\omega}, \quad (2.63)$$

where $\check{\mathbf{\Gamma}}$ is a 3×4 orthogonal matrix, and is expressed in terms of Euler parameters as

$$\check{\mathbf{\Gamma}} = \mathbf{R}^\dagger \cdot \mathbf{\Gamma} = \begin{bmatrix} -q_1 & q_0 & -q_3 & q_2 \\ -q_2 & q_3 & q_0 & -q_1 \\ -q_3 & -q_2 & q_1 & q_0 \end{bmatrix}. \quad (2.64)$$

The equation of motion for the orientation of a body can be expressed in terms of Euler parameters, \mathbf{q}_i . Combining Eqs. (2.44) and (2.63) results in,

$$\dot{\mathbf{q}}_i^* = \check{\mathbf{\Gamma}}_i \cdot \left\{ \mathbf{b}_i^* + \mathbf{C}_i^{-1} \cdot \left[\frac{3}{4r_{ps}^2} \sum_j^{N_{C_i}} \tilde{\mathbf{G}}_{ij}^* \cdot \mathbf{F}_{ij}^{\text{fric}*} \right] \right\}$$

$$+ \left. \frac{3}{4r_{p_s}} \tilde{\mathbf{p}}_i \cdot [\mathbf{X}_{i+1}^* + \mathbf{X}_i^*] \right\} + \lambda_i \mathbf{q}_i. \quad (2.65)$$

where $\dot{\mathbf{q}}_i^* = \dot{\mathbf{q}}_i/\dot{\gamma}$ is the dimensionless time derivative of the Euler parameters. The term λ_i is an unknown Lagrange multiplier that is found by including the normalization constraint for the Euler parameters, $\mathbf{q}_i \cdot \mathbf{q}_i = 1$.

2.9 Solution methods

The dynamics of the flexible fibers in our model are determined by solving the equations of motion coupled with the constraint equations given previously. This forms a system of index-2 differential-algebraic equations (DAEs) to solve for the unknown fiber segment positions \mathbf{r}^* , Euler parameters \mathbf{q} , inextensibility constraint forces \mathbf{X}^* , friction forces $\mathbf{F}^{\text{fric}^*}$, and Euler parameter constraint constants $\boldsymbol{\lambda}$, as a function of time. The system of DAEs is summarized

$$\dot{\mathbf{r}}^* - \mathcal{F}(\mathbf{r}^*, \mathbf{q}, \mathbf{X}^*, \mathbf{F}^{\text{fric}^*}) = \mathbf{0}, \quad (2.66)$$

$$\dot{\mathbf{q}}^* - \mathcal{G}(\mathbf{r}^*, \mathbf{q}, \mathbf{X}^*, \mathbf{F}^{\text{fric}^*}, \boldsymbol{\lambda}) = \mathbf{0}, \quad (2.67)$$

$$\Psi^*(\mathbf{r}^*, \mathbf{q}) = \mathbf{0}, \quad (2.68)$$

$$\Lambda(\mathbf{q}) = \mathbf{0}, \quad (2.69)$$

$$\Xi^*(\mathbf{r}^*, \mathbf{q}, \dot{\mathbf{r}}^*, \dot{\mathbf{q}}^*, \mathbf{F}^{\text{fric}^*}) = \mathbf{0}, \quad (2.70)$$

$$\Theta(\mathbf{q}) = \mathbf{0}, \quad (2.71)$$

where each coordinate and force vector represents all of the fiber segments in the system of N_{fib} fibers,

$$\mathbf{r}^* = \begin{pmatrix} \mathbf{r}_1^* \\ \mathbf{r}_2^* \\ \vdots \\ \mathbf{r}_{N_{\text{fib}} N_{\text{seg}}}^* \end{pmatrix}, \quad \mathbf{q} = \begin{pmatrix} \mathbf{q}_1 \\ \mathbf{q}_2 \\ \vdots \\ \mathbf{q}_{N_{\text{fib}} N_{\text{seg}}} \end{pmatrix}, \quad \mathbf{X}^* = \begin{pmatrix} \mathbf{X}_2^* \\ \mathbf{X}_3^* \\ \vdots \\ \mathbf{X}_{N_{\text{fib}}(N_{\text{seg}}-1)}^* \end{pmatrix},$$

$$\mathbf{F}^{\text{fric}*} = \begin{pmatrix} \mathbf{F}_1^{\text{fric}*} \\ \mathbf{F}_2^{\text{fric}*} \\ \vdots \\ \mathbf{F}_{N_C}^{\text{fric}*} \end{pmatrix}, \quad \boldsymbol{\lambda} = \begin{pmatrix} \lambda_1 \\ \lambda_2 \\ \vdots \\ \lambda_{N_{\text{fib}}N_{\text{seg}}} \end{pmatrix},$$

in which N_C is the total number of contacts in the system. The components of \mathcal{F} and \mathcal{G} come from Eqs. (2.43) and (2.65). For segment i , the functions are

$$\begin{aligned} \mathcal{F}_i &= \mathbf{a}_i^* + \mathbf{A}_i^{-1} \cdot \left[\sum_j^{N_{C_i}} \mathbf{F}_{ij}^{\text{fric}*} + \mathbf{X}_{i+1}^* - \mathbf{X}_i^* \right], \\ \mathcal{G}_i &= \check{\Gamma}_i \cdot \left\{ \mathbf{b}_i^* + \mathbf{C}_i^{-1} \cdot \left[\frac{3}{4r_{ps}^2} \sum_j^{N_{C_i}} \check{\mathbf{G}}_{ij}^* \cdot \mathbf{F}_{ij}^{\text{fric}*} + \frac{3}{4r_{ps}} \check{\mathbf{p}}_i \cdot [\mathbf{X}_{i+1}^* + \mathbf{X}_i^*] \right] \right\} + \lambda_i \mathbf{q}_i. \end{aligned}$$

The dimensionless constraint for inextensibility at a joint Ψ_i^* , the Euler normalization constraint for each segment Λ_i , the friction constraint for each contact Ξ_{ij}^* , and the anisotropic bending constraint at a pin joint Θ_i (only needed if fibers bend anisotropically via pin joints) are

$$\begin{aligned} \Psi_i^* &= \mathbf{r}_i^* + r_{ps} \mathbf{p}_i - (\mathbf{r}_{i+1}^* - r_{ps} \mathbf{p}_{i+1}), \\ \Lambda_i &= \mathbf{q}_i \cdot \mathbf{q}_i - 1, \\ \Xi_{ij}^* &= \begin{pmatrix} \Delta \mathbf{u}_{ij}^* \cdot \mathbf{e}_{ij}^1 \\ \Delta \mathbf{u}_{ij}^* \cdot \mathbf{e}_{ij}^2 \\ \mathbf{F}_{ij}^{\text{fric}*} \cdot \mathbf{n}_{ij} \end{pmatrix} \\ \Theta &= \boldsymbol{\vartheta}_i \cdot \mathbf{p}_{i+1} - \cos \theta'. \end{aligned}$$

The complete system of DAEs [Eqs. (2.66)-(2.71)] consists of $7N_{\text{fib}}N_{\text{seg}}$ equations of motion (first order, ordinary differential equations), $3N_{\text{fib}}(N_{\text{seg}} - 1)$ algebraic equations for the inextensible joints, $N_{\text{fib}}N_{\text{seg}}$ algebraic equations for the Euler parameter normalization constraint, $3N_C$ equations for the friction constraint, and $3N_{\text{fib}}(N_{\text{seg}} - 1)$ equations if the fibers bend anisotropically with pin joints. The numerical solution to Eqs. (2.66)-(2.71) can be accomplished using a variety of techniques

including: finite difference (backward or forward) substitution for the derivatives to yield non-linear algebraic equations in the unknown generalized coordinates and constraint forces [15], direct numerical integration [36, 92], and constraint stabilization [9, 36, 92]. Direct integration will be investigated in more detail below.

2.9.1 Direct integration

One method to numerically solve these equations is called *direct integration* [36, 92]. Direct integration involves the simultaneous solution of the translational velocities $\dot{\mathbf{r}}^*$, angular velocities $\boldsymbol{\omega}$, and the constraint forces $(\mathbf{X}^*, \mathbf{F}^{\text{fric}^*})$ (assuming an isotropically bending fiber). Then, $\boldsymbol{\omega}^*$ is transformed into $\dot{\mathbf{q}}^*$, and the time derivatives of the positions and Euler parameters of the fiber segments are numerically integrated. In this way, the Euler parameter normalization constraints $(\boldsymbol{\Lambda})$ are eliminated, and the Euler parameters can be renormalized after the integration.

We must first express the constraint equations in terms of $\dot{\mathbf{r}}^*$ and $\boldsymbol{\omega}^*$. This is done by taking the time derivative of the inextensibility constraint $d\Psi^*/dt$ (the friction constraint is already in this form). The values of $\dot{\mathbf{r}}^*$ and $\boldsymbol{\omega}^*$ in the two constraint equations are then replaced with the expressions in Eqs. (2.43) and (2.44). This yields a linear system of equations for the unknown constraint forces of the form,

$$\begin{bmatrix} \mathcal{R}_X & \mathcal{Z}_F \\ \mathcal{Z}_X & \mathcal{R}_F \end{bmatrix} \begin{pmatrix} \mathbf{X}^* \\ \mathbf{F}^{\text{fric}^*} \end{pmatrix} = \begin{pmatrix} \boldsymbol{\nu}_X \\ \boldsymbol{\nu}_F \end{pmatrix}. \quad (2.72)$$

The terms \mathcal{R}_X , \mathcal{Z}_F , and $\boldsymbol{\nu}_X$ arise from the time derivative of the inextensibility constraint $(\dot{\Psi}^*)$, and \mathcal{Z}_X , \mathcal{R}_F , and $\boldsymbol{\nu}_F$ result from the friction constraint (Ξ^*) . Once $(\mathbf{X}^*, \mathbf{F}^{\text{fric}^*})$ are known, we solve for $\dot{\mathbf{r}}^*$ and $\boldsymbol{\omega}^*$ using Eqs. (2.43) and (2.44).

Evaluation of the modified inextensibility constraint

The constraint that keeps a fiber at a constant length is modified by taking the time derivative,

$$\begin{aligned}
\dot{\Psi}_i^* &= \frac{d}{dt^*} [\mathbf{r}_i^* + r_{ps} \mathbf{p}_i - (\mathbf{r}_{i+1}^* - r_{ps} \mathbf{p}_{i+1})] \\
&= \dot{\mathbf{r}}_i^* + r_{ps} \dot{\mathbf{p}}_i^* - (\dot{\mathbf{r}}_{i+1}^* - r_{ps} \dot{\mathbf{p}}_{i+1}^*) \\
&= \dot{\mathbf{r}}_i^* - \dot{\mathbf{r}}_{i+1}^* + r_{ps} [\boldsymbol{\omega}_i^* \times \mathbf{p}_i + \boldsymbol{\omega}_{i+1}^* \times \mathbf{p}_{i+1}] = \mathbf{0}, \tag{2.73}
\end{aligned}$$

where for any segment $\dot{\mathbf{p}}_i^* = \boldsymbol{\omega}_i^* \times \mathbf{p}_i$. The equations of motion [Eqs. (2.43)-(2.44)] are substituted into Eq. (2.73) for $\dot{\mathbf{r}}_i^*$ and $\boldsymbol{\omega}_i^*$ which makes the only unknown quantities the constraint forces. The constraint becomes

$$\begin{aligned}
\dot{\Psi}_i^* &= \mathcal{S}_i \cdot \mathbf{X}_i^* + \mathcal{T}_i \cdot \mathbf{X}_{i+1}^* + \mathcal{U}_i \cdot \mathbf{X}_{i+2}^* + \\
&\quad \sum_k^{N_{C_i}} \mathcal{W}_{ik}^- \cdot \mathbf{F}_{ik}^{\text{fric}*} + \sum_l^{N_{C_{i+1}}} \mathcal{W}_{i+1l}^+ \cdot \mathbf{F}_{i+1l}^{\text{fric}*} + \\
&\quad \mathbf{a}_i^* - \mathbf{a}_{i+1}^* - r_p [\tilde{\mathbf{p}}_i \cdot \mathbf{b}_i^* + \tilde{\mathbf{p}}_{i+1} \cdot \mathbf{b}_{i+1}^*] = \mathbf{0}, \tag{2.74}
\end{aligned}$$

The orientation tensors \mathcal{S} , \mathcal{T} , \mathcal{U} , \mathcal{W}^- , and \mathcal{W}^+ are functions of the fiber segment position and orientation:

$$\begin{aligned}
\mathcal{S}_i &= -\mathbf{A}_i^{-1} - \frac{3}{4Y_C} \tilde{\mathbf{p}}_i^2, \\
\mathcal{T}_i &= \mathbf{A}_i^{-1} + \mathbf{A}_{i+1}^{-1} - \frac{3}{4Y_C} (\tilde{\mathbf{p}}_i^2 + \tilde{\mathbf{p}}_{i+1}^2), \\
\mathcal{U}_i &= -\mathbf{A}_{i+1}^{-1} - \frac{3}{4Y_C} \tilde{\mathbf{p}}_{i+1}^2, \\
\mathcal{W}_{ik}^- &= \mathbf{A}_i^{-1} - \frac{3}{4r_{ps} Y_C} \tilde{\mathbf{p}}_i \cdot \tilde{\mathbf{G}}_{ik}^*, \\
\mathcal{W}_{i+1l}^+ &= -\mathbf{A}_{i+1}^{-1} - \frac{3}{4r_{ps} Y_C} \tilde{\mathbf{p}}_{i+1} \cdot \tilde{\mathbf{G}}_{i+1l}^*.
\end{aligned}$$

Evaluation of the friction constraint

The friction constraint is already expressed in terms of velocities, thus no further derivatives need to be taken. The relative velocity between contacts points on fiber segments i and j is

$$\Delta \mathbf{u}_{ij}^* = \mathbf{r}_i^* + \boldsymbol{\omega}_i^* \times \mathbf{G}_{ij}^* - \mathbf{r}_j^* - \boldsymbol{\omega}_j^* \times \mathbf{G}_{ji}^*. \quad (2.75)$$

Once again, Eqs. (2.43) and (2.44) replace \mathbf{r}_i^* and $\boldsymbol{\omega}_i^*$ above, and the first two terms of the friction constraint become

$$\begin{aligned} (\Xi_{ij})_{1 \text{ or } 2}^* &= \left(\mathcal{Q}_i^\dagger \cdot \mathbf{e}_{ij}^{1 \text{ or } 2} \right) \cdot \mathbf{X}_i^* + \left(\mathcal{Q}'_i \cdot \mathbf{e}_{ij}^{1 \text{ or } 2} \right) \cdot \mathbf{X}_{i+1}^* + \\ &\left(\mathcal{M}_j^\dagger \cdot \mathbf{e}_{ij}^{1 \text{ or } 2} \right) \cdot \mathbf{X}_j^* + \left(\mathcal{M}'_j \cdot \mathbf{e}_{ij}^{1 \text{ or } 2} \right) \cdot \mathbf{X}_{j+1}^* + \\ &\sum_k^{N_{C_i}} \left(\mathcal{J}_{ik}^\dagger \cdot \mathbf{e}_{ij}^{1 \text{ or } 2} \right) \cdot \mathbf{F}_{ik}^{\text{fric}*} + \sum_l^{N_{C_j}} \left(\mathcal{J}'_{jl} \cdot \mathbf{e}_{ij}^{1 \text{ or } 2} \right) \cdot \mathbf{F}_{jl}^{\text{fric}*} + \\ &(\mathbf{a}_i^* - \mathbf{a}_j^* - \tilde{\mathbf{G}}_{ij}^* \cdot \mathbf{b}_i^* + \tilde{\mathbf{G}}_{ji}^* \cdot \mathbf{b}_j^*) \cdot \mathbf{e}_{ij}^{1 \text{ or } 2} \end{aligned} \quad (2.76)$$

where the frictional orientation tensors \mathcal{Q} , \mathcal{Q}' , \mathcal{M} , \mathcal{M}' , \mathcal{J} , and \mathcal{J}' are

$$\begin{aligned} \mathcal{Q}_i &= -\mathbf{A}_i^{-1} - \frac{3}{4r_{\text{ps}} Y^{\text{C}}} \tilde{\mathbf{G}}_{ij}^* \cdot \tilde{\mathbf{p}}_i, \\ \mathcal{Q}'_i &= \mathbf{A}_i^{-1} - \frac{3}{4r_{\text{ps}} Y^{\text{C}}} \tilde{\mathbf{G}}_{ij}^* \cdot \tilde{\mathbf{p}}_i, \\ \mathcal{M}_j &= \mathbf{A}_j^{-1} + \frac{3}{4r_{\text{ps}} Y^{\text{C}}} \tilde{\mathbf{G}}_{ji}^* \cdot \tilde{\mathbf{p}}_j, \\ \mathcal{M}'_j &= -\mathbf{A}_j^{-1} + \frac{3}{4r_{\text{ps}} Y^{\text{C}}} \tilde{\mathbf{G}}_{ji}^* \cdot \tilde{\mathbf{p}}_j, \\ \mathcal{J}_{ik} &= \mathbf{A}_i^{-1} - \frac{3}{4r_{\text{ps}}^2} \tilde{\mathbf{G}}_{ij}^* \cdot \mathbf{C}_i^{-1} \cdot \tilde{\mathbf{G}}_{ik}^*, \\ \mathcal{J}'_{jl} &= -\mathbf{A}_j^{-1} + \frac{3}{4r_{\text{ps}}^2} \tilde{\mathbf{G}}_{ji}^* \cdot \mathbf{C}_j^{-1} \cdot \tilde{\mathbf{G}}_{jl}^*. \end{aligned}$$

Anisotropic bending: Pin joint constraint

If the fiber joints are changed from ball and socket joints to pin joints, we must modify the equations of motion for angular velocity, the constraint equations $\dot{\Psi}^*$ and Ξ^* , and add the new constraint equation Θ . The angular velocity [Eq. (2.44)] is changed to

$$\begin{aligned} \boldsymbol{\omega}_i^* &= \mathbf{b}_i^* + \mathbf{C}_i^{-1} \cdot \left[\frac{3}{4r_{ps}^2} \sum_j^{N_{C_i}} \tilde{\mathbf{G}}_{ij}^* \cdot \mathbf{F}_{ij}^{\text{fric}*} + \frac{3}{4r_{ps}} \tilde{\mathbf{p}}_i \cdot [\mathbf{X}_{i+1}^* + \mathbf{X}_i^*] \right. \\ &\quad \left. + Y_{i+1}^{\text{an}*} \mathbf{e}_{i+1}^{\text{an}} - Y_i^{\text{an}*} \mathbf{e}_i^{\text{an}} \right], \end{aligned} \quad (2.77)$$

where $Y_i^{\text{an}*}$ is the magnitude of the dimensionless torque in the direction of \mathbf{e}_i^{an} [Eq. (2.74)] which limits the rotational motion of the connected segments to that about $\boldsymbol{\vartheta}_i$.

The inextensibility constraint equation is the same as Eq. (2.74) with three additional terms,

$$(\dot{\Psi}_{\text{aniso}}^*)_i = \dot{\Psi}_i^* + \mathcal{S}_i^{\text{an}} Y_i^{\text{an}*} + \mathcal{T}_i^{\text{an}} Y_{i+1}^{\text{an}*} + \mathcal{U}_i^{\text{an}} Y_{i+2}^{\text{an}*}, \quad (2.78)$$

where $\dot{\Psi}_i^*$ includes all of the terms from Eq. (2.40) and the tensors $\mathcal{S}_i^{\text{an}}$, $\mathcal{T}_i^{\text{an}}$, and $\mathcal{U}_i^{\text{an}}$ are

$$\begin{aligned} \mathcal{S}_i^{\text{an}} &= \frac{r_{ps}}{Y_C} \tilde{\mathbf{p}}_i \cdot \mathbf{e}_i^{\text{an}}, \\ \mathcal{T}_i^{\text{an}} &= \frac{r_{ps}}{Y_C} (\tilde{\mathbf{p}}_{i+1} - \tilde{\mathbf{p}}_i) \cdot \mathbf{e}_{i+1}^{\text{an}}, \\ \mathcal{U}_i^{\text{an}} &= -\frac{r_{ps}}{Y_C} \tilde{\mathbf{p}}_{i+1} \cdot \mathbf{e}_{i+2}^{\text{an}}. \end{aligned}$$

Similarly, the friction constraint is modified to take into account the new angular velocity. The first two terms of the friction constraint for contact between segments i and j are changed to

$$\begin{aligned} (\Xi_{ij})_{1 \text{ or } 2}^{\text{an}*} &= (\Xi_{ij})_{1 \text{ or } 2}^* + (\mathcal{Q}_i^{\text{an}} \cdot \mathbf{e}_{ij}^{1 \text{ or } 2}) Y_i^{\text{an}*} + (\mathcal{Q}_i^{\text{an}} \cdot \mathbf{e}_{ij}^{1 \text{ or } 2}) Y_{i+1}^{\text{an}*} \\ &\quad + (\mathcal{M}_j^{\text{an}} \cdot \mathbf{e}_{ij}^{1 \text{ or } 2}) Y_j^{\text{an}*} + (\mathcal{M}_j^{\text{an}} \cdot \mathbf{e}_{ij}^{1 \text{ or } 2}) Y_{j+1}^{\text{an}*} \end{aligned} \quad (2.79)$$

where $(\Xi_{ij})_{1 \text{ or } 2}^*$ is obtained from Eq. (2.76) and the vectors \mathcal{Q}_i^{an} and \mathcal{M}_i^{an} are

$$\begin{aligned}\mathcal{Q}_i^{an} &= \tilde{\mathbf{G}}_{ij}^* \cdot \mathbf{C}_i^{-1} \cdot \mathbf{e}_i^{\text{an}}, \\ \mathcal{Q}_i'^{an} &= -\tilde{\mathbf{G}}_{ij}^* \cdot \mathbf{C}_i^{-1} \cdot \mathbf{e}_{i+1}^{\text{an}}, \\ \mathcal{M}_j^{an} &= -\tilde{\mathbf{G}}_{ji}^* \cdot \mathbf{C}_j^{-1} \cdot \mathbf{e}_j^{\text{an}}, \\ \mathcal{M}_j'^{an} &= \tilde{\mathbf{G}}_{ji}^* \cdot \mathbf{C}_j^{-1} \cdot \mathbf{e}_{j+1}^{\text{an}}.\end{aligned}$$

We must also include the pin joint constraint, Θ_i , at each joint [Eq. (2.41)].

The time derivative of Θ_i is

$$\begin{aligned}\dot{\Theta}_i^* &= \frac{d}{dt^*} (\boldsymbol{\vartheta}_i \cdot \mathbf{p}_{i+1} - \cos \theta'), \\ &= \boldsymbol{\vartheta}_i \cdot [\boldsymbol{\omega}_{i+1}^* \times \mathbf{p}_{i+1}] + [\boldsymbol{\omega}_i^* \times \boldsymbol{\vartheta}_i] \cdot \mathbf{p}_{i+1}, \\ &= [\boldsymbol{\vartheta}_i \times \mathbf{p}_{i+1}] \cdot (\boldsymbol{\omega}_i^* - \boldsymbol{\omega}_{i+1}^*), \\ &= \mathbf{e}_i^{\text{an}} \cdot (\boldsymbol{\omega}_i^* - \boldsymbol{\omega}_{i+1}^*) = 0,\end{aligned}\tag{2.80}$$

and the angular velocity is replaced with Eq. (2.77). The constraint becomes

$$\begin{aligned}\dot{\Theta}_i^* &= \mathcal{H}_i^0 \cdot \mathbf{X}_i^* + \mathcal{H}_i^1 \cdot \mathbf{X}_{i+1}^* + \mathcal{H}_i^2 \cdot \mathbf{X}_{i+2}^* \\ &+ \mathcal{P}_i^0 Y_i^{\text{an}*} + \mathcal{P}_i^1 Y_{i+1}^{\text{an}*} + \mathcal{P}_i^2 Y_{i+2}^{\text{an}*} \\ &+ (\mathbf{b}_{i+1} - \mathbf{b}_i) \cdot \mathbf{e}_i^{\text{an}},\end{aligned}\tag{2.81}$$

where the orientation vectors \mathcal{H}_i^0 , \mathcal{H}_i^1 , \mathcal{H}_i^2 and scalars \mathcal{P}_i^0 , \mathcal{P}_i^1 , \mathcal{P}_i^2 are

$$\begin{aligned}\mathcal{H}_i^0 &= \frac{3}{4r_{ps} Y^C} \tilde{\mathbf{p}}_i \cdot \mathbf{e}_i^{\text{an}}, \\ \mathcal{H}_i^1 &= \frac{3}{4r_{ps} Y^C} (\tilde{\mathbf{p}}_i - \tilde{\mathbf{p}}_{i+1}) \cdot \mathbf{e}_i^{\text{an}}, \\ \mathcal{H}_i^2 &= -\frac{3}{4r_{ps} Y^C} \tilde{\mathbf{p}}_{i+1} \cdot \mathbf{e}_i^{\text{an}}, \\ \mathcal{P}_i^0 &= -(\mathbf{C}_i^{-1} \cdot \mathbf{e}_i^{\text{an}}) \cdot \mathbf{e}_i^{\text{an}}, \\ \mathcal{P}_i^1 &= [(\mathbf{C}_i^{-1} + \mathbf{C}_i^{-1}) \cdot \mathbf{e}_{i+1}^{\text{an}}] \cdot \mathbf{e}_i^{\text{an}}, \\ \mathcal{P}_i^2 &= -(\mathbf{C}_{i+1}^{-1} \cdot \mathbf{e}_{i+2}^{\text{an}}) \cdot \mathbf{e}_i^{\text{an}}.\end{aligned}$$

2.9.2 Approximate method of direct integration

The numerical solution to the system of DAEs derived here involves the solution of a linear system of $3N_{\text{fib}}(N_{\text{seg}} - 1) + 3N_C$ equations with an equal number of unknowns [Eqs. (2.66)-(2.70), assuming isotropically bending fibers]. The values of $(\mathbf{X}^*, \mathbf{F}^{\text{fric}*})$ are then used to find \mathbf{r}^* and $\boldsymbol{\omega}^*$, in which $\boldsymbol{\omega}^*$ is transformed to the derivatives of the Euler parameters by $\dot{\mathbf{q}}^* = \check{\mathbf{\Gamma}}^\dagger \cdot \boldsymbol{\omega}^*/2$. Finally, the $7N_{\text{fib}}N_{\text{seg}}$ equations of motion are integrated by an explicit method.

As the concentration increases in a fiber suspension, the number of contacts increases to the point that a network is formed in which the motion of a single fiber can then transmit a force through the entire network. This requires the solution of a very large linear system of equations. For example, a system of $N_{\text{fib}} = 450$ fibers with $N_{\text{seg}} = 5$ that form a network with two contacts per fiber, would require nearly 1 GB of computer memory and $\sim 10^{11}$ operations [65] to solve the linear system for the constraint force for one time step (assuming that an exact method such as LU decomposition is used to solve the system). We would like to use an approximate method to calculate the constraint forces in order to reduce the number of calculations and amount of computer memory required.

One method to decrease the size of the system of equations is to decouple the solution of the constraint forces \mathbf{X}^* from the friction forces $\mathbf{F}^{\text{fric}*}$. We accomplish this by assuming that the value of \mathbf{X}_i^* for a joint remains constant over the course of one time step. By making this assumption, the friction force can be found by using the values $\mathbf{X}_{[\text{prev}]}$ from the previous time step,

$$\mathcal{R}_F \cdot \mathbf{F}^{\text{fric}*} = \mathcal{V}_F - \mathcal{Z}_X \cdot \mathbf{X}_{[\text{prev}]}. \quad (2.82)$$

This simplification allows us to temporarily ignore the connectivity of the fiber and

consider segments as individual rigid bodies. The segments are sorted into N_G groups that share contacts. Then, Eq. (2.82) is used to solve for the friction force of each group of contacting *segments* (rather than each group of contacting fibers), which has a total of N_{C_s} contacts, where $N_{C_s} \ll N_C$.

For each group, the matrix \mathcal{R}_F has the form,

$$\mathcal{R}_F = \begin{bmatrix} \boldsymbol{\varrho}_{11} & \boldsymbol{\varrho}_{12} & \cdot & \cdot & \boldsymbol{\varrho}_{1N_{C_s}} \\ \boldsymbol{\varrho}_{21} & \boldsymbol{\varrho}_{22} & \cdot & & \cdot \\ \cdot & \cdot & \cdot & \cdot & \cdot \\ \boldsymbol{\varrho}_{N_{C_s}1} & \cdot & \cdot & \cdot & \boldsymbol{\varrho}_{N_{C_s}N_{C_s}} \end{bmatrix} \quad (2.83)$$

where $\boldsymbol{\varrho}$ (described below) are the interaction tensors, and the subscripts denote the contact number. The friction force at a contact point has a *direct contribution* to contact between i and j , which is accounted for by the diagonal terms in \mathcal{R}_F . The off-diagonal terms are necessary to find the *indirect contributions* of the friction forces that arise from multiple contacts on segments i and j with other fiber segments.

The interaction tensors can be expressed in terms of components from Eq. (2.76). Consider a contact between segments i and j . The diagonal components of \mathcal{R}_F are $\boldsymbol{\varrho}_{ij,ji}$, and have the form

$$\boldsymbol{\varrho}_{ij,ji} = \begin{bmatrix} (\mathcal{J}_{ij}^\dagger - \mathcal{J}'_{ji}{}^\dagger) \cdot \mathbf{e}_{ij}^1 \\ (\mathcal{J}_{ij}^\dagger - \mathcal{J}'_{ji}{}^\dagger) \cdot \mathbf{e}_{ij}^2 \\ \mathbf{n}_{ij} \end{bmatrix}. \quad (2.84)$$

where we have made use of the fact that $\mathbf{F}_{ji}^{\text{fric}*} = -\mathbf{F}_{ij}^{\text{fric}*}$. In general, when the first index of a vector or tensor term is larger than the second (i.e., $j > i$), the following substitutions are made:

$$\begin{aligned} \mathbf{F}_{ji}^{\text{fric}*} &= -\mathbf{F}_{ij}^{\text{fric}*}, \\ \mathbf{n}_{ji} &= -\mathbf{n}_{ij}, \\ g_{ji}^* &= g_{ij}^*, \end{aligned}$$

Table 2.2: Summary of the interaction tensor for the off-diagonal components of \mathcal{R}_F for contact between segments i and j ($i < j$) in which an indirect contact occurs with segment m (see also Fig. 2.12).

Case	Off diagonal \mathbf{F}^{fric}	ξ	term used for $\boldsymbol{\varrho}$ (\mathcal{J} or \mathcal{J}')
I: $i < m$	$\mathbf{F}_{im}^{\text{fric}*}$	+1	\mathcal{J}_{im}
II: $i > m$	$\mathbf{F}_{mi}^{\text{fric}*}$	-1	\mathcal{J}_{im}
III: $j < m$	$\mathbf{F}_{jm}^{\text{fric}*}$	+1	\mathcal{J}'_{jm}
IV: $j > m$	$\mathbf{F}_{mj}^{\text{fric}*}$	-1	\mathcal{J}'_{jm}

which make the vectors \mathbf{G}_{ij}^* and \mathbf{G}_{ji}^* ,

$$\mathbf{G}_{ij}^* = s_{ij}^* \mathbf{p}_i + \frac{g_{ij}^*}{2} \mathbf{n}_{ij},$$

$$\mathbf{G}_{ji}^* = s_{ji}^* \mathbf{p}_j - \frac{g_{ij}^*}{2} \mathbf{n}_{ij}.$$

If segment i has an additional contact with segment m , there is an indirect contribution to the friction force between i and j , that leads to an off-diagonal interaction tensor of the form

$$\boldsymbol{\varrho}_{ij,im} = \xi \begin{bmatrix} \mathcal{J}_{im}^\dagger \cdot \mathbf{e}_{ij}^1 \\ \mathcal{J}_{im}^\dagger \cdot \mathbf{e}_{ij}^2 \\ \mathbf{0} \end{bmatrix}, \quad (2.85)$$

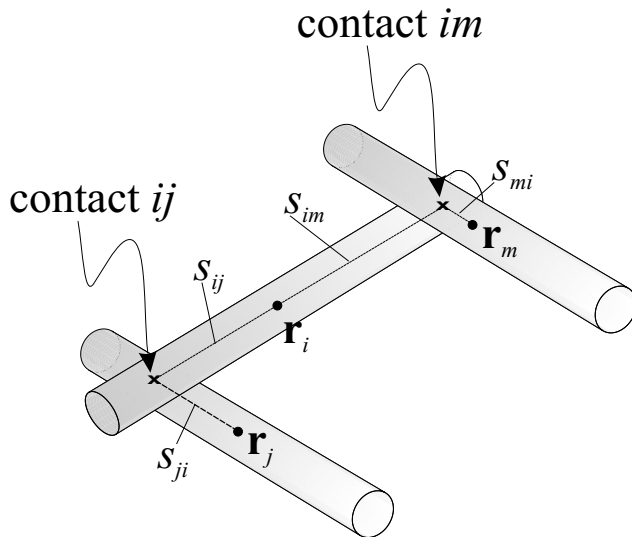
where $\xi = \pm 1$, which takes into account the sign of $\mathbf{F}_{im}^{\text{fric}*}$ based on the indices i and m . If m contacts segment j , the off-diagonal term is

$$\boldsymbol{\varrho}_{ij,jm} = \xi \begin{bmatrix} \mathcal{J}'_{jm} \cdot \mathbf{e}_{ij}^1 \\ \mathcal{J}'_{jm} \cdot \mathbf{e}_{ij}^2 \\ \mathbf{0} \end{bmatrix}. \quad (2.86)$$

The evaluation of the off-diagonal components of \mathbf{varrho} of \mathcal{R}_F leads to four possible scenarios for any three-segment system. This is outlined in Fig. 2.12 and the construction of the off-diagonal components of $\boldsymbol{\varrho}$ terms is summarized in Table 2.2.

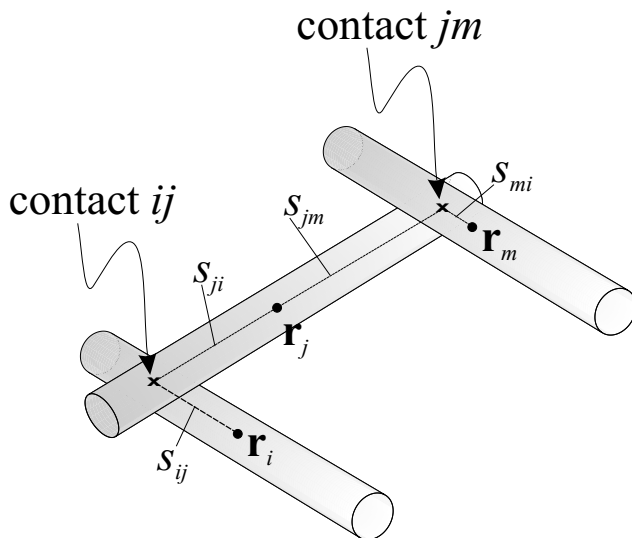
The right side of Eq. 2.82 contains the geometric dependencies and the inextensibility constraint forces. This results in

$$(\mathcal{V}_F - \mathcal{Z}_X \cdot \mathbf{X}_{[\text{prev}]})_{ij} = \begin{pmatrix} \mathcal{I}_{ij} \cdot \mathbf{e}_{ij}^1 \\ \mathcal{I}_{ij} \cdot \mathbf{e}_{ij}^2 \\ \mathbf{0} \end{pmatrix}, \quad (2.87)$$



Case I : contact ij counted
before contact im
(i.e. $i < m$)

Case II: contact im counted
before contact ij
(i.e. $i > m$)



Case III: contact ij counted
before contact jm
(i.e. $j < m$)

Case IV: contact jm counted
before contact ij
(i.e. $j > m$)

Figure 2.12: Scenarios for contacts among any three segments i , j , and m , where the main contact of interest is between i and j .

where the term \mathcal{I}_{ij} is

$$\begin{aligned}
\mathcal{I}_{ij} = & -(\mathcal{Q}_i \cdot (\mathbf{X}_{[\text{prev}]}^*)_i + \mathcal{Q}' \cdot (\mathbf{X}_{[\text{prev}]}^*)_{i+1}) \\
& + \mathcal{M} \cdot (\mathbf{X}_{[\text{prev}]}^*)_j + \mathcal{M}' \cdot (\mathbf{X}_{[\text{prev}]}^*)_{j+1} \\
& + \mathbf{a}_i^* - \mathbf{a}_j^* - \tilde{\mathbf{G}}_{ij}^* \cdot \mathbf{b}_i^* + \tilde{\mathbf{G}}_{ji}^* \cdot \mathbf{b}_j^*.
\end{aligned} \tag{2.88}$$

Appendix C contains an example of how to build the matrix \mathcal{R}_F .

If the fiber joints bend anisotropically via pin joints, we treat the constraint torques $Y_i^{\text{an}*}$ in a manner similar to that for \mathbf{X}_i^* , in that we use the values from the previous time step. Thus, the right side of the friction constraint equation $[(\mathcal{I}_{ij})_{\text{aniso.}}]$ for fibers with pin joints is

$$\begin{aligned}
(\mathcal{I}_{ij})_{\text{aniso.}} = \mathcal{I}_{ij} & - \mathcal{Q}_i^{\text{an}} Y_i^{\text{an}*} - \mathcal{Q}'_i{}^{\text{an}} Y_{i+1}^{\text{an}*} \\
& - \mathcal{M}_j^{\text{an}} Y_j^{\text{an}*} - \mathcal{M}'_j{}^{\text{an}} Y_{j+1}^{\text{an}*}
\end{aligned} \tag{2.89}$$

Once all of the friction forces are known, we can update the inextensibility constraint forces as if the fibers were isolated bodies. For each fiber, a linear system of equations of the form

$$\mathcal{R}_X \cdot \mathbf{X}^* = \mathcal{V}_X - \mathcal{Z}_F \cdot \mathbf{F}^{\text{fric}*}, \tag{2.90}$$

is solved. The term \mathcal{R}_X has a band diagonal structure that contains five terms immediately to the left (below) and right (above) the main diagonal. Using the orientation matrices defined in Eq. (2.74), \mathcal{R}_X for a single fiber with N_{seg} segments is

$$(\mathcal{R}_X) = \begin{bmatrix} \mathcal{T}_1 & \mathcal{U}_1 & \mathbf{0} \dots & & \\ \mathcal{S}_2 & \mathcal{T}_2 & \mathcal{U}_2 & \mathbf{0} \dots & \\ \mathbf{0} & \mathcal{S}_3 & \mathcal{T}_3 & \mathcal{U}_3 & \mathbf{0} \dots \\ \vdots & & \ddots & \ddots & \ddots \\ & & & \dots \mathbf{0} & \mathcal{S}_{N_{\text{seg}}-1} & \mathcal{T}_{N_{\text{seg}}-1} \end{bmatrix}, \tag{2.91}$$

If the fibers have pin joints to model anisotropic bending, Eq. (2.90) has a different form on the left hand side,

$$(\mathcal{R}_X)_{\text{aniso.}} \cdot \begin{pmatrix} \mathbf{X}^* \\ \mathbf{Y}^{\text{an}*} \end{pmatrix} = \mathcal{V}_X - \mathcal{Z}_F \cdot \mathbf{F}^{\text{fric}*}, \quad (2.92)$$

in which the matrix $(\mathcal{R}_X)_{\text{aniso.}}$ has the form

$$(\mathcal{R}_X)_{\text{aniso.}} = \begin{bmatrix} \mathcal{T}_1 & \mathcal{U}_1 & \mathbf{0} \dots & & & \mathcal{T}_1^{\text{an}} & \mathcal{U}_1^{\text{an}} & \mathbf{0} \dots & & & \\ \mathcal{S}_2 & \mathcal{T}_2 & \mathcal{U}_2 & \mathbf{0} \dots & & \mathcal{S}_2^{\text{an}} & \mathcal{T}_2^{\text{an}} & \mathcal{U}_2^{\text{an}} & \mathbf{0} \dots & & \\ \mathbf{0} & \mathcal{S}_3 & \mathcal{T}_3 & \mathcal{U}_3 & \mathbf{0} \dots & \mathbf{0} & \mathcal{S}_3^{\text{an}} & \mathcal{T}_3^{\text{an}} & \mathcal{U}_3^{\text{an}} & \mathbf{0} \dots & \\ \vdots & & \ddots & \ddots & \ddots & \vdots & & \ddots & \ddots & \ddots & \\ \dots \mathbf{0} & \mathcal{S}_{N_{\text{seg}}-1} & \mathcal{T}_{N_{\text{seg}}-1} & & & \dots \mathbf{0} & \mathcal{S}_{N_{\text{seg}}-1}^{\text{an}} & \mathcal{T}_{N_{\text{seg}}-1}^{\text{an}} & & & \\ \mathcal{H}_1^1 & \mathcal{H}_1^2 & \mathbf{0} \dots & & & \mathcal{P}_1^1 & \mathcal{P}_1^2 & \mathbf{0} \dots & & & \\ \mathcal{H}_2^0 & \mathcal{H}_2^1 & \mathcal{H}_2^2 & \mathbf{0} \dots & & \mathcal{P}_2^0 & \mathcal{P}_2^1 & \mathcal{P}_2^2 & \mathbf{0} \dots & & \\ \mathbf{0} & \mathcal{H}_3^0 & \mathcal{H}_3^1 & \mathcal{H}_3^2 & \mathbf{0} \dots & \mathbf{0} & \mathcal{P}_3^0 & \mathcal{P}_3^1 & \mathcal{P}_3^2 & \mathbf{0} \dots & \\ \vdots & & \ddots & \ddots & \ddots & \vdots & & \ddots & \ddots & \ddots & \\ \dots \mathbf{0} & \mathcal{H}_{N_{\text{seg}}-1}^0 & \mathcal{H}_{N_{\text{seg}}-1}^1 & & & \dots \mathbf{0} & \mathcal{P}_{N_{\text{seg}}-1}^0 & \mathcal{P}_{N_{\text{seg}}-1}^1 & \mathcal{P}_{N_{\text{seg}}-1}^2 & & \end{bmatrix},$$

Each term on the right side of Eq.(2.90) has the form

$$(\mathcal{V}_X - \mathcal{Z}_F \cdot \mathbf{F}^{\text{fric}*})_i = - \left(\mathbf{a}_i^* - \mathbf{a}_{i+1}^* - r_p [\tilde{\mathbf{p}}_i \cdot \mathbf{b}_i^* + \tilde{\mathbf{p}}_{i+1} \cdot \mathbf{b}_{i+1}^*] \right) \quad (2.93)$$

$$+ \sum_k^{N_{C_i}} \mathcal{W}_{ik}^- \cdot \mathbf{F}_{ik}^{\text{fric}*} + \sum_l^{N_{C_{i+1}}} \mathcal{W}_{i+1l}^+ \cdot \mathbf{F}_{i+1l}^{\text{fric}*} + [\mathbf{b}_{i+1} - \mathbf{b}_i] \cdot \mathbf{e}_i^{\text{an}}, \quad (2.94)$$

where \mathbf{e}_i^{an} equals zero for isotropic bending fibers.

2.10 The computational algorithm

Simulations of fiber suspensions consists of three basic tasks: (1) initialization, (2) constraint evaluation and integration, and (3) post-processing. Initialization consists of constructing the initial configuration and choosing run parameters. The constraint evaluation and integration involves numerically solving for the constraint forces, po-

sitions, and orientations of the fiber for a specified strain (γ_{fin}). Finally, the stored data is post-processed to calculate suspension averaged quantities.

2.10.1 Initialization

A fiber suspension is simulated by solving for the motion of the fibers in a sample volume of fluid, the size of which is chosen based on the available computer memory, desired computational time, and the length scale of particle interactions. In order to avoid the surface effects in the sample volume, *periodic boundary conditions* are employed [1]. The sample volume, called the central simulation cell, can be chosen as any semi-regular space-filling polyhedra (i.e., cube, octahedron). The central cell is replicated throughout space forming a periodic lattice of images, and the fibers in the replicated cells move in the same way as the central cell. If a fiber leaves one face of the cell, its periodic image enters through the opposite face. In these simulations, a cubic simulation cell is used in which the side lengths are proportional to the length of the fiber, ζL . The parameter ζ is a scaling factor that must be large enough so that a fiber cannot interact with itself. For the simulations reported here $1.5 \leq \zeta \leq 4$.

A concentration of the fiber suspension is chosen in terms of the dimensionless concentration, nL^3 , or the volume fraction, Φ . The number of fibers N_{fib} in the simulation cell is

$$N_{\text{fib}} = \zeta^3(nL^3) = \frac{4\zeta^3 r_p^2}{\pi} \Phi. \quad (2.95)$$

The centers-of-mass of N_{fib} fibers with N_{seg} segments and a predetermined equilibrium shape (θ_i^{eq} and ϕ_i^{eq}) are randomly placed in the simulation cell with a random orientation, such that no fiber segments overlap (i.e., $h_{ij}^* > 2$). After the initial configuration of fibers is chosen, additional simulations parameters are set. Table 2.3 summarizes the input parameters for a simulation.

Table 2.3: Input parameter for fiber simulations

Parameter	Description
N_{fib}	number of fibers in the system
N_{seg}	number of segments per fiber
r_{p_s}	aspect ratio of a segment, $r_{p_s} = r_p/N_{\text{seg}}$
κ_b^*	dimensionless bending constant, $\kappa_b^* = N_{\text{seg}}^4 S^{\text{eff}}/\pi$
μ^{stat}	static coefficient of friction
μ^{kin}	kinetic coefficient of friction
h_{cut}^*	contact cutoff distance, usually $h_{\text{cut}}^* = 0.33$
h_{lim}^*	normal force interaction distance, usually $h_{\text{lim}}^* = 2h_{\text{cut}}^*$
$h_{\text{neighb.}}^*$	neighbor list cutoff distance, $h_{\text{neighb.}}^* \approx r_{p_s}/2$
T_{cut}	number of time steps between neighbor list updates
$\Delta\gamma$	dimensionless time step
γ_{fin}	total strain for the simulation run

2.10.2 Constraint evaluation and integration

For each time step, the quantities that only depend on positions and orientations, \mathbf{a}_i and \mathbf{b}_i from Eqs. (2.43)-(2.44), are first calculated. This consists of finding the surface to surface separation distance for each fiber segment pair and calculating the normal forces, $\mathbf{F}_{ij}^{\text{N}*}$, as described in Section 2.4. The process of finding separations can be sped up by using neighbor lists [1]. Instead of seeking the separation distance for every fiber segment pair at every time step, a list of “neighbors” is maintained for each segment, which contains the numbers of all other segments that are separated by a distance $h_{ij}^* < h_{\text{neighb.}}^*$ from the given segment. We assume that the number of fiber segments that may interact with a given segment changes infrequently. Thus, we only need to update the neighbor list every T_{cut} time steps. The fiber segments are sorted into groups that share contacting segments. Restoring torques \mathbf{Y}_i^* are then calculated using the equations derived in Section 2.6.

The next step is calculate the constraint forces. The friction forces $\mathbf{F}_{ij}^{\text{fric}*}$ are found by solving Eq. (2.82) for each group of contacting fiber segments, in which the values of the inextensibility constraint forces are that of the previous time step,

$\mathbf{X}_{[\text{prev}]i}^*$. Once the forces $\mathbf{F}_{ij}^{\text{fric}*}$ are known, the values of \mathbf{X}_i^* are calculated for each fiber using Eq. (2.90).

With all of the forces calculated for each fiber segment, the final step is to integrate the equations of motion. The translational velocities $\dot{\mathbf{r}}_i^*$ and angular velocities $\dot{\boldsymbol{\omega}}_i^*$ are calculated for every fiber segment using Eqs. (2.43) and (2.44). The new fiber positions are found by integrating the velocity of the center-of-mass of the fiber $\dot{\mathbf{R}}_{\text{cm}}^*$,

$$\dot{\mathbf{R}}_{\text{cm}}^* = \frac{1}{N_{\text{seg}}} \sum_{i=1}^{N_{\text{seg}}} \dot{\mathbf{r}}_i^*. \quad (2.96)$$

The orientational motion of each fiber segment is specified by the time derivative of the the Euler parameters $\dot{\mathbf{q}}_i^*$ as calculated with Eq. (2.63). The fiber center-of-mass and the segment Euler parameters for the next time step are obtained using the Adams-Bashforth two-step integration scheme of the form [38]

$$\mathbf{R}_{\text{cm}}^*(\gamma + \Delta\gamma) = \mathbf{R}_{\text{cm}}^*(\gamma) + \left[1.5\dot{\mathbf{R}}_{\text{cm}}^*(\gamma) - 0.5\dot{\mathbf{R}}_{\text{cm}}^*(\gamma - \Delta\gamma) \right] \Delta\gamma, \quad (2.97)$$

$$\mathbf{q}_i(\gamma + \Delta\gamma) = \mathbf{q}_i(\gamma) + [1.5\dot{\mathbf{q}}_i^*(\gamma) - 0.5\dot{\mathbf{q}}_i^*(\gamma - \Delta\gamma)] \Delta\gamma, \quad (2.98)$$

where $\gamma = \dot{\gamma}t$. Finally, the fibers are “regrown” based on the values of the fiber centers-of-mass and the orientations, in order to correct for integration and round-off errors,

$$\mathbf{r}_1^* = \mathbf{R}_{\text{cm}}^* - \frac{r_{p_s}}{N_{\text{seg}}} \sum_{i=2}^{N_{\text{seg}}} \left(\mathbf{p}_1 + \mathbf{p}_i + 2 \sum_{j=2}^{i-1} \mathbf{p}_j \right), \quad (2.99)$$

$$\mathbf{r}_{i \neq 1}^* = \mathbf{r}_1^* + r_{p_s} \mathbf{p}_1 + 2r_{p_s} \sum_{j=2}^{i-1} \mathbf{p}_j + r_{p_s} \mathbf{p}_i. \quad (2.100)$$

2.10.3 Post-processing

During the simulation run, the fiber positions (\mathbf{R}_{cm}^*), orientations (\mathbf{q}_i), inextensibility constraint forces (\mathbf{X}_i^*), and total number of contacts in the suspension are written

to files at predetermined strain intervals. These files are post-processed to determine various suspension averaged quantities such as the pair distribution function, average number of contacts at steady state, and the suspension stress.

We determine a steady state by monitoring the average number of contacts per fiber $\langle n_C(\gamma) \rangle$. We find that this quantity approaches a constant (with small fluctuations) after simulating to a strain γ_{ss} , which varies from run to run. The average number of contacts per fiber at steady state is $\langle n_C(\gamma) \rangle_{ss}$, is calculated by averaging $\langle n_C \rangle$ from γ_{ss} to γ_{fin} .

The pair distribution function for the fiber centers-of-mass is calculated at steady state for each simulation run. The pair distribution function $g(r)$ is defined as the probability of finding the centers-of-mass of any two fibers at a distance r apart, relative to the probability expected for a completely random distribution of fibers at the same density. The algorithm of Allen and Tildesley [1] is used to calculate $g(r)$ for the fiber centers-of-mass. We define a system to be flocculated when $g(r = 0.01L) \gtrsim 3$. This somewhat arbitrary criterion was established by comparing pair distribution functions with snapshots of numerous suspension configurations.

The particle contribution to the stress in a fiber suspension is calculated using slender body theory [Eq. (1.22)], in a manner similar to that developed by Mackaplow and Shaqfeh [54]. For a fiber made up of N_{seg} segments, the extra particle stress is written in terms of the dimensionless quantities $\mathbf{F}_i^*(s^*)$, \mathbf{F}_i^{hyd*} , s^* , and \mathbf{r}_i^* ,

$$\frac{\boldsymbol{\sigma}^p}{\eta_o \dot{\gamma}} = \frac{\pi n L^3}{16 N_{seg}^3 r_p^3} \left\langle \sum_i^{N_{seg}} \left\{ \int_{-r_{ps}}^{r_{ps}} [s^* \mathbf{F}_i^*(s^*) \mathbf{p}_i + s^* \mathbf{p}_i \mathbf{F}_i^*(s^*)] ds^* \right. \right. \quad (2.101)$$

$$\left. \left. + r_{ps} (\mathbf{F}_i^{hyd*} \mathbf{r}_i^* + \mathbf{r}_i^* \mathbf{F}_i^{hyd*}) \right\} \right\rangle + \Upsilon \boldsymbol{\delta},$$

where $\Upsilon \boldsymbol{\delta}$ is an isotropic contribution to the stress tensor of no interest. The expressions for the dimensionless forces per unit length and net hydrodynamic force for each

segment are (neglecting hydrodynamic interactions between segments)

$$\mathbf{F}_i^*(s^*) = \frac{4}{\ln(2r_{ps})} \left[\boldsymbol{\delta} - \frac{1}{2} \mathbf{p}_i \mathbf{p}_i \right] \cdot (\mathbf{U}_i^{\infty*}(s^*) - \dot{\mathbf{r}}_i^* - s^* \dot{\mathbf{p}}_i^*), \quad (2.102)$$

$$\mathbf{F}_i^{\text{hyd}*} = \frac{4}{\ln(2r_{ps})} \left[\boldsymbol{\delta} - \frac{1}{2} \mathbf{p}_i \mathbf{p}_i \right] \cdot (\mathbf{U}_i^{\infty*} - \dot{\mathbf{r}}_i^*). \quad (2.103)$$

Combining the equations above and assuming a simple shear flow $[\mathbf{U}_i^{\infty*}(s^*) = \dot{\gamma}(\mathbf{r}_i^* + s^* \mathbf{p}_i) \cdot \mathbf{e}_{\text{grad}} \mathbf{e}_{\text{flow}}$, where \mathbf{e}_{grad} is a unit vector in the gradient direction and \mathbf{e}_{flow} is a unit vector in the flow direction], the particle contribution to the stress simplifies to

$$\begin{aligned} \frac{\boldsymbol{\sigma}^P}{\eta_o \dot{\gamma}} &= \frac{\pi n L^3}{6 N_{\text{seg}}^3 \ln(2r_{ps})} \left\langle \sum_{i=1}^{N_{\text{seg}}} \left\{ \mathbf{E}^{\infty*} \cdot \mathbf{p}_i \mathbf{p}_i + \mathbf{p}_i \mathbf{p}_i \cdot \mathbf{E}^{\infty*} - \right. \right. \\ &\quad \left. \left. \mathbf{p}_i \mathbf{p}_i \mathbf{p}_i \mathbf{p}_i : \mathbf{E}^{\infty*} - (\mathbf{p}_i \dot{\mathbf{p}}_i^* + \dot{\mathbf{p}}_i^* \mathbf{p}_i) \right. \right. \\ &\quad \left. \left. \frac{3}{r_{ps}^2} \left(\left[\boldsymbol{\delta} - \frac{1}{2} \mathbf{p}_i \mathbf{p}_i \right] \cdot (\mathbf{U}_i^{\infty*} - \dot{\mathbf{r}}_i^*) \mathbf{r}_i^* + \mathbf{r}_i^* \left[\boldsymbol{\delta} - \frac{1}{2} \mathbf{p}_i \mathbf{p}_i \right] \cdot (\mathbf{U}_i^{\infty*} - \dot{\mathbf{r}}_i^*) \right) \right\} \right\rangle \\ &\quad + \Upsilon \boldsymbol{\delta}. \end{aligned} \quad (2.104)$$

2.11 Planar fiber networks

2.11.1 Network formation

We employ a slight modification of the simulation technique described above to simulate the formation of planar fiber networks, or “sheets,” and then subject the sheets to elongation to determine their tensile strength. Formation of the networks was accomplished by starting with a random distribution of fibers between parallel plates. The plates were located at $z = 0$ and $z = 2\zeta L$ as shown in Fig. 2.13, while periodic boundary conditions were employed in the x and y directions. The top plate has a mass M , and the fiber sheet is formed by allowing the top plate to fall in the $-z$ direction under the force of gravity while pushing the fibers towards the bottom plate.

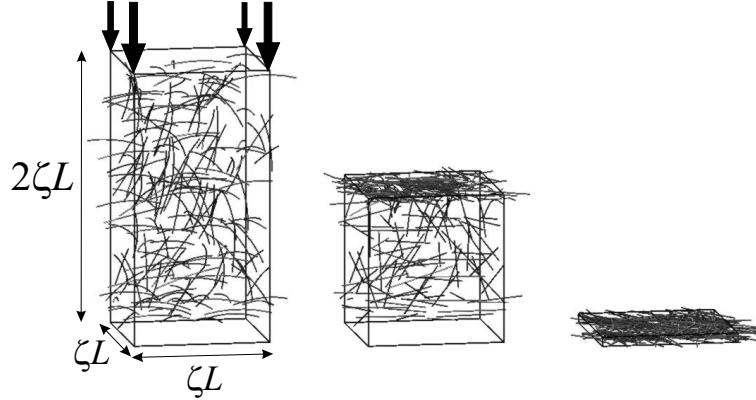


Figure 2.13: Formation of a planar fiber network is accomplished by squeezing a randomly oriented fiber suspension between two plates.

The bottom plate is a smooth planar screen that is only permeable to the suspending liquid. The motion of the top plate is governed by

$$M \frac{d^2 z_{\text{pl}}}{dt^2} = -Mg + \sum_i^{N_{\text{c,pl}}} F_{z_i}^{\text{N}}, \quad (2.105)$$

where z_{pl} is the vertical position of the top plate, g the acceleration of gravity, $F_{z_i}^{\text{N}}$ is the force in the z direction due to frictionless interactions between the top plate and fiber segments [using Eq. (2.7)], and $N_{\text{c,pl}}$ is the number of fiber contacts with the top plate. Quantities in Eq. (2.105) are scaled as defined previously, except that the characteristic deformation rate is now defined $\dot{\gamma} = \sqrt{g/b}$. The dimensionless equation for the motion of the top plate is thus

$$\frac{d^2 z_{\text{pl}}^*}{dt^{*2}} = -1 + \frac{1}{F_g} \sum_i^{N_{\text{c,pl}}} F_{z_i}^{\text{N}*}, \quad (2.106)$$

where the weight parameter F_g is

$$F_g = \frac{M\dot{\gamma}}{6\pi\eta_o\ell}. \quad (2.107)$$

The value of the weight parameter used in the simulations was $F_g = 10^5$.

The fiber motion is determined as explained previously, and the motion of the top plate is obtained by solving Eq. (2.106) numerically. When the desired network

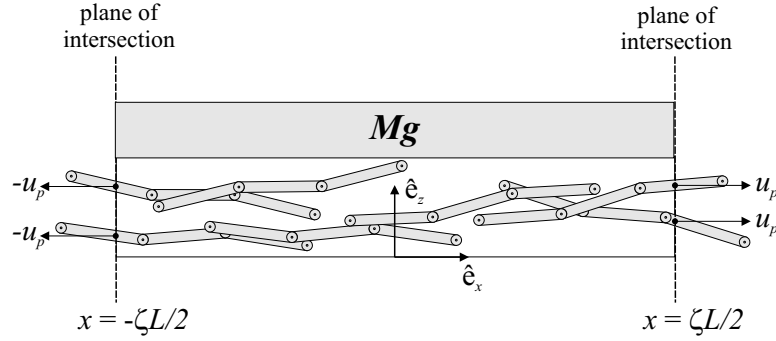


Figure 2.14: Example of fiber that intersects the end plane of the planar network.

thickness is reached, the motion of the top plate is stopped. The suspension is then relaxed between the plates at the desired separation, by running the simulation with no fluid or plate motion (i.e., constant plate separation).

2.11.2 Elongation of planar networks

The strength of the network formed is tested by elongating the network at a constant velocity u_p in the x direction. The samples have a length in the x direction of ζL , and periodic boundary conditions in the y direction. The tensile force is found by applying a constraint on fibers that pass through opposing planes at $x = \pm\zeta L/2$, as illustrated in Fig. 2.14. The fibers intersect the planes at the point $\mathbf{r}_i + \nu_i \mathbf{p}_i$, where ν_i is the distance from the segment center to the point of intersection with the plane in the direction of \mathbf{p}_i ,

$$\nu_i = \frac{\pm\zeta L/2 - r_{x_i}}{p_{x_i}}, \quad (2.108)$$

where the \pm corresponds to intersection with the planes at $x = \zeta L/2$ or $x = -\zeta L/2$, respectively. The constraint for the N_p fiber segments that are “grabbed” at the planes is

$$(\dot{\mathbf{r}}_i + \nu_i \boldsymbol{\omega} \times \mathbf{p}_i) \cdot \hat{\mathbf{e}}_x = \pm u_p. \quad (2.109)$$

The equations of motion for pulled fiber segments are modified by the addition of an unknown constraint force in the x direction, $F_i^{p*} \hat{\mathbf{e}}_x$. The quantity F_i^p is the magnitude of the force necessary to pull the fiber segment at a constant speed, u_p . The equations are scaled as described in Section 2.7, except that now the characteristic deformation rate is $\dot{\gamma} = u_p/b$. The dimensionless equations of motion are now

$$\dot{\mathbf{r}}_i^* = \mathbf{a}_i^* + \mathbf{A}_i^{-1} \cdot \left[\sum_j^{N_{C_i}} \mathbf{F}_{ij}^{\text{fric}*} + \mathbf{X}_{i+1}^* - \mathbf{X}_i^* + F_i^{p*} \hat{\mathbf{e}}_x \right], \quad (2.110)$$

$$\begin{aligned} \boldsymbol{\omega}_i^* = \mathbf{b}_i^* + \mathbf{C}_i^{-1} \cdot & \left[\frac{3}{4r_{ps}^2} \sum_j^{N_{C_i}} \tilde{\mathbf{G}}_{ij}^* \cdot \mathbf{F}_{ij}^{\text{fric}*} + \frac{3}{4r_{ps}} \tilde{\mathbf{p}}_i \cdot [\mathbf{X}_{i+1}^* + \mathbf{X}_i^*] \right. \\ & \left. + \frac{3}{4r_{ps}^2} [\nu_i^* \mathbf{p}_i \times F_i^{p*} \hat{\mathbf{e}}_x] \right]. \end{aligned} \quad (2.111)$$

We must add additional terms to the substituted constraint equations as well, to take into account the unknown force magnitude F^{p*} . The time derivative of the inextensibility constraint [Eq. (2.74)] has the new form $(\dot{\Psi}_i^*)_{\text{pull}}$,

$$(\dot{\Psi}_i^*)_{\text{pull}} = \dot{\Psi}_i^* + \mathcal{K}_i \cdot F_i^{p*} \hat{\mathbf{e}}_x + \mathcal{K}'_i \cdot F_{i+1}^{p*} \hat{\mathbf{e}}_x, \quad (2.112)$$

in which the orientation tensors \mathcal{K}_i and \mathcal{K}'_i are

$$\begin{aligned} \mathcal{K}_i &= \mathbf{A}_i^{-1} - \frac{3\nu_i^*}{4r_{ps} Y_C} \tilde{\mathbf{p}}_i^2, \\ \mathcal{K}'_i &= -\mathbf{A}_{i+1}^{-1} - \frac{3\nu_{i+1}^*}{4r_{ps} Y_C} \tilde{\mathbf{p}}_{i+1}^2. \end{aligned}$$

The first two terms of the substituted friction constraint [Eq. (2.76)] are also modified to the form

$$\begin{aligned} (\Xi_{ij})_{1 \text{ or } 2}^{\text{pull}*} = (\Xi_{ij})_{1 \text{ or } 2}^* &+ (\mathcal{L}_i \cdot \mathbf{e}_{ij}^{1 \text{ or } 2}) \cdot F_i^{p*} \hat{\mathbf{e}}_x \\ &+ (\mathcal{N}_j \cdot \mathbf{e}_{ij}^{1 \text{ or } 2}) \cdot F_j^{p*} \hat{\mathbf{e}}_x, \end{aligned} \quad (2.113)$$

where the tensors \mathcal{L}_i and \mathcal{N}_i are

$$\begin{aligned}\mathcal{L}_i &= \mathbf{A}_i^{-1} - \frac{3\nu_i^*}{4r_{ps}YC} \tilde{\mathbf{G}}_{ij} \cdot \tilde{\mathbf{p}}_i, \\ \mathcal{N}_j &= -\mathbf{A}_j^{-1} + \frac{3\nu_j^*}{4r_{ps}YC} \tilde{\mathbf{G}}_{ji} \cdot \tilde{\mathbf{p}}_j.\end{aligned}$$

Finally, we substitute \mathbf{r}_i^* and $\boldsymbol{\omega}_i^*$ into the pulling constraint [Eq. (2.109)],

$$\mathcal{B}_i^0 \cdot \mathbf{X}_i^* + \mathcal{B}_i^1 \cdot \mathbf{X}_{i+1}^* + \sum_j^{N_{C_i}} \mathcal{D}_{ij} \cdot \mathbf{F}_{ij}^{\text{fric}*} + \boldsymbol{\varepsilon}_i \cdot F_i^{p*} \hat{\mathbf{e}}_x + \mathcal{I}_i^{\text{pull}} = 0, \quad (2.114)$$

where the orientation vectors \mathcal{B}_i^0 , \mathcal{B}_i^1 , \mathcal{D}_{ij} , $\boldsymbol{\varepsilon}_i$ and the term $\mathcal{I}_i^{\text{pull}}$ are

$$\begin{aligned}\mathcal{B}_i^0 &= \left[-\mathbf{A}_i^{-1} - \frac{3\nu_i^*}{4r_{ps}YC} \tilde{\mathbf{p}}_i^2 \right] \cdot \hat{\mathbf{e}}_x, \\ \mathcal{B}_i^1 &= \left[\mathbf{A}_i^{-1} - \frac{3\nu_i^*}{4r_{ps}YC} \tilde{\mathbf{p}}_i^2 \right] \cdot \hat{\mathbf{e}}_x, \\ \mathcal{D}_{ij} &= \left[\mathbf{A}_i^{-1} - \frac{3\nu_i^*}{4r_{ps}^2YC} \tilde{\mathbf{p}}_i \cdot \tilde{\mathbf{G}}_{ij} \right] \cdot \hat{\mathbf{e}}_x, \\ \boldsymbol{\varepsilon}_i &= \left[\mathbf{A}_i^{-1} - \frac{3\nu_i^{*2}}{4r_{ps}^2YC} \tilde{\mathbf{p}}_i^2 \right] \cdot \hat{\mathbf{e}}_x, \\ \mathcal{I}_i^{\text{pull}} &= [\mathbf{a}_i - \nu_i^* \tilde{\mathbf{p}}_i \cdot \mathbf{b}_i] \cdot \hat{\mathbf{e}}_x - 1.\end{aligned}$$

The unknown constraint forces $\mathbf{F}_{ij}^{\text{fric}*}$, \mathbf{X}_i^* , and F_i^p are found using the approximate method described in Section 2.9.2. The previous values of the pulling forces F_i^p are used to find $\mathbf{F}_{ij}^{\text{fric}*}$, and then \mathbf{X}_i^* , and F_i^p are found simultaneously (as done for fibers with pin joints). Finally, the magnitude of the tensile force T of the network at a particular time step is found by

$$T = \frac{1}{2} \left(\sum_i^{N_p^{\text{pos}}} F_i^p - \sum_j^{N_p^{\text{neg}}} F_j^p \right), \quad (2.115)$$

where N_p^{pos} and N_p^{neg} are the number of segments pulled at the planes $x = +\zeta L/2$ and $x = -\zeta L/2$, respectively.

Chapter 3

Flocculation in sheared fiber suspensions

3.1 Introduction

Suspensions of non-Brownian fibers are found in a variety of applications, such as pulp and paper and fiber-filled composites processing. The physical characteristics of the suspensions, as well as the properties of the final products, depend on the structure of the suspensions. The structure is affected by such features as the fiber properties, interactions, and flow fields. Understanding the relationships among these features, the suspension structure, and the macroscopic properties can therefore aid in the design and optimization of processes and products. In this chapter, we employ a fiber-level simulation method to probe the relationships between fiber properties, interactions, and the suspension structure.

Many applications require a homogenous dispersion of fibers to yield a uniform product. Long flexible fibers tend to aggregate in a process known as flocculation, which produces spatially heterogeneous structures. While aggregation in colloidal dis-

persions typically arises from attractive interparticle forces [72], Mason [55, 56] suggested that non-Brownian fibers can aggregate by a mechanical mechanism. Fibers in shear flow translate and rotate, resulting in collisions between fibers. Above a critical concentration ($nL^3 \gtrsim 1$, where n is the fiber number density and L is the fiber length), the frequent forced collisions between fibers can lead to flocculation via mechanical entanglement. Meyer and Wahren and Soszynski and Kerekes [58, 82, 81] expanded on this notion, proposing a more detailed picture of the flocculation process. Flexible fibers in a flow with nonzero velocity gradients will be exposed to viscous and dynamic forces [58], as well as interfiber contact forces [82, 81], which elastically deform the fibers. When the flow ceases, the fibers attempt to relax, but if the concentration is sufficiently large, the fibers will contact other fibers and come to rest in elastically-strained configurations. The result is a mechanically-coherent fiber network or floc. Soszynski and Kerekes [82] provided evidence for this mechanism by conducting experiments with suspensions of nylon fibers. Suspensions subjected to flow in a rotating, half-filled cylinder formed coherent fiber flocs above a critical concentration. These flocs possessed sufficient mechanical strength to be manually extracted from the cylinder. Some of these flocs were heated above the glass transition temperature of nylon to relax the stored elastic stresses within the fibers, and then cooled to room temperature. The heat-treated flocs dispersed easily under gentle stirring, while the never-heated flocs only dispersed under intense stirring. The authors called this mechanism of flocculation “interlocking by the elastic bending of fibers.” While other forces, such as colloidal forces and interfacial tension arising from entrained gas bubbles, can certainly contribute to fiber aggregation in some systems, it appears that the elastic-interlocking mechanism can contribute to flocculation in any sufficiently concentrated suspension of flexible fibers.

Meyer and Wahren [58] modelled concentrated suspensions of flexible fibers as elastically-interlocked networks, where each fiber is in contact with at least three others. The predicted dependence of the shear modulus on fiber aspect ratio $r_p = L/d$ (d is the fiber diameter), volume fraction Φ , and fiber Young's modulus E_Y agreed reasonably well with experimental data on pulp suspensions [2, 87]. Bennington et al. [12] applied a similar network theory to describe their experimental data on the yield stress of suspensions of synthetic and wood fibers. The predicted dependence of the yield stress on fiber aspect ratio and volume fraction agreed fairly well with experimental results. However, the predicted dependence on the fiber elastic modulus did not agree well with experiments, particularly for the wood fibers. The authors attributed the lack of agreement to more complex surface interactions than that accounted for in the model. It is also possible that, contrary to the assumption in the network theory, the structure of the network may depend on the fiber modulus, and thus the predicted simple dependence of the network properties on fiber modulus may not hold. Indeed, the flocculation behavior of suspensions and thus their microstructure depends on numerous variables, including the suspending fluid viscosity [101], the deformation rate [39, 85], the fiber length [46, 82, 81], the concentration [45], and the type and amount of additives [11, 100]. We will show in this chapter that the structure predicted by simulations also depends on the fiber modulus.

Particle-level simulations are common methods for probing particulate suspensions, and more specifically, for understanding the relationships between particle properties and interactions, the suspension structure, and macroscopic behavior (see, for example, Bossis and Brady [14]). The equations of motion for each particle are solved numerically, subject to the forces and torques identified, in order to evolve the particle positions and orientations in time, and thus produce a prediction of the

suspension microstructure. This method is sufficiently general to allow the inclusion of a variety of features, such as elongated and flexible particles, as well as various forces, such as hydrodynamic forces and interactions, colloidal forces and friction, to name a few. The complexity of the physical model is only limited by the computational resources required to evaluate the forces and torques and solve the equations of motion.

Numerous fiber suspension studies have focused on rigid, elongated bodies in Newtonian fluids. Claeys and Brady [20, 21] modelled fibers as rigid prolate spheroids (ellipsoids of revolution). They developed a method for accurately evaluating the hydrodynamic forces and torques, including both short-range hydrodynamic interactions (lubrication forces) as well as long-range, many-body hydrodynamic interactions. Mackaplow and Shaqfeh [54] employed slender-body theory to accurately evaluate the long-range hydrodynamic interactions between prolate spheroids or cylinders. As with the method of Claeys and Brady, the calculations were so computationally demanding that results for suspensions of long fibers in simple shear flow were limited to prescribed suspension structures. Thus these methods were not employed to predict the suspension structure resulting from flow. Simulations by Yamane et al. and Fan et al. [28, 98] employed approximations for the hydrodynamic interactions between rigid fibers. These authors did not report fiber flocculation under the conditions simulated ($nL^3 \lesssim 50$, $r_p \lesssim 30$).

Sundararajakumar and Koch and Harlen et al. [35, 84] simulated suspensions of rigid, slender rods interacting via contact forces. They argued that for flowing suspensions of fibers, lubrication forces cannot prevent fibers from contacting, and thus short-range hydrodynamic interactions were neglected. Harlen et al. [35] simulated single spheres falling through neutrally-buoyant fiber suspensions to illustrate

the importance of fiber-fiber contacts on the flow properties of fiber suspensions. For low concentrations, interfiber contacts are rare and the flow behavior is dominated by long-range hydrodynamic interactions. However, as the concentration is increased such that the fibers are in frequent contact, the flow behavior is strongly influenced by the contacts. In fact, for $nL^3 \geq 12$ ($r_p = 20$), the drag on the settling sphere calculated by including long-range hydrodynamic interactions and contact forces is indistinguishable from that calculated by including contact forces alone (and in good agreement with experimental results reported by Milliken et al. [59]). Although the falling sphere influences the suspension structure, the authors did not report any tendency toward fiber flocculation.

Several studies have focused on simulating suspensions of flexible fibers. Yamamoto and Matsuoka [93, 94] modelled flexible fibers as chains of rigid spheres connected through springs, with potentials to mimic resistance to bending and twisting. Chain connectivity is maintained by constraints, producing equations that must be solved simultaneously with the equations of motion. Ross and Klingenberg [71] modelled flexible fibers as inextensible chains of rigid prolate spheroids connected through ball and socket joints. This model eliminates the need for iterative constraints to maintain fiber connectivity, and can represent large aspect ratio fibers with relatively few bodies. These features help to reduce computations, facilitating simulation of concentrated suspensions. Schmid et al. [75] extended this method, modelling flexible fibers as chains of spherocylinders connected by ball and socket joints, that interacted via short-range repulsive forces as well as friction forces. While attractive forces can certainly give rise to fiber aggregation, Schmid [74] demonstrated that interfiber friction—in the absence of attractive forces—can produce fiber flocculation.

In this chapter, we expand upon the study of Schmid et al. [75] to probe flocculation in flexible fiber suspensions caused by friction forces. The fiber model and simulation method are briefly described in Section 3.2. In Section 3.3.1, we summarize the results obtained by Schmid et al., illustrating the importance of friction, fiber stiffness, and fiber shape on flocculation. These relationships are investigated further in subsequent sections. In Section 3.3.2, we show that the coefficient of friction necessary to hold model flocs intact decreases with increasing fiber stiffness, and that friction-induced flocculation can occur for values of friction coefficients and fiber stiffnesses similar to those measured experimentally. We also illustrate how friction-induced flocculation is consistent with several experimental observations. The effects of fiber shape are probed in Section 3.3.3. The concentration at which U-shaped fibers flocculate decreases with increasing fiber curvature. We show that sliding friction (Section 3.3.4) and weak attractive forces (Section 3.3.5) have little impact on friction-induced flocculation. In Section 3.3.6, we show that, in some cases, anisotropic fiber bending can inhibit flocculation. Conclusions from this chapter are summarized in Section 3.4.

3.2 Simulation method

Flexible fiber suspensions are modelled as neutrally-buoyant chains of linked rigid bodies immersed in a Newtonian liquid. The model includes realistic features such as fiber flexibility, irregular equilibrium shapes, and mechanical contact forces between fibers. The model and simulation method are similar to those employed by Schmid et al. [74] and are described in more detail in Chapter 2.

Each fiber in the suspension is represented by N_{seg} rigid cylinders (length 2ℓ ,

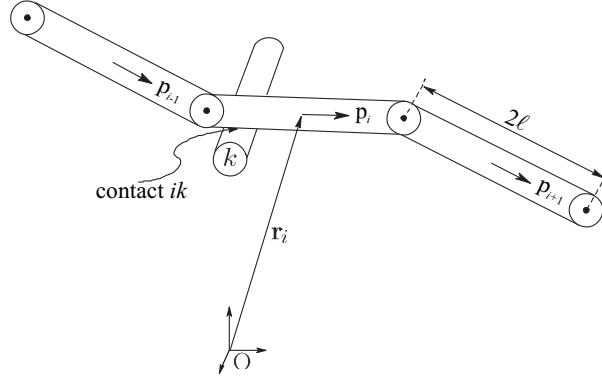


Figure 3.1: Schematic diagram of a model fiber composed of rigid spherocylinders linked by ball and socket joints. Here, segment i is in contact with segment k from another fiber.

radius b) with hemi-spherical end caps, connected end-to-end by ball and socket joints (Fig. 3.1). The motion of the fiber segments is described by Newton's laws of motion in which we neglect fiber inertia. The force balance on a fiber segment i includes contributions from hydrodynamic drag ($\mathbf{F}_i^{\text{hyd}}$), mechanical contact forces ($\mathbf{F}_{ik}^{\text{con}}$), and forces at each joint that maintain the segment connectivity (\mathbf{X}_i),

$$\mathbf{F}_i^{\text{hyd}} + \mathbf{X}_{i+1} - \mathbf{X}_i + \sum_k^{N_{C_i}} \mathbf{F}_{ik}^{\text{con}} = \mathbf{0}, \quad (3.1)$$

where N_{C_i} is the number of contacts on fiber segment i . The torque balance on fiber segment i includes similar contributions with the addition of a restoring torque at each joint (\mathbf{Y}_i),

$$\mathbf{T}_i^{\text{hyd}} + \mathbf{Y}_{i+1} - \mathbf{Y}_i + \ell \mathbf{p}_i \times [\mathbf{X}_{i+1} + \mathbf{X}_i] + \sum_k^{N_{C_i}} [\mathbf{G}_{ik} \times \mathbf{F}_{ik}^{\text{con}}] = \mathbf{0}, \quad (3.2)$$

where $\mathbf{T}_i^{\text{hyd}}$ is the hydrodynamic torque, \mathbf{p}_i is the orientation vector of the segment, and \mathbf{G}_{ik} is a vector from the center of segment i to the point of contact with segment k .

In this model, hydrodynamic interactions are neglected based on simulations performed by Sundararajakumar and Koch and Harlen et al. [35, 84], as previously

explained. This assumption allows us to evaluate the hydrodynamic drag force and torque as that on an isolated body, $\mathbf{F}_i^{\text{hyd}} = \mathbf{A}_i \cdot [\mathbf{U}_i^\infty - \dot{\mathbf{r}}_i]$ and $\mathbf{T}_i^{\text{hyd}} = \mathbf{C}_i \cdot [\boldsymbol{\Omega}_i^\infty - \boldsymbol{\omega}_i] + \tilde{\mathbf{H}}_i : \mathbf{E}^\infty$, where the resistance tensors \mathbf{A}_i , \mathbf{C}_i , and $\tilde{\mathbf{H}}_i$ for the spherocylinder segments are approximated by the resistance tensors of a prolate spheroid with an equivalent aspect ratio $r_{es} = 0.7r_p/N_{\text{seg}}$ (see Chapter 2). The ambient velocity \mathbf{U}_i^∞ , angular velocity $\boldsymbol{\Omega}_i^\infty$, and rate of strain tensor \mathbf{E}^∞ are evaluated at the center-of-mass of each segment, and only simple shear flows are simulated [i.e., $\mathbf{U}^\infty = (\dot{\gamma}z, 0, 0)$, where $\dot{\gamma}$ is the shear rate]. The segment translational and angular velocities are $\dot{\mathbf{r}}_i$ and $\boldsymbol{\omega}_i$, respectively.

The restoring torque \mathbf{Y}_i describes the resistance of the elastic fibers to bending and twisting. The bending and twisting components of this torque are assumed to be linear in the difference between the bending and twisting angles (θ_i and ϕ_i respectively) and their equilibrium values (θ_i^{eq} and ϕ_i^{eq}),

$$|\mathbf{Y}_i| = \kappa_b(\theta_i - \theta_i^{\text{eq}}) + \kappa_t(\phi_i - \phi_i^{\text{eq}}), \quad (3.3)$$

where κ_b and κ_t are the bending and twisting constants of the fiber. The bending constant is related to the stiffness of the fiber material by $\kappa_b = E_Y I / 2\ell$, where E_Y is the Young's modulus, and $I \equiv \pi b^4 / 4$ is the area moment. The twisting constant is set to $\kappa_t = 0.67\kappa_b$ in this study, equal to that of a linearly elastic circular cylinder with a Poisson's ratio of 0.5. The fiber flexibility is characterized by a single parameter which we call the effective stiffness, $S^{\text{eff}} \equiv E_Y I / \eta_o \dot{\gamma} L^4$, where η_o is the suspending fluid viscosity, $\dot{\gamma}$ is the shear rate, and L is the total fiber length.

Fibers of circular cross section are assumed to have no preferential bending direction (isotropic bending). However, many fibers, such as refined wood fibers, have a ribbon-like appearance and tend to bend easier in one direction. This may be modelled by defining two orthogonal bending directions with $(\kappa_b)_{\text{hard}} = E_Y I_{\text{hard}} / 2\ell$ and $(\kappa_b)_{\text{easy}} = E_Y I_{\text{easy}} / 2\ell < (\kappa_b)_{\text{hard}}$, as illustrated in Fig 3.2. For such anisotropic

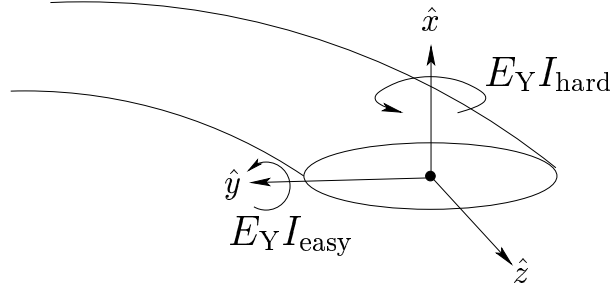


Figure 3.2: Schematic illustration of an anisotropic fiber with a preferred bending axis \hat{y} . In simulations with anisotropic fibers reported here, the fiber cross-section remains circular.

bending situations, the twisting constant remains fixed at $\kappa_t = 0.67(\kappa_b)_{\text{easy}}$. When $E_Y I_{\text{hard}} \rightarrow \infty$, the joint may be modelled as a hinge, resulting in an additional constraint that restricts bending at a joint to that about a preferred axis (e.g., the \hat{y} axis in Fig. 3.2),

$$\hat{\mathbf{y}}_i \cdot \mathbf{p}_{i+1} = \cos \theta', \quad (3.4)$$

where $\hat{\mathbf{y}}_i$ is the preferred bending axis, defined with respect to segment i , and θ' is a constant ($\theta' = \pi/2$ for all simulations with anisotropic bending reported here).

The fiber segments remain connected by applying a constraint for each joint,

$$\mathbf{r}_i + \ell \mathbf{p}_i = \mathbf{r}_{i+1} - \ell \mathbf{p}_{i+1}, \quad (3.5)$$

where \mathbf{r}_i is the position of the center of segment i . These constraint equations allow for the solution of the constraint forces \mathbf{X}_i at each joint. Since the segments are rigid and remain connected, the fibers are inextensible (but still flexible).

Fibers experience mechanical contacts with other fibers in the suspension. Two fiber segments i and k are considered to be in contact if the separation between their surfaces, h_{ik} , is less than $0.33b$. The force that results from each contact is decomposed into two components—a force in the normal direction of the contact ($\mathbf{F}_{ik}^{\text{N}}$) and a frictional force ($\mathbf{F}_{ik}^{\text{fric}}$) in the plane of the contact. The purely repulsive normal force

exerted on segment i by segment k is modelled as $\mathbf{F}_{ik}^N = -F \exp[-ah_{ik}]\mathbf{n}_{ik}$, where \mathbf{n}_{ik} is the unit normal vector directed from segment i to k , $F = 900\pi\eta_o\ell b\dot{\gamma}$ is the force magnitude, and $a = 20/b$. The friction force is determined by the constraint of no relative motion in the plane of contact,

$$\begin{pmatrix} \Delta\mathbf{u}_{ik} \cdot \mathbf{e}_1^{\text{loc}} \\ \Delta\mathbf{u}_{ik} \cdot \mathbf{e}_2^{\text{loc}} \\ \mathbf{F}_{ik}^{\text{fric}} \cdot \mathbf{n}_{ik} \end{pmatrix} = \mathbf{0}, \quad (3.6)$$

where $\Delta\mathbf{u}_{ik}$ is the relative velocity between segments i and k at the point of contact, and the plane of contact is defined by the vectors $\mathbf{e}_1^{\text{loc}}$ and $\mathbf{e}_2^{\text{loc}}$. The calculated friction force is then subjected to a Coulombic friction law of the form

$$\begin{aligned} |\mathbf{F}_{ik}^{\text{fric}}| &\leq \mu^{\text{stat}}|\mathbf{F}_{ik}^N| \Rightarrow \text{contact remains intact} \\ &> \mu^{\text{stat}}|\mathbf{F}_{ik}^N| \Rightarrow \mathbf{F}_{ik}^{\text{fric}} = \mu^{\text{kin}}|\mathbf{F}_{ik}^N| \frac{\Delta\mathbf{u}_{ik}}{|\Delta\mathbf{u}_{ik}|}, \end{aligned} \quad (3.7)$$

where μ^{stat} and μ^{kin} are the static and kinetic coefficients of friction.

The equations of motion and the constraint equations for all of the fiber segments in the suspension can be expressed as a system of differential algebraic equations (DAEs) for the unknown coordinates and constraint forces,

$$\begin{aligned} \dot{\mathbf{q}} - \mathbf{F}(\mathbf{q}, \boldsymbol{\lambda}) &= \mathbf{0}, \\ \boldsymbol{\Psi}(\mathbf{q}) &= \mathbf{0}, \\ \boldsymbol{\Xi}(\mathbf{q}, \dot{\mathbf{q}}, \boldsymbol{\lambda}) &= \mathbf{0}, \end{aligned} \quad (3.8)$$

where \mathbf{q} is a vector containing the generalized coordinates of each fiber segment (positions and orientations), and $\boldsymbol{\lambda}$ is a vector containing all the constraint forces (\mathbf{X} and \mathbf{F}^{fric}) in the suspension. If the segment orientations are represented by Euler parameters [92], there are $7N_{\text{fib}}N_{\text{seg}}$ equations of motion to be solved. The inextensibility constraint [Eq. (3.5)], represented by the vector $\boldsymbol{\Psi}$, is made up of $3N_{\text{fib}}(N_{\text{seg}} - 1)$ constraint equations that depend on only the positions and orientations. The $3N_{\text{C}}$

friction constraint equations [Eq. (3.6)] are contained in Ξ , where N_C is the total number of contacts in the system.

Simulations are performed by randomly placing fibers at their equilibrium shape into a cubic simulation cell of size $(\zeta L)^3$, where ζ is the cell size scaling factor ($1.5 \leq \zeta \leq 4$). A linear shear field is imposed and periodic boundary conditions are applied with the Lees-Edwards modification for shearing systems [1], to simulate an infinite suspension. The fiber motions are obtained by the numerical solution of the system of DAEs in Eq. (3.8). An approximate solution method was developed to solve this system, the details of which are described in Chapter 2.

3.3 Results and discussion

3.3.1 Illustration of flocculation via friction

Suspensions of flexible fibers in simple shear flow were simulated for a variety of values of the parameters introduced in the previous section. Consider first the behavior of fibers that bend isotropically with $N_{\text{seg}} = 5$, aspect ratio $r_p = 75$, concentration $nL^3 = 20$, and that interact only via short-range repulsive forces and static friction ($\mu^{\text{kin}} = 0$ throughout this chapter, unless specifically stated otherwise). This model is similar to that studied by Schmid et al. [75]. As reported therein, this system can flocculate for certain ranges of values of the remaining parameters (fiber shape, stiffness, and coefficient of static friction), even though attractive forces between fibers are absent, as illustrated in Fig. 3.3.

In Fig. 3.3(a), the coefficient of friction is large ($\mu^{\text{stat}} = 20$), the fibers are relatively stiff ($S^{\text{eff}} = 0.05$), and the equilibrium shape is not straight ($\theta^{\text{eq}} = 0.8$, $\phi^{\text{eq}} = 0.7$). The resulting suspension structure is heterogeneous, with two fiber flocs

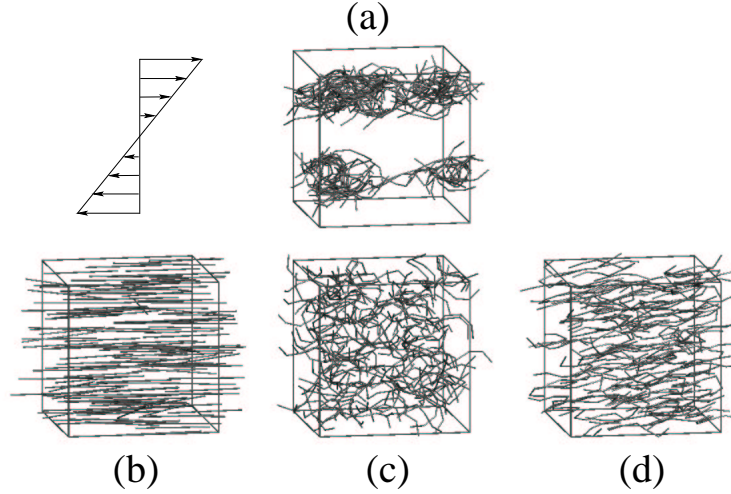


Figure 3.3: Simulation snapshots after shearing to a strain of $\gamma = 1500$, with parameters $nL^3 = 20$, $r_p = 75$, $N_{\text{seg}} = 5$, and (a) $\mu^{\text{stat}} = 20$, $S^{\text{eff}} = 0.05$, $\theta^{\text{eq}} = 0.8$, $\phi^{\text{eq}} = 0.7$ (flocculated suspension); (b) same as (a) except $\theta^{\text{eq}} = \phi^{\text{eq}} = 0$; (c) same as (a) except $\mu^{\text{stat}} = 0$; and (d) same as (a) except $S^{\text{eff}} = 0.0005$.

apparent in the simulation box. For each of Figs. 3.3(b)-(d), one of the above features is removed, and as a result, the suspension structure remains homogeneous in simple shear flow. In Fig. 3.3(b), the equilibrium shape is straight ($\theta^{\text{eq}} = \phi^{\text{eq}} = 0$); in Fig. 3.3(c), friction is absent ($\mu^{\text{stat}} = 0$); and in Fig. 3.3(d), the fibers are more flexible ($S^{\text{eff}} = 0.0005$). Thus the parameter values employed in Fig. 3.3(a) are sufficient to achieve flocculation in sheared suspensions. The effects of these parameters, as well as others, on the suspension structure are probed in more detail below.

The suspension structure can be characterized quantitatively by the pair distribution function of the fiber centers-of-mass, $g(r)$, and the average number of contacts per fiber, $\langle n_c \rangle$. The pair distribution functions are plotted as a function of separation in Fig. 3.4(a) for the systems depicted in Fig. 3.3. For the homogeneous suspensions, there is an equal probability of finding fiber pair centers-of-mass with any separation. The flocculated suspension, however, has a high probability of finding fiber centers at small separations. The pair distribution function can be used to identify systems that

flocculate. We define a suspension as flocculated if $g(r = 0.01L) \geq 3$. The average number of contacts per fiber is plotted as a function of shear strain γ in Fig. 3.4(b) for each of the systems in Fig. 3.3. For the nonflocculated systems, $\langle n_c \rangle$ rapidly achieves a constant, steady-state value. For the flocculated system, $\langle n_c \rangle$ increases to a constant steady-state value greater than those for the nonflocculated system, over a strain of several hundred. Monitoring $\langle n_c(\gamma) \rangle$ during a simulation run is an effective way of determining when steady state is achieved. The steady-state value of $\langle n_c \rangle$ also describes the extent to which a fiber network is formed. Meyer and Wahren [58] defined a fiber network as a system of fibers in which each fiber is held in position by contact with at least three other fibers. This is consistent with the flocculated system illustrated in Fig. 3.3(a), where $\langle n_c \rangle \approx 3$ at steady state.

3.3.2 Effects of friction and fiber stiffness

Fibers in contact interact via friction forces characterized by a static coefficient of friction, μ^{stat} . For $\mu^{\text{stat}} = 0$, the suspension structure remains homogeneous regardless of the other parameter values. As illustrated in Fig. 3.3, for certain ranges of parameter values, suspensions will tend to flocculate for sufficiently large values of μ^{stat} . For such systems, as μ^{stat} is increased from zero above $\mu_{\text{min}}^{\text{stat}}$, which depends on the other parameter values, suspensions begin to show increased heterogeneity. For the parameter values $(N_{\text{seg}}, r_p, nL^3, S^{\text{eff}}, \theta^{\text{eq}}, \phi^{\text{eq}}) = (5, 75, 20, 0.05, 0.8, 0.7)$, $\mu_{\text{min}}^{\text{stat}} \approx 5$. As μ^{stat} is increased further, the degree of heterogeneity increases; however, for $\mu^{\text{stat}} \geq \mu_{\text{max}}^{\text{stat}}$, the structure as characterized by $g(r = 0.01L)$ or $\langle n_c(\gamma \rightarrow \infty) \rangle$ no longer changes appreciably. The value of $\mu_{\text{max}}^{\text{stat}}$ is also a function of the other parameter values; for the values listed above, $\mu_{\text{max}}^{\text{stat}} \approx 10$. For most simulated flexible fiber suspensions that we have observed to flocculate, $10 < \mu_{\text{max}}^{\text{stat}} < 100$.

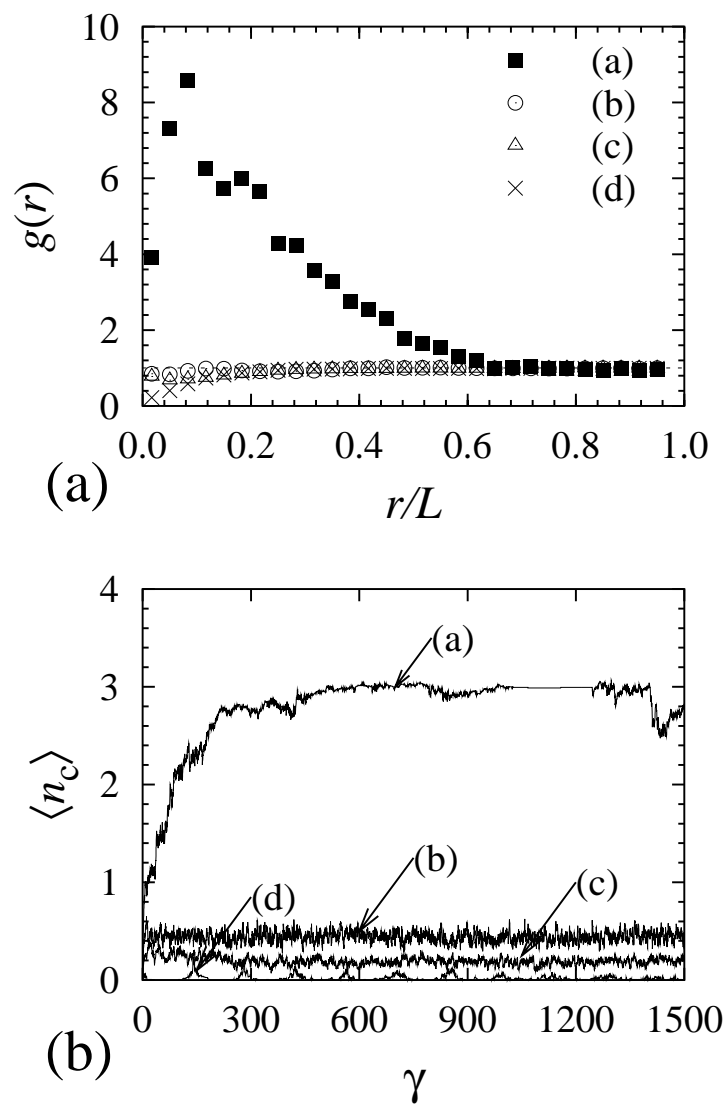


Figure 3.4: (a) Pair distribution function, and (b) average number of contacts per fiber versus strain for the runs depicted in Figure 3.3.

Similar behavior is observed as the fiber flexibility is varied. All suspensions will remain homogenous for sufficiently small effective stiffness ($S^{\text{eff}} \equiv E_Y I / \eta_0 \dot{\gamma} L^4 \ll 1$). As illustrated in Fig. 3.3, some suspensions will flocculate when the effective stiffness is increased above a certain value (which depends on the other parameter values).

The requirement of both a sufficiently large effective fiber stiffness and a sufficiently large coefficient of friction in order to produce heterogeneous structures is consistent with the elastic interlocking mechanism of flocculation proposed by Kerekes et al. [47] (also called Type-C cohesion). They proposed that the cohesive forces that hold fibers within flocs are caused by interfiber friction. The strength of the friction force is proportional to the normal force between contacting fibers, and this normal force is a function of the fiber stiffness. Soszynski and Kerekes [82] confirmed this mechanism experimentally; nylon fiber flocs readily dispersed when the fiber stiffness was reduced by heating above the glass transition temperature of nylon. Schmid et al. [75] reported similar behavior using a model and simulation method similar to those employed here. Flocs formed in simple shear become trapped in elastically-strained configurations upon cessation of shear. When the flocs are extracted from the simulation box and placed in an unbounded shear flow, the floc slowly disperses. If the effective fiber stiffness or the coefficient of friction is reduced, the fibers disperse much more rapidly (see also Schmid et al. [75] and Chapter 4).

Although the simulation results presented thus far appear to agree with experimental observations, unreasonably large values of μ^{stat} are necessary to see flocculation for the conditions described above ($\mu^{\text{stat}} > 1$). The value of μ^{stat} measured experimentally for contacting cellulose surfaces and cellulose fibers is approximately 0.5 [3, 99]. However, we also find that the effective stiffness values employed thus far

are small compared to those typically achieved in experiments. Choosing dimensional parameter values typical for wood fibers sheared in water ($E_Y I \approx 10^{-12} \text{N} \cdot \text{m}^2$ [86], $L \approx 2.3 \text{mm}$, $d \approx 30 \mu\text{m}$, $\eta_0 = 0.001 \text{Pa} \cdot \text{s}$, $\dot{\gamma} \simeq 10$), the dimensionless stiffness is $S^{\text{eff}} \approx 4$. This is much larger than the values used in the simulations with equivalent aspect ratios ($r_p = 75$). Simulating suspensions of fibers this stiff requires a very small time step ($\dot{\gamma} \Delta t < 10^{-8}$) and thus significantly more computational power than is currently available to simulate to shear strains $\gamma > 1000$.

To probe the behavior of flocculating suspensions composed of much stiffer fibers, we investigated the behavior of a test floc made up of five inherently straight fibers interwoven into a “star” configuration (illustrated in the inset of Fig. 3.5; $N_{\text{seg}} = 7$, $r_p = 56$, $\theta^{\text{eq}} = 0, \phi^{\text{eq}} = 0$) similar to the test structure proposed by Farnood et al. [29]. The test floc was placed in a simple shear field and sheared to a strain $\gamma = 100$ (in the plane of shear). For a fixed value of S^{eff} , the test floc would remain intact if μ^{stat} were large enough, and the test floc would disperse if μ^{stat} were too small. The minimum value of μ^{stat} necessary keep the floc intact was defined as a “critical” friction coefficient, $\mu_{\text{crit}}^{\text{stat}}$, which is a function S^{eff} . The critical friction coefficient is plotted as a function of S^{eff} for the star in Fig. 3.5. As the stiffness increases, the coefficient of friction necessary to hold the floc together decreases. These results suggest that for large values of S^{eff} , comparable to those typically encountered experimentally ($S^{\text{eff}} > 1$), the coefficient of friction necessary to see flocculation in simulations of sheared suspensions may indeed approach the coefficient of friction values measured experimentally.

Varying the dimensionless stiffness S^{eff} can be achieved by varying the intrinsic fiber stiffness ($E_Y I$), the fiber length (L), the suspending fluid viscosity (η_0), or the shear rate ($\dot{\gamma}$). Soszynski and Kerekes [81, 82] showed the importance of the effective

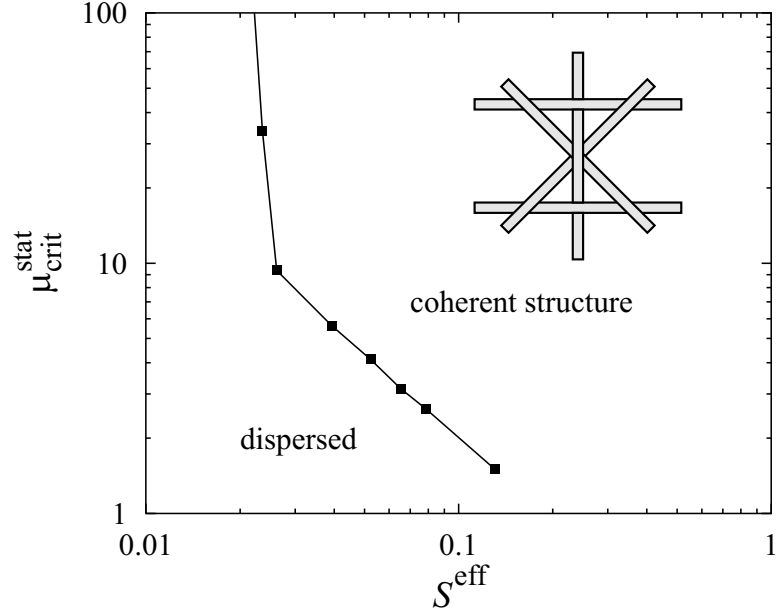


Figure 3.5: Critical coefficient of friction as a function of the effective stiffness for the star test floc in simple shear flow, $(N_{\text{seg}}, r_p, \theta^{\text{eq}}, \phi^{\text{eq}}) = (7, 56, 0, 0)$.

fiber stiffness in producing flocs in a recirculating flow of nylon fiber suspensions. As η_0 was increased (effective stiffness decreased) the concentration at which flocs first formed [threshold concentration, $(nL^3)_{\text{thr}}$] increased. Above a certain value of η_0 , flocs would no longer form. This phenomenon was investigated with the simulation method presented here, by shearing suspensions with a fixed effective stiffness to $\gamma = 1500$ and varying concentrations in order to determine the threshold concentration. The results are shown in Fig. 3.6 where $(nL^3)_{\text{thr}}$ is plotted as a function of $1/S^{\text{eff}} \propto \eta_0$ for the parameter values $(N_{\text{seg}}, r_p, \theta^{\text{eq}}, \phi^{\text{eq}}, \mu^{\text{stat}}) = (5, 75, 0.6, 0, 20)$. The threshold concentration increases as $1/S^{\text{eff}}$ increases, with no flocs observed for $1/S^{\text{eff}} \gtrsim 500$, qualitatively consistent with the experimental observations reported by Soszynski and Kerekes. Soszynski and Kerekes [82] explain the dependence of flocculation tendency on η_0 in terms of a competition between the different forces that determine fiber motion. In low η_0 suspending fluids, fiber motion is dominated by fiber interactions

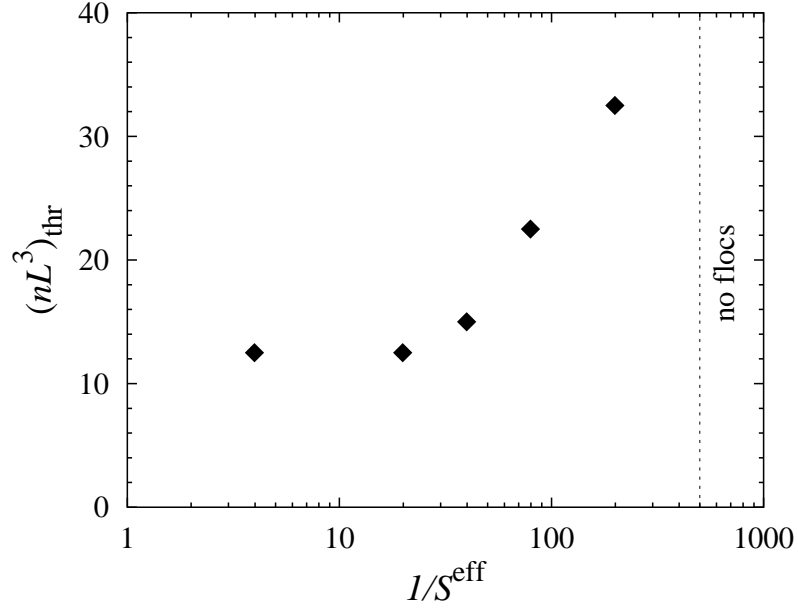


Figure 3.6: Threshold concentration to produce flocs as a function of the inverse of the effective stiffness, $1/S^{\text{eff}} \propto \eta_o$; $(N_{\text{seg}}, r_p, \theta^{\text{eq}}, \phi^{\text{eq}}, \mu^{\text{stat}}) = (5, 75, 0.6, 0, 20)$.

(as well as acceleration and deceleration in unsteady flows), and the fibers do not closely follow the suspending fluid motion. In sufficiently concentrated suspensions, this nonaffine motion can result in local “crowding,” which leads to entanglement and floc formation. The fiber motion in large η_o fluids is dominated by hydrodynamic forces, resulting in affine motion and perhaps a higher degree of fiber alignment (in shear flows). Crowding is thus inhibited, resulting in no floc formation. This explanation is consistent with the model and simulation results presented here. The relevant dimensionless quantity, the effective stiffness $S^{\text{eff}} = E_Y I / \eta_o \dot{\gamma} L^4$, characterizes the relative importance of viscous and elastic forces, the latter of which is intimately related to fiber interactions. Furthermore, as illustrated in Figs. 3.3(a) and (d), decreasing S^{eff} sufficiently (i.e., increasing η_o) clearly results in more aligned structures in addition to a more homogeneous system.

3.3.3 Effects of fiber shape

The equilibrium shape of a fiber significantly impacts the suspension microstructure. The dependence of fiber equilibrium shape on flocculation behavior has been investigated by performing simulations with suspensions of U-shaped fibers. The shape may be characterized by the common equilibrium angle θ^{eq} ($\phi^{\text{eq}} = 0$) at each joint, or equivalently by the fiber radius of curvature, defined here for linked rigid bodies as

$$R_{\text{U}} = \frac{1}{2} \left(\frac{\ell}{\sin(\theta^{\text{eq}}/2)} + \frac{\ell}{\tan(\theta^{\text{eq}}/2)} \right), \quad (3.9)$$

where ℓ is the segment half-length. The first term in parentheses is the radius of a circle passing through the ball and socket joints, and the second term is the radius of a circle tangent to the centers of the fiber segments. The radius R_{U} is the average of these two radii.

Suspensions with specific radii of curvature and various concentrations were simulated in simple shear flow to $\gamma = 1500$, with all other parameters fixed $[(N_{\text{seg}}, r_p, S^{\text{eff}}, \mu^{\text{stat}}) = (5, 75, 0.05, 20)]$. The results are summarized in Fig. 3.7(a) where the homogeneity of the suspensions is mapped as a function of curvature and concentration. Suspensions that remained homogeneous are represented by open circles, while suspensions that flocculated are represented by filled circles. Suspensions flocculate at lower concentrations as the dimensionless fiber curvature (b/R_{U}) is increased. As the fibers become nearly straight ($b/R_{\text{U}} \rightarrow 0$), the suspensions only flocculate at high concentrations, and perfectly straight fibers have never been observed to produce heterogeneous structures in the simulations. However, it is possible that flocs formed at sufficiently large concentration may exceed the simulation box size, or that there is a transition to the formation of space-filling, elastically interlocked networks [75].

The variation in suspension structure with fiber shape can also be characterized

by the average number of contacts per fiber at steady state $\langle n_c \rangle_{\text{ss}}$, as illustrated in Fig. 3.7(b). Here, $\langle n_c \rangle_{\text{ss}}$ is plotted as a function of b/R_U for $N_{\text{seg}} = 3$ and 5, with the remaining parameter values $(nL^3, S^{\text{eff}}, r_p, \mu^{\text{stat}}) = (20, 0.05, 75, 20)$. As b/R_U increases (the fibers become more curved), $\langle n_c \rangle_{\text{ss}}$ increases. This is likely caused by the decreased rotation period of higher curvature fibers resulting in more interfiber collisions. The values of $\langle n_c \rangle_{\text{ss}}$ increase slowly with increasing b/R_U at first. When the curvature becomes large enough to cause flocculation, $\langle n_c \rangle_{\text{ss}}$ increases rapidly.

The fiber shape also depends on the number of segments, and thus so do the details of the suspension structure, as illustrated in Fig. 3.7(b). Flocculation for suspensions of three-segment fibers is shifted to slightly larger curvatures compared to suspensions with five-segment fibers. Suspensions of fibers with $N_{\text{seg}} \geq 5$ show approximately the same behavior at an aspect ratio of $r_p = 75$, under these conditions. One would expect the influence of the number of segments on the suspension structure to be a function of the fiber aspect ratio and flexibility.

3.3.4 Effects of kinetic friction

All of the results presented thus far employ only the static friction constraint ($\mu^{\text{kin}} = 0$ in Eq. [3.7]); if the force required to keep contacting segments i and k from sliding exceeds $\mu^{\text{stat}} |\mathbf{F}_{ik}^{\text{N}}|$, the segments are allowed to slide unimpeded (except for hydrodynamic drag). To investigate the influence of kinetic friction on suspension structure, shear flow was simulated for the parameter values $(N_{\text{seg}}, r_p, nL^3, S^{\text{eff}}, \theta^{\text{eq}}, \phi^{\text{eq}}) = (5, 75, 20, 0.05, 0.6, 0)$, and various values of μ^{stat} and μ^{kin} . The steady-state pair distribution functions for some of these simulations are plotted in Fig. 3.8, and the results are summarized below.

In the absence of kinetic friction ($\mu^{\text{kin}} = 0$), flocculation only occurs for $\mu^{\text{stat}} \geq$

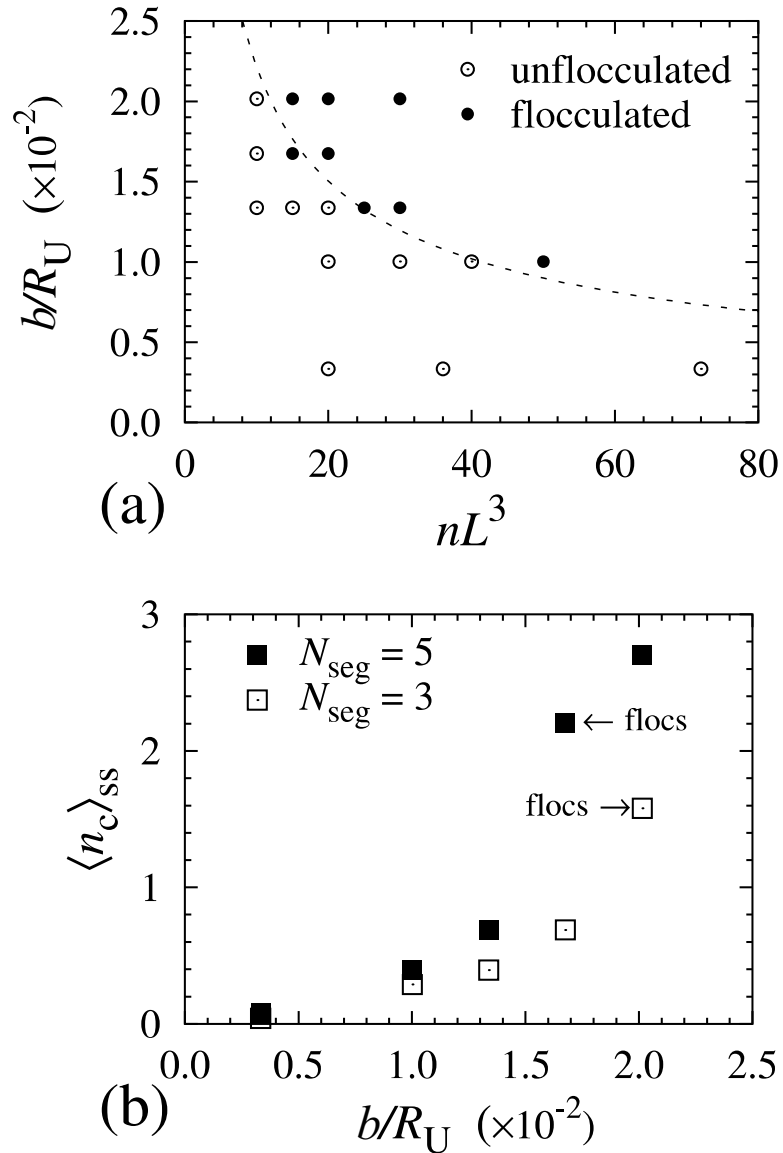


Figure 3.7: (a) Suspension homogeneity (at $\gamma = 1500$) mapped as a function of curvature (b/R_U) and concentration [$(N_{seg}, r_p, S^{eff}, \mu^{stat}) = (5, 75, 0.05, 20)$]; (b) Average number of contacts per fiber at steady state ($\langle n_c \rangle_{ss}$) as a function of b/R_U for suspensions at $nL^3 = 20$ after shearing for $\gamma = 1500$ [$(N_{seg}, r_p, S^{eff}, \mu^{stat}) = (5, 75, 0.05, 20)$].

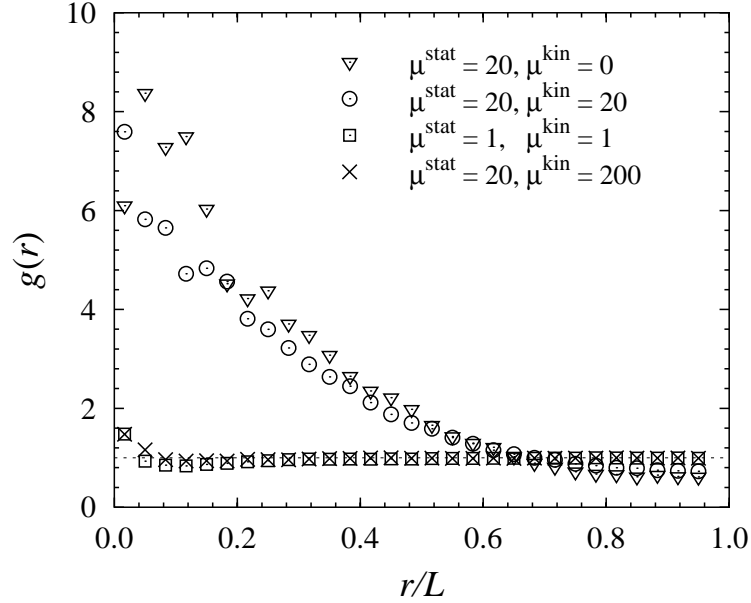


Figure 3.8: Pair distribution function for the fiber centers-of-mass of suspensions in simple shear flow at steady state $\gamma > 1000$, for various values of the coefficients of static and kinetic friction $(N_{\text{seg}}, r_p, nL^3, S^{\text{eff}}, \theta^{\text{eq}}, \phi^{\text{eq}}) = (5, 75, 20, 0.05, 0.6, 0)$.

$\mu_{\text{min}}^{\text{stat}} \approx 10$. Such behavior is illustrated in Fig. 3.8, where the pair distribution function for a simulation with $\mu^{\text{stat}} = 20$ and $\mu^{\text{kin}} = 0$ exhibits a flocculated structure ($g(r = 0.01L) \approx 9$). Adding sliding friction does not substantially influence the structure, as illustrated by the similar pair distribution function for $\mu^{\text{stat}} = 20$ and $\mu^{\text{kin}} = 20$.

Consider next the “incipient” situation where $\mu^{\text{stat}} = 1$, which is less than that required to observe flocculation ($\mu^{\text{kin}} = 0$). The addition of kinetic friction with $\mu^{\text{kin}} = \mu^{\text{stat}} = 1$ is not sufficient to cause the suspension to flocculate. This is illustrated in Fig. 3.8 where the pair distribution function for this case reflects a homogeneous structure. Similar behavior is observed for all simulations with $\mu^{\text{kin}} \leq \mu^{\text{stat}} < \mu_{\text{min}}^{\text{stat}}$. We thus conclude that kinetic friction does not significantly influence flocculation behavior. In other words, kinetic friction cannot significantly reduce the coefficient of static friction necessary to induce flocculation.

Not only is kinetic friction unable to induce flocculation in nearly flocculated systems, but the addition of kinetic friction can actually inhibit flocculation when $\mu^{\text{kin}} \gg \mu^{\text{stat}} > \mu_{\text{min}}^{\text{stat}}$. This is illustrated in Fig. 3.8 in which the pair distribution function for $\mu^{\text{stat}} = 20$ and $\mu^{\text{kin}} = 200$ characterizes a structure less heterogenous than that obtained for $\mu^{\text{stat}} = 20$ and $\mu^{\text{kin}} = 0$.

While kinetic friction can affect the suspension structure, it apparently does not significantly influence flocculation behavior. Thus in the remainder of this chapter, only results from simulations with $\mu^{\text{kin}} = 0$ are reported.

3.3.5 Effects of weak attractive forces

All of the simulations discussed thus far have been performed in the absence of attractive forces between fibers. However, experiments have shown that weak attractive forces can exist between fibers in suspension. Shchukin et al. [79] reported attractive force magnitudes of $|\mathbf{F}^{\text{att}}| \approx 0.04 \mu\text{N}$ for cellulose fibers in water, and Chaouche and Koch [18] reported attractive force magnitudes in the range $|\mathbf{F}^{\text{att}}| \approx 0.01 - 6 \mu\text{N}$ for nylon fibers in various fluids. While attractive forces may themselves cause aggregation, they may also serve to lower the coefficient of friction necessary to see friction-induced flocculation. To model attractive forces in the simulations, we added a weak attractive term to the normal force between fibers $\mathbf{F}_{ik}^{\text{N}} = -6\pi\eta_o\ell b\dot{\gamma}[F \exp(-ah) - A_{\text{N}} \exp(-a_{\text{A}}h^2)]\mathbf{n}_{ik}$, where A_{N} is the dimensionless magnitude of the attractive force and a_{A} is related to the decay length of the attractive force. The parameter values were selected so that the maximum attractive force is $|\mathbf{F}_{\text{max}}^{\text{N}}| \approx 0.02 \mu\text{N}$ (for $F = 150$, $a = 20$, $A_{\text{N}} = 9$, and $a_{\text{A}} = 35$, and the suspension parameters $\eta_o = 1 \text{ Pa} \cdot \text{s}$, $L = 2\ell N_{\text{seg}} = 2.5 \text{ mm}$, $b = 16 \mu\text{m}$, and $\dot{\gamma} = 10 \text{ s}^{-1}$). The structures of suspensions in simple shear flow with purely repulsive interactions ($A_{\text{N}} = 0$) and with weak

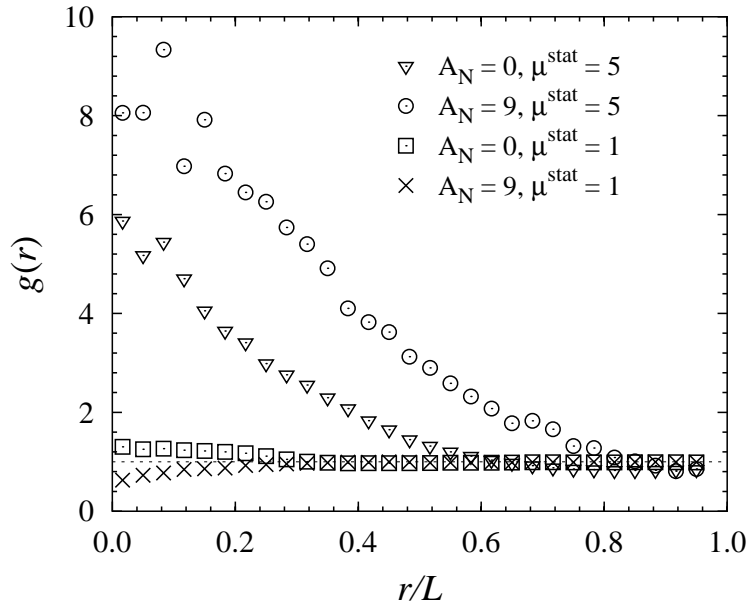


Figure 3.9: Pair distribution function for the fiber centers-of-mass of suspensions in simple shear flow at steady state $\gamma > 1000$, with and without attractive potentials $(N_{\text{seg}}, r_p, nL^3, S^{\text{eff}}, \theta^{\text{eq}}, \phi^{\text{eq}}) = (5, 75, 20, 0.05, 0.8, 0.7)$.

attractive forces ($A_N = 9$) are compared in Fig. 3.9 where the steady state pair distribution functions are presented for various values of μ^{stat} and the remaining parameters values fixed at $(N_{\text{seg}}, r_p, nL^3, S^{\text{eff}}, \theta^{\text{eq}}, \phi^{\text{eq}}, \mu^{\text{kin}}) = (5, 75, 20, 0.05, 0.8, 0.7, 0)$. With $\mu^{\text{stat}} = 5$, suspensions with and without attractive forces flocculate. The fibers with weak attractive forces have a slightly higher probability of having small separations between the fiber centers-of-mass than fibers with purely repulsive interactions [$g(r = 0.01L) \approx 8$ and $g(r = 0.01L) \approx 6$ for $A_N = 9$ and $A_N = 0$, respectively]. However, for $\mu^{\text{stat}} = 1 < \mu_{\text{min}}^{\text{stat}} \approx 5$, the pair distribution functions reflect a homogeneous structure for both $A_N = 0$ and $A_N = 9$. Thus weak attractive forces do not significantly alter the minimum coefficient of friction necessary to induce flocculation.

Schmid [73] demonstrated the effect of using larger attractive forces between fibers ($|\mathbf{F}_{\text{max}}^{\text{N}}| \approx 10 \mu\text{N}$) in the absence of friction ($\mu^{\text{stat}} = \mu^{\text{kin}} = 0$). Although larger

attractive forces did lead to flocculation in the absence of friction, the behavior of the systems was markedly different than that exhibited by systems that flocculate by friction. The fibers did not elastically interlock, as observed experimentally [81, 82]. In particular, increasing the effective stiffness lead to a less coherent structure. Thus attractive forces alone cannot explain the observation reported by Soszynski and Kerekes [82] that reducing elastic stresses leads to less coherent structures.

Chaouche and Koch [18] observed flocculation in suspensions of nearly straight nylon fibers in viscous fluids with smaller aspect ratios ($r_p \approx 36$) sheared at very low shear rates ($\dot{\gamma} \ll 1$). They hypothesized that flocculation was due to attractive forces between fibers because the fibers were sufficiently stiff to be considered rigid rods, suggesting that they could not deform and elastically interlock ($S^{\text{eff}} \gg 1$). Simulations of perfectly rigid fibers both with ($A_N = 9$) and without weak attractive forces at conditions similar to those employed by Chaouche and Koch ($r_p = 35$ and $nL^3 \approx 17 - 52$) did not flocculate even as $\mu^{\text{stat}} \rightarrow \infty$. If the fibers were made flexible and slightly deformed ($N_{\text{seg}}, r_p, nL^3, S^{\text{eff}}, \theta^{\text{eq}}, \phi^{\text{eq}}, \mu^{\text{stat}} = (5, 75, 17 - 52, 0.7, 0.1, 0, 20)$), the simulation still did not produce a flocculated structure with or without weak attractive forces. However, the simulations could not be performed at the large values of the effective stiffness reported by Chaouche and Koch ($S^{\text{eff}} \approx 2000$); it is possible that the simulations could produce flocs at larger values of S^{eff} if such simulations could be performed.

3.3.6 Effects of anisotropic bending

We investigated the effect of changing the bending stiffness in the joints such that the fibers have a preferential bending direction (anisotropic bending). The fiber joints were changed from ball and socket joints to pin joints, which constrain the motion

of adjacent fiber segments to a plane. This makes the effective stiffness infinite for a restoring torque parallel to the plane $[(S^{\text{eff}})_{\text{hard}} \rightarrow \infty]$, while allowing the effective stiffness for bending perpendicular to the plane $[(S^{\text{eff}})_{\text{easy}}]$ to remain finite.

The pair distribution functions for the fiber centers-of-mass for suspensions of isotropic fibers ($S^{\text{eff}} = 0.05$) at $\mu^{\text{stat}} = 20$ and for suspensions of anisotropic fibers with pin joints [(A) $(S^{\text{eff}})_{\text{easy}} = 0.05$, $\mu^{\text{stat}} = 20$; (B) $(S^{\text{eff}})_{\text{easy}} = 0.05$, $\mu^{\text{stat}} \rightarrow \infty$; and (C) $(S^{\text{eff}})_{\text{easy}} = 0.01$, $\mu^{\text{stat}} = 20$], in which all other variables are held constant $[(N_{\text{seg}}, r_p, nL^3, \theta^{\text{eq}}, \phi^{\text{eq}}, \mu^{\text{kin}}) = (5, 75, 20, 0.6, 0, 0)]$, are plotted in Fig. 3.10. The anisotropically bending fibers (A), result in a relatively homogenous suspension at steady state, in contrast to the isotropic fibers that flocculate strongly at the same conditions. Increasing the coefficient of friction for the anisotropic fibers to infinity (B) results in a flocculated suspension, although it is less heterogeneous than the equivalent suspension of isotropic fibers with $\mu^{\text{stat}} = 20$. Decreasing the effective stiffness in the bending direction also results in a homogeneous distribution of fibers (C). If the pin joints are replaced by anisotropic ball and socket joints with $(S^{\text{eff}})_{\text{hard}} = 5(S^{\text{eff}})_{\text{easy}} = 0.25$ or $(S^{\text{eff}})_{\text{hard}} = 2(S^{\text{eff}})_{\text{easy}} = 0.1$ with all other conditions the same as those given above, the suspension no longer flocculates.

At present, we are unable to explain the behavior observed for simulations of anisotropically bending fibers. One possible explanation for this change in flocculation behavior may be that the number of configurations the anisotropic fibers can assume is too limited to allow the fibers to entangle and interlock. However, wood fibers have ribbon-like structures which give them preferential bending directions, and wood fibers will flocculate. While the model does take into account preferential bending, the real fiber geometry is not considered. These “flattened” wood fibers can contact one another over much larger areas than our model fibers (circular cross-section),

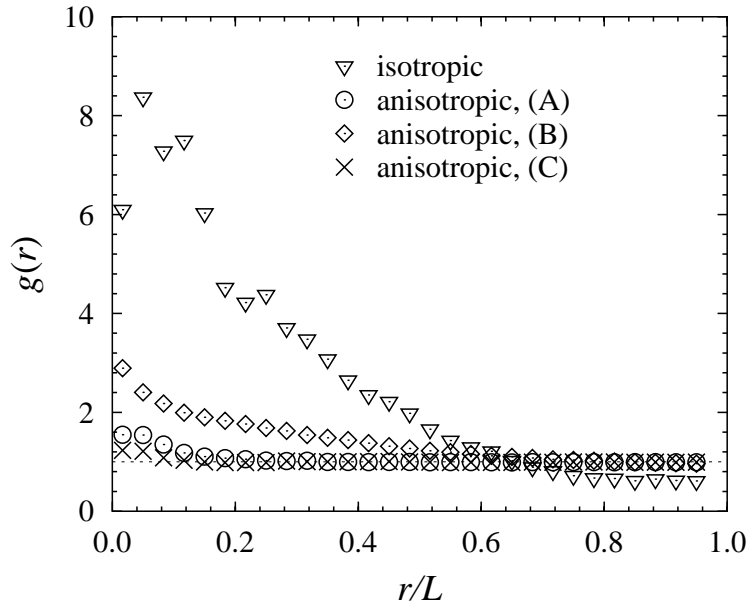


Figure 3.10: Pair distribution function for the centers-of-mass of fibers with isotropic ($S^{\text{eff}} = 0.05$, $\mu^{\text{stat}} = 20$) and anisotropic bending [(A) $(S^{\text{eff}})_{\text{easy}} = 0.05$, $\mu^{\text{stat}} = 20$; (B) $(S^{\text{eff}})_{\text{easy}} = 0.05$, $\mu^{\text{stat}} \rightarrow \infty$; and (C) $(S^{\text{eff}})_{\text{easy}} = 0.01$, $\mu^{\text{stat}} = 20$] using pin joints after shearing for $\gamma = 1500$ with $(N_{\text{seg}}, r_p, nL^3, \theta^{\text{eq}}, \phi^{\text{eq}}, \mu^{\text{kin}}) = (5, 75, 20, 0.6, 0, 0)$.

which may result in enhanced frictional interactions or even bonding. Indeed, the model has shown that anisotropic fibers will flocculate by substantially increasing μ^{stat} . Also, real fibers have a distribution of lengths, stiffnesses, cross-sectional areas, and shapes that we have not considered in the results reported here.

3.4 Conclusions

We have employed a model for flexible fibers and a particle-level simulation technique to investigate the relationships between fiber properties, interactions, and the structure of non-Brownian, flexible fiber suspensions in simple shear flow. The fiber model includes such realistic features as non-straight equilibrium shapes, flexibility, and frictional contacts. Each fiber is composed of a series of linked rigid spherocylinders

connected by ball and socket joints.

The simulations show that suspensions of flexible fibers interacting via frictional contacts can flocculate, even in the absence of attractive interfiber forces. The flocculation process observed is consistent with the elastic interlocking mechanism proposed by Soszynski and Kerekes [82]. The tendency toward flocculation depends on several parameters. A suspension of fibers that are too flexible, or whose coefficient of static friction is too small will not flocculate, regardless of the values of the remaining parameters. The minimum coefficient of friction necessary to observe flocculation appears to decrease as the fiber stiffness increases. The dependence of the homogeneity of the suspension structure on the dimensionless fiber stiffness (effective stiffness, $S^{\text{eff}} \equiv E_Y I / \eta_o \dot{\gamma} L^4$) agrees qualitatively with numerous experimental observations. Fiber shape also influences the suspension structure, as the concentration at which fibers begin to flocculate decreases with increasing fiber curvature (for U-shaped fibers). Other parameters have a weaker influence on the suspension structure. Kinetic (sliding) friction and weak attractive forces have little effect on the structural behavior of fiber suspensions (for the ranges of parameter values investigated). Anisotropic bending tends to shift the onset of flocculation to larger values of the coefficient of static friction.

The main limitation of this approach is the computational demand. The maximum allowable time step (for obtaining stable, accurate solutions to the DAEs) decreases with increasing fiber stiffness, which limits simulations with many fibers to relatively small stiffnesses, well below that expected in many practical situations of interest. Improving the computation speed will not only allow us to investigate more realistic fiber stiffnesses, but also to investigate a greater range of parameter space.

Chapter 4

Fiber floc dispersion

4.1 Introduction

In the processing of wood pulp to make paper, one desires a homogeneous dispersion of fibers to aid in producing a uniform product. However, fibers in flowing suspensions tend to aggregate or form *flocs*, leading to undesirable, heterogeneous suspensions. In this chapter, we employ fiber-level simulations to investigate the dispersion of fiber flocs in various linear flow fields.

Mason [55] described flocculation as a dynamic equilibrium process dominated by fiber collisions, where fibers continually enter and leave flocs. Meyer and Wahren [58] theoretically examined the elastic properties of fiber networks. They showed that the strength and elasticity of fiber networks are affected by fiber flexibility and the number of contacts a fiber experiences with other fibers in the suspension. Soszynski and Kerekes [81, 82] extended this idea to identify a mechanism for fiber flocculation called elastic fiber interlocking. Fibers in flowing suspensions deform as a result of viscous and interfiber forces. As bent fibers attempt to regain their equilibrium shapes, they can become locked in elastically strained configurations by contacts with other fibers. It is the combination of flexibility and frictional interactions that help

to form flocs as well as to make them coherent. Other factors such as suspension viscosity [101], shear rate [39], fiber length [81, 82], and suspension concentration [45] all impact floc formation and structure.

Turbulent flow is most often used to try to create a homogeneous suspension. The disruption of flocs results from supplying sufficient energy to break the contact points in the network of fibers. Andersson [4] developed an expression for the probability of floc rupture in turbulent flow of pulp suspensions which was based on knowing the tensile stress exerted on the network of fibers. Takeuchi et al. [85] studied the destruction of flocs in a turbulent flow and found that the rate of destruction increased with increasing flow velocity. Kerekes [43] examined floc behavior in a converging channel to approximate elongational flow. Flocs in this flow tended to stretch and then rupture rather than shear apart.

Floc dispersion has been characterized as occurring at two levels—global scale disruption and small scale surface erosion [52]. Global scale disruption accounts for large visual changes such as a floc splitting into smaller secondary flocs (doublets), elongating into string like structures, or simply disintegrating into individual fibers. Surface scale erosion is the loss of individual fibers from the surface of the floc. This type of disruption can occur over the entire surface of the floc and is attributed to shearing forces. Flocs may disperse at some level between the global and surface erosion limits, which is referred to as “shedding” [52]. Shedding involves the loss of small bunches of fibers from a floc, in which the rate of fiber loss from the floc is approximated by an exponential decay process.

The mechanism of floc disruption—whether by shear or tensile forces—is difficult to observe in experiments, as suspensions are often opaque. An alternative is to use simulation methods to understand floc dispersion, in which individual particles

can be tracked and the parameters of the suspension are easily varied. Numerous researchers have simulated suspensions of rigid fibers modelled as prolate spheroids [20] or cylinders that interact hydrodynamically [28, 98]. Sundararamumar and Koch and Harlen et al. [35, 84] simulated the flow of suspensions of rigid cylinders that interacted via mechanical contacts. They found that contact forces were very important in determining the motion of the rods, and that hydrodynamic interactions between fibers were less important as the concentration and number of contacts per fiber increased.

Rigid fiber simulations, however, have not reproduced flocculation behavior in fiber suspensions. Ross and Klingenberg [71] developed a model to simulate the motion of flexible fibers represented by linked prolate spheroids. Schmid et al. [75] further refined this model to examine the behavior of suspensions of linked spherocylinders that interact through frictional contacts. By including flexibility, deformed equilibrium shapes, and friction, the simulations produced flocculated states for fiber suspensions in simple shear flow in the absence of attractive interfiber forces.

In this chapter, a dynamic, particle-level simulation technique similar to that developed by Schmid et al. [75] and presented in Chapter 2 is employed to study the disruption of fiber flocs in three linear flow fields—simple shear, uniaxial extension and planar extension. The model and simulation method are described briefly in the following section. Flocs were formed by simulating suspensions in simple shear. Flocs that formed were then extracted from the suspension and placed in an unbounded flow field to observe the disruption of isolated flocs. The results of these simulations are presented in Section 4.3. The rate and extent of disruption depends on numerous variables, including fiber stiffness, the fluid viscosity, the ambient deformation rate, and the coefficient of interfiber friction, as well as the nature of the flow field.

Flocs in simple shear flow disperse completely, but more slowly than that observed in extensional flows of similar deformation rates. However, flocs in extensional flows tend to disperse incompletely, leaving behind secondary flocs that contain numerous fibers.

4.2 Simulation method

Flexible fiber suspensions are modelled as neutrally-buoyant chains of linked rigid bodies immersed in a Newtonian liquid. The model includes realistic features such as fiber flexibility, irregular equilibrium shapes, and mechanical contact forces between fibers. The model and simulation method are similar to that employed by Schmid et al. [75] and are described in more detail in Chapter 2

Each fiber in the suspension is represented by N_{seg} rigid cylinders (length 2ℓ , radius b ; overall length $L = 2\ell N_{\text{seg}}$) with hemi-spherical end caps, connected end-to-end by ball and socket joints (Fig. 4.1). The motion of the fiber segments is described by Newton's laws of motion in which we neglect fiber inertia. The force balance on a fiber segment i includes contributions from hydrodynamic drag ($\mathbf{F}_i^{\text{hyd}}$), mechanical contact forces ($\mathbf{F}_{ik}^{\text{con}}$), and forces at each joint that maintain the segment connectivity (\mathbf{X}_i),

$$\mathbf{F}_i^{\text{hyd}} + \mathbf{X}_{i+1} - \mathbf{X}_i + \sum_k^{N_{C_i}} \mathbf{F}_{ik}^{\text{con}} = \mathbf{0}, \quad (4.1)$$

where N_{C_i} is the number of contacts on fiber segment i . The torque balance on fiber segment i includes similar contributions with the addition of a restoring torque at each joint (\mathbf{Y}_i),

$$\mathbf{T}_i^{\text{hyd}} + \mathbf{Y}_{i+1} - \mathbf{Y}_i + \ell \mathbf{p}_i \times [\mathbf{X}_{i+1} + \mathbf{X}_i] + \sum_k^{N_{C_i}} [\mathbf{G}_{ik} \times \mathbf{F}_{ik}^{\text{con}}] = \mathbf{0}, \quad (4.2)$$

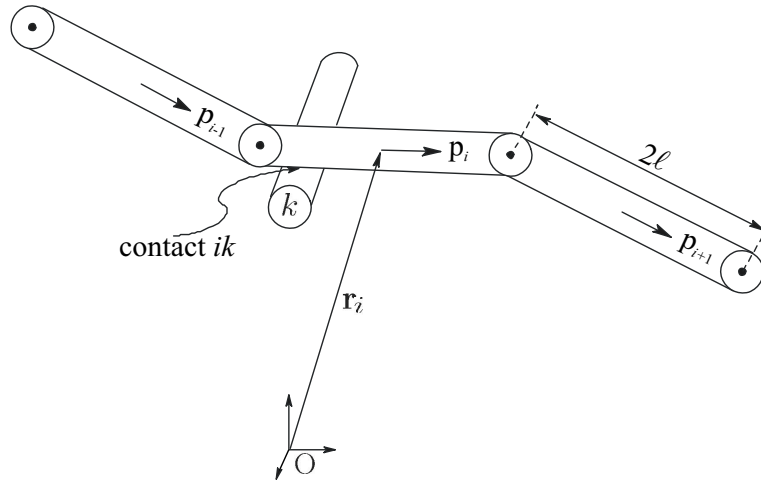


Figure 4.1: Schematic diagram of a model fiber composed of rigid spherocylinders linked by ball and socket joints. Here, segment i is in contact with segment k from another fiber.

where $\mathbf{T}_i^{\text{hyd}}$ is the hydrodynamic torque, \mathbf{p}_i is the orientation vector of the segment, and \mathbf{G}_{ik} is a vector from the center of segment i to the point of contact with segment k .

In this model, hydrodynamic forces and torques are treated in the small Reynolds number limit in order to investigate the effects of viscous forces on floc dispersion. Hydrodynamic interactions are neglected based on simulations performed by Sundararajakumar and Koch and Harlen et al. [35, 84]. This assumption allows us to evaluate the hydrodynamic force and torque as that on an isolated body, $\mathbf{F}_i^{\text{hyd}} = \mathbf{A}_i \cdot [\mathbf{U}_i^\infty - \dot{\mathbf{r}}_i]$ and $\mathbf{T}_i^{\text{hyd}} = \mathbf{C}_i \cdot [\boldsymbol{\Omega}_i^\infty - \boldsymbol{\omega}_i] + \tilde{\mathbf{H}}_i : \mathbf{E}^\infty$, where the resistance tensors \mathbf{A}_i , \mathbf{C}_i , and $\tilde{\mathbf{H}}_i$ for the spherocylinder segments are approximated by the resistance tensors of a prolate spheroid with an equivalent aspect ratio $r_e = 0.7r_p/N_{\text{seg}}$ (see Chapter 2), where $r_p = L/2b$ is the aspect ratio of the entire fiber. The ambient velocity \mathbf{U}_i^∞ , angular velocity $\boldsymbol{\Omega}_i^\infty$, and rate of strain tensor \mathbf{E}^∞ are evaluated at the center-of-mass of each segment. The segment translational and angular velocities are $\dot{\mathbf{r}}_i$ and $\boldsymbol{\omega}_i$, respectively.

The restoring torque \mathbf{Y}_i describes the resistance of the elastic fibers to bending

and twisting. The bending and twisting components of this torque are assumed to be linear in the difference between the bending and twisting angles (θ_i and ϕ_i respectively) and their equilibrium values (θ_i^{eq} and ϕ_i^{eq}),

$$|\mathbf{Y}_i| = \kappa_b(\theta_i - \theta_i^{\text{eq}}) + \kappa_t(\phi_i - \phi_i^{\text{eq}}), \quad (4.3)$$

where κ_b and κ_t are the bending and twisting constants of the fiber. The bending constant is related to the stiffness of the fiber material by $\kappa_b = E_Y I / 2\ell$, where E_Y is the Young's modulus, and $I \equiv \pi b^4 / 4$ is the area moment. The twisting constant is set to $\kappa_t = 0.67\kappa_b$ in this study, equal to that of a linearly elastic circular cylinder with a Poisson's ratio of 0.5. The fiber flexibility is characterized by a single parameter which we call the effective stiffness $S^{\text{eff}} \equiv E_Y I / \eta_o \dot{\gamma} L^4$, where η_o is the suspending fluid viscosity, $\dot{\gamma} \equiv (2\mathbf{E}^\infty : \mathbf{E}^\infty)^{1/2}$ is the deformation rate, and L is the total fiber length.

The fiber segments remain connected by applying a constraint for each joint,

$$\mathbf{r}_i + \ell \mathbf{p}_i = \mathbf{r}_{i+1} - \ell \mathbf{p}_{i+1}, \quad (4.4)$$

where \mathbf{r}_i is the position of the center of segment i . These constraint equations allow for the solution of the constraint forces at each joint \mathbf{X}_i . Since the segments are rigid and remain connected, the fibers are inextensible (but still flexible).

Fibers experience mechanical contacts with other fibers in the suspension. Two fiber segments i and k are considered to be in contact if the separation between their surfaces, h_{ik} , is less than $0.33b$. The force that results from each contact is decomposed into two components—a force in the normal direction of the contact ($\mathbf{F}_{ik}^{\text{N}}$) and a frictional force ($\mathbf{F}_{ik}^{\text{fric}}$) in the plane of the contact. The purely repulsive normal force exerted on segment i by segment k is modelled as $\mathbf{F}_{ik}^{\text{N}} = -F \exp[-ah_{ik}] \mathbf{n}_{ik}$, where \mathbf{n}_{ik} is the unit normal vector directed from segment i to k , $F = 900\pi\eta_o l b \dot{\gamma}$ is the repulsive

force magnitude, and $a = 20/b$. The friction force is determined by the constraint of no relative motion in the plane of contact,

$$\begin{pmatrix} \Delta \mathbf{u}_{ik} \cdot \mathbf{e}_1^{\text{loc}} \\ \Delta \mathbf{u}_{ik} \cdot \mathbf{e}_2^{\text{loc}} \\ \mathbf{F}_{ik}^{\text{fric}} \cdot \mathbf{n}_{ik} \end{pmatrix} = \mathbf{0}, \quad (4.5)$$

where $\Delta \mathbf{u}_{ik}$ is the relative velocity between segments i and k at the point of contact, and the plane of contact is defined by the vectors $\mathbf{e}_1^{\text{loc}}$ and $\mathbf{e}_2^{\text{loc}}$. The calculated friction force is then subjected to a Coulombic friction law of the form

$$\begin{aligned} |\mathbf{F}_{ik}^{\text{fric}}| &\leq \mu^{\text{stat}} |\mathbf{F}_{ik}^{\text{N}}| \Rightarrow \text{contact remains intact} \\ &> \mu^{\text{stat}} |\mathbf{F}_{ik}^{\text{N}}| \Rightarrow \mathbf{F}_{ik}^{\text{fric}} = \mu^{\text{kin}} |\mathbf{F}_{ik}^{\text{N}}| \frac{\Delta \mathbf{u}_{ik}}{|\Delta \mathbf{u}_{ik}|}, \end{aligned} \quad (4.6)$$

where μ^{stat} and μ^{kin} are the static and kinetic coefficients of friction. In this chapter, $\mu^{\text{kin}} = 0$ for all results reported.

The equations of motion and the constraint equations for all of the fiber segments in the suspension can be expressed as a system of differential algebraic equations (DAEs) for the unknown coordinates and constraint forces,

$$\begin{aligned} \dot{\mathbf{q}} - \mathbf{F}(\mathbf{q}, \boldsymbol{\lambda}) &= \mathbf{0}, \\ \boldsymbol{\Psi}(\mathbf{q}) &= \mathbf{0}, \\ \boldsymbol{\Xi}(\mathbf{q}, \dot{\mathbf{q}}, \boldsymbol{\lambda}) &= \mathbf{0}, \end{aligned} \quad (4.7)$$

where \mathbf{q} is a vector containing the generalized coordinates of each fiber segment (positions and orientations), and $\boldsymbol{\lambda}$ is a vector containing all the constraint forces (\mathbf{X} and \mathbf{F}^{fric}) in the suspension. If the segment orientations are represented by Euler parameters [92], there are $7N_{\text{fib}}N_{\text{seg}}$ equations of motion to be solved. The inextensibility constraint [Eq. (4.4)], represented by the vector $\boldsymbol{\Psi}$, is made up of $3N_{\text{fib}}(N_{\text{seg}} - 1)$ constraint equations that depend on only the positions and orientations. The $3N_C$ friction constraint equations [Eq. (4.5)] are contained in $\boldsymbol{\Xi}$, where N_C is the total number of contacts in the system.

4.2.1 Creating flocs

Simulations to form flocs are performed by randomly placing fibers at their equilibrium shapes into a simulation cell of size $(\zeta L)^3$, where ζ is the cell size scaling factor that ranges from $\zeta = 1.5$ -4. A linear shear field is imposed on the suspending fluid [$\mathbf{U}^\infty = (\dot{\gamma}z, 0, 0)$], and periodic boundary conditions are applied with the Lees-Edwards modification for sheared systems [1] to simulate an infinite suspension. Determining the motion of the fibers requires the solution of the system of DAEs in Eq. (4.7). An approximate solution method was developed to solve this system, the details of which are presented in Chapter 2.

Fiber flocs were observed to form in simulations under a variety of conditions, the details of which are described by Schmid et al. [75] and in Chapter 3. The suspensions were sheared until a steady-state structure persisted for a strain $\gamma \geq 500$, which was identified by monitoring the average number of contacts per fiber. In this chapter, all of the flocs tested were formed using fibers with $N_{\text{seg}} = 5$, aspect ratio $r_p = 75$, effective stiffness $S^{\text{eff}} = 0.05$, and coefficient of friction $\mu^{\text{stat}} = 20$. The equilibrium shape of the fibers was either U-shaped $(\theta^{\text{eq}}, \phi^{\text{eq}}) = (0.6, 0)$ or helical $(\theta^{\text{eq}}, \phi^{\text{eq}}) = (0.8, 0.7)$, examples of which are illustrated in Fig. 4.2.

In suspensions that formed flocs, the number of fibers in each floc was counted. The floc with the most fibers was designated as the test floc, and all of the other fibers in the suspension were removed. The test floc was then subjected to a linear flow in which the periodic boundary conditions were eliminated, thus leaving the test floc in an unbounded flow field. Figure 4.3 illustrates an example of a floc formed with periodic boundary conditions as well as the extracted test floc in an unbounded shear flow.

The flocs were put in three different linear ambient velocity fields \mathbf{U}^∞ , to

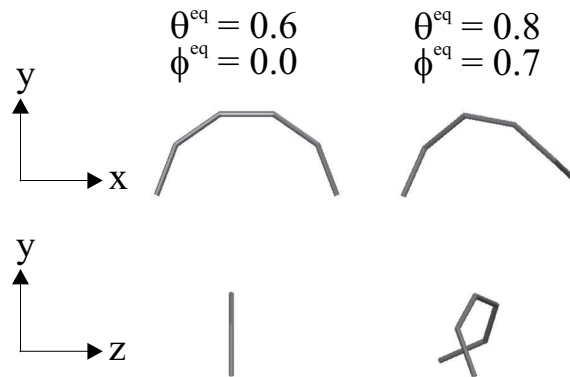


Figure 4.2: Examples of equilibrium shapes for U-shaped fibers $(\theta^{\text{eq}}, \phi^{\text{eq}}) = (0.6, 0)$ and helical fibers $(\theta^{\text{eq}}, \phi^{\text{eq}}) = (0.8, 0.7)$ from two perspectives.

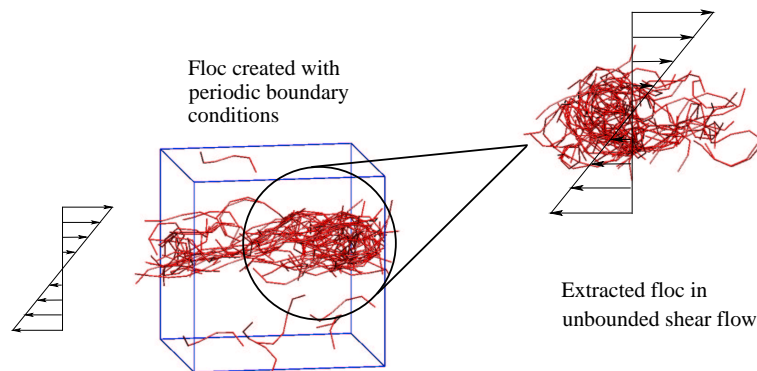


Figure 4.3: Flocs are created in a suspension with periodic boundary conditions and the largest floc is extracted to an unbounded linear flow to observe disruption.

observe floc dispersion: simple shear flow,

$$\mathbf{U}_{\text{shear}}^{\infty} = \dot{\gamma} (z, 0, 0), \quad (4.8)$$

uniaxial extensional flow,

$$\mathbf{U}_{\text{uni.}}^{\infty} = \frac{\sqrt{3}}{6} \dot{\epsilon} (2x, -y, -z), \quad (4.9)$$

and planar extensional flow,

$$\mathbf{U}_{\text{pla.}}^{\infty} = \frac{1}{2} \dot{\epsilon} (x, 0, -z), \quad (4.10)$$

where $\dot{\gamma}$ is the shear rate and $\dot{\epsilon}$ is the extension rate. Equation (4.8) describes simple shear flow in which the fluid flows in the x direction with a velocity gradient in the z direction. The expressions in Eqs. (4.9) and (4.10) represent extensional flows, in which the extension is in the x direction. Uniaxial extensional flow is similar to a filament of fluid that is being extended due to forces exerted on the ends, while planar extensional flow is similar to the elongation of a sheet of fluid by forces exerted on opposite ends. The coefficients of the velocity components are chosen such that the magnitude of the rate of deformation $(2\mathbf{E}^{\infty} : \mathbf{E}^{\infty})^{1/2}$, where $\mathbf{E}^{\infty} = \frac{1}{2}[\nabla\mathbf{U}^{\infty} + (\nabla\mathbf{U}^{\infty})^{\dagger}]$, is the same for each flow field. Thus, the effective stiffness is defined $S^{\text{eff}} = E_Y I / \eta_o \dot{\gamma} L^4$ for simple shear flow, and $S^{\text{eff}} = E_Y I / \eta_o \dot{\epsilon} L^4$ for uniaxial and planar extensional flows.

4.3 Results and discussion

4.3.1 Simple shear flow

Isolated flocs placed in unbounded shear flow rotate, and shed individual fibers or small groups of fibers. Dispersion of a typical floc in simple shear flow is illustrated

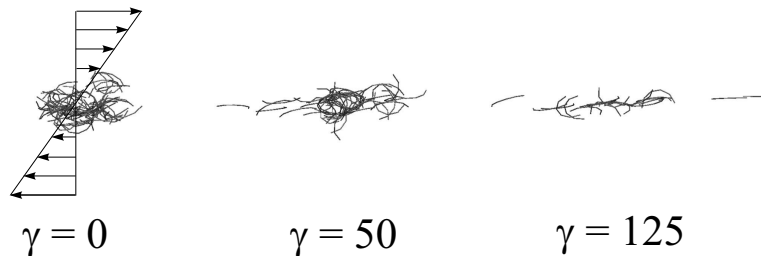


Figure 4.4: Snapshots of the largest fragment of a flocculated structure in a simple shear flow field at various strains ($N_{\text{fib}}^0 = 69$, $r_p = 75$, $S^{\text{eff}} = 0.05$, $\theta^{\text{eq}} = 0.6$, $\phi^{\text{eq}} = 0$, $\mu^{\text{stat}} = 20$).

in Fig. 4.4, where the snapshots of the largest portion of the flocculated structure at different shear strains ($\gamma = \dot{\gamma}t$) are shown (N_{fib}^0 is the initial number of fibers in the flocculated structure). Flocculation dispersion is apparent as the number of fibers in the flocculated structure decreases with increasing strain (fibers that have been carried more than a few fiber lengths away from the main flocculated structure are not shown). Flocculated structures also deform like an elastic body, compressing and stretching as the structure rotates in the flow. Almost all fiber loss occurred as the fibers stretched in the direction of maximum tension—the primary principal direction of \mathbf{E}^∞ which lies at 45° measured from the x -axis toward the z -axis.

The rate of flocculation dispersion is a function of the characteristics of the fiber, the fiber interactions, and the suspending fluid. The relative magnitudes of the elastic and viscous torques exerted on the fiber segments are characterized by the effective stiffness, $S^{\text{eff}} \equiv E_Y I / \eta_o \dot{\gamma} L^4$, and the frictional interactions are characterized by the static coefficient of friction, μ^{stat} .

The effects of varying the stiffness and coefficient of friction on flocculation dispersion in unbounded simple shear are demonstrated in Fig. 4.5, where the fraction of the initial number of fibers remaining in the flocculated structure $N_{\text{fib}} / N_{\text{fib}}^0$, is plotted as a function of strain γ for different values of S^{eff} and μ^{stat} . The flocculated structure was originally formed with $S^{\text{eff}} = 0.05$ and $\mu^{\text{stat}} = 20$, and the equilibrium configuration of the fibers is U-shaped with $(\theta^{\text{eq}}, \phi^{\text{eq}}) = (0.6, 0)$. As S^{eff} decreases, the flocculated structure disperses more rapidly as illustrated

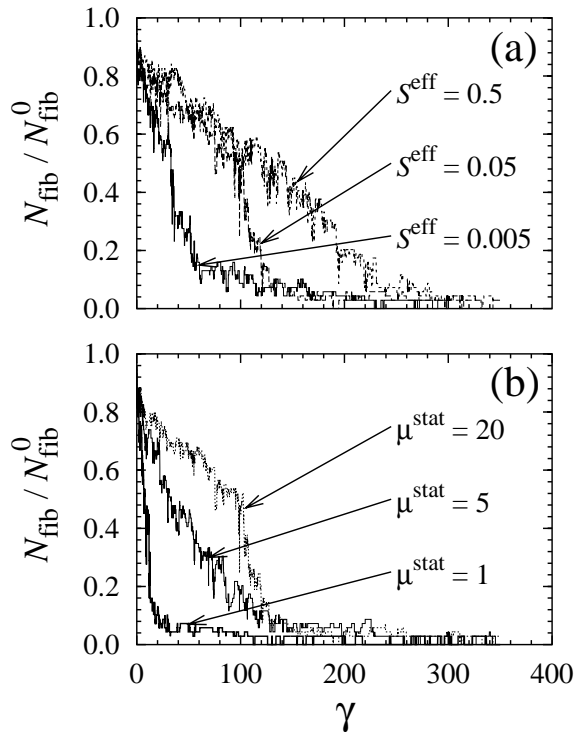


Figure 4.5: Fraction of the initial number of fibers (U-shaped) remaining in the largest floc fragment as a function of strain for various values of (a) S^{eff} (with $\mu^{\text{stat}} = 20$) and (b) μ^{stat} (with $S^{\text{eff}} = 0.05$) in unbounded simple shear flow ($N_{\text{fib}}^0 = 69$, $\theta^{\text{eq}} = 0.6$, $\phi^{\text{eq}} = 0$).

in Fig. 4.5(a). This indicates that increasing the viscous stress ($\eta_o \dot{\gamma}$) or increasing fiber flexibility ($1/E_Y I$) causes flocs to disrupt faster. Similarly, the floc disperses more rapidly as μ^{stat} is decreased, as illustrated in Fig. 4.5(b). Lee and Brodkey [52] examined disruption of isolated wood fiber flocs in turbulent shear flow. At low viscous stress levels, the characteristic length of the flow was much larger than the floc size, and thus the flow could be approximated by simple shear. Lee and Brodkey observed that flocs dispersed by shedding single fibers or small clumps of fibers, and increasing the viscous stress level in suspension increased the rate of dispersion, as observed in the simulations.

The effects of varying S^{eff} and μ^{stat} on the rate of floc break-up for a larger floc

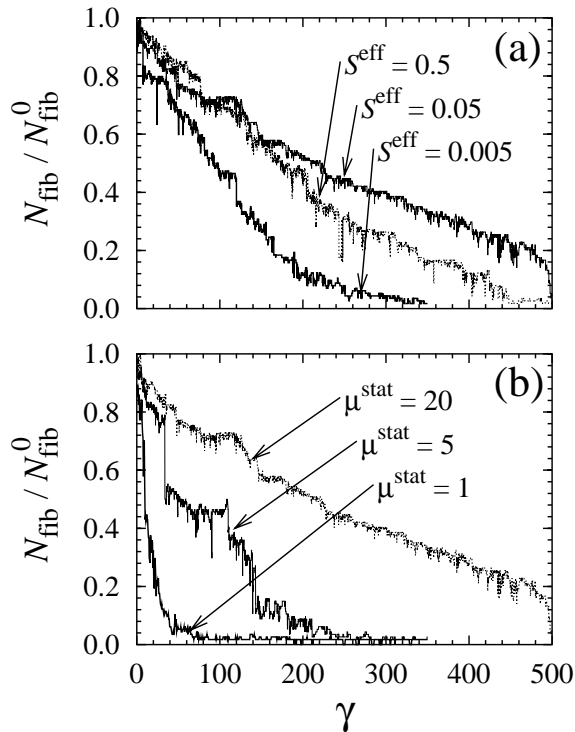


Figure 4.6: Fraction of the initial number of fibers (helical) remaining in the largest floc fragment as a function of strain for various values of (a) S^{eff} (with $\mu^{\text{stat}} = 20$) and (b) μ^{stat} (with $S^{\text{eff}} = 0.05$) in unbounded simple shear flow ($N_{\text{fib}}^0 = 114$, $\theta^{\text{eq}} = 0.8$, $\phi^{\text{eq}} = 0.7$).

of helical fibers $(\theta^{\text{eq}}, \phi^{\text{eq}}) = (0.8, 0.7)$ are illustrated in Fig. 4.6(a) and (b), respectively. At small strains ($\gamma \leq 130$), the flocs composed of fibers with $S^{\text{eff}} = 0.5$ and 0.05 disperse at approximately the same rate, in contrast to the behavior illustrated in Fig. 4.5(a) (the floc containing fibers with $S^{\text{eff}} = 0.005$ still disperses more rapidly). This change in behavior appears to be indicative of run-to-run variations in structure, rather than nonmonotonicity in the stiffness dependence of the rate of dispersion; i.e. numerous simulation runs show that, on average, the rate of dispersion increases as S^{eff} decreases. Fig. 4.6(b) illustrates that the rate of floc break-up increases with decreasing μ^{stat} for the helical fiber floc over the entire range of strains, as described previously for the U-shaped fiber floc.

Fibers that are elastically strained within flocs give the floc strength through frictional forces, which are proportional to the normal forces, and the normal forces are in turn increasing functions of fiber stiffness. The association of elastically interlocked fibers to floc coherence has been demonstrated experimentally by Soszynski and Kerekes [82]. They formed strong flocs of nylon fibers, and then heated the flocs past the glass transition temperature of nylon, thus lowering the bending stresses in the fibers. These heat-treated flocs were observed to disperse with a small amount of agitation, while flocs that were never heated required substantially stronger agitation to be dispersed. This is consistent with the simulation results, where decreasing the fiber stiffness increases the rate of dispersion. By lowering the coefficient of friction in simulations, the flocs also disperse more readily, consistent with the elastic-interlocking picture of floc coherence, where the strength of interfiber contacts is controlled by both fiber stiffness and interfiber friction.

4.3.2 Extensional flows

Simple shear flow always completely disperses isolated flocs in the simulations. Most of the floc disruption occurs while the floc is in a state of maximum tension, which suggests that extensional flow fields may be more effective for dispersing flocs. Flocs that were formed with helical fibers $(\theta^{\text{eq}}, \phi^{\text{eq}}) = (0.8, 0.7)$ were placed in uniaxial extensional flow, as defined by Eq. (4.9). When the fibers are sufficiently flexible ($S^{\text{eff}} = 0.005$), the flocs experience a global level of disruption in which they are literally torn apart by tensile forces exerted by the fluid, as illustrated in simulation snapshots in Fig. 4.7(a). After only a strain of $\varepsilon \equiv \dot{\varepsilon}t = 20$, the floc with $S^{\text{eff}} = 0.005$ has less than 20% of the original number of fibers left. If the effective stiffness is increased to $S^{\text{eff}} = 0.5$, the floc remains coherent, and deforms into an elongated

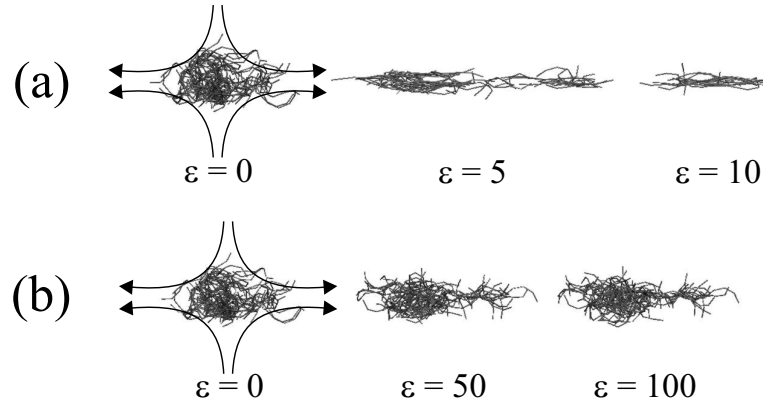


Figure 4.7: Snapshots of fiber floc structures in uniaxial extensional flow with (a) $S^{\text{eff}} = 0.005$ and (b) $S^{\text{eff}} = 0.5$ at various strains ($\theta^{\text{eq}} = 0.8$, $\phi^{\text{eq}} = 0.7$, $\mu^{\text{stat}} = 20$).

structure in which only a few fibers are lost, as illustrated in Fig. 4.7(b). Lee and Brodkey [52] observed similar behavior in highly turbulent shear flow. Kerekes [43] noted the elongation of wood fiber flocs as they entered a converging channel. This type of behavior was also observed for simulated flocs with U-shaped fibers ($\theta^{\text{eq}}, \phi^{\text{eq}} = (0.6, 0)$).

When the uniaxial extensional flow is stopped in the simulations, the flocs that remain intact partially recoil into a new floc shape due to the stored elastic energy in the stretched fibers. This is in contrast to the observation of Lee and Brodkey [52] in which elongated flocs did not appear to recoil upon cessation of flow. This discrepancy may be caused by the floc recoil being too insignificant to detect experimentally, but is easily measured in simulations. Kerekes [43] also observed that flocs elongated as they flowed into a converging channel, which approximates extensional flow. Experiments showed that flocs only ruptured if the extension rate was large, where the extension rate was defined as the velocity difference between the large and small cross-sections of the channel divided by the height of the small channel. Large extension rates correspond to smaller values of S^{eff} , which are indeed

observed to enhance floc dispersion in the simulations.

The initial time scale for disruption of a helical fiber floc is much smaller for extensional flow than for simple shear flow. The fraction of fibers left in the floc is plotted as a function of strain in Fig. 4.8 for flocs with $(\theta^{\text{eq}}, \phi^{\text{eq}}, \mu^{\text{stat}}) = (0.8, 0.7, 20)$, for uniaxial extensional flow with various values of S^{eff} , as well as for shear flow with $S^{\text{eff}} = 0.05$. Flocs in uniaxial extension are stretched and broken into smaller secondary flocs very quickly, relative to shear flow. The size of the largest secondary floc decreases as the effective stiffness decreases. Flocs in uniaxial extensional flow generally do not completely disperse, leaving a secondary floc with fewer fibers than the original floc, that is stretched out into a string-like shape. In contrast, flocs in shear flow always disperse completely, but take longer to reach the ultimate level of disruption observed in uniaxial extension. The reason that flocs in shear flow disrupt completely is likely related to the many conformations the floc assumes as it tumbles. Flocs in shear flow are constantly being stretched and compressed as they rotate in simple shear, which allows fibers to assume configurations that may be favorable for breaking contacts. In extensional flow however, the floc does not rotate and contacts become stronger as the floc is compressed in the two directions normal to the direction of elongation.

Figure 4.9 illustrates the rate of disruption of isolated flocs made up of U-shaped fibers $[(\theta^{\text{eq}}, \phi^{\text{eq}}, \mu^{\text{stat}}) = (0.6, 0, 20)]$ for uniaxial extensional flow with various values of S^{eff} , as well as for simple shear flow with $S^{\text{eff}} = 0.05$. As with the helical fiber flocs, the extensional flow causes global disruption of the U-shaped fiber flocs very quickly, resulting in smaller secondary flocs that remain intact. In this case, the secondary flocs that remain intact are larger than the secondary helical fiber flocs at equivalent stiffnesses. This may be attributed to the differences in fiber

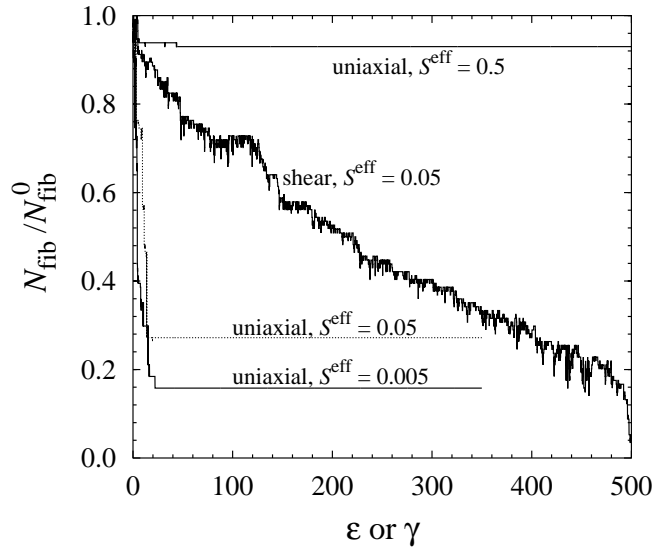


Figure 4.8: Fraction of the initial number of fibers (helical) in the largest floc fragment as a function of strain for dispersion in uniaxial extensional flow for various values of S^{eff} , compared to that for shear flow with $S^{\text{eff}} = 0.05$ ($N_{\text{fib}}^0 = 114$, $\theta^{\text{eq}} = 0.8$, $\phi^{\text{eq}} = 0.7$, $\mu^{\text{stat}} = 20$).

equilibrium shape, but may also be due to differences in the initial structures. Many more simulations need to be performed to discern such effects.

Behavior in planar extensional flow is qualitatively similar to that observed in uniaxial extensional flow. Flocs are stretched and experience global disruption in which large fragments are torn off due to tensile forces exerted by the fluid on the floc. Planar extensional flow appears to result in steady-state structures with fewer fibers than in uniaxial flow. The time scale of disruption, however, is 4-5 times longer for planar extensional flow, as shown in Fig. 4.10, in which the fraction of fibers remaining in the largest floc fragment is plotted as a function strain for a floc of U-shaped fibers in planar and uniaxial extension at two different values of S^{eff} . The difference in final structures of the secondary flocs in the two extensional flows appears to arise from of the compressive nature of the flow fields. Uniaxial extensional flow has inward flow in

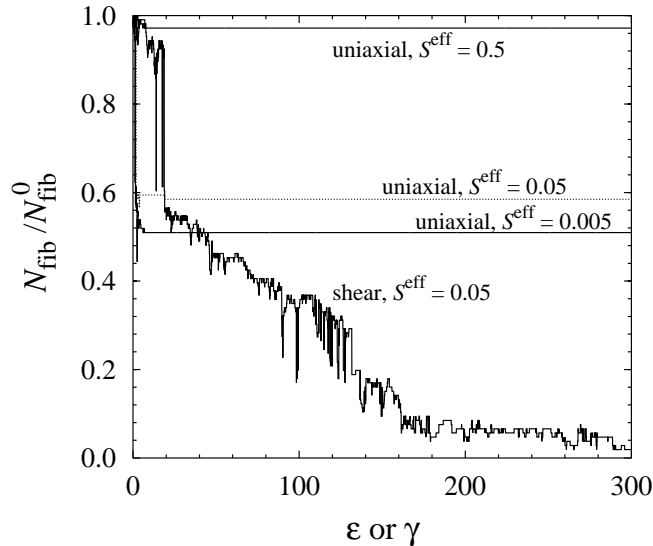


Figure 4.9: Fraction of the initial number of fibers (U-shaped) in the largest floc fragment as a function of strain in uniaxial extensional flow for various values of S^{eff} , compared to that for simple shear flow with $S^{\text{eff}} = 0.05$ ($N_{\text{fib}}^0 = 106$, $\theta^{\text{eq}} = 0.6$, $\phi^{\text{eq}} = 0$, $\mu^{\text{stat}} = 20$).

the y and z directions with extension in the x direction which compresses the floc into a tightly bound string-like structure. Flocs in planar extensional flow only experience compression due to inward flow in the z direction resulting in elongated “sheet-like” structures with larger surface areas, in which fibers can more easily escape the faces and edges by surface erosion or shedding. Qualitatively similar behavior is observed for flocs made of helical fibers.

As with flocs in shear flow, the strength of the flocs in extensional flow is a function of the effective stiffness and static coefficient of friction. The relationship between these parameters has been investigated by identifying the critical values that induce floc break-up in uniaxial extensional flow. We define a floc as dispersed when less than 25% of the initial number of fibers remain in the largest floc fragment ($N_{\text{fib}}/N_{\text{fib}}^0 < 0.25$). The smallest value of μ^{stat} required to maintain $N_{\text{fib}}/N_{\text{fib}}^0 \geq 0.25$

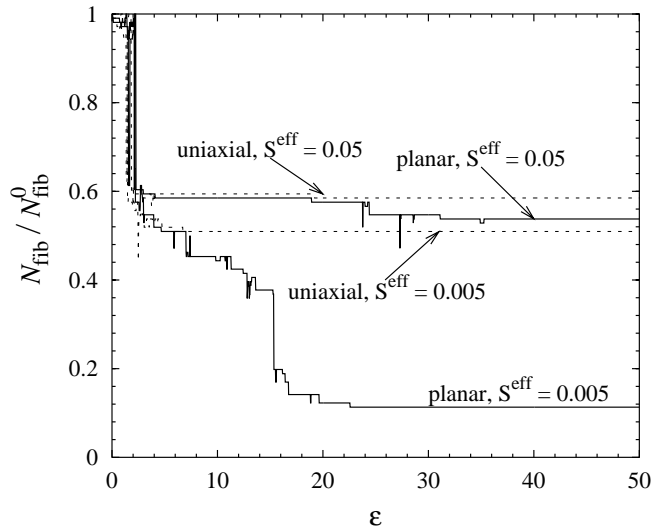


Figure 4.10: Fraction of the initial number of fibers (U-shaped) in the largest floc fragment as a function of strain for dispersion in planar and uniaxial extensional flows for various values of S^{eff} ; ($N_{\text{fib}}^0 = 106$, $\theta^{\text{eq}} = 0.6$, $\phi^{\text{eq}} = 0$, $\mu^{\text{stat}} = 20$).

after exposing the floc to extensional flow to a strain of $\varepsilon = 300$ is defined as a critical coefficient of friction, $\mu_{\text{crit}}^{\text{stat}}$, which is a function of S^{eff} . The critical coefficient of friction is plotted as a function of S^{eff} in Fig. 4.11 for flocs composed of U-shaped fibers ($\theta^{\text{eq}}, \phi^{\text{eq}} = (0.6, 0)$). The critical coefficient of friction decreases as the fiber stiffness increases. This is again consistent with the elastic fiber interlocking mechanism of floc coherence, in which interfiber contact strength is determined by both fiber stiffness and interfiber friction.

Coefficients of friction reported for cellulose fibers and other cellulose systems are significantly smaller than those employed here ($\mu^{\text{stat}} \approx 0.5$ [79, 99]). However, the values for the effective stiffness tend to be larger than those employed here. Using a value for the fiber stiffness of cellulose fibers in the range obtained by Tam Doo and Kerekes [86] ($E_Y I \approx 10^{-12} \text{ Nm}^2$), effective stiffnesses for sheared fiber suspensions in water at a typical experimental shear rate ($\dot{\gamma} \approx 10$), are $(S^{\text{eff}})_{\text{expt.}} > 1$. Thus,

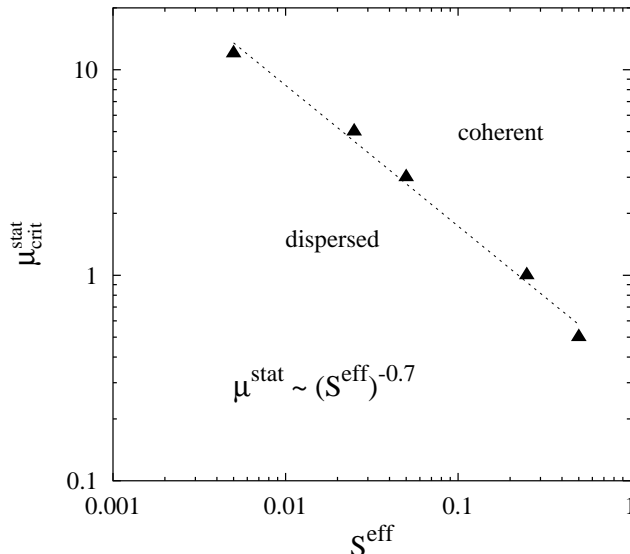


Figure 4.11: Critical values of S^{eff} and μ^{stat} in uniaxial extensional flow in which flocs remain coherent ($N_{\text{fb}}^0 = 106$, $\theta^{\text{eq}} = 0.6$, $\phi^{\text{eq}} = 0$).

Fig. 4.11 suggests that more realistic values of S^{eff} and μ^{stat} should indeed be capable of maintaining floc coherency. Unfortunately, the current simulation method requires a very large amount of computation time to directly evaluate fiber suspensions and flocs of such large effective stiffnesses ($S^{\text{eff}} > 1$), because the time step required for integrating the equations of motion decreases with increasing S^{eff} .

4.4 Conclusions

A dynamic, particle-level simulation technique has been employed to study the dispersion of fiber flocs in various linear flow fields. The model fiber consists of linked, rigid sphero-cylinders connected with flexible ball and socket joints that allow for the fiber to be of a deformed equilibrium shape. Fibers interact with one another via short-range repulsion and interfiber friction. Flocs were formed in simulations of

simple shear flow with periodic boundary conditions. Individual flocs were identified, extracted, and placed in unbounded linear flow fields (i.e., simple shear, uniaxial extension, and planar extension) to observe floc disruption.

The isolated flocs were observed to disperse at varying rates in the different flow fields. Simple shear flow completely breaks up flocs by shedding clumps of fibers from the main floc when aligned with the direction of maximum tension. Extensional flows initially disrupt flocs much faster than in simple shear flow; this rapid dispersion regime is then followed by a period in which the remaining floc fragments remain intact. The size of the remaining floc fragments decreases as the fiber stiffness or coefficient of friction are decreased. For all flows, the rate of dispersion increases as the stiffness or coefficient of friction are decreased. The observations reported here are consistent with numerous experimental results, and support the elastic fiber interlocking mechanism of floc coherence proposed by Soszynski and Kerekes [81, 82].

Chapter 5

Rheology of flexible fiber suspensions via simulations

5.1 Introduction

Suspensions of non-Brownian fibers are found in a variety of applications, such as pulp and paper and fiber-filled composites processing. Fiber suspensions exhibit non-Newtonian fluid characteristics similar to polymer melts and solutions, such as the Weissenberg effect (i.e., rod-climbing) [57, 61], shear thinning [34, 50], and viscoelasticity [87, 91]. Rheological properties, as well as other macroscopic quantities, depend on the structure of the suspensions. The structure is affected by such features as the fiber properties, interactions, suspending fluid properties, and the imposed flow field. Understanding the relationships among these features, the suspension structure, and the macroscopic properties can therefore aid in the design and optimization of processes and products. In this chapter, we employ the simulation method described in Chapter 2 to probe the relationships between fiber properties, interactions, suspension structure and the rheological properties of fiber suspensions in shear flow.

Adding fibers to a fluid can significantly alter its flow properties. Shear thinning of long fiber suspensions (aspect ratio $r_p \equiv L/d \geq 100$, where L and d are the fiber length and diameter, respectively) was reported by Kitano and Kataoka [50] for vinylon fibers in silicone oil and by Goto et al. [34] for nylon, glass, and vinylon fibers in glycerin. Goto et al. observed that shear thinning became more pronounced as the fiber aspect ratio increased or the flexibility increased (flexibility $\propto 1/E_Y$, where E_Y is the fiber Young's modulus). These researchers also reported first normal stress differences that were similarly influenced by fiber aspect ratio. The rheology of short glass fiber suspensions ($r_p \leq 50$) was investigated by Petrich et al. [64]. The viscosity increased nearly linearly with concentration, consistent with predictions for noninteracting fibers from slender body theory [6]. Chaouche and Koch [18] observed shear thinning for suspensions of short nylon fibers in various silicone oils at very low shear rates. They attributed the shear thinning behavior to adhesive contacts between fibers, and measured adhesive forces on the order of $0.01 \mu\text{N}$. None of these researchers reported on the effect of fiber shape on rheological properties. Glass fibers tend to be straight, while nylon and vinylon fibers often have permanent deformations.

Meyer and Wahren [58] proposed that sufficiently concentrated fiber suspensions form networks of contacting fibers that exhibit viscoelastic properties. Thalén and Wahren [87] measured the shear modulus of pulp suspensions and obtained results in qualitative agreement with the simple network theory of Meyer and Wahren [58]. A sufficient force must be applied to the suspension to overcome the contact forces and cause the suspension to flow, and this behavior is characterized by a yield stress. The yield stress of various wood and nylon fiber suspensions was measured by Bennington et al. [12]. The yield stress (σ_0) scaled with the volume fraction (Φ) as $\sigma_0 \sim \Phi^\beta$, where the exponent β varied from 2.5-3.5. This is consistent with the

simple fiber network theory of Meyer and Wahren [58] which gives $\beta = 3$. However, the measured values of β varied with fiber elasticity and aspect ratio, which is not predicted by the simple network theory. The dependence of the yield stress on fiber elasticity was significantly different for suspensions of wood fibers and nylon fibers. Bennington et al. suggested the wood fibers have rougher surfaces than nylon which leads to different contact dynamics. Kitano and Kataoka [50] also measured yield stresses for suspensions of vinylon fibers in silicone oil. The exponent β decreased as the aspect ratio increased, which was attributed to fiber interactions, increased apparent flexibility, and wall effects.

Suspensions of flexible fibers often flocculate, forming heterogeneous structures called *flocs* that affect the flow characteristics of the suspension. Soszynski and Kerekes [82] suggested that fiber flocs are mainly formed by mechanical contacts. They proposed a mechanism for fiber flocculation called “elastic fiber interlocking” in which fibers become locked in strained configurations due to their elasticity and friction forces at fiber contacts which serve to strengthen the network. Chen et al. [19] measured the stress in wood and polyethylene terephthalate (PET) fiber suspensions that were observed to flocculate. At low shear rates, the suspensions behaved as Newtonian fluids. As the shear rate was increased, the suspensions would begin to flocculate which corresponded to jumps in the the shear stress. As the shear rate was increased further, the flocs began to disappear and the fluid again exhibited Newtonian behavior.

The stress in a suspension of fibers is related to the distribution of fiber positions and orientations. The bulk average stress $\langle \boldsymbol{\sigma} \rangle$ for a suspension of fibers in a Newtonian fluid is [7]

$$\langle \boldsymbol{\sigma} \rangle \simeq -p\boldsymbol{\delta} + 2\eta_o\mathbf{E}^\infty + \boldsymbol{\sigma}^p, \quad (5.1)$$

where p is an isotropic pressure, $\boldsymbol{\delta}$ is the identity tensor, \mathbf{E}^∞ is the rate of strain tensor of the imposed flow field, η_o is the suspending fluid viscosity, and $\boldsymbol{\sigma}^p$ is the particle contribution to the average stress. The particle contribution to the stress can be divided into two parts: (1) a particle-fluid interaction, and (2) a particle-particle interaction contribution which results from non-zero hydrodynamic forces on the fibers. Batchelor [6] derived an expression for the particle stress using slender body theory for dilute suspensions of rigid, straight fibers that interact only via hydrodynamic disturbances,

$$\boldsymbol{\sigma}^p \approx \frac{\pi\eta_o n L^3}{6 \ln(2r_p)} \left[\langle \mathbf{p}\mathbf{p}\mathbf{p}\mathbf{p} \rangle - \frac{1}{3} \langle \mathbf{p}\mathbf{p} \rangle \boldsymbol{\delta} \right] : \mathbf{E}^\infty, \quad (5.2)$$

where n is the number of fibers per unit volume, L is the fiber length, and \mathbf{p} is the unit fiber orientation vector. Slender-body theory can be used more generally to approximate the particle stress for suspensions of hydrodynamically interacting fibers into the semi-dilute regime ($nL^3 > 1$),

$$\begin{aligned} \boldsymbol{\sigma}^p = & \frac{n}{2} \left\langle \int_{-\ell}^{\ell} \left[s\mathbf{p}\mathbf{F}(s) + s\mathbf{F}(s)\mathbf{p} - \frac{2}{3}(s\mathbf{p} \cdot \mathbf{F}(s))\boldsymbol{\delta} \right] ds \right. \\ & \left. + \mathbf{F}^H \mathbf{r} + \mathbf{r}\mathbf{F}^H - \frac{1}{3}(\mathbf{F}^H \cdot \mathbf{r})\boldsymbol{\delta} \right\rangle, \end{aligned} \quad (5.3)$$

where \mathbf{F}^H is the net hydrodynamic force on a fiber, \mathbf{r} is the fiber center-of-mass, and $\mathbf{F}(s)$ is the hydrodynamic force per unit length acting on the fiber at axial position s . The quantity $\mathbf{F}(s)$ depends on the geometry of the particle, properties of the suspending fluid, and the orientation of the fibers in the flow field. The integral in the above equation represents the purely hydrodynamic contribution to the particle stress [54], and the remaining terms arise from the non-hydrodynamic particle interactions [84].

Particle-level simulations are a common method for probing particulate suspensions, and more specifically, for understanding the relationships between particle

properties and interactions, the suspension microstructure, and macroscopic behavior (see, for example, Bossis and Brady [14]). The equations of motion for each particle are solved numerically, subject to the forces and torques identified, in order to evolve the particle positions and orientations in time and thus produce a prediction of the suspension microstructure. This method is sufficiently general to allow the inclusion of a variety of features, such as elongated and flexible particles, as well as various forces, such as hydrodynamic forces and interactions, colloidal forces and friction, to name a few. The complexity of the physical model is only limited by the computational resources required to evaluate the forces and torques and solve the equations of motion.

Numerous fiber suspension studies have focused on rigid, elongated bodies in Newtonian fluids. Claeys and Brady [20, 21] modelled fibers as rigid prolate spheroids (ellipsoids of revolution). They developed a method for accurately evaluating the hydrodynamic forces and torques, including both the short-range hydrodynamic interactions (lubrication forces) as well as the long-range, many-body hydrodynamic interactions. Mackaplow and Shaqfeh [54] employed slender-body theory to accurately evaluate the long-range hydrodynamic interactions between prolate spheroids or cylinders. As with the method of Claeys and Brady, the calculations were so computationally demanding that results for suspensions of long fibers in simple shear flow were limited to prescribed suspension structures. Thus, these methods were not employed to predict the suspension structure resulting from flow. Simulations by Yamane et al. and Fan et al. [28, 98] employed approximations for the hydrodynamic interactions between rigid fibers. These authors obtained good agreement with experimental results for the suspension viscosity as a function of concentration, but did not report shear thinning behavior ($nL^3 \lesssim 50$, $r_p \lesssim 30$).

Sundararajakumar and Koch and Harlen et al. [35, 84] simulated suspensions of rigid, slender rods interacting via contact forces. They argued that for flowing suspensions of fibers, lubrication forces cannot prevent fibers from contacting, and thus short-range hydrodynamic interactions were neglected. Harlen et al. [35] simulated single spheres falling through neutrally-buoyant fiber suspensions to illustrate the importance of fiber-fiber contacts on the flow properties of fiber suspensions. For low concentrations, interfiber contacts are rare and the flow behavior is dominated by long-range hydrodynamic interactions. However, as the concentration is increased such that the fibers are in frequent contact, the flow behavior is strongly influenced by the contacts. In fact, for $nL^3 \geq 12$ ($r_p = 20$), the drag on the settling sphere calculated by including long-range hydrodynamic interactions and contact forces is indistinguishable from that calculated by including contact forces alone (and in good agreement with experimental results reported by Milliken et al. [59]). Although the falling sphere influences the suspension structure, the authors did not report any tendency toward fiber flocculation.

Several studies have focused on simulating suspensions of flexible fibers. Yamamoto and Matsuoka [93, 94] modelled flexible fibers as chains of rigid spheres connected through springs, with potentials to mimic resistance to bending and twisting. Chain connectivity is maintained by constraints, producing equations that must be solved simultaneously with the equations of motion. Ross and Klingenberg [71] modelled flexible fibers as inextensible chains of rigid prolate spheroids connected through ball and socket joints. This model eliminates the need for iterative constraints to maintain fiber connectivity, and can represent large aspect ratio fibers with relatively few bodies. These features help to reduce computations, facilitating simulation of concentrated suspensions. Schmid et al. [75] extended this method, modelling

flexible fibers as chains of spherocylinders connected by ball and socket joints, that interact via short-range repulsive forces as well as friction forces. They demonstrated that fiber equilibrium shape, flexibility, and inter-fiber friction are important in determining the suspensions microstructure, and in particular for predicting flocculation behavior.

In this chapter, we build on the method of Schmid et al. (details in Chapter 2) to investigate relationships between fiber properties and interactions, and the resulting suspension rheological properties for simple shear flow. In Section 5.2, we briefly describe the flexible fiber model and simulation method. The model fiber consists of rigid spherocylinders connected by ball and socket joints. The fibers interact with other fibers via short-range repulsive forces and friction. Fiber and suspension characteristics such as equilibrium shape, flexibility, aspect ratio, friction, concentration, and suspending fluid characteristics have been shown to impact the structure of fiber suspensions in simulations (see Schmid et al. [75] and Chapter 3). Varying these parameters can result in drastic changes to the suspension structure including the formation of heterogeneities (i.e. flocs). In Section 5.3, we show that suspension rheological properties also depend sensitively on these features. The dependence of the shear thinning behavior and first normal stress differences on fiber aspect ratio is similar to that observed in experiments. Calculated yield stresses exhibited a scaling with concentration in agreement with network theory and experiment. Fiber suspensions were also seen to flocculate under certain conditions, and this affected the shear thinning behavior of the suspensions.

5.2 Simulation method

Flexible fiber suspensions are modelled as chains of neutrally-buoyant, linked rigid bodies immersed in a Newtonian liquid. The model includes realistic features such as fiber flexibility, deformed equilibrium shapes, and mechanical contact forces between fibers. The model and simulation method are similar to that employed by Schmid et al. [75] and is described in more detail in Chapter 2.

Each fiber in the suspension is represented by N_{seg} rigid cylinders (length 2ℓ , radius b) with hemi-spherical end caps, connected end-to-end by ball and socket joints (Fig. 5.1). The motion of the fiber segments is described by Newton's laws of motion in which we neglect fiber inertia. The force balance on a fiber segment i includes contributions from hydrodynamic drag ($\mathbf{F}_i^{\text{hyd}}$), mechanical contact forces ($\mathbf{F}_{ik}^{\text{con}}$), and forces at each joint that keep the fiber at a constant length (\mathbf{X}_i),

$$\mathbf{F}_i^{\text{hyd}} + \mathbf{X}_{i+1} - \mathbf{X}_i + \sum_k^{N_{C_i}} \mathbf{F}_{ik}^{\text{con}} = \mathbf{0}, \quad (5.4)$$

where N_{C_i} is the number of contacts on fiber segment i . The torque balance on fiber segment i includes similar contributions with the addition of a restoring torque at each joint (\mathbf{Y}_i),

$$\mathbf{T}_i^{\text{hyd}} + \mathbf{Y}_{i+1} - \mathbf{Y}_i + \ell \mathbf{p}_i \times [\mathbf{X}_{i+1} + \mathbf{X}_i] + \sum_k^{N_{C_i}} [\mathbf{G}_{ik} \times \mathbf{F}_{ik}^{\text{con}}] = \mathbf{0}, \quad (5.5)$$

where $\mathbf{T}_i^{\text{hyd}}$ is the hydrodynamic torque, \mathbf{p}_i is the orientation vector of the segment, and \mathbf{G}_{ik} is a vector from the center of segment i to the point of contact with segment k .

In this model, hydrodynamic interactions are neglected based on results reported by Sundararajakumar and Koch and Harlen et al. [35, 84], as previously explained. This assumption allows us to evaluate the hydrodynamic force and torque as

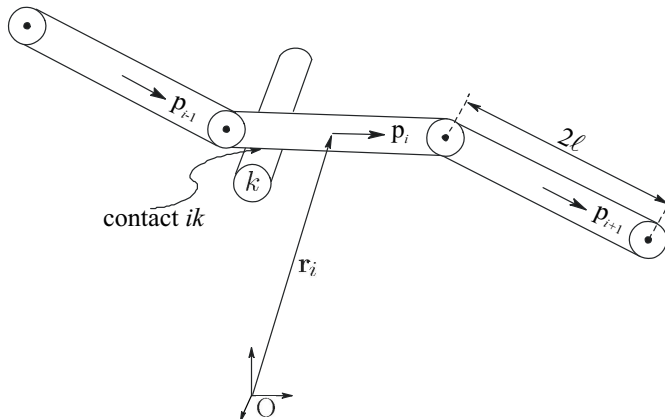


Figure 5.1: Model fiber of rigid spherocylinders linked by ball and socket joints that experience mechanical contacts with other fibers in the suspension.

that on an isolated body, $\mathbf{F}_i^{\text{hyd}} = \mathbf{A}_i \cdot [\mathbf{U}_i^\infty - \dot{\mathbf{r}}_i]$ and $\mathbf{T}_i^{\text{hyd}} = \mathbf{C}_i \cdot [\boldsymbol{\Omega}_i^\infty - \boldsymbol{\omega}_i] + \tilde{\mathbf{H}}_i : \mathbf{E}^\infty$, where the resistance tensors \mathbf{A}_i , \mathbf{C}_i , and $\tilde{\mathbf{H}}_i$ are approximated with the resistance tensors of a prolate spheroid with an equivalent aspect ratio, $r_{\text{es}} = 0.7r_{\text{ps}}$ (see Chapter 2), where r_{ps} is the aspect ratio of a segment. The ambient velocity, angular velocity, and rate of strain tensor are \mathbf{U}_i^∞ , $\boldsymbol{\Omega}_i^\infty$, and \mathbf{E}^∞ , respectively, and only simple shear flows are simulated [i.e., $\mathbf{U}^\infty = (\dot{\gamma}z, 0, 0)$]. The segment translational and angular velocities are $\dot{\mathbf{r}}_i$ and $\boldsymbol{\omega}_i$.

The restoring torque \mathbf{Y}_i describes the resistance of the elastic fibers to bending and twisting. The bending and twisting components of this torque are assumed to be linear in the difference between the bending and twisting angles (θ_i and ϕ_i respectively) and their equilibrium values (θ_i^{eq} and ϕ_i^{eq}),

$$|\mathbf{Y}_i| = \kappa_b(\theta_i - \theta_i^{\text{eq}}) + \kappa_t(\phi_i - \phi_i^{\text{eq}}), \quad (5.6)$$

where κ_b and κ_t are the bending and twisting constants of the fiber. The bending constant is related to the stiffness of the fiber material by $\kappa_b = E_Y I / 2\ell$, where E_Y is the Young's Modulus, $I \equiv \pi b^4 / 4$ is the area moment, and ℓ is the half length of a fiber segment. The twisting constant is set to $\kappa_t = 0.67\kappa_b$ in this study, equal to

that of a elastic circular cylinder with a Poisson's ratio of 0.5. The fiber flexibility is characterized by a single parameter which we call the effective stiffness $S^{\text{eff}} \equiv E_Y I / \eta_o \dot{\gamma} L^4$, where η_o is the suspending fluid viscosity, $\dot{\gamma}$ is the shear rate, and L is the total fiber length. The effective stiffness characterizes the relative importance of fiber stiffness and hydrodynamic torque in determining the amount a fiber will bend in shear flow. As $S^{\text{eff}} \rightarrow 0$, fibers behave like completely flexible threads, whereas for $S^{\text{eff}} \rightarrow \infty$, fibers become rigid and retain their equilibrium shapes during flow.

The fiber length is kept constant by applying a constraint for each joint,

$$\mathbf{r}_i + \ell \mathbf{p}_i = \mathbf{r}_{i+1} - \ell \mathbf{p}_{i+1}, \quad (5.7)$$

where \mathbf{r}_i is the segment position. These constraint equations allow for the solution of the constraint forces at each joint \mathbf{X}_i .

Fibers experience mechanical contacts with other fibers in the suspension. The force that results from each contact is decomposed into two components—a force in the normal direction of the contact ($\mathbf{F}_{ik}^{\text{N}}$) and a frictional force ($\mathbf{F}_{ik}^{\text{fric}}$) in the plane of the contact. The purely repulsive normal force exerted on segment i by segment k is modelled as $\mathbf{F}_{ik}^{\text{N}} = -F \exp[-ah_{ik}] \mathbf{n}_{ik}$, where h_{ik} is the separation between the surfaces of segments i and k , \mathbf{n}_{ik} is the unit normal vector directed from segment i to k , $F = 900\pi\eta_o\ell b\dot{\gamma}$ is the magnitude of the repulsive force, and $a = 20/b$. The friction force is determined by the constraint of no relative motion in the plane of contact,

$$\begin{pmatrix} \Delta \mathbf{u}_{ik} \cdot \mathbf{e}_1^{\text{loc}} \\ \Delta \mathbf{u}_{ik} \cdot \mathbf{e}_2^{\text{loc}} \\ \mathbf{F}_{ik}^{\text{fric}} \cdot \mathbf{n}_{ik} \end{pmatrix} = \mathbf{0}, \quad (5.8)$$

where $\Delta \mathbf{u}_{ik}$ is the relative velocity between segments i and k at the point of contact, and the plane of contact is defined by the vectors $\mathbf{e}_1^{\text{loc}}$ and $\mathbf{e}_2^{\text{loc}}$. The calculated friction

force is then subjected to a Coulombic friction law of the form

$$\begin{aligned} |\mathbf{F}_{ik}^{\text{fric}}| &\leq \mu^{\text{stat}} |\mathbf{F}_{ik}^{\text{N}}| \Rightarrow \text{contact remains intact} \\ &> \mu^{\text{stat}} |\mathbf{F}_{ik}^{\text{N}}| \Rightarrow \mathbf{F}_{ik}^{\text{fric}} = \mu^{\text{kin}} |\mathbf{F}_{ik}^{\text{N}}| \frac{\Delta \mathbf{u}_{ik}}{|\Delta \mathbf{u}_{ik}|}, \end{aligned} \quad (5.9)$$

where μ^{stat} and μ^{kin} are the static and kinetic coefficients of friction. For all of the simulation results presented in this chapter, the kinetic coefficient of friction is $\mu^{\text{kin}} = 0$ (i.e., no sliding friction).

The equations of motion and the constraint equations for all of the fiber segments in the suspension can be expressed as a system of differential algebraic equations (DAEs) for the unknown coordinates and constraint forces,

$$\begin{aligned} \dot{\mathbf{q}} - \mathbf{F}(\mathbf{q}, \boldsymbol{\lambda}) &= \mathbf{0}, \\ \boldsymbol{\Psi}(\mathbf{q}) &= \mathbf{0}, \\ \boldsymbol{\Xi}(\mathbf{q}, \dot{\mathbf{q}}, \boldsymbol{\lambda}) &= \mathbf{0}, \end{aligned} \quad (5.10)$$

where the vector \mathbf{q} contains the generalized coordinates of each fiber segment (positions and orientations) and $\boldsymbol{\lambda}$ is the vector of constraint forces (\mathbf{X} and \mathbf{F}^{fric}) in the suspension. If the segment orientations are represented by Euler parameters [92], there are $7N_{\text{fib}}N_{\text{seg}}$ equations of motion to be solved. The inextensibility constraint [Eq. (5.7)], represented by the vector $\boldsymbol{\Psi}$, is made up of $3N_{\text{fib}}(N_{\text{seg}} - 1)$ constraint equations that depend on only the positions and orientations. The $3N_C$ friction constraint equations [Eq. (5.8)] are contained in $\boldsymbol{\Xi}$, where N_C is the total number of contacts in the system.

Simulations are performed by randomly placing fibers at their equilibrium shape into a simulation cell of size $(\zeta L)^3$ as illustrated in Figure 5.2, where ζ is the cell size scaling factor ($\zeta = 1.5\text{--}4$). A linear shear field is imposed and periodic boundary conditions are applied with the Lees-Edwards modification for shearing systems [Allen and Tildesley (1991)], to simulate an infinite suspension. The fiber

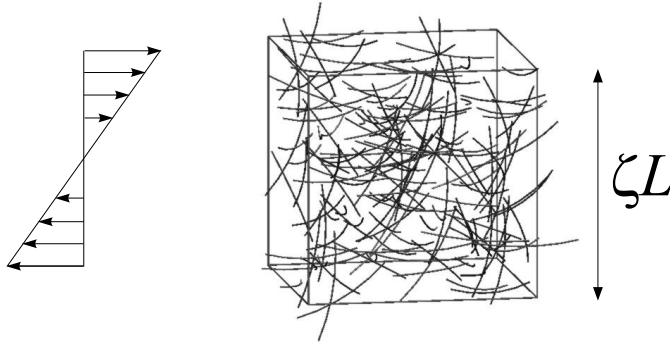


Figure 5.2: Example of the starting configuration of fibers randomly placed in a periodic simulation cell.

motions are obtained by the numerical solution of the system of DAEs in Eq. (5.10). An approximate solution method was developed to solve this system, the details of which are found in Chapter 2.

The particle positions and orientations are postprocessed in order to calculate the stress and other suspension properties. Using slender body theory, the extra particle stress [Eq. (5.3)] may be simplified to the form (see Appendix A)

$$\begin{aligned} \boldsymbol{\sigma}^p = \frac{4\pi n\ell^3\eta_o}{3\ln(2r_p)} \left\langle \sum_{i=1}^{N_{\text{seg}}} \left\{ \mathbf{E}^\infty \cdot \mathbf{p}_i\mathbf{p}_i + \mathbf{p}_i\mathbf{p}_i \cdot \mathbf{E}^\infty - \mathbf{p}_i\mathbf{p}_i\mathbf{p}_i\mathbf{p}_i : \mathbf{E}^\infty - \right. \right. \\ \left. \left. (\mathbf{p}_i\dot{\mathbf{p}}_i + \dot{\mathbf{p}}_i\mathbf{p}_i) + \right. \right. \\ \left. \left. \frac{3}{\ell^2} \left(\left[\boldsymbol{\delta} - \frac{1}{2}\mathbf{p}_i\mathbf{p}_i \right] \cdot (\mathbf{U}^\infty - \dot{\mathbf{r}}_i)\mathbf{r}_i + \right. \right. \right. \\ \left. \left. \left. \mathbf{r}_i \left[\boldsymbol{\delta} - \frac{1}{2}\mathbf{p}_i\mathbf{p}_i \right] \cdot (\mathbf{U}^\infty - \dot{\mathbf{r}}_i) \right) \right\} \right\rangle + \Upsilon\boldsymbol{\delta}, \quad (5.11) \end{aligned}$$

where Υ represents an isotropic contribution of no interest. Suspensions were sheared for at least 500 strain units after reaching steady state. The particle stress for particular runs were averaged over all configurations saved after steady state was reached. Most data reported in the following section are for single runs. Some runs were replicated with different initial conditions; uncertainties estimated from the replicates are indicated by error bars in the figures.

θ^{eq} (rad.)	shape
0.0	
0.1	
0.3	
0.6	

Figure 5.3: Examples of U-shaped fibers ($\phi^{\text{eq}} = 0$, $r_p = 75$) for various values of θ^{eq} .

5.3 Results and discussion

5.3.1 Effects of fiber shape and friction

In this section we investigate the effects of fiber shape and static friction on the shear viscosity of fiber suspensions. Simple shear flow was simulated for suspensions of U-shaped fibers ($r_p = 75$, $S^{\text{eff}} = 0.05$) at various concentrations and for several different equilibrium bending angles and coefficients of friction. U-shaped fibers with different equilibrium bending angles are illustrated in Fig. 5.3.

The specific viscosity $\eta_{\text{sp}} \equiv \eta/\eta_o - 1$ ($\eta \equiv \sigma_{xz}/\dot{\gamma}$ is the suspension viscosity) is plotted as a function of concentration (nL^3) in Figs. 5.4(a) and (b) for suspensions of U-shaped fibers. Results are presented for simulations of flexible fibers ($S^{\text{eff}} = 0.05$, $r_p = 75$, $N_{\text{seg}} = 5$) with $\theta^{\text{eq}} = 0, 0.1$ and 0.3 , as well as for straight, rigid fibers ($r_p = 75$, $N_{\text{seg}} = 1$). Results for simulations without friction ($\mu^{\text{stat}} = 0$) are represented by

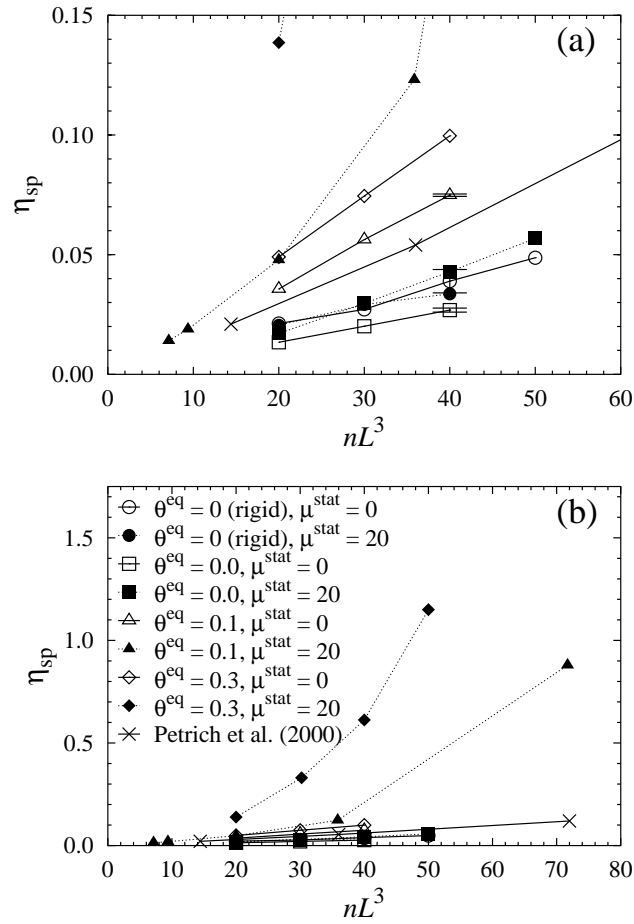


Figure 5.4: Steady-state specific viscosity as a function of concentration for suspensions with fibers of different shapes and coefficients of friction.

open symbols, and results for simulations with friction ($\mu^{stat} = 20$) are represented by filled symbols. Fig. 5.4(b) illustrates data over wider ranges of concentrations and specific viscosities than that presented in Fig. 5.4(a). The data points indicate individual simulation runs in which the average value is computed from at least 500 steady state configurations. Uncertainties (95% confidence interval) estimated from replicate simulations with different initial configurations are indicated by the error bars.

Consider first the effect of fiber flexibility in the absence of friction in these

simulations, illustrated by the results for suspensions of rigid, straight fibers (open circles) and the results for suspensions of flexible, straight fibers (open squares) in Fig. 5.4(a). For both systems, η_{sp} is small, and increases roughly linearly with concentration in agreement with previous simulations at relatively small concentrations [84]. The linear dependence of the viscosity with concentration is consistent with the predictions of slender body theory for dilute fiber suspensions. For an ambient flow field $\mathbf{U}^\infty = (\dot{\gamma}z, 0, 0)$, the slender body theory prediction for the specific viscosity in a dilute suspension of rigid rods is [6]

$$\eta_{\text{sp}}^{\text{sb}} = nL^3 \frac{\pi}{6 \ln(2r_p)} \langle p_x^2 p_z^2 \rangle - 1. \quad (5.12)$$

For suspensions of non-interacting particles, the orientation distribution is approximately constant which suggests $\eta_{\text{sp}}^{\text{sb}} \propto nL^3$. Petrich et al. [64] also observed this type of behavior in experiments of very stiff and straight glass fibers ($S^{\text{eff}} \approx 1$) with an aspect ratio $r_p = 72$ at approximately the same concentration range as our simulations (illustrated in Fig. 5.4).

The differences between the results for suspensions of straight, rigid fibers and suspensions of straight, flexible fibers are very small, approximately equal to the uncertainties. This is not unexpected, since the flexible fibers in this case are actually quite stiff. For these simulations, the average deviation of the bending angles from the equilibrium value is $\langle |\theta_i - \theta^{\text{eq}}| \rangle = 6 \times 10^{-4}$. Indeed, the degree of deformation for all the runs depicted in Fig. 5.4 is quite small, and thus the results appear to represent the behavior of stiff fibers ($\langle |\theta_i - \theta^{\text{eq}}| \rangle = 4.6 \times 10^{-3}$ for $\theta^{\text{eq}} = 0.1$; $\langle |\theta_i - \theta^{\text{eq}}| \rangle = 1.6 \times 10^{-2}$ for $\theta^{\text{eq}} = 0.3$). Effects of flexibility for suspensions of more flexible fibers are discussed in Section 5.3.2.

Next consider the effect of fiber shape in the absence of friction, illustrated by the results for straight, rigid and flexible fibers (open circles and squares, respectively),

and U-shaped, flexible fibers ($\theta^{\text{eq}} = 0.1$, open triangles) in Fig. 5.4(a). The specific viscosities of the suspensions of U-shaped fibers are significantly larger than that for the suspensions of straight fibers. At $nL^3 = 40$, η_{sp} for the U-shaped fibers is approximately twice as large as that for the straight fibers. We note that for $\theta^{\text{eq}} = 0.1$, the fiber shape is nearly straight (see Fig. 5.3). Thus a small amount of curvature can have a significant effect on the suspension viscosity.

The results presented in Fig. 5.4 also illustrate the impact of interfiber friction on the shear viscosity. For suspensions of straight, rigid fibers, adding static friction ($\mu^{\text{stat}} = 20$) does not alter the shear viscosity. For suspensions of straight, flexible fibers, adding static friction produces a small increase in the specific viscosity. The effect of static friction is much more pronounced for the U-shaped fibers. For $nL^3 \gtrsim 30$, adding static friction more than doubles the specific viscosity. In addition, the concentration dependence changes from a linear dependence in the absence of friction to a higher-order dependence with $\mu^{\text{stat}} = 20$.

The viscosity of fiber suspensions is thus significantly influenced by both the fiber shape and static friction. Furthermore, there is also an additional synergistic effect of these features, as friction influences the viscosity of suspensions of U-shaped fibers more than it influences the viscosity of suspensions of straight fibers. The effects of fiber shape and friction are explored in more detail below.

The effect of shape on the specific viscosity of suspensions of U-shaped fibers is further illustrated in Fig. 5.5, in which all other suspension properties are held constant $[(N_{\text{seg}}, r_p, nL^3, S^{\text{eff}}, \phi^{\text{eq}}, \mu^{\text{stat}}) = (5, 75, 20, 0.05, 0, 20)]$. The specific viscosity gradually increases as the fiber curvature increases (θ^{eq} increases). At a certain curvature, $\theta^{\text{eq}} = 0.5$ for the conditions listed above, the specific viscosity undergoes a large jump in value. This corresponds to the formation of fiber flocs in the suspen-

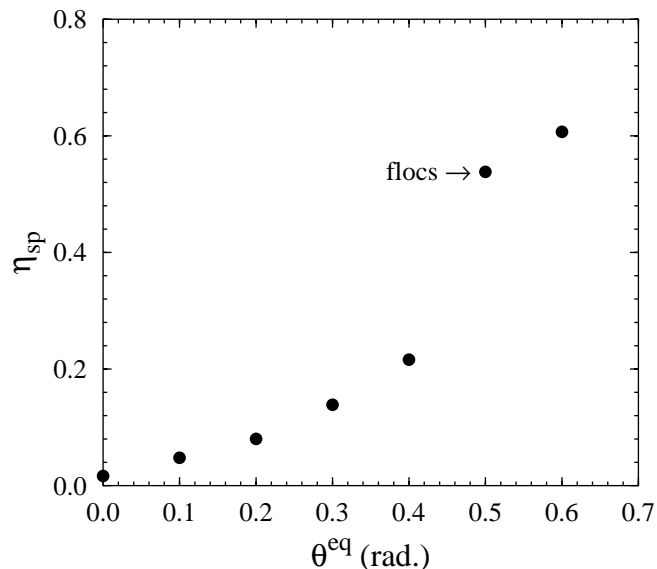


Figure 5.5: Specific viscosity as a function of equilibrium shape of U-shaped fibers after shearing for $\gamma = 1500$ ($N_{\text{seg}}, r_p, nL^3, S^{\text{eff}}, \phi^{\text{eq}}, \mu^{\text{stat}} = (5, 75, 20, 0.05, 0, 20)$).

sion. Further increases in the equilibrium bending angle also result in a flocculated suspension and a gradual increase in η_{sp} . The effect of flocculation on rheological properties is discussed further in Section 5.3.4.

Deviations of the fiber shape from perfectly straight can influence the stress in the suspension in several ways. Consider first dilute suspensions in which fiber rotation dynamics are similar to that of isolated fibers. U-shaped fibers have a smaller rotation period than straight fibers of the same aspect ratio, and thus spend a larger fraction of the time out of the plane of shear. In addition, for U-shaped fibers, some fiber segment orientation vectors \mathbf{p}_i will always have nonzero components normal to the plane of shear (except in the rare situation in which the plane of the “U” lies within a shearing plane), in contrast to straight fibers that spend most of the time nearly aligned with the flow and contribute little to the suspension viscosity. These features directly affect the hydrodynamic contribution to the stress represented by the integral term in Eq. 5.3. Fiber shape can also influence the nonhydrodynamic

contribution to the stress (represented by the terms containing products of \mathbf{F}^H and \mathbf{r} in Eq. 5.3) by impacting the frequency of contacts between fibers. The interfiber contacts result in nonzero hydrodynamic forces \mathbf{F}^H , and thus more frequent contacts are expected to increase the time-averaged stress. The contacts also affect the fiber segment orientation distribution, indirectly influencing the hydrodynamic contribution to the stress. Fiber curvature indeed leads to an increased number of contacts. For the simulation runs depicted in Fig. 5.5, the average number of contacts per fiber at steady state $\langle n_c \rangle_{ss}$ increases from 0.03 for $\theta^{eq} = 0$ to 1.12 for $\theta^{eq} = 0.3$.

The increase in the number of contacts per fiber as the fiber curvature increases arises from two features. The shorter rotation period of U-shaped fibers compared to that for straight fibers of the same aspect ratio leads to more opportunities for fiber contacts. U-shaped fibers also tend to sweep out a larger volume as they rotate, further increasing the probability of contacting other fibers. These effects of shape on the number of contacts per fiber should hold for any type of deviation from straight shapes (i.e., U-shaped, helical, etc.).

Figure 5.6 demonstrates the effect of changing μ^{stat} on the specific viscosity of fiber suspensions with two different equilibrium shapes [U-shaped: $(\theta^{eq}, \phi^{eq}) = (0.1, 0)$; and helical: $(\theta^{eq}, \phi^{eq}) = (0.8, 0.7)$] with all other parameters held constant $[(N_{seg}, nL^3, r_p, S^{eff}) = (5, 20, 75, 0.05)]$. The specific viscosity of suspensions of U-shaped fibers first increases as μ^{stat} increases, and then approaches a constant. The helical fiber suspensions show a more substantial change in specific viscosity as μ^{stat} increases. This may be attributed in part to an increase in the number of contacts. For a value of $\mu^{stat} = 5$, the number of contacts per fiber at steady state for the U-shaped fibers is $\langle n_c \rangle_{ss} = 0.08$, while for the helical fibers $\langle n_c \rangle_{ss} = 2.3$. The helical fibers also flocculate for $\mu^{stat} \geq 5$; flocculated suspensions show different rheological

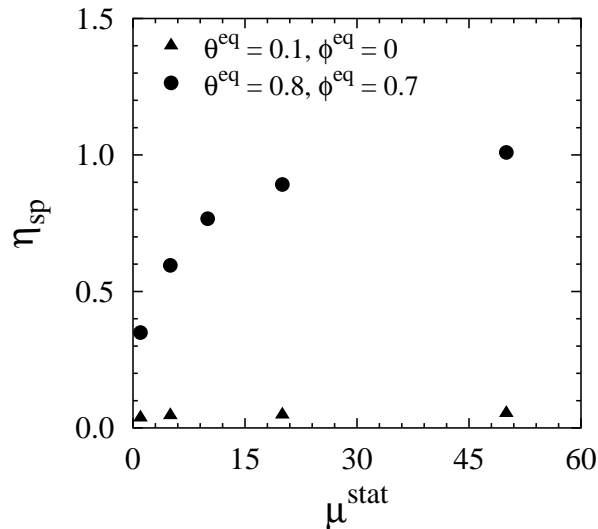


Figure 5.6: The specific viscosity as a function of the static coefficient of friction for suspensions of fibers that are U-shaped ($\theta^{\text{eq}} = 0.1, \phi^{\text{eq}} = 0$) and helical ($\theta^{\text{eq}} = 0.8, \phi^{\text{eq}} = 0.7$) after shearing for $\gamma = 1500$ with all other parameter constant ($N_{\text{seg}}, nL^3, r_p, S^{\text{rmeff}}$) = (5, 20, 75, 0.05).

behavior than homogenous suspensions as described in Section 5.3.4.

5.3.2 Effects of aspect ratio and stiffness

Suspensions of flexible, U-shaped fibers in simple shear flow were simulated at a fixed volume fraction, $\Phi = 0.003$, with three different aspect ratios, $r_p = 75, 100$, and 150 ($nL^3 = 21.5, 38.2$, and 85.9, respectively), and for various values of the dimensionless stiffness $S^{\text{eff}} = E_Y I / \eta_o \dot{\gamma} L^4$. All other parameter values were fixed at $(N_{\text{seg}}, \theta^{\text{eq}}, \phi^{\text{eq}}, \mu^{\text{stat}}) = (5, 0.1, 0, 20)$. The steady-state specific viscosity is plotted as a function of the dimensionless shear rate $\eta_o \dot{\gamma} / E_Y$ in Fig. 5.7(a) for the various values of r_p . All suspensions show shear thinning behavior over the range of dimensionless shear rates investigated. As the aspect ratio increases, the shear thinning behavior

becomes more pronounced. At large shear rates, the specific viscosities for all aspect ratios appear to collapse onto a single curve, suggesting that for sufficiently flexible fibers, the viscosity depends only on Φ , regardless of the aspect ratio. This is in contrast to results for suspensions of straight, rigid fibers where the viscosity scales with $nL^2d \propto \Phi/r_p$, regardless of the aspect ratio [84]. Figure 5.7(b) shows the first normal stress difference normalized by the fiber Young's modulus N_1/E_Y , as a function of $\eta_o\dot{\gamma}/E_Y$ for the same fiber aspect ratios discussed above. The first normal stress difference also increases with increasing aspect ratio, and the increase is more noticeable at lower shear rates. The dependence of the rheological properties on fiber aspect ratio and shear rate observed in the simulations is consistent with the experimental results of Goto et al. [34] for nylon fibers in glycerin and Kitano and Kataoka [50] for vinylon fibers in silicone oil.

The simulation results presented in Fig. 5.7(a) suggest that increasing the fiber flexibility (decreasing E_Y) will lead to smaller suspension viscosities. This apparently contradicts the experimental results of Goto et al. [34] which demonstrate that nylon fiber suspensions ($E_Y \approx 2$ GPa) have larger viscosities than glass fiber suspensions ($E_Y \approx 75$ GPa) at the same aspect ratio ($r_p = 300$) and concentration ($\Phi = 0.005$). This discrepancy may be explained by examining the equilibrium shapes of the nylon and glass fibers depicted in Goto et al. The glass fibers appear to be nearly straight at equilibrium, while the nylon fibers have permanent deformations at equilibrium. As described in Section 5.3.1, the differences in the rheological properties of the glass and nylon fibers observed by Goto et al. may be attributed to differences in fiber shape as well as differences in fiber stiffness.

We also performed simulations for suspensions of fibers with aspect ratio $r_p = 35$ in order to compare with the experimental results of Chaouche and Koch

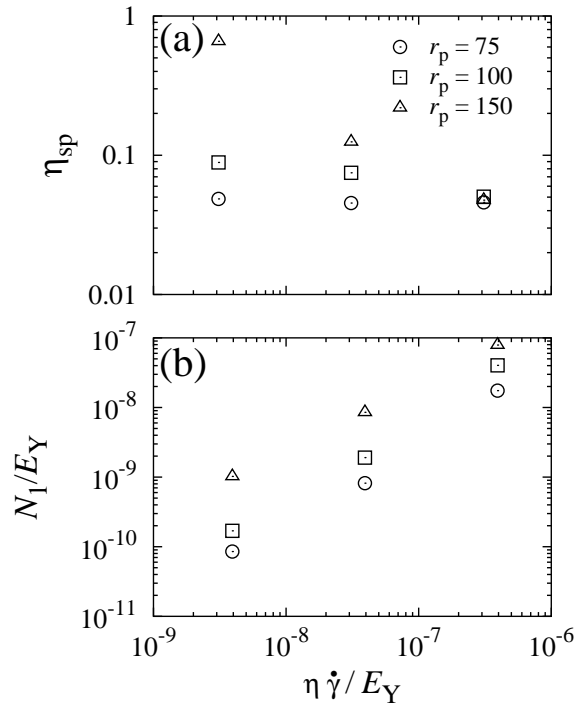


Figure 5.7: (a) Specific viscosity and (b) normalized first normal stress difference N_1/E_Y as a function of the dimensionless shear rate $\eta_o\dot{\gamma}/E_Y$ for fibers of various aspect ratios suspension and constant stiffness ($E_Y I$) after shearing for $\gamma = 1500$ ($N_{\text{seg}}, r_p, \Phi, \theta^{\text{eq}}, \phi^{\text{eq}}, \mu^{\text{stat}}$) = (5, 75, 0.003, 0.1, 0, 20).

[18] for nylon fibers in a silicone oil ($r_p = 36$, $\eta_o = 12.2$ Pa s). For this system at a shear rate of $\dot{\gamma} = 9.8$ s $^{-1}$, the effective stiffness is $S^{\text{eff}} \approx 0.8$. Under these conditions, the suspensions appeared to be essentially Newtonian. Simulation results for the steady-state specific viscosity as a function of concentration for suspensions of fibers of various shapes are compared with the experimental results of Chaouche and Koch [18] in Fig. 5.8. Results for suspensions of rigid rods [$(N_{\text{seg}}, S^{\text{eff}}, \theta^{\text{eq}}, \phi^{\text{eq}}, \mu^{\text{stat}}) = (1, \infty, 0, 0, 20)$] agree reasonably well with the experimental measurements, with deviations becoming more apparent as the concentration increases. As described in Section 5.3.1, friction does not significantly affect the results for straight fibers in the concentration range reported. If the fibers are made

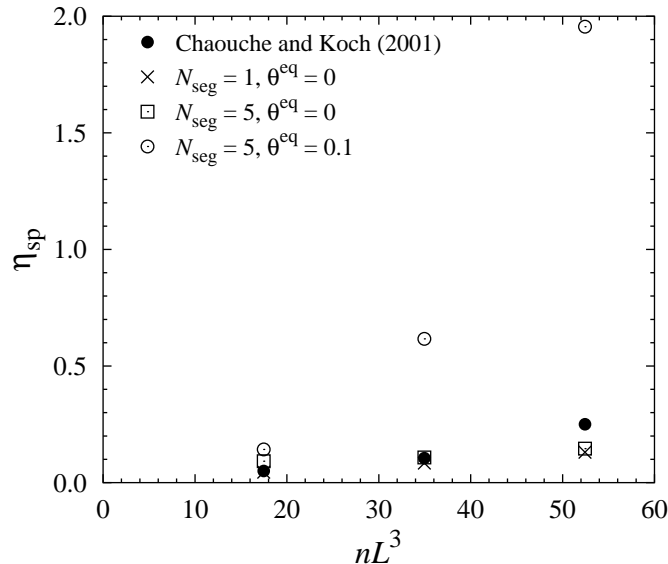


Figure 5.8: Specific viscosity as a function of concentration for shorter fiber suspensions ($r_p = 35$), using rigid fibers $(N_{\text{seg}}, S^{\text{eff}}, \mu^{\text{stat}}) = (1, \infty, 20)$, straight flexible fibers $(N_{\text{seg}}, S^{\text{eff}}, \theta^{\text{eq}}, \phi^{\text{eq}}, \mu^{\text{stat}}) = (5, 0.7, 0, 0, 20)$, and slightly deformed flexible fibers $(N_{\text{seg}}, S^{\text{eff}}, \theta^{\text{eq}}, \phi^{\text{eq}}, \mu^{\text{stat}}) = (5, 0.7, 0.1, 0, 20)$ compared with the experimental data of Chaouche and Koch [18].

flexible and inherently straight with a dimensionless stiffness similar to that of the experimental system $[(N_{\text{seg}}, S^{\text{eff}}, \theta^{\text{eq}}, \phi^{\text{eq}}, \mu^{\text{stat}}) = (5, 0.7, 0, 0, 20)]$, there is only a slight improvement in predicting the specific viscosity at large concentrations. Simulations with slightly U-shaped, flexible fibers $[(N_{\text{seg}}, S^{\text{eff}}, \theta^{\text{eq}}, \phi^{\text{eq}}, \mu^{\text{stat}}) = (5, 0.7, 0.1, 0, 20)]$ overpredict η_{sp} by nearly an order of magnitude. These results suggest that the small discrepancy between the experimental results and the predictions for suspensions of straight fibers may be accounted for by a very small deviation of the shape (from perfectly straight) of the fibers employed in the experiments.

5.3.3 Yield stress

Fibers in suspension can form networks if the concentration is sufficiently large that each fiber experiences multiple contacts with other fibers. The networks exhibit

mechanical strength and visco-elastic behavior [87, 91]. The network strength is controlled by the cohesive nature of the contact points. Kerekes et al. [47] proposed that the cohesive force that imparts strength to the network is caused by friction generated by normal forces at points of contact between elastically bent fibers. Bennington et al. [12] derived an expression for the yield stress of a suspension of elastically interlocked fibers,

$$\sigma_0 = \alpha\Phi^3, \quad (5.13)$$

where σ_0 is the yield stress and the coefficient α is a function of the fiber Young's modulus and aspect ratio. Bennington et al. measured the yield stress for a variety of suspensions of wood and synthetic fibers, and found that the yield stress scaled with the volume fraction as $\sigma_0 \sim \Phi^\beta$ where β ranged from 2.5–3.5, in reasonable agreement with their model.

We performed simulations in simple shear flow to determine the yield stress of fiber suspensions at various volume fractions with $(N_{\text{seg}}, r_p, \theta^{\text{eq}}, \phi^{\text{eq}}, \mu^{\text{stat}}) = (5, 75, 0.1, 0, 20)$. The effective stiffness was varied to obtain the dimensionless shear stress ($\sigma_{xz}L^4/E_Y I$) as a function of dimensionless shear rate ($1/S^{\text{eff}} \propto \dot{\gamma}$), which is plotted for different volume fractions in Fig 5.9(a). The data exhibit roughly Bingham-like behavior, with the yield stress varying linearly with shear rate and a nonzero intercept. The apparent dimensionless yield stress at each volume fraction was determined by fitting the data to a straight line and equating the intercept at $1/S^{\text{eff}} = 0$ to the dimensionless (dynamic) yield stress. The yield stresses obtained in this manner are plotted as a function of volume fraction in Fig. 5.9(b). The simulated yield stresses scale with volume fraction as $\sigma_0 \sim \Phi^{2.75 \pm 0.8}$, and thus the exponent is in the same range as the values obtained experimentally by Bennington et al. [12].

The predicted value of α does not agree as well with that obtained experimen-

tally. Using the parameter values for nylon fibers $r_p \approx 76$, $E_Y I \approx 3.5 \times 10^{-10} \text{ N} \cdot \text{m}^2$, and $L \approx 3.45 \text{ mm}$ [12], the simulations predict a value of $\alpha \approx 6 \times 10^6 \text{ N/m}^2$, whereas Bennington et al. measured $\alpha \approx 10^5 \text{ N/m}^2$. The discrepancy between the simulated and experimentally measured values of α may be explained by a variety of effects. The fiber shapes and values of the coefficients of friction employed in the simulations certainly differ from those of the experimental systems, and as discussed in Section 5.3.1, we expect the stresses to depend fairly sensitively on these parameter values. Unfortunately, the fiber shapes and coefficients of friction for the systems employed in the experiments were not reported.

The network model of Bennington et al. [12] suggests that the yield stress should vary linearly with the fiber Young's modulus. The same conclusion is obtained for the simulations reported here, since the yield stress scaled by the Young's modulus is obtained by extrapolating the dimensionless shear stress to $1/S^{\text{eff}} \rightarrow 0$. The dimensionless yield stress is thus independent of the Young's modulus, and the dimensional yield stress varies linearly with the Young's modulus. Bennington et al., however, did not observe this scaling in their experiments. This discrepancy may also be related to the fiber properties. Bennington et al. obtained results for different fiber Young's moduli by employing different types of wood and synthetic fibers. Inspection of the fiber images presented in their paper reveals that the fiber shapes varied, sometimes quite significantly, from one system to another. Thus the variation of the yield stresses from one system to another may be due to differences in fiber shape as well as differences in Young's moduli, and thus the predicted scaling with stiffness alone is not expected to hold.

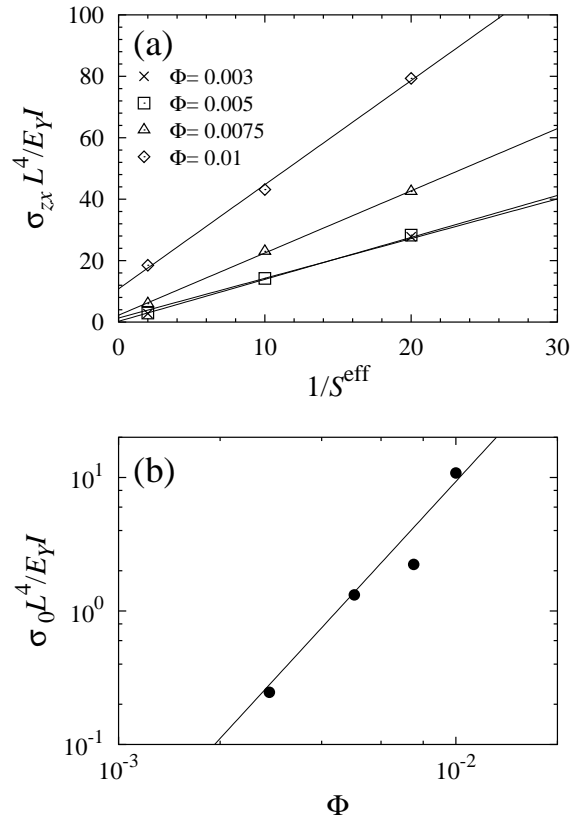


Figure 5.9: (a) Shear stress (σ_{xz}) as a function of shear rate for simulations of fiber suspensions at different volume fractions, and (b) the extrapolated apparent yield stress (σ_0) from (a) as a function of volume fraction; $(N_{\text{seg}}, r_p, \theta^{\text{eq}}, \phi^{\text{eq}}, \mu^{\text{stat}}) = (5, 75, 0.1, 0, 20)$.

5.3.4 Rheology in flocculated suspensions

Under the appropriate conditions, fiber networks subjected to shear flow develop into a heterogeneous or flocculated state. Flocculation can occur when the fibers are sufficiently stiff and interact with a sufficiently large coefficient of friction, even in the absence of attractive interfiber forces (see Chapter 3 and [73, 74, 75]). Fibers within flocs are caught in elastically strained configurations due to fiber bending and friction forces at the contact points. A flocculated state in a simulated fiber

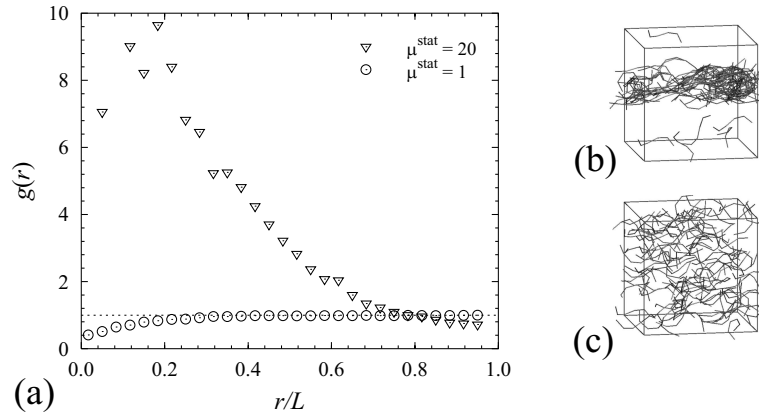


Figure 5.10: Pair distribution function for the fiber centers-of-mass for a flocculated suspension ($\mu^{\text{stat}} = 20$) and a homogeneous suspension ($\mu^{\text{stat}} = 1$) after shearing for $\gamma = 1500$; $(N_{\text{seg}}, r_p, nL^3, S^{\text{eff}}, \theta^{\text{eq}}, \phi^{\text{eq}}) = (5, 75, 15, 0.05, 0.1, 0)$.

suspension can be characterized by the pair distribution function, $g(r)$, where r is the separation between fiber centers-of-mass. Pair distribution functions for two fiber suspensions after shearing to steady state (strain $\gamma = 1500$) are plotted in Fig. 5.10(a). The parameter values for the two simulations are the same $[(N_{\text{seg}}, r_p, nL^3, S^{\text{eff}}, \theta^{\text{eq}}, \phi^{\text{eq}}) = (5, 75, 15, 0.05, 0.8, 0.7)]$, except for the values of the coefficient of friction ($\mu^{\text{stat}} = 1$ and $\mu^{\text{stat}} = 20$). For $\mu^{\text{stat}} = 1$, fibers have an equal probability of having their centers-of-mass at any separation. This resulting suspension structure is homogeneous, as illustrated pictorially in Fig. 5.10(c). For sufficiently large values of μ^{stat} , the suspension flocculates [Fig. 5.10(b)] and there is a high probability of finding the fiber centers-of-mass at small separations.

Flocculation changes the rheological properties of a suspension. Figure 5.11 shows the specific viscosity as a function of $1/S^{\text{eff}}$ ($\propto \dot{\gamma}$) for fiber suspensions with the same concentration and aspect ratio ($nL^3 = 15$ and $r_p = 75$), but with different shapes and coefficients of friction. Results labelled (A) are for simulations with helical fibers $[(\theta^{\text{eq}}, \phi^{\text{eq}}) = (0.8, 0.7)]$ with $\mu^{\text{stat}} = 20$, results labelled (B) are for simulations with the same helical fiber shape and $\mu^{\text{stat}} = 1$, and results labelled (C) are for runs

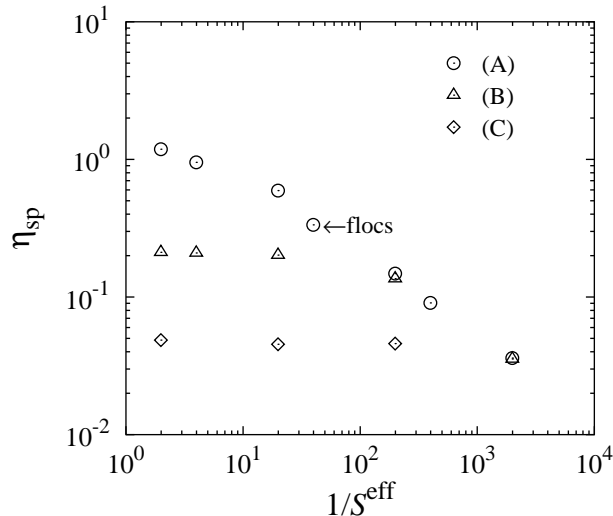


Figure 5.11: Specific viscosity versus the reciprocal of the effective stiffness for suspensions of equivalent concentration ($nL^3 = 15$) and aspect ratio ($r_p = 75$) in which (A) flocculates and (B) and (C) remain homogeneous: (A) $(\theta^{\text{eq}}, \phi^{\text{eq}}, \mu^{\text{stat}}) = (0.8, 0.7, 20)$; (B) $(\theta^{\text{eq}}, \phi^{\text{eq}}, \mu^{\text{stat}}) = (0.8, 0.7, 1)$; (C) $(\theta^{\text{eq}}, \phi^{\text{eq}}, \mu^{\text{stat}}) = (0.1, 0, 20)$.

with U-shaped fibers $[(\theta^{\text{eq}}, \phi^{\text{eq}}) = (0.1, 0)]$ and $\mu^{\text{stat}} = 20$. Systems (B) and (C) remain homogeneous for all values of S^{eff} . The specific viscosity exhibits a low shear rate plateau, with shear thinning behavior as $1/S^{\text{eff}}$ increases. The value of η_{sp} at small values of $1/S^{\text{eff}}$ is larger for system (B) than run for (C), because the fiber equilibrium shapes in system (B) deviate more from perfectly straight. Thus, fiber segments in system (B) are never all aligned with the flow direction, which leads to a larger hydrodynamic contribution to the stress compared to the slightly deformed fibers in system (C) which can approximately align with the direction of flow. The helical fibers also experience more interfiber contacts, further increasing the stress.

System (A) remains homogeneous at large values of $1/S^{\text{eff}}$ (high shear rates), but for $1/S^{\text{eff}} \lesssim 400$ the suspension flocculates at steady state (following Schmid et al. [75], we define a suspension as flocculated when $g(r = 0.01L) \geq 3$). Shear

thinning behavior is observed over the entire range of $1/S^{\text{eff}}$. The specific viscosity is also much larger in the flocculated state at small values of $1/S^{\text{eff}}$ because there are many frictional contacts that give the network mechanical strength. Chen et al. [19] observed large jumps in the shear stress for wood and nylon fiber suspensions when they flocculated at small shear rates. The simulation results depicted in Fig. 5.11 do not exhibit large jumps in the shear stress over the range of dimensionless shear rates investigated, but may do so at smaller shear rates.

At large values of $1/S^{\text{eff}}$, all of the systems described in Fig. 5.11 approach the same value for η_{sp} , where the suspension structures are homogeneous. This is consistent with the results of Chen et al. [19] in which they observed that suspensions dispersed from a flocculated state as the shear rate increased. Goto et al. [34] also reported that fibers of various Young's moduli and shape tended to approach the same viscosity at high shear rates (for equivalent concentrations), where the suspensions behaved essentially as a Newtonian fluids. This is consistent with the simulation results reported here, and corresponds to a limiting state where viscous forces dominate over fiber elasticity and interfiber forces.

5.4 Conclusions

We have employed particle-level simulations to probe the effects of various features of flexible fibers and their interactions on the rheology of fiber suspensions in simple shear flow. The fibers are modeled as linked, rigid spherocylinders connected by ball and socket joints. The fiber segments are acted upon by short-range repulsive forces and interfiber static friction, but hydrodynamic interactions are ignored. Since we are primarily interested in situations where there are significant numbers of inter-

fiber contacts, hydrodynamic interactions are likely of secondary importance [35, 84]. Comparisons with previous simulations and experiments show reasonable agreement.

The viscosity of fiber suspensions is influenced strongly by the particle shape and interfiber friction. Relatively small deviations in the particle shape from perfectly straight can have $O(1)$ effects on the specific viscosity. Interfiber friction impacts the viscosity more for suspensions of nonstraight fibers than for suspensions of straight fibers. These results suggest that these features should be quantified in experimental studies.

Fiber flexibility results in shear thinning behavior. This is caused by a competition between hydrodynamic forces (which attempt to deform the fibers) and fiber elasticity (which attempts to retain the equilibrium fiber shapes), characterized by a dimensionless effective stiffness, $S^{\text{eff}} = E_Y I / \eta_o \dot{\gamma} L^4$, where E_Y is the Young's modulus of the fiber material, I is the cross-sectional area moment, η_o is the suspending fluid viscosity, $\dot{\gamma}$ is the shear rate, and L is the fiber length; $1/S^{\text{eff}}$ can be interpreted as a dimensionless shear rate. Shear thinning proceeds from a low shear rate plateau to a shape-independent high shear rate limit. The height of the low shear rate plateau depends on the fiber shape and the coefficient of friction.

Suspensions that flocculate show shear thinning over wider ranges of shear rates. However, the high shear rate behavior of these systems is the same as that of suspensions that do not flocculate (at the same volume fraction). Results for the concentration dependence of the apparent yield stress agree reasonably well with experiments. Effects of fiber shape and friction make quantitative comparison with existing experimental data difficult.

Chapter 6

Handsheet formation and mechanical testing via fiber-level simulations

6.1 Introduction

Understanding the characteristics that give strength to a fiber network is important, for example, in controlling wet web formation on a paper machine and making paper with the desired physical properties. Fiber properties, such as the shape, length, and flexibility, and suspension characteristics, such as fiber interactions and flow history, influence the mechanical properties of the network. Understanding these relationships can be useful for designing and optimizing suspension compositions and processes for making paper and fiber-reinforced composites. In this chapter, we employ the fiber-level simulation method discussed in Chapter 2 to probe the relationships between fiber properties and interactions, and the mechanical properties of planar fiber networks subjected to elongational deformations.

Fiber characteristics affect both the formation of a planar fiber network and the resultant tensile strength. Mohlin et al. [60] examined the effect of shape on the tensile strength of softwood fiber handsheets. They characterized fiber shape in terms of curl, which is related to the ratio of the end-to-end distance and the contour length, and the number of defects (i.e., kinks, twists, microcompressions, etc.) per fiber. Mohlin et al. observed that the network tensile strength was larger for handsheets composed of straighter fibers or fibers with fewer defects. Seth [77] observed that as the fiber length increased and the coarseness (mass per unit length of fiber) decreased, the tensile strength also increased in wet webs. This was attributed to the fact that longer fibers experience more contacts per fiber, and it is the contacts that give the network strength. Fibers that are less coarse have thinner walls that allow them to collapse and bond over larger areas.

The fiber shape, length, and coarseness are all affected by refining which decreases the freeness, or drainability, of the fiber network. In general, refining leads to fiber shortening, increased external fibrillation, equilibrium shape changes, and fiber collapse [53]. Thus, networks formed from refined fibers have greater tensile strengths than unrefined fibers [53, 62]. Forgacs et al. [33] also observed that the tensile strength of wet webs increased with decreasing freeness, which they attributed to the importance of friction forces between contacting fibers.

Theoretical efforts have also investigated how fiber network properties depend on fiber characteristics. Meyer and Wahren [58] modelled concentrated suspensions of fibers as elastically-interlocked networks, where each fiber is in contact with at least three others. They determined that the strength of a network depends on the fiber aspect ratio $r_p = L/d$ (L is the fiber length and d is the diameter), volume fraction Φ , and fiber Young's modulus E_Y . Networks can be formed from flowing

fiber suspensions, in which fibers come to rest in elastically strained configurations. Soszynski and Kerekes [81, 82] reasoned that elastic fiber interlocking results from friction forces acting at the contacts between elastically deformed fibers, that maintain the mechanical integrity of the network. They demonstrated the importance of fiber elasticity in the strength of nylon flocs, by showing that flocs in which the elastic stresses were reduced by heating could be dispersed more easily than never-heated flocs.

Experimental investigation of fiber networks can be supplemented with particle-level simulations of idealized suspensions, in which the effects of individual fiber properties and interactions (i.e., shape, flexibility, size, and friction) can be systematically investigated, which is challenging to accomplish in laboratory experiments. The equations of motion for each particle are solved numerically, subject to the forces and torques identified, in order to evolve the particle positions and orientations in time, and thus produce a prediction of the network microstructure and mechanical properties. Numerous simulation studies have focused on predicting the rheology of rigid fiber suspensions [35, 84, 98]. Flexible fibers were simulated by Yamamoto and Matsuoka [93, 94] who modelled fibers as chains of rigid spheres connected through springs, with potentials to mimic resistance to bending and twisting. Ross and Klingenberg [71] modelled flexible fibers as inextensible chains of rigid prolate spheroids connected through ball and socket joints. This model can represent large aspect ratio fibers with relatively few bodies, thus reducing computational cost and facilitating simulation of concentrated suspensions. Schmid et al. [75] extended this method, modelling flexible fibers as chains of spherocylinders connected by ball and socket joints, that interact via short-range repulsive forces as well as interfiber friction. These simulation studies illustrated the importance of fiber equilibrium shape,

flexibility, and frictional interactions in determining flocculation behavior.

In this chapter, we modify the method utilized by Schmid et al. [75] (see Chapter 2) to investigate the relationships between fiber properties and interactions and the mechanical properties of planar networks of idealized fibers. The fiber model and simulation method are briefly described in Section 6.2. Fibers are modelled as flexible chains of rigid spherocylinders that interact through a variety of forces. Fiber networks are formed by simulating the compression of a fiber suspension over a screen permeable only to the suspending fluid. The fiber networks thus formed are subjected to a constant straining in the plane of the network, and the tensile force required is calculated. A device and experimental method for measuring the mechanical response of fiber networks (e.g., handsheet samples) for deformations similar to that employed in the simulations are also briefly described. In Section 6.3, we present an example of the mechanical response to the elongation of a handsheet sample. Simulations of planar network elongation exhibit features similar to that observed experimentally. We then employ the simulations to illustrate the relationships between the mechanical properties of planar fiber networks and such fiber characteristics as shape, length, flexibility, as well as the frictional interactions between fibers. Although trends produced by the simulations agree qualitatively with those observed experimentally, quantitative differences are significant. The differences, as well as possible explanations and methods for resolving discrepancies, are discussed in Section 6.4. The main conclusions from this chapter are summarized in Section 6.5.

6.2 Methods

6.2.1 Fiber model and simulations

Flexible fibers are modelled as neutrally-buoyant chains of linked rigid bodies immersed in a Newtonian liquid. The model includes realistic features such as fiber flexibility, irregular equilibrium shapes, and mechanical contact forces between fibers. The model and simulation method are similar to that employed by Schmid et al. [75] and are described in more detail in Chapter 2.

Each fiber in the suspension is represented by N_{seg} rigid cylinders (length 2ℓ , radius b) with hemi-spherical end caps, connected end-to-end by ball and socket joints (Fig. 6.1). The motion of the fiber segments is described by Newton's laws of motion in which we neglect fiber inertia. The force balance on a fiber segment i includes contributions from hydrodynamic drag ($\mathbf{F}_i^{\text{hyd}}$), mechanical contact forces ($\mathbf{F}_{ik}^{\text{con}}$), externally applied forces (\mathbf{F}_i^p), and forces at each joint that maintain the segment connectivity (\mathbf{X}_i),

$$\mathbf{F}_i^{\text{hyd}} + \mathbf{F}_i^p + \mathbf{X}_{i+1} - \mathbf{X}_i + \sum_k^{N_{C_i}} \mathbf{F}_{ik}^{\text{con}} = \mathbf{0}, \quad (6.1)$$

where N_{C_i} is the number of contacts on fiber segment i . The torque balance on fiber segment i includes similar contributions with the addition of a restoring torque at each joint (\mathbf{Y}_i),

$$\mathbf{T}_i^{\text{hyd}} + \mathbf{Y}_{i+1} - \mathbf{Y}_i + \nu_i \mathbf{p} \times \mathbf{F}_i^p + \ell \mathbf{p}_i \times [\mathbf{X}_{i+1} + \mathbf{X}_i] + \sum_k^{N_{C_i}} [\mathbf{G}_{ik} \times \mathbf{F}_{ik}^{\text{con}}] = \mathbf{0}, \quad (6.2)$$

where $\mathbf{T}_i^{\text{hyd}}$ is the hydrodynamic torque, \mathbf{p}_i is the orientation vector of the segment, ν_i is the distance from the segment center to the location of the externally applied force, and \mathbf{G}_{ik} is a vector from the center of segment i to the point of contact with body k .

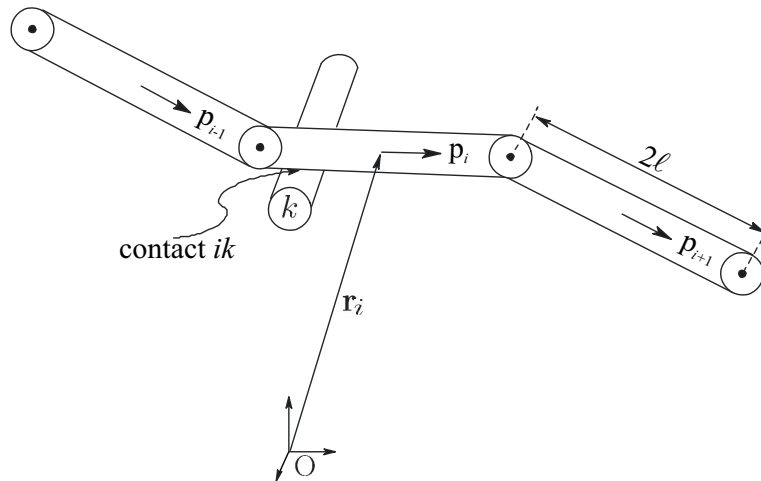


Figure 6.1: Schematic diagram of a model fiber composed of rigid spherocylinders linked by ball and socket joints. Here, segment i is in contact with segment k from another fiber.

In this model, hydrodynamic interactions are neglected, and the hydrodynamic force and torque are approximated as that on an isolated body, $\mathbf{F}_i^{\text{hyd}} = \mathbf{A}_i \cdot [\mathbf{U}_i^\infty - \dot{\mathbf{r}}_i]$ and $\mathbf{T}_i^{\text{hyd}} = \mathbf{C}_i \cdot [\boldsymbol{\Omega}_i^\infty - \boldsymbol{\omega}_i] + \tilde{\mathbf{H}}_i : \mathbf{E}^\infty$, where the resistance tensors \mathbf{A}_i , \mathbf{C}_i , and $\tilde{\mathbf{H}}_i$ for the spherocylinder segments are approximated by the resistance tensors of a prolate spheroid with an equivalent aspect ratio $r_e = 0.7r_p/N_{\text{seg}}$ (see Chapter 2). The ambient velocity \mathbf{U}_i^∞ , angular velocity $\boldsymbol{\Omega}_i^\infty$, and rate of strain tensor \mathbf{E}^∞ are evaluated at the center-of-mass of each segment. The segment translational and angular velocities are $\dot{\mathbf{r}}_i$ and $\boldsymbol{\omega}_i$, respectively.

In this study, we examine the limiting situation in which fiber motion is dominated by interactions with other fibers and externally applied forces, and not influenced by an ambient flow (e.g., for very slow ambient flows within networks). Thus fiber segments will still experience hydrodynamic drag, although \mathbf{U}_i^∞ , $\boldsymbol{\Omega}_i^\infty$, and \mathbf{E}^∞ are set to zero.

The restoring torque \mathbf{Y}_i describes the resistance of the elastic fibers to bending and twisting. The bending and twisting components of this torque are assumed

to be linear in the difference between the bending and twisting angles (θ_i and ϕ_i respectively) and their equilibrium values (θ_i^{eq} and ϕ_i^{eq}),

$$|\mathbf{Y}_i| = \kappa_b(\theta_i - \theta_i^{\text{eq}}) + \kappa_t(\phi_i - \phi_i^{\text{eq}}), \quad (6.3)$$

where κ_b and κ_t are the bending and twisting constants of the fiber. The bending constant is related to the stiffness of the fiber material by $\kappa_b = E_Y I / 2\ell$, where E_Y is the Young's modulus, and $I \equiv \pi b^4 / 4$ is the area moment. The twisting constant is set to $\kappa_t = 0.67\kappa_b$ in this study, equal to that of a linearly elastic circular cylinder with a Poisson's ratio of 0.5. The fiber flexibility is characterized by a single parameter which we call the effective stiffness $S^{\text{eff}} \equiv E_Y I / \eta_o \dot{\gamma} L^4$, where η_o is the suspending fluid viscosity, $\dot{\gamma}$ is the characteristic deformation rate (described further below), and L is the total fiber length.

The fiber segments remain connected by applying a constraint for each joint,

$$\mathbf{r}_i + \ell \mathbf{p}_i = \mathbf{r}_{i+1} - \ell \mathbf{p}_{i+1}, \quad (6.4)$$

where \mathbf{r}_i is the position of the center of segment i . These constraint equations allow for the solution of the constraint forces at each joint \mathbf{X}_i . Since the segments are rigid and remain connected, the fibers are inextensible (but still flexible).

Fibers experience mechanical contacts with other fibers in the suspension. Two fiber segments i and k are considered to be in contact if the separation between their surfaces, h_{ik} , is less than $0.33b$. The force that results from each contact is decomposed into two components—a force in the normal direction of the contact ($\mathbf{F}_{ik}^{\text{N}}$) and a frictional force ($\mathbf{F}_{ik}^{\text{fric}}$) in the plane of the contact. The purely repulsive, short-range normal force exerted on body i by body k is modelled $\mathbf{F}_{ik}^{\text{N}} = -F \exp[-ah_{ik}] \mathbf{n}_{ik}$, where \mathbf{n}_{ik} is the unit normal vector directed from body i to body k , $F = 900\pi\eta_o\ell b\dot{\gamma}$ is the magnitude of the repulsive force, and $a = 20/b$. The friction force is determined by

the constraint of no relative motion in the plane of contact,

$$\begin{pmatrix} \Delta \mathbf{u}_{ik} \cdot \mathbf{e}_1^{\text{loc}} \\ \Delta \mathbf{u}_{ik} \cdot \mathbf{e}_2^{\text{loc}} \\ \mathbf{F}_{ik}^{\text{fric}} \cdot \mathbf{n}_{ik} \end{pmatrix} = \mathbf{0}, \quad (6.5)$$

where $\Delta \mathbf{u}_{ik}$ is the relative velocity between bodies i and k at the point of contact, and the plane of contact is defined by the vectors $\mathbf{e}_1^{\text{loc}}$ and $\mathbf{e}_2^{\text{loc}}$. The calculated friction force is then subjected to a Coulombic friction law of the form

$$\begin{aligned} |\mathbf{F}_{ik}^{\text{fric}}| &\leq \mu^{\text{stat}} |\mathbf{F}_{ik}^{\text{N}}| \Rightarrow \text{contact remains intact} \\ &> \mu^{\text{stat}} |\mathbf{F}_{ik}^{\text{N}}| \Rightarrow \mathbf{F}_{ik}^{\text{fric}} = \mu^{\text{kin}} |\mathbf{F}_{ik}^{\text{N}}| \frac{\Delta \mathbf{u}_{ik}}{|\Delta \mathbf{u}_{ik}|}, \end{aligned} \quad (6.6)$$

where μ^{stat} and μ^{kin} are the static and kinetic coefficients of friction.

Network formation is modelled using a piston of mass M which falls in the $-z$ direction under the force of gravity, pushing the fibers it contacts downward toward a smooth, planar screen permeable only to the suspending liquid. The motion of the piston in the z direction is governed by Newton's equation of motion,

$$M \frac{d^2 z_{\text{pl}}}{dt^2} = -Mg + \sum_{i=1}^{N_{c,\text{pl}}} F_{z,i}^{\text{con}}, \quad (6.7)$$

where z_{pl} is the position of the piston, g is the acceleration of gravity, $F_{z,i}^{\text{con}}$ is the (frictionless) contact force in the z direction caused by the interaction with segment i , and $N_{c,\text{pl}}$ is the number of contacts with the piston. We acknowledge that this physical model of network formation does not accurately represent the formation of real handsheets; it is used here simply as a method for obtaining planar fiber networks. For the network formation process, the characteristic deformation rate is defined $\dot{\gamma} \equiv \sqrt{g/b}$.

Elongation of the planar networks is modelled by specifying constant velocities for fiber segments that intersect planes at opposite faces of the simulation box, as

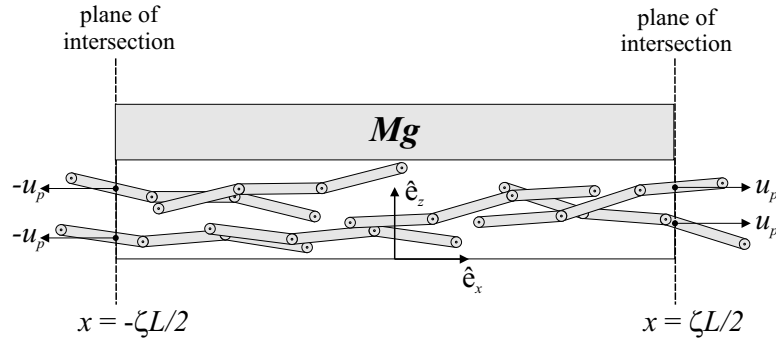


Figure 6.2: Schematic diagram illustrating the simulation cell after the formation of the planar network, and the location of the planes containing the fibers that experience external forces to simulate elongation.

depicted schematically in Fig. 6.2. Referring to this figure for elongation in the $\pm x$ direction, the constraint for a fiber segment i intersecting one of the x faces of the box is

$$(\dot{\mathbf{r}}_i + \nu_i \boldsymbol{\omega} \times \mathbf{p}_i) \cdot \hat{\mathbf{e}}_x = \pm u_p, \quad (6.8)$$

where u_p is the speed at which the sample faces are displaced, and the positive or negative sign is chosen for fibers intersecting the face at $x = \zeta L/2$ or $-\zeta L/2$, respectively. These constraints permit the evaluation of the corresponding externally applied forces (\mathbf{F}_i^p) introduced in Eq. (6.1). For elongation, the characteristic deformation rate employed in the definition of S^{eff} is $\dot{\gamma} = u_p/b$. The tensile force required to maintain this motion is

$$T = \frac{1}{2} \left(\sum_{\text{right face}} \mathbf{F}_i^p - \sum_{\text{left face}} \mathbf{F}_i^p \right) \cdot \mathbf{e}_x. \quad (6.9)$$

The equations of motion and the constraint equations for all of the fiber segments in the suspension can be expressed as a system of differential algebraic equa-

tions (DAEs) for the unknown coordinates and constraint forces,

$$\begin{aligned}
 \dot{\mathbf{q}} - \mathbf{F}(\mathbf{q}, \boldsymbol{\lambda}) &= \mathbf{0}, \\
 \boldsymbol{\Psi}(\mathbf{q}) &= \mathbf{0}, \\
 \boldsymbol{\Xi}(\mathbf{q}, \dot{\mathbf{q}}, \boldsymbol{\lambda}) &= \mathbf{0}, \\
 \boldsymbol{\Theta}(\mathbf{q}, \dot{\mathbf{q}}) &= \mathbf{0},
 \end{aligned} \tag{6.10}$$

where \mathbf{q} is a vector containing the generalized coordinates of each fiber segment (positions and orientations), and $\boldsymbol{\lambda}$ is a vector containing all the constraint forces (\mathbf{X} and \mathbf{F}^{fric}) in the suspension. If the segment orientations are represented by Euler parameters [92], there are $7N_{\text{fib}}N_{\text{seg}}$ equations of motion to be solved. The inextensibility constraint [Eq. (6.4)], represented by the vector $\boldsymbol{\Psi}$, is composed of $3N_{\text{fib}}(N_{\text{seg}} - 1)$ constraint equations that depend on only the positions and orientations. The $3N_C$ friction constraint equations [Eq. (6.5)] are contained in $\boldsymbol{\Xi}$, where N_C is the total number of contacts in the system. The tensile force constraints [Eq. (6.8)] are represented by the vector $\boldsymbol{\Theta}$.

Simulations of planar network formation are performed by randomly placing fibers in a simulation cell with dimensions $\zeta L \times \zeta L$ at the base (i.e., xy planar dimensions of the desired network; $\zeta = 2$ for all results reported here), and a height of $2\zeta L$ in the z -direction. The solid piston is initially located at the top ($z = 2\zeta L$), the semipermeable screen is located at the bottom ($z = 0$), and periodic boundary conditions are applied in the x and y directions. The system of DAEs [Eq. (6.10)] is solved numerically for the motion of the fibers and the piston (in the absence of the tensile force constraint, $\boldsymbol{\Theta}$). The suspending fluid is effectively “squeezed” out, and a network is formed of the desired thickness. The piston mass M is chosen such the final volume fraction of the network is $\Phi = 0.05 \pm 0.005$. This produces a planar fiber network. For the results presented, the “sheets” formed were approximately 10–15 fiber diameters in thickness. Once the network is formed, it is relaxed with the piston

fixed before beginning elongation.

Simulation of the the network elongation is then performed by first identifying the fiber segments that intersect the planes $x = \pm\zeta L/2$, for which the tensile force constraints are applied [Eq. (6.8)]. The system of DAEs [Eq. (6.10)] is solved numerically for the motion of the fibers as the network is elongated (with the piston position fixed). The tensile force T is evaluated via Eq. (6.9) to determine the force as a function of deformation. An approximate solution method was developed to solve the system equations, the details of which are described in Chapter 2.

6.2.2 Experiments

A miniature tensile testing device was constructed, as shown in Fig. 6.3, to measure the tensile force exerted on a fiber sheet sample, and to visualize deformation of the network structure as the sheet is elongated. The device and experimental method are summarized briefly here, and will be described in more detail in a future publication [76]. The sample was held in place horizontally by two clamps. One clamp was attached to a 50 gram load cell, and the other was attached to a lead screw driven at a constant speed of $2u_p \approx 3$ mm/min. The pulp employed was unrefined and bleached softwood market pulp screened in a Bauer-McNett classifier. The fractions from the 25 mesh screens were collected for experiments. Handsheets of dimensions 5 cm \times 5 cm were formed in a sheet mold, in which a dilute fiber suspension was drained over a 400 mesh nylon screen screen. The resulting network was air dried. The formed sheets tested had a basis weight of approximately 10 g/m². The sheets were cut into strips with a width $w = 3.2$ mm, and the exposed length between the clamps was $x_o = 8$ mm. A microscope with a CCD camera was mounted above the sample to capture images as the sample elongated (using the program UTHSCSA ImageTool

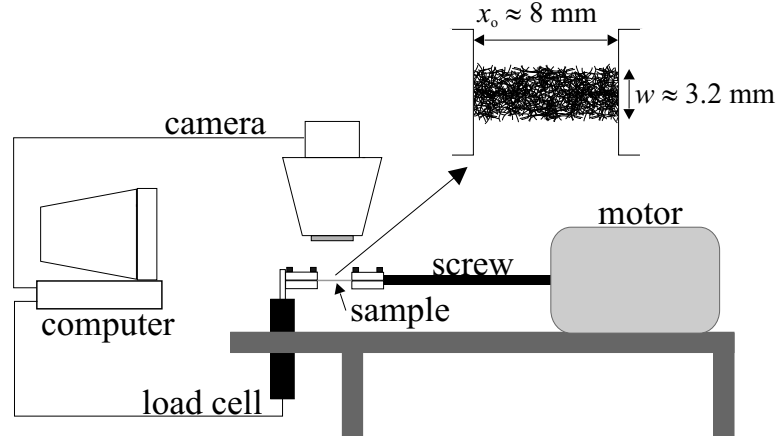


Figure 6.3: Schematic diagram of the tensile apparatus developed to test small planar fiber networks.

available free via anonymous FTP from <ftp://maxrad6.uthscsa.edu>).

6.3 Results and discussion

6.3.1 Experiments on small fiber sheets

The tensile force T is plotted as a function of elongational deformation $\Delta x/L$ [where Δx is the change in length between clamps and L is the average fiber length ($L \approx 2.5$ mm)] for a typical handsheet sample in Fig. 6.4. The tensile force initially increases linearly with deformation, indicative of a linear elastic response. The tensile force then begins to vary nonlinearly with deformation, before passing through a maximum. For deformations beyond the linear region, the tensile force fluctuates significantly. The decrease in tensile force with deformation after the maximum proceeds more slowly than the initial linear increase.

The images of the deformation process reveal several distinct processes associated with the features in Fig. 6.4. When the deformation commences, fibers start to align in the direction of the extension, and some of the fibers bend. Within the lin-

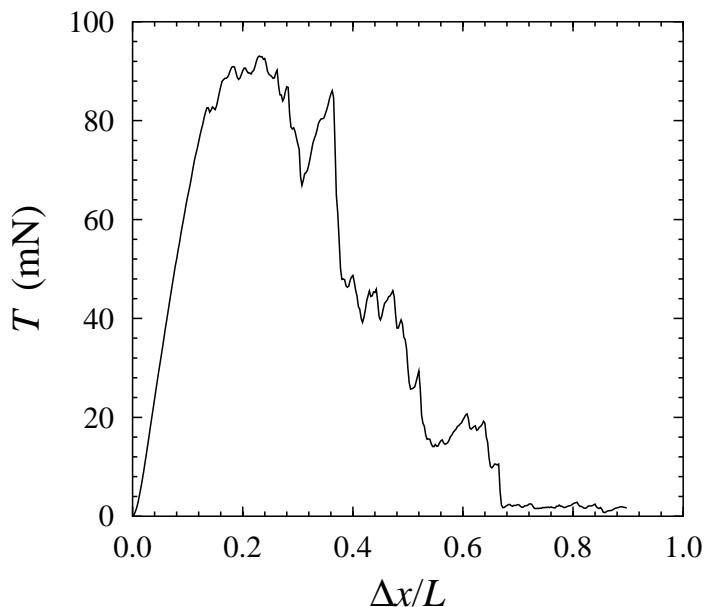


Figure 6.4: Tensile force as a function of deformation for a typical handsheet as described in the text.

ear portion of the tension–deformation curve, fiber contacts appear to remain intact. Further deformation causes contacts to break, after which fibers often rapidly spring back to form new contacts with other fibers. These contact breaking and reforming processes likely give rise to the tensile force fluctuations (contacts formed initially may be bonds, and may differ substantially from contacts reformed at larger deformations). The maximum tensile force is associated with a relatively sudden release of numerous contact points, and fibers are not observed to rupture. At deformations beyond that corresponding to the maximum tensile force, we observed small clusters of fibers that break contacts, and the fibers are simply pulled from the sample. Some fibers that are bent during the elongation are observed to spring back to their equilibrium shape upon breaking contacts. As the tension approaches zero, most fibers have pulled out from either side of the network, leaving a clear fracture zone in the network.

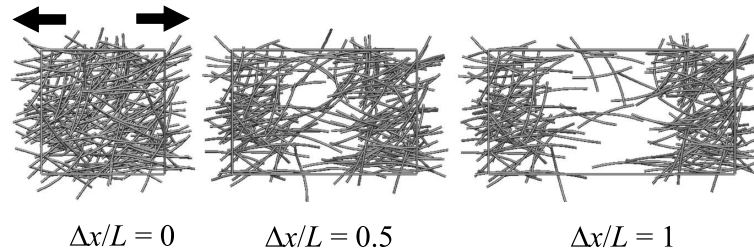


Figure 6.5: Snapshots of the structure of a typical fiber network subjected to elongation at various deformations.

6.3.2 Simulations: effect of fiber equilibrium shape, length, flexibility, and friction

Fiber network strength is influenced by a number of parameters including fiber equilibrium shape, length, flexibility, and coefficient of static friction. In this work, we investigated the effects of these parameters on the mechanical response of fiber networks subjected to elongational deformation as described in Section 6.2. In all of the simulation results presented here, the fibers are made up of $N_{\text{seg}} = 5$ segments, are monodisperse with respect to length and stiffness, interact only with short-range repulsive forces and static friction ($\mu^{\text{kin}} = 0$), and are formed to a volume fraction $\Phi = 0.05 \pm 0.005$. The extension rate u_p is inversely proportional to the effective stiffness, $u_p \propto 1/S^{\text{eff}}$.

Fig. 6.5 illustrates snapshots of structures from a typical simulation run at three different deformations $\Delta x/L$, where Δx is the distance the sample is stretched and L is the length of a fiber, for a suspension of straight, flexible fibers ($S^{\text{eff}}, r_p, \theta^{\text{eq}}, \phi^{\text{eq}}, \mu^{\text{stat}} = (0.05, 75, 0, 0, 20)$).

The mechanical response of the simulation depicted in Fig. 6.5 is illustrated in Fig. 6.6, where the dimensionless tensile force $T/\eta_o u_p L$ is plotted as a function of deformation $\Delta x/L$. Features of the response are similar to that observed experimen-

tally. The tensile force initially varies linearly with deformation corresponding to a linearly elastic region. The tensile force then varies nonlinearly and passes through a maximum, accompanied with large fluctuations. The (average) rate of decrease of the tensile force with deformation after the maximum is slower than the initial rate of increase in the linear region. The only feature that differs qualitatively from the experimental response is that the tensile force at large deformations does not decay to zero. This arises because the fibers experience hydrodynamic drag as they are deformed, and the viscosity employed in the simulations is significantly larger than that employed in the experiments (i.e., the simulations correspond more closely to a wet network). A larger viscosity is employed in the simulations for computational reasons, which are discussed in more detail below.

The fluctuations in tensile force correspond to fiber contacts breaking and reforming, analogous to that observed experimentally. The larger rapid decreases in the tensile force correspond to multiple contacts breaking virtually simultaneously. The fact that the fluctuations are rapid implies that the fibers are relatively stiff; when a contact breaks, fibers are able to spring back and reform new contacts very quickly relative to the rate of deformation.

Equilibrium shape

Natural and artificial fibers are not perfectly straight at equilibrium. Wood fibers, for example, display a variety of configurations like those seen in Fig. 6.7(a). The equilibrium fiber shapes utilized in the simulations were either inherently straight ($\theta^{\text{eq}} = 0$, $\phi^{\text{eq}} = 0$) or U-shaped ($\theta^{\text{eq}} > 0$, $\phi^{\text{eq}} = 0$). Examples of the fiber equilibrium shapes used in the simulations are displayed in Fig. 6.7(b).

Fiber networks were formed using straight and U-shaped fibers ($\theta^{\text{eq}} = 0.1$ and

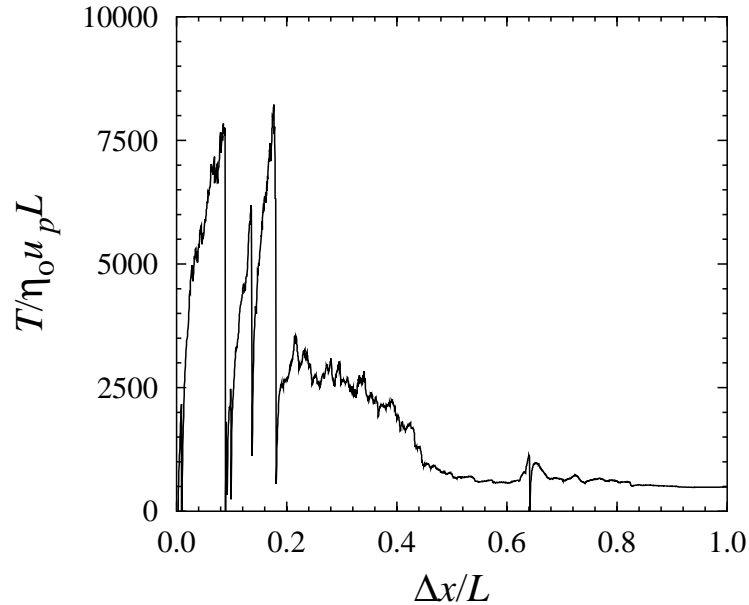


Figure 6.6: Dimensionless tensile force $T/\eta_o u_p L$ versus deformation $\Delta x/L$ for the simulation run shown in Fig. 6.5 .

$\theta^{\text{eq}} = 0.5$), in which the remaining parameters were held constant $(S^{\text{eff}}, r_p, \mu^{\text{stat}}) = (0.05, 75, 20)$. The dimensionless tensile force $(T/\eta_o u_p L)$ is plotted as a function deformation $(\Delta x/L)$ for elongation of these systems in Fig. 6.8. Tensile force data were averaged over deformation intervals of $\Delta(\Delta x/L) \approx 0.02$. Each set of symbols Fig. 6.8 represent an average of two simulation runs. The straight fiber network exhibits a rapid increase in tensile force as the sample is strained, to a maximum value T_u defined as the tensile strength of the network. If the fibers are slightly deformed at equilibrium ($\theta^{\text{eq}} = 0.1$), the network exhibits similar behavior, but with a smaller tensile strength. The tensile force for fiber networks with substantially deformed fibers ($\theta^{\text{eq}} = 0.5$) increases more slowly with increasing deformation, implying that the network is more flexible (smaller elastic modulus) than that for the straighter fibers. The tensile force for the networks with highly deformed fibers also does not pass through a maximum over the deformation range simulated.

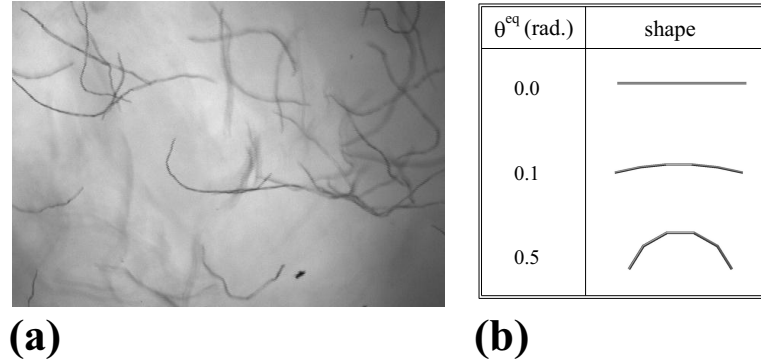


Figure 6.7: (a) Softwood fibers in water, and (b) examples of U-shaped fibers ($\phi^{\text{eq}} = 0$) for various values of θ^{eq} .

The different responses for networks composed of straight and highly deformed fibers correspond to different structure evolutions, as illustrated by the snapshots at $\Delta x/L = 1.0$ in Fig. 6.8. At this deformation, the network of straight fibers has developed a clear fracture zone extending vertically across the entire picture, with most fibers either pulled out from the opposite side of the fracture zone, or in contact with only one other fiber. In contrast, the network composed of highly curved fibers exhibits an incomplete fracture, with the network intact across the bottom of the picture. The network of highly curved fibers is thus capable of transmitting a larger force horizontally across the system at large deformations (although the magnitude of the force transmitted at small deformations is smaller than that transmitted by the networks of straighter fibers).

The effect of shape on the tensile strength of fiber networks can be further understood by examining fiber dynamics during the extension process. For a network that contains nearly straight fibers, the fibers start to align in the x direction as the sample is deformed. The extension continues until the groups of fibers are aligned or the network is locked in a nearly rigid configuration. At this point, the network fails at the the weakest frictional contact points, resulting in a global disruption of

the system. Fibers that are deformed at equilibrium also attempt to align in the x direction as the deformation increases. However, they can accommodate some of the applied stress by bending into straighter configurations. The simulations show that deformed fibers first start to align, become locked in position due to contacts, and then start to straighten before contacts break. This results in a lower overall tensile strength and a more elastic network (longer breaking lengths and lower elastic modulus) for networks of deformed fibers relative to that for straight fibers.

These simulation results are consistent with tensile force experiments performed on dry pulp handsheets. Mohlin et al. [60] observed that the tensile strength of handsheets increased as the shape factor increased (decreasing shape factor corresponds to more highly deformed fibers). They also noticed that the stretch-to-break value increased with decreasing shape factor.

Fiber length

Fiber length also effects the strength of planar fiber networks. We performed simulations using fibers of various lengths by changing the fiber aspect ratio ($r_p = 50, 75,$ and 100), while holding all other parameters constant. The fibers were U-shaped and all had the same radius of curvature $R_U = 60b$. The radius of curvature is defined here as the average of the radii of circles tangent to the joints and segment centers, $R_U = \ell/2 \cdot [1/\sin(\theta^{\text{eq}}/2) + 1/\tan(\theta^{\text{eq}}/2)]$. The effective stiffness $S^{\text{eff}} = E_Y I / \eta_o \dot{\gamma} L^4$ was chosen to make the fiber stiffness ($E_Y I$) constant [$r_p = 50 \Rightarrow S^{\text{eff}} = 0.25$, $r_p = 75 \Rightarrow S^{\text{eff}} = 0.05$, $r_p = 100 \Rightarrow S^{\text{eff}} = 0.016$]. All fibers interact with the same coefficient of static friction, $\mu^{\text{stat}} = 20$.

The results for the network tensile force $T/E_Y b^2$ as a function of deformation are illustrated in Fig. 6.9(a). The network strength increases and the maximum tensile

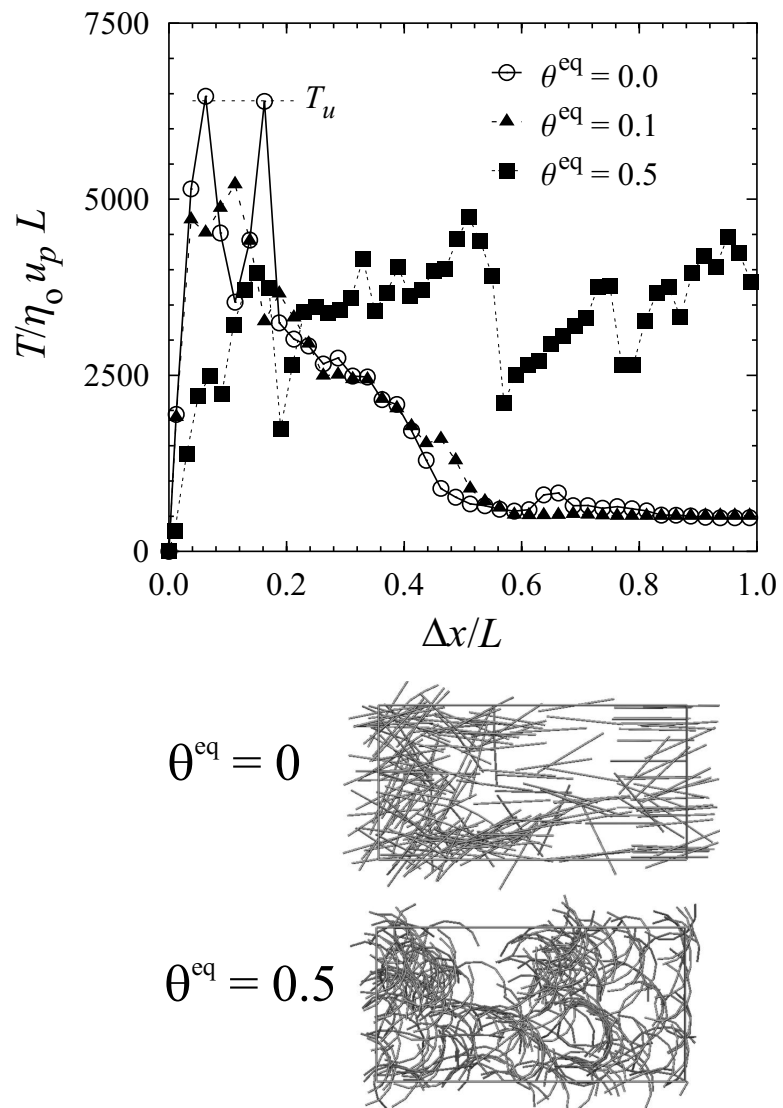


Figure 6.8: Dimensionless tensile force $T/\eta_0 u_p L$ as a function of the deformation $\Delta x/L$ for fiber networks of different shapes, and configuration snapshots at $\Delta x/L = 1$.

strength is shifted to larger deformations, as the fiber aspect ratio is increased. The maximum value of the tensile strength $T_u/E_Y b^2$ and the network elastic modulus E_{xx} , normalized with respect to the fiber Young's modulus E_Y , are plotted as a function of fiber aspect ratio in Fig. 6.9(b). The maximum tensile strength and the elastic modulus increase linearly with fiber aspect ratio. The results indicate that the network strength increases and the network becomes stiffer with fiber length. This can be explained by the average number of contacts per fiber, which increases with fiber aspect ratio (2.5, 2.7 and 3.2 for aspect ratios 50, 75 and 100, respectively).

The fact that the network strength increases approximately linearly with aspect ratio is consistent with the experimental results of Seth [77]. Seth measured the wet-web tensile strength of softwood pulp and found a linear dependence with respect to the average fiber length. This was attributed to longer fibers having an increased number of frictional contacts with other fibers. As described above, the simulations indeed show that longer fibers experience more contacts.

Flexibility and friction

Fiber networks with various values of the effective stiffness S^{eff} were simulated with $(r_p, \theta^{\text{eq}}, \phi^{\text{eq}}, \mu^{\text{stat}}) = (75, 0.1, 0, 20)$. Figure 6.10 illustrates the results for the dimensionless tensile force $T/\eta_o u_p L$ as a function of deformation $\Delta x/L$ for $S^{\text{eff}} = 0.005, 0.025, 0.05$ and 0.5 . As S^{eff} increases, the maximum value of the tensile strength and the elastic modulus of the network increase. This is not unexpected, as the force required to deform individual fibers increases with increasing fiber stiffness. The network strength increases more slowly as S^{eff} is increased beyond 0.05.

By increasing the coefficient of static friction μ^{stat} , a greater force is necessary to break fiber-fiber contacts. Thus, the tensile strength of a fiber network is expected

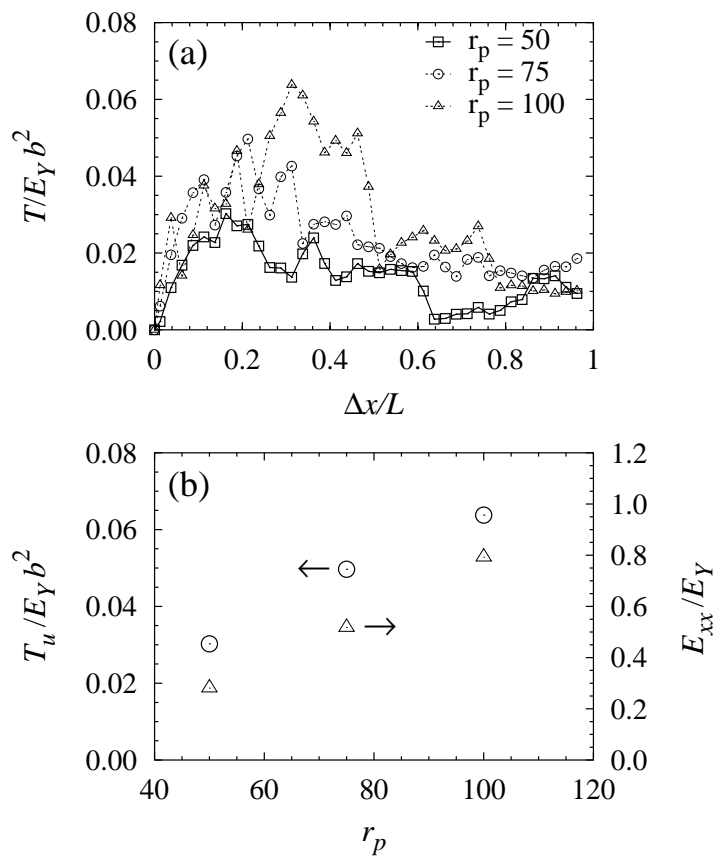


Figure 6.9: (a) Dimensionless tensile force $T/E_Y b^2$ as a function of deformation $\Delta x/L$ for fibers of different aspect ratios, and (b) the dimensionless maximum tensile strength $T_u/E_Y b^2$ and elastic modulus of the fiber networks E_{xx}/E_Y as a function of fiber aspect ratio

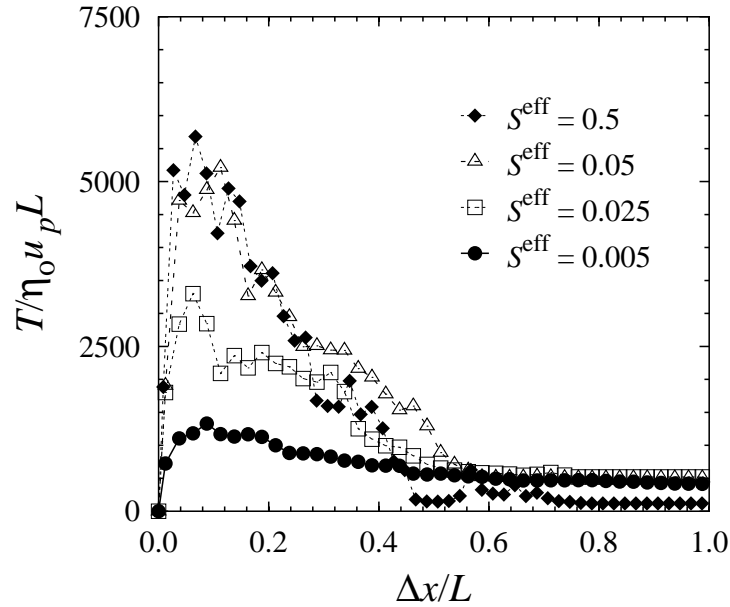


Figure 6.10: Dimensionless tensile force $T/\eta_0 u_p L$ as a function of deformation $\Delta x/L$ for planar fiber networks at various effective stiffness values.

to increase as μ^{stat} increases. Elongation of fiber networks with $(r_p, S^{\text{eff}}, \theta^{\text{eq}}, \phi^{\text{eq}}) = (75, 0.05, 0.1, 0)$ were simulated using various values of μ^{stat} , and the results for the dimensionless tensile force as a function of deformation are presented in Fig. 6.11. As expected, the network is strengthened with increasing values of μ^{stat} . The elastic modulus of the fiber network also increases with μ^{stat} , indicating that the network is becoming stiffer as the contacts between fibers become stronger.

Soszynski and Kerekes [82] proposed that the cohesive forces that hold fibers within networks are caused by interfiber friction. The strength of the friction force is proportional to the normal force between contacting fibers, and this normal force is a function of the fiber stiffness. Soszynski and Kerekes [82] demonstrated this mechanism experimentally; nylon fiber flocs readily dispersed when the fiber stiffness was reduced by heating the flocs above the glass transition temperature of nylon. Fibers caught in elastically strained configurations strengthen the network as the

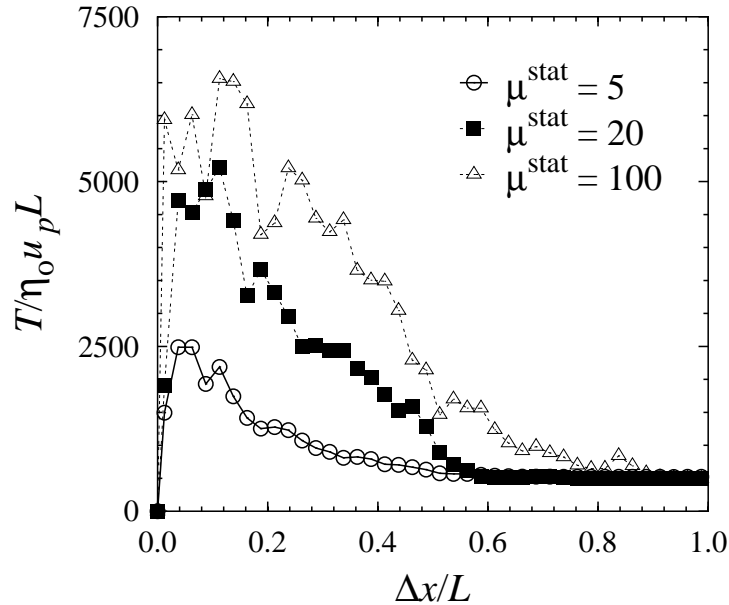


Figure 6.11: Dimensionless tensile force $T/\eta_0 u_p L$ as a function of deformation $\Delta x/L$ for planar fiber networks in which the coefficient of friction is varied.

fiber stiffness increases, by increasing the friction force at contacts. The simulation results are thus consistent with the notion that fiber flexibility and friction contribute to the overall strength of a fiber network.

6.4 Discussion

The simulations qualitatively reproduce numerous experimentally observed features of the mechanical response of planar fiber networks. However, as described below, quantitative agreement is lacking. This discrepancy is due at least in part to computational limitations that prevent us from performing the simulations for the actual experimental conditions, in addition to possible shortcomings of the model.

The values of μ^{stat} employed in the simulations are much larger than those measured experimentally, which for contacting cellulose surfaces and cellulose fibers

is $\mu^{\text{stat}} \approx 0.5$ [79, 99]. For values of $\mu^{\text{stat}} \lesssim 1$, the simulated networks exhibit no significant tensile strength beyond that provided by the hydrodynamic drag. Possible reasons that such large values of μ^{stat} are needed to produce mechanical responses similar to those observed experimentally are related to the nature of contacts formed and the values of the effective stiffness employed.

Real fibers can bond at contact points, and large coefficients of friction may serve to approximately model fiber bonding. Explicitly adding fiber bonding to the present model should produce similar mechanical responses at lower values of μ^{stat} (i.e., interfiber bonds would increase the load at contact points, thus increasing the friction force at fixed μ^{stat}). Wood fibers are also significantly more complex than the simple fiber model employed here. Fibrillation and other surface features may impede fibers from sliding over one another and cause surface entanglements, yielding larger apparent coefficients of friction. Seth [77] observed that the tensile strength of wet softwood fiber webs decreased with fiber coarseness (linear density). Fiber coarseness is approximately proportional to wall thickness. Fibers that are less coarse can collapse to ribbon-like structures, producing contact areas greater than those for thick-walled fibers that do not show the same extent of collapse. Such features are not included in the present model.

The values of the effective stiffness $S^{\text{eff}} \equiv E_Y I / \eta_o \dot{\gamma} L^4$ used in the simulations are also significantly smaller than those encountered experimentally. Choosing parameter values representative of the experimental system described in Section 6.3.1 ($E_Y I = 10^{-12} \text{ Nm}^2$ [86], $\eta_o = 2 \times 10^{-5} \text{ Pa}\cdot\text{s}$ for air [13], $u_p = 3 \text{ mm/min}$, $b = 16 \text{ }\mu\text{m}$, $\dot{\gamma} = u_p/b = 3.1 \text{ s}^{-1}$, and $L = 2.5 \text{ mm}$), the experimental value of the dimensionless stiffness is $(S^{\text{eff}})_{\text{exp}} = 410$, which is much larger than that employed in the simulations ($S^{\text{eff}} < 1$). Computational limitations prevent us from performing simulations with

such large stiffnesses. As the stiffness increases, the maximum allowable time step for stable integration of the equations of motion decreases rapidly. Thus simulations for $S^{\text{eff}} > 1$ cannot be performed in a reasonable time.

In Chapter 3, we performed simulations to study the flocculation behavior of flexible fiber suspensions, similar to the method employed here. Flocculation was observed for various combinations of S^{eff} and μ^{stat} . As S^{eff} was increased, the mechanical integrity of model fiber flocs was maintained for smaller values μ^{stat} . This suggests that qualitative agreement between experimental measurements and simulations of the mechanical response of planar fiber networks may be achieved for reasonable values of the coefficient of friction if simulations could be performed for larger values of S^{eff} .

Alternatively, experiments may be modified to be performed at conditions more amenable to the simulations. For example, the viscosity of the suspending fluid can be increased to produce smaller values of S^{eff} . In order to obtain $S^{\text{eff}} = 0.05$ as commonly employed in the simulations, a viscosity of $\eta_0 = 0.16$ Pa·s is required (using the values for $E_Y I$, $\dot{\gamma}$ and L defined above). This is roughly four orders of magnitude larger than that of air.

Finally, we consider the magnitudes of the tensile forces. The experiments produced tensile forces on the order $T \approx 5 \times 10^{-2}$ N (see Fig. 6.4). The dimensionless tensile forces produced by the simulations are on the order $T/\eta_0 u_p L \approx 5 \times 10^3$. Choosing the parameter values $\eta_0 = 0.16$ Pa·s (to match experimental and simulated values of $S^{\text{eff}} = 0.05$), $u_p = 3$ mm/min, and $L = 2.5$ mm, the dimensional simulated tensile force magnitudes are on the order $T \approx 1 \times 10^{-4}$ N, significantly smaller than the experimentally measured values.

The difference between the measured and simulated tensile forces may be due

to shortcomings in the model, or from the computational limitations that prevent us from simulating the precise experimental conditions. Resolving this discrepancy will require either overcoming the computational limitations, or conducting experiments under conditions that can be simulated efficiently.

6.5 Conclusions

We have presented a model and simulation method to investigate the mechanical response of planar networks subjected to elongational deformation. The simulated responses agree qualitatively with numerous experimental observations. Simulations exhibit shapes and features of plots of tensile force as a function of deformation similar to that measured experimentally. The trends observed as the fiber shape and length are varied agree with experimentally observed trends. The dependence of the mechanical response on the coefficient of friction and fiber stiffness are consistent with the elastic interlocking mechanism of network strength proposed previously. Thus it appears that such simulation methods may be useful for probing the effects of fiber features and interactions on the mechanical properties of fiber networks.

Quantitative agreement with experiments, however, is lacking. The discrepancies may be attributed to shortcomings of the model, as well as computational limitations that prevent us from performing the simulations at precisely the same conditions employed in typical experiments. Resolving this discrepancy requires overcoming the computational limitations, or conducting experiments under conditions more amenable to the simulations.

Chapter 7

Conclusions and recommendations

7.1 Summary

In this thesis, we have described a model for flexible fibers and a simulation technique to determine their motion in suspensions and networks. The model incorporates such fiber features as flexibility, deformed equilibrium shapes, and interfiber friction. The model fibers consist of linked rigid spherocylinders connected by ball and socket joints (for isotropically bending fibers). Simulations were performed to study flocculation, floc dispersion, the rheology of fiber suspensions subjected to simple shear flow, and the formation and strength of planar fiber networks.

Simulations demonstrated that suspensions of flexible fibers that experience interfiber friction can flocculate in the absence of attractive forces in simple shear flow. The observations are consistent with the elastic fiber interlocking mechanism proposed by Soszynski and Kerekes [81, 82]. If fibers are too flexible, or the coefficient of friction is too small, fibers will not flocculate. As the fiber stiffness is increased, the coefficient of friction necessary to hold flocs together decreases. Fiber equilibrium shape also impacts flocculation behavior. As the inherent curvature of fibers increases, the tendency to form flocs shifts to lower concentrations. Model features such as

kinetic friction and weak attractive forces have little impact on fiber flocculation. Fibers that bend anisotropically shift flocculation conditions to larger coefficients of friction compared to those required for the flocs of isotropically bending fibers.

Flocs that were formed in simple shear flow simulations were extracted and placed in unbounded linear flow fields (i.e., simple shear, uniaxial extension, and planar extension) to investigate floc dispersion. Flocs placed in unbounded simple shear flow slowly dispersed by losing small clumps of fibers from the main floc. Extensional flows initially dispersed flocs much more quickly, but coherent secondary flocs remained. The rate of floc dispersion increased in all of the flow fields by making the fibers more flexible or by decreasing the coefficient of friction. This is again consistent with the elastic fiber interlocking mechanism of floc coherency.

Simulations of fiber suspensions demonstrate the importance of fiber characteristics on rheological properties. Small permanent deformations to the fiber shape from perfectly straight lead to $O(1)$ effects on the specific suspension viscosity. Interfiber fiber friction has less of an impact on the specific viscosity as the fiber shape becomes straighter. Fiber suspensions exhibit shear thinning behavior, which depends on fiber shape and aspect ratio at lower shear rates, while the viscosity appears to be independent of shape and fiber length at high shear rates. When flocs form in suspensions, the shear thinning behavior persists to lower shear rates than that observed for homogenous suspensions.

The model and simulation method were modified to simulate the formation of planar fiber networks, and subsequently, to test their mechanical strength. The mechanical response to elongation measured in simulations contains features similar to those observed experimentally. The tensile strength increases as the fiber length is increased, and as the fibers become straighter, consistent with experimental ob-

servations. The network strength also increases with increasing the fiber stiffness or coefficient of friction, consistent with the elastic fiber interlocking mechanism for network strength.

7.2 Recommendations for future Research

7.2.1 Experimental research

Numerous experimental research themes may be investigated to gain a better understanding of fiber suspensions and networks. We list here three areas of research for experimental work, including flow visualization, determining individual fiber properties, and measuring planar network strength.

As discussed previously, flocculation in fiber suspensions is a process that is not completely understood. The simulation method has allowed us to probe the flocculation process at the fiber level. An experimental technique to visualize floc formation in flowing systems, in order to observe the floc formation process and track particle dynamics similar to that achieved by the simulations, would be very useful. It would also be useful to develop measures of the suspension structure, and particularly the heterogeneity associated with flocculation, that are amenable to both experimental measurements and simulations. In the past, light scattering methods have been used to quantify heterogeneities in fiber suspensions [55, 85], and new methods are being developed, such as NMR imaging [5], to understand the structure of flowing fiber systems.

The simulations suggested that fiber shape, flexibility, and interactions have important effects on the suspension microstructure. We would like to gain a better understanding of individual fiber characteristics and their impact on suspension

structure through experiments.

The shape of fibers is difficult to characterize, and is usually described in terms of the curl and kink. The curl is related to the ratio of the end-to-end distance of a fiber to the contour length, while the kink is a measure of the number of abrupt direction changes along a fiber contour [63]. A fiber may also contain microcompressions and angular twists, which have been characterized generically as “defects” [60, 63]. Devising more detailed methods for quantifying fiber shapes would be very useful for directly comparing experiments and simulations.

Fiber flexibility is another quantity that is very dependent on the individual fiber structure, such as the fiber cross sectional structure (i.e., hollow tube, solid tube, etc.) and the presence of weak points. Past attempts to measure pulp fiber flexibility have used ideal fibers [86]. Experimental methods for measuring flexibility that take into account fiber properties such as shape, coarseness, and non-uniformities are desirable.

Simulations have shown that fiber interactions are important in determining fiber dynamics. We would like to gain a better understanding of individual fiber-fiber interactions. This may include a visual investigation of two fibers in contact in order to determine the effect of surface structure and interactions on relative fiber motion. Experimental techniques for measuring friction forces and bond strengths for individual fiber contacts are also needed to improve our model and simulation method.

We demonstrated qualitative agreement between experimental and simulation results for the tensile strength of small planar fiber networks in Chapter 6. The experiments are currently being expanded to study the tensile strength of small networks of various fibers. These will include hardwood and softwood fibers that have been

screened and refined to various degrees, as well as nylon fibers. The tensile tests on these small networks will probe the effects of fiber properties, interactions, and testing parameters on network strength, as well as failure mechanisms. In order to compare directly with the simulation, the experimental approach must be modified in order to investigate system parameters (e.g., fiber stiffness) accessible to the simulations.

7.2.2 Simulations

Simulating flexible fiber suspensions has aided in the understanding of the factors that affect the microstructure of fiber suspensions. The current model may be further utilized to probe the parameter space, thus performing a more exhaustive study of factors such as fiber aspect ratio, shape, flexibility, and friction, which would include multiple initial configurations to gain better statistical data. Additional model features may be added, such as hydrodynamic interactions, fibers of various cross sectional shapes, rigid fibers with permanent deformations, and distributions of fiber shapes and lengths, to name a few.

We suggested in Chapter 3 that the values of the stiffnesses used in the simulations were much lower than experimental values. Simulating suspensions of fibers with large stiffnesses requires vast amounts of computer time. Therefore, it may be prudent to develop a new model specifically for very stiff fibers that experience only small perturbations in shape, such as that employed by Joung et al. [42].

In the model employed in this thesis, fibers are assumed to be large enough that Brownian motion is negligible. However, numerous interesting and important fiber systems exist in which Brownian motion becomes a factor; for example, carbon nanotubes and tubular viruses. Brownian motion fundamentally changes the model employed here, in that one needs to solve stochastic differential equations for the

motion of a fiber, which involves small time scales. Investigation of the relative importance and interplay between the various dynamics on different time scales (i.e., Brownian fluctuations, fiber bending, fiber rotations) appears to be well-suited for particle-level simulations.

Appendix A

Stress in a suspension of interacting fibers

A.1 Generalized particle stress contribution

The bulk average stress in a suspension of particles is found by averaging the stress σ over a volume of fluid V that contains many particles [7],

$$\langle \sigma_{ij} \rangle = \frac{1}{V} \int_V \sigma_{ij} dV. \quad (\text{A.1})$$

The integral can be separated into an integral over the fluid volume alone, and integrals over the particle volumes,

$$\langle \sigma_{ij} \rangle = \frac{1}{V} \int_{V-\sum V_p} \sigma_{ij} dV + \frac{1}{V} \sum^N \int_{V_p} \sigma_{ij} dV, \quad (\text{A.2})$$

where V_p is the volume of a particle and N is the number of particles in the volume V .

Assuming that the fluid is a Newtonian liquid (viscosity η_o), the bulk stress becomes

$$\begin{aligned} \langle \sigma_{ij} \rangle &= -P\delta_{ij} + \frac{1}{V} \int_V \eta_o \left(\frac{\partial u_i}{\partial x_j} + \frac{\partial u_j}{\partial x_i} \right) dV \\ &+ \frac{1}{V} \sum^N \int_{V_p} \sigma_{ij} - \eta_o \left(\frac{\partial u_i}{\partial x_j} + \frac{\partial u_j}{\partial x_i} \right) dV, \end{aligned} \quad (\text{A.3})$$

where the isotropic part of the stress is lumped into an effective pressure P , and \mathbf{u} is the velocity at point \mathbf{x} in the fluid. The first integral contains the volume averaged rate of strain tensor, which may be equated with the applied, macroscopic rate of strain, \mathbf{E}^∞ . The sum of the integrals over the particles is simply the particle contribution to the stress $\boldsymbol{\sigma}^p$ and the bulk suspension stress may be written

$$\langle \sigma_{ij} \rangle = -P\delta_{ij} + 2\eta_o E_{ij}^\infty + \sigma_{ij}^p, \quad (\text{A.4})$$

where P is the bulk pressure.

The particle contribution to the stress may be simplified by rearranging terms,

$$\sigma_{ij}^p = \frac{1}{V} \sum \int_{V_p} \left[\frac{\partial}{\partial x_k} (\sigma_{ik} x_j) - \frac{\partial \sigma_{ik}}{\partial x_k} x_j - \eta_o \left(\frac{\partial u_i}{\partial x_j} + \frac{\partial u_j}{\partial x_i} \right) \right] dV. \quad (\text{A.5})$$

The second term in the integrand contains the divergence of the stress field, $\nabla \cdot \boldsymbol{\sigma}$, and this term vanishes for a system in which inertia and body forces may be neglected. The divergence theorem is then applied to convert the volume integrals to surface integrals to give

$$\sigma_{ij}^p = \frac{1}{V} \sum \oint_{S_p} [n_k (\sigma_{ik} x_j) - \eta_o (u_i n_j + n_i u_j)] dS, \quad (\text{A.6})$$

where \mathbf{n} is the outward directed unit normal vector to the particle surface. The second term in Eq. (A.6) integrates to zero if the particle is rigid. The particle stress can be assumed to be symmetric as well, if no external torques act on the suspension [7], which simplifies $\boldsymbol{\sigma}^p$ to

$$\sigma_{ij}^p = \sum \left\{ \frac{1}{2V} \oint_{S_p} [(\sigma_{ik} n_k) x_j + x_i (\sigma_{jk} n_k)] dS - \frac{1}{3V} \delta_{ij} \oint_{S_p} \sigma_{mk} n_k x_m dS \right\}, \quad (\text{A.7})$$

where the second integral is subtracted in order to force the stress to be traceless.

The particle contribution to the stress can be further simplified by separating the integrals in Eq. (A.7) into two parts: that representing the contribution to the

stress arising from the disturbance to the flow field caused by the presence of the particles, and that representing the contribution caused by non-hydrodynamic interactions. Inserting $\mathbf{x} = (\mathbf{x} - \mathbf{x}_i) + \mathbf{r}_i$, where \mathbf{r}_i is the center-of-mass of particle i , the particle stress becomes (using vector notation)

$$\begin{aligned} \boldsymbol{\sigma}^p = \frac{1}{V} \sum \left\{ \frac{1}{2} \oint_{S_p} [(\boldsymbol{\sigma} \cdot \mathbf{n})(\mathbf{x} - \mathbf{r}_i) + (\mathbf{x} - \mathbf{r}_i)(\boldsymbol{\sigma} \cdot \mathbf{n})] dS - \right. \\ \left. \frac{1}{3} \boldsymbol{\delta} \oint_{S_p} [(\boldsymbol{\sigma} \cdot \mathbf{n}) \cdot (\mathbf{x} - \mathbf{r}_i)] dS \right\} + \\ \frac{1}{V} \sum \left\{ \frac{1}{2} \oint_{S_p} [(\boldsymbol{\sigma} \cdot \mathbf{n})\mathbf{r}_i + \mathbf{r}_i(\boldsymbol{\sigma} \cdot \mathbf{n})] dS - \frac{1}{3} \boldsymbol{\delta} \oint_{S_p} [(\boldsymbol{\sigma} \cdot \mathbf{n}) \cdot \mathbf{r}_i] dS \right\}. \end{aligned} \quad (\text{A.8})$$

The second summation may be simplified by recognizing that \mathbf{r}_i can be brought outside the integral. The resulting integral is the definition of the hydrodynamic drag force ($\mathbf{F}_i^{\text{hyd}}$) on the particle, and thus

$$\oint_{S_p} (\boldsymbol{\sigma} \cdot \mathbf{n})\mathbf{r}_i dS = \left[\oint_{S_p} (\boldsymbol{\sigma} \cdot \mathbf{n}) dS \right]_i \mathbf{r}_i = \mathbf{F}_i^{\text{hyd}} \mathbf{r}_i. \quad (\text{A.9})$$

The hydrodynamic force is zero for particles that only interact via hydrodynamic disturbances, but has a non-zero value if there are mechanical contacts between particles.

Thus, the particle contribution to the stress may be written

$$\boldsymbol{\sigma}^p = \frac{1}{V} \sum \left[\mathbf{S}_i + \frac{1}{2} \left(\mathbf{F}_i^{\text{hyd}} \mathbf{r}_i + \mathbf{r}_i \mathbf{F}_i^{\text{hyd}} \right) - \frac{1}{3} \left(\mathbf{F}_i^{\text{hyd}} \cdot \mathbf{r}_i \right) \boldsymbol{\delta} \right], \quad (\text{A.10})$$

where

$$\mathbf{S}_i = \frac{1}{2} \oint_{S_p} [(\boldsymbol{\sigma} \cdot \mathbf{n})(\mathbf{x} - \mathbf{r}_i) + (\mathbf{x} - \mathbf{r}_i)(\boldsymbol{\sigma} \cdot \mathbf{n})] dS - \frac{1}{3} \boldsymbol{\delta} \oint_{S_p} [(\boldsymbol{\sigma} \cdot \mathbf{n}) \cdot (\mathbf{x} - \mathbf{r}_i)] dS, \quad (\text{A.11})$$

represents the contribution that remains non-zero in the absence of non-hydrodynamic interparticle forces.

A.2 Particle stress for a flexible fiber suspension

The particle contribution to the stress is desired for suspensions of flexible model fibers, each composed of N_{seg} rigid spherocylinders. The expression for $\boldsymbol{\sigma}^{\text{P}}$ for a volume of the suspension containing N_{fib} particles is

$$\boldsymbol{\sigma}^{\text{P}} = n \left\langle \sum_{i=1}^{N_{\text{seg}}} \left[\mathbf{S}_i + \frac{1}{2} \left(\mathbf{F}_i^{\text{hyd}} \mathbf{r}_i + \mathbf{r}_i \mathbf{F}_i^{\text{hyd}} \right) - \frac{1}{3} \left(\mathbf{F}_i^{\text{hyd}} \cdot \mathbf{r}_i \right) \boldsymbol{\delta} \right] \right\rangle, \quad (\text{A.12})$$

where n is the number density of fibers and the angled brackets $\langle \dots \rangle$ represent the average over all fibers. To evaluate $\boldsymbol{\sigma}^{\text{P}}$, an approximate expression for \mathbf{S}_i from slender-body theory is employed [6].

In slender-body theory, valid for particles that have large ratios of the length to diameter ($r_{\text{p}} \gg 1$), the force around the edge of a cross section of the particle is approximated as a point force on the centerline of the particle, $\boldsymbol{\sigma} \cdot \mathbf{n}|_s \approx \mathbf{F}(s)$, where s is a point along the centerline of the fiber. The vector from the center of the segment to a point on the surface can be approximated as $\mathbf{x} - \mathbf{r}_i \approx s\mathbf{p}_i$, where \mathbf{p}_i is the orientation vector of the fiber segment. Incorporating these approximation into Eq. (A.11), the surface integral becomes a line integral along the contour of the fiber segment, giving

$$\mathbf{S}_i = \frac{1}{2} \int_{-\ell}^{\ell} [s\mathbf{F}_i(s)\mathbf{p}_i + s\mathbf{p}_i\mathbf{F}_i(s)] ds - \frac{1}{3} \boldsymbol{\delta} \int_{-\ell}^{\ell} (s\mathbf{F}_i(s) \cdot \mathbf{p}_i) ds. \quad (\text{A.13})$$

where ℓ is the segment half-length. Batchelor [6] derived an expression for $\mathbf{F}(s)$ for a body of circular cross section of the form

$$\mathbf{F}_i(s) = \frac{4\pi\eta_o}{\ln(2r_{\text{p}})} \left[\boldsymbol{\delta} - \frac{1}{2} \mathbf{p}_i \mathbf{p}_i \right] \cdot (\mathbf{U}^{\infty}(s) - \mathbf{u}(s)), \quad (\text{A.14})$$

where $\mathbf{u}(s) = \dot{\mathbf{r}}_i(s) + s\dot{\mathbf{p}}_i(s)$ is the velocity at position s along the segment. Equation (A.14) is inserted into Eq. (A.13) and the integration is performed assuming that

the imposed flow field \mathbf{U}^∞ is linear, which results in

$$\mathbf{S}_i = \frac{4\pi\eta_o\ell^3}{3\ln(2r_p)} \left[\mathbf{E}^\infty \cdot \mathbf{p}_i\mathbf{p}_i + \mathbf{p}_i\mathbf{p}_i \cdot \mathbf{E}^\infty - \mathbf{p}_i\mathbf{p}_i\mathbf{p}_i\mathbf{p}_i : \mathbf{E}^\infty - \right. \quad (\text{A.15}) \\ \left. (\mathbf{p}_i\dot{\mathbf{p}}_i + \dot{\mathbf{p}}_i\mathbf{p}_i) - \frac{1}{6}\mathbf{p}_i\mathbf{p}_i : \mathbf{E}^\infty \boldsymbol{\delta} \right].$$

The net hydrodynamic drag force on a segment, $\mathbf{F}_i^{\text{hyd}}$, is also approximated using Eq. (A.14), in which the velocities are based on those at the fiber segment centers, to give

$$\mathbf{F}_i^{\text{hyd}} = \frac{8\pi\eta_o\ell}{\ln(2r_p)} \left[\boldsymbol{\delta} - \frac{1}{2}\mathbf{p}_i\mathbf{p}_i \right] \cdot (\mathbf{U}^\infty(\mathbf{r}_i) - \dot{\mathbf{r}}_i). \quad (\text{A.16})$$

Finally, the terms \mathbf{S}_i and the net force contributions are combined to calculate the total particle contribution to the bulk stress by substituting Eq. (A.15) and (A.16) into Eq. (A.12) to give

$$\boldsymbol{\sigma}^p = \frac{4\pi n\ell^3\eta_o}{3\ln(2r_p)} \left\langle \sum_{i=1}^{N_{\text{seg}}} \left\{ \mathbf{E}^\infty \cdot \mathbf{p}_i\mathbf{p}_i + \mathbf{p}_i\mathbf{p}_i \cdot \mathbf{E}^\infty - \mathbf{p}_i\mathbf{p}_i\mathbf{p}_i\mathbf{p}_i : \mathbf{E}^\infty - \right. \quad (\text{A.17}) \\ \left. (\mathbf{p}_i\dot{\mathbf{p}}_i + \dot{\mathbf{p}}_i\mathbf{p}_i) - \frac{1}{6}\mathbf{p}_i\mathbf{p}_i : \mathbf{E}^\infty \boldsymbol{\delta} + \right. \\ \left. \frac{3}{\ell^2} \left(\left[\boldsymbol{\delta} - \frac{1}{2}\mathbf{p}_i\mathbf{p}_i \right] \cdot (\mathbf{U}^\infty - \dot{\mathbf{r}}_i)\mathbf{r}_i + \mathbf{r}_i \left[\boldsymbol{\delta} - \frac{1}{2}\mathbf{p}_i\mathbf{p}_i \right] \cdot (\mathbf{U}^\infty - \dot{\mathbf{r}}_i) \right) - \right. \\ \left. \frac{1}{\ell^2} \left[\left[\boldsymbol{\delta} - \frac{1}{2}\mathbf{p}_i\mathbf{p}_i \right] : (\mathbf{U}^\infty - \dot{\mathbf{r}}_i)\mathbf{r}_i \right] \boldsymbol{\delta} \right\} \right\rangle.$$

Appendix B

Fiber bending

B.1 Radius of curvature for a U-shaped model fiber

The shape of fibers at equilibrium may not be inherently straight, where equilibrium is defined as the state of a fiber in which there are no forces or torques acting on the body. The fiber model employed in this thesis is capable of representing a variety of shapes which are only limited by the number of bodies in the fiber. One simple equilibrium shape that was used is a U-shaped fiber. Its shape may be characterized by a *radius of curvature* (R_U) regardless of the number of segments in the body.

The radius of curvature is defined by fitting a circle to the equilibrium shape of the fiber. Since the fiber is made up of a discrete number of bodies, several different circles may be selected to represent the shape of the fiber. Figure B.1 demonstrates two such circles: (a) a circle passing through the joints of the fiber, and (b) a circle that is tangent to the segments at their centers. The equilibrium bending angle, θ_i^{eq} , is the angle between the orientation vectors of two connected segments, $\theta_i^{\text{eq}} = \cos^{-1}(\mathbf{p}_{i-1} \cdot \mathbf{p}_i)$ (e.g., $\theta_i^{\text{eq}} = 0$ for a straight fiber). The radius of curvature of the fiber is defined as

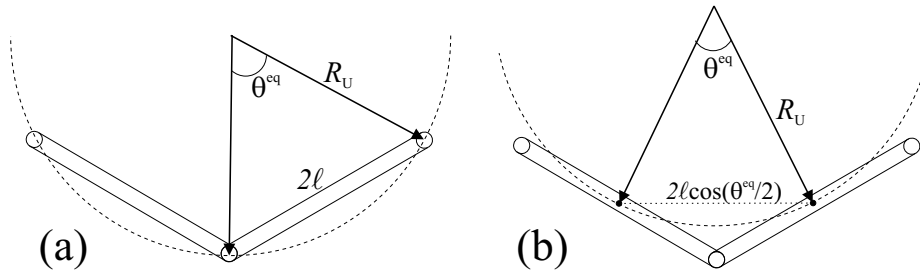


Figure B.1: Two methods to describe the radius of curvature R_U for a U-shaped fiber the average of the radii of curvature of methods (a) and (b),

$$R_U = \frac{1}{2} \left[\underbrace{\frac{\ell}{\sin(\theta^{\text{eq}}/2)}}_{\text{method (a)}} + \underbrace{\frac{\ell}{\tan(\theta^{\text{eq}}/2)}}_{\text{method (b)}} \right]. \quad (\text{B.1})$$

B.2 Fiber flexibility

The flexibility of a model fiber made up of discrete bodies that only deforms at joints may be approximated from continuum theory [37]. Consider a continuous body that has been deformed slightly from its equilibrium configuration due to an external torque \mathbf{M} as shown in Fig. B.2. There exists a surface in the body that does not change length after bending called the *neutral surface*. The normal strain ϵ is defined with respect to the neutral surface as,

$$\epsilon \equiv \lim_{\Delta s \rightarrow 0} \frac{\Delta s'|_y - \Delta s|_y}{\Delta s|_y}, \quad (\text{B.2})$$

where $\Delta s|_y$ is the length of a line segment in a thin slice of the body at position y from the neutral surface and $\Delta s'|_y$ is the length of the same line segment after straining. If the body is deformed slightly from the equilibrium configuration, the value of $\Delta s|_y$ is approximated using the radius of curvature R'_U and the amount of angular deformation $\Delta\theta$ (see Fig. B.2). The normal strain becomes

$$\epsilon \approx \lim_{\Delta\theta \rightarrow 0} \frac{(R'_U - y)\Delta\theta - R'_U\Delta\theta}{R'_U\Delta\theta} = \frac{-y}{R'_U}. \quad (\text{B.3})$$

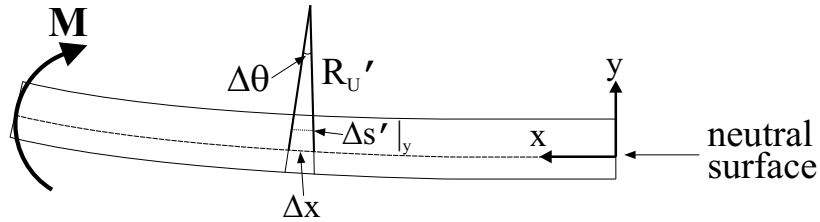


Figure B.2: Continuous fiber subjected to an external torque and deformed slightly from its equilibrium configuration.

The external torque that bends the body is balanced by an internal restoring torque that tries to force the body back into its equilibrium configuration. The restoring torque Y is defined as

$$Y = -M = - \int y \, dF^n, \quad (\text{B.4})$$

where F^n is the force acting parallel to the neutral surface, and is calculated from the normal stress (σ) on a cross section of the body (positive torque is in the clockwise direction). If the material is approximated as Hookean (perfectly elastic, $\sigma = E_Y \epsilon$), the restoring torque becomes

$$Y = - \int y(-\sigma) \, dA = - \int y(-E_Y \epsilon) \, dA, \quad (\text{B.5})$$

where A is the cross sectional area of the body and E_Y is the Young's modulus of the material. Equation (B.3) is substituted for the strain to give

$$Y = - \frac{E_Y}{R'_U} \underbrace{\int y^2 \, dA}_I = - \frac{E_Y I}{R'_U}, \quad (\text{B.6})$$

where I is the cross-sectional area moment. The value of the radius of curvature is approximated as $R'_U \approx 2\ell/\Delta\theta$ where ℓ is the half length of the body. The restoring torque is thus approximated by

$$Y = - \frac{E_Y I}{2\ell} \Delta\theta. \quad (\text{B.7})$$

The continuous body result in Eq. (B.7) can be applied to a system of discrete segments by imagining a spring at each joint that attempts to push or pull segments back to an equilibrium configuration as shown in Fig. B.3. The segments are 2ℓ in length which makes the magnitude of the restoring torque acting on a segment $Y = -\ell k_s \Delta x$ where k_s is the spring constant and Δx is the distance the spring is deformed from equilibrium. If $\ell \gg \Delta x$, the deformation of the spring is $\Delta x \approx \ell \Delta\theta$, and for small deformations Y is then

$$Y = -\underbrace{k_s \ell^2}_{\kappa_b} \Delta\theta = -\kappa_b \Delta\theta, \quad (\text{B.8})$$

in which $\Delta\theta = \theta - \theta^{\text{eq}}$ is the change in the bending angle of the joint from its equilibrium position, and κ_b is called the bending constant. Equating Eq. (B.7) to Eq. (B.8), the bending constant κ_b can be related to the properties of the material as

$$2\ell\kappa_b = E_Y I. \quad (\text{B.9})$$

The direction of the bending torque on a fiber segment is in the direction opposite to the direction in which $\Delta\theta$ is measured.

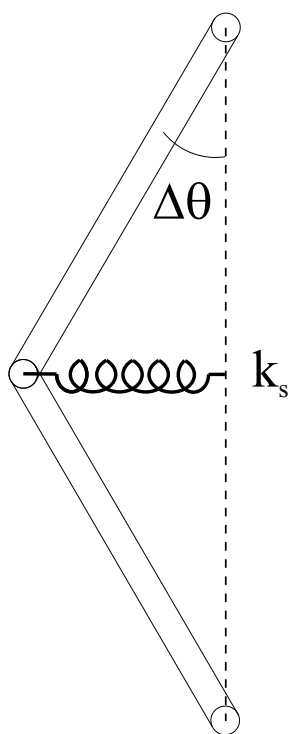


Figure B.3: Fiber restoring torques at each joint are modelled as a virtual spring.

Appendix C

Details of the friction constraints

The first step in determining the dynamics of a suspension of fibers using our simulation technique is to identify the groups of contacting segments. This is accomplished by calculating the separation distances h_{ij}^* . If $h_{ij}^* \leq h_{cut}^*$, then the contact is counted. Figure C.1 illustrates a cluster of four fiber segments with three contacts. Note that the contact between fiber 5 and fiber 1 forms a separate group from the highlighted bodies, because the contact on fiber 1 occurs on a different segment. For simplicity, we will ignore the segment number involved in the group (all segment 2), and just refer to the fiber segments as segments 1-4.

To find the friction forces \mathbf{F}^{fric} for each of the three contacts, we solve Eq. (2.82), which is restated here,

$$\mathcal{R}_F \cdot \mathbf{F}^{\text{fric}} = \mathcal{V}_F - \mathcal{Z}_X \cdot \mathbf{X}. \quad (\text{C.1})$$

Using the nomenclature developed in Chapter 2, the matrix \mathcal{R}_F necessary to solve for the forces $(\mathbf{F}_{14}^{\text{fric}}, \mathbf{F}_{23}^{\text{fric}}, \mathbf{F}_{34}^{\text{fric}})$ is

$$\mathcal{R}_F = \begin{bmatrix} \boldsymbol{\rho}_{14,41} & \mathbf{0} & \boldsymbol{\rho}_{14,43} \\ \mathbf{0} & \boldsymbol{\rho}_{23,32} & \boldsymbol{\rho}_{23,34} \\ \boldsymbol{\rho}_{34,41} & \boldsymbol{\rho}_{34,32} & \boldsymbol{\rho}_{34,43} \end{bmatrix}. \quad (\text{C.2})$$

The diagonal components are direct contributions to the contact force, and the off-diagonal tensors represent indirect contributions to the contact forces because of

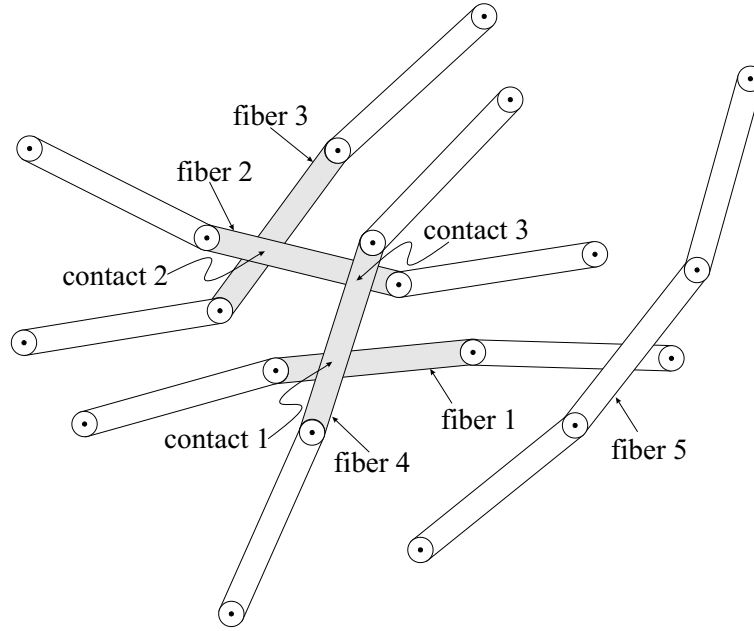


Figure C.1: Example contact group consisting of 4 segments (highlighted) and 3 contacts.

multiple contacts on a single segment. The diagonal tensors have the form expressed in Eq. (2.84). For example, for the first contact,

$$\boldsymbol{\rho}_{14,41} = \begin{bmatrix} (\mathcal{J}_{14}^\dagger - \mathcal{J}'_{41}{}^\dagger) \cdot \mathbf{e}_{14}^1 \\ (\mathcal{J}_{14}^\dagger - \mathcal{J}'_{41}{}^\dagger) \cdot \mathbf{e}_{14}^2 \\ \mathbf{n}_{14} \end{bmatrix}. \quad (\text{C.3})$$

The off-diagonal components are classified according to Fig. 2.12, and the example here corresponds to the following cases,

$$\begin{aligned} \boldsymbol{\rho}_{14,43} &\longrightarrow \text{Case IV,} \\ \boldsymbol{\rho}_{23,34} &\longrightarrow \text{Case III,} \\ \boldsymbol{\rho}_{34,41} &\longrightarrow \text{Case IV,} \\ \boldsymbol{\rho}_{34,32} &\longrightarrow \text{Case II,} \end{aligned}$$

and the values in terms of the tensors \mathcal{J} and \mathcal{J}' defined in Eq. (2.76) are

$$\begin{aligned} \mathcal{Q}_{14,43} &= - \begin{bmatrix} \mathcal{J}'_{43}{}^\dagger \cdot \mathbf{e}_{14}^1 \\ \mathcal{J}'_{43}{}^\dagger \cdot \mathbf{e}_{14}^2 \\ \mathbf{0} \end{bmatrix}, \\ \mathcal{Q}_{23,34} &= + \begin{bmatrix} \mathcal{J}'_{34}{}^\dagger \cdot \mathbf{e}_{23}^1 \\ \mathcal{J}'_{34}{}^\dagger \cdot \mathbf{e}_{23}^2 \\ \mathbf{0} \end{bmatrix}, \\ \mathcal{Q}_{34,41} &= - \begin{bmatrix} \mathcal{J}'_{41}{}^\dagger \cdot \mathbf{e}_{34}^1 \\ \mathcal{J}'_{41}{}^\dagger \cdot \mathbf{e}_{34}^2 \\ \mathbf{0} \end{bmatrix}, \\ \mathcal{Q}_{34,32} &= - \begin{bmatrix} \mathcal{J}_{32}{}^\dagger \cdot \mathbf{e}_{34}^1 \\ \mathcal{J}_{32}{}^\dagger \cdot \mathbf{e}_{34}^2 \\ \mathbf{0} \end{bmatrix}. \end{aligned}$$

Appendix D

Simulation codes

D.1 Flexible fiber code

This section contains the FORTRAN 90 code (compiled with PGI Workstation 3.2, from Portland Group, Inc.) utilized to simulate flexible fiber suspensions with periodic boundary conditions in arbitrary linear flow fields, using the approximation to the direct integration method described in Section 2.9.2. The main body of the code is contained in the program file `flexfric.f90`. The subroutines called in `flexfric.f90` are separate files and include:

`neighbor_list.f90` This file contains the subroutine `neighbor_list` which calculates the neighbor list of each fiber segment. It also contains the subroutine `parallel`, which is used to find the separation between two segments with centerlines that are parallel to each other.

`delta_twist.f90` This file contains the subroutine `delta_twist`, which calculates the separation distances between fiber segments and calls the sorting subroutine (`sort`, described below). The subroutine also calculates the bending and twisting restoring torques in each joint.

`sort.f90` This file contains the subroutine `sort`, which sorts contacting *segments* into groups.

`friction_forces.f90` This file contains the subroutine `friction_forces`, which calculates the friction forces (\mathbf{F}^{fric}) at contact points based on the inextensibility forces from the previous time step ($\mathbf{X}_{[\text{prev.}]}$).

`x_forces.f90` This file contains the subroutine `x_forces`, which calculates the new values of the inextensibility constraint forces.

`motion_integrate.f90` This file contains the subroutine `motion_integrate`, which integrates the fiber center of mass velocities ($\dot{\mathbf{R}}_{\text{cm}}$) and the time derivatives of the Euler parameters ($\dot{\mathbf{q}}$), to obtain the new positions and orientations.

Sliding friction is included by substituting the file `kinetic_friction_forces.f90` for the file `friction_forces.f90`, which contains the updated version of the subroutine `friction_forces` for kinetic friction.

D.1.1 Definition of variables

The following section defines the variables used in the code `flexfric` and subsequent subroutines, and how they relate to the nomenclature used in this document. The input parameters read into the code from the file `Parameters.in` are:

nfib: number of fibers in the simulation cell (N_{fib})

nseg: number of segments per fiber (N_{seg})

rp: fiber segment aspect ratio ($r_{ps} = r_p/N_{\text{seg}}$)

kb: the dimensionless fiber bending constant (κ_b^*)

mu_stat: static coefficient of friction (μ^{stat})

mu_kin: kinetic coefficient of friction (μ^{kin})

contact_cutoff: cut-off distance for counting a segment-segment contact (h_{cut}^*)

rep_cutoff: cut-off distance for calculating the normal force between fiber segments (h_{lim}^*)

neighb_cutoff: cut-off distance for finding neighbors to a fiber segment ($h_{\text{neigh.}}^*$)

dt: dimensionless time step for integration ($\Delta\gamma$)

strain: total strain of the simulation run (γ_{fin})

sidex, sidey, sidez: the dimensions of the central simulation cell in the x , y , and z directions, respectively.

fstar: magnitude of the repulsive normal force (F^*)

fact: decay parameter of the repulsive normal force (a^*)

Astar: magnitude of the attractive normal force (A_N^*)

decatt: decay parameter of the attractive normal force (a_N^*)

dudxdx, dudxdy, dudxdz, ..., dudzdz: nine components of the ambient flow velocity gradient tensor of the ($\nabla^* \mathbf{U}^{\infty*}$)

Three additional input files, `Centers_of_Mass.in`, `Euler_Parameters.in`, and `Equilibrium_Angles.in`, are used to initialize the values of the fiber positions, orientations, and equilibrium angles, respectively. The following variables are initialized:

$\text{rcmx}(m), \text{rcmy}(m), \text{rcmz}(m)$: coordinates of the center-of-mass of fiber m (\mathbf{R}_{cm}^*) in `Centers_of_Mass.in`

$\text{q0}(m, i), \text{q1}(m, i), \text{q2}(m, i), \text{q3}(m, i)$: Euler parameters of fiber segment i on fiber m (\mathbf{q}_i) in `Euler_Parameters.in`

$\text{theta_eq}, \text{phi_eq}$: the equilibrium angles at a joint ($\theta_i^{\text{eq}}, \phi_i^{\text{eq}}$), in `Equilibrium_Angles.in`

The remaining important variables in the code include:

$\text{A11}(m, i), \text{A12}(m, i), \text{A13}(m, i), \text{A22}(m, i), \text{A23}(m, i), \text{A33}(m, i)$: inverse of the translational resistance tensor for fiber m segment i (\mathbf{A}_i^{-1})

$\text{C11}(m, i), \text{C12}(m, i), \text{C13}(m, i), \text{C22}(m, i), \text{C23}(m, i), \text{C33}(m, i)$: inverse of the rotational resistance tensor for fiber m segment i (\mathbf{C}_i^{-1})

$\text{D1}(m, i), \text{D2}(m, i), \text{D3}(m, i)$: the rotational term from the hydrodynamic torque on an isolated segment ($\tilde{\mathbf{H}} : \mathbf{E}^{\infty*}$)

$\text{E11}, \text{E12}, \text{E13}, \text{E22}, \text{E23}, \text{E33}$: independent terms of the rate of strain tensor of the ambient velocity field ($\mathbf{E}^{\infty*}$)

$\text{ex1}(gc, nc), \text{ex2}(gc, nc), \text{ex3}(gc, nc)$: unit vector that describes the plane of contact, for contact nc in group gc (\mathbf{e}_{ij}^1)

$\text{ey1}(gc, nc), \text{ey2}(gc, nc), \text{ey3}(gc, nc)$: unit vector that describes the plane of contact, for contact nc in group gc (\mathbf{e}_{ij}^2)

$\text{fcx}(m, i), \text{fcy}(m, i), \text{fcz}(m, i)$: components of the total normal force exerted on fiber m , segment i ($\sum_j^{N_{C_i}} \mathbf{F}_{ij}^{N*}$)

$\mathbf{fx}(m,i), \mathbf{fy}(m,i), \mathbf{fz}(m,i)$: components of the total friction force exerted on fiber

m , segment i ($\sum_j^{N_{C_i}} \mathbf{F}_{ij}^{\text{fric}*}$)

$\mathbf{g}(gc,nc)$: centerline separation distance between fiber segments at contact nc in

group gc (g_{ij}^*)

$\mathbf{G}_{ijx}(gc,nc), \mathbf{G}_{ijy}(gc,nc), \mathbf{G}_{ijz}(gc,nc)$: coordinates of the vector from the segment center i to the contact point with segment j , for contact nc in group gc

(\mathbf{G}_{ij}^*)

$\mathbf{G}_{jix}(gc,nc), \mathbf{G}_{jiy}(gc,nc), \mathbf{G}_{jiz}(gc,nc)$: coordinates of the vector from the segment center j to the contact point with segment i , for contact nc in group gc

(\mathbf{G}_{ji}^*)

$\text{ifiber}(k,nc,gc)$: the fiber segments involved in contact nc in group gc ($k = 1$ gives fiber m , $k = 2$ gives segment i , $k = 3$ gives fiber n , and $k = 4$ gives segment j)

kt : twisting constant at a joint ($\kappa_i^* = 0.67\kappa_b^*$)

$\text{nclose}(m,i)$: number of neighbors of fiber m segment i

$\text{ncnt}(gc)$: number of contacts in group gc (N_{C_s})

$\text{next}(k,nc,i)$: neighbor nc of segment i (neighbor list)

$\text{ngrp}(i)$: group number of fiber segment i

$\mathbf{nx}(gc,nc), \mathbf{ny}(gc,nc), \mathbf{nz}(gc,nc)$: coordinates of the normal vector from segment i to segment j for contact nc in group gc (\mathbf{n}_{ij})

$\text{Omega}_x, \text{Omega}_y, \text{Omega}_z$: the angular velocity of the ambient flow field ($\mathbf{\Omega}^{\infty*}$)

$\text{px}(m, i), \text{py}(m, i), \text{pz}(m, i)$: coordinates of the orientation vector of fiber m , segment i (\mathbf{P}_i)

$\text{q0dot}(m, i), \text{q1dot}(m, i), \text{q2dot}(m, i), \text{q3dot}(m, i)$: time derivatives of the Euler parameters of fiber segment i on fiber m ($\dot{\mathbf{q}}_i^*$)

$\text{R11}(m, i), \text{R12}(m, i), \text{R13}(m, i), \text{R21}(m, i), \text{R22}(m, i), \text{R23}(m, i)$: body rotation matrix components of fiber m segment i , where row 3 of the matrix is the fiber segment orientation vector components, $\text{px}(m, i), \text{py}(m, i), \text{pz}(m, i)$; (\mathcal{R}_i)

$\text{R11eq}(m, i), \text{R12eq}(m, i), \dots, \text{R33}(m, i)$: equilibrium frame body rotation matrix of the joint (m, i) ($\mathcal{R}_i^{\text{eq}}$)

$\text{rx}(m, i), \text{ry}(m, i), \text{rz}(m, i)$: coordinates of the center of segment i on fiber m (\mathbf{r}_i^*)

$\text{si}(gc, nc)$: distance from the center of segment i to the point of contact with segment j with respect to the orientation vector (s_{ij}^*)

$\text{sj}(gc, nc)$: distance from the center of segment j to the point of contact with segment i with respect to the orientation vector (s_{ji}^*)

$\text{Stress}(i, j)$: the ij component of the dimensionless stress tensor at the given strain interval ($\boldsymbol{\sigma}^p(\gamma)/\sigma^*$, where $\sigma^* = \pi n L^3 \eta_o \dot{\gamma} / 6 N_{\text{seg}}^3 \ln 2r_p$)

$\text{Stress_Avg}(i, j)$: the ij component of the dimensionless time averaged stress tensor (same term as Stress averaged over all of the configurations obtained for $\gamma \geq \gamma_{\text{ss}}$)

$\text{tcx}(m, i), \text{tcy}(m, i), \text{tcz}(m, i)$: components of the total normal torque exerted on fiber m , segment i ($\sum_j^{N_{C_i}} [\mathbf{G}_{ij}^* \times \mathbf{F}_{ij}^{N^*}]$)

$\mathbf{tx}(m, i), \mathbf{ty}(m, i), \mathbf{tz}(m, i)$: components of the total friction torque exerted on fiber

m , segment i ($\sum_j^{N_{C_i}} [\mathbf{G}_{ij}^* \times \mathbf{F}_{ij}^{\text{fric}*}]$)

$\text{ucmx}(m), \text{ucmy}(m), \text{ucmz}(m)$: coordinates of the translational velocity of the center-

of-mass of fiber m ($\dot{\mathbf{R}}_{\text{cm}}^*$)

$\text{ux}(m, i), \text{uy}(m, i), \text{uz}(m, i)$: components of the translational velocity of segment i

on fiber m ($\dot{\mathbf{r}}_i^*$)

$\text{wx}(m, i), \text{wy}(m, i), \text{wz}(m, i)$: components of the angular velocity of segment i on fiber

m ($\boldsymbol{\omega}_i^*$)

X_a, Y_a, X_c, Y_c, Y_h : scalar resistance functions for a prolate spheroid of aspect ratio

$0.7r_{ps}$ (X^A, Y^A, X^C, Y^C , and Y^H)

$X_x(m, i), X_y(m, i), X_z(m, i)$: the coordinates of the inextensibility force at joint i on

fiber m (\mathbf{X}_i^*)

$Y_x(m, i), Y_y(m, i), Y_z(m, i)$: the coordinates of the total restoring torque at joint i

on fiber m (\mathbf{Y}_i^*)

At the specified time intervals, the code outputs various quantities. The output files include:

`center_mass.dat`: all of the fiber centers of mass at the given strain interval

`euler_param.dat`: all of the fiber segment Euler parameters at the given strain interval

`inextens_next_guess.dat`: all of the inextensibility constraint forces at the given strain interval

Number_of_Contacts.dat: the number of groups, contacts, and overlapping fibers is written at the given time interval

Contact_info.dat: this file contains the fiber segments involved in a contact, the number of the contact, and the values of s_{ij}^* , s_{ji}^* , and g_{ij}^* at the given strain interval

flexfric.f90

```

! Approximate code for flexible fibers with static friction.
! This code first solves for the motion of nfib flexible fibers
! made up of nseg rigid spherocylinders. The main body of the code
! is contained within the file flexfric.f90. The following
! files are read by flexfric.f90:
! 1. arraysize.f - gives dimension parameters for arrays
! 2. config.f90 - gives configurations
! 3. delta twist.f90 - contains the subroutine 'delta twist' which
! finds the separation between fiber surfaces and the
! bend/twisting potentials
! 4. files.f90 - read/write files
! 5. friction forces.f90 - contains the subroutine 'friction forces'
! which calculates the explicit contact friction forces
! 6. initialize.f90 - this section reads the input files and set
! initial values for numerous variables
! 7. isotropic bend.f90 - code to calculate the bend/twisting
! potential (included in 'delta twist')
! 8. motion integrate.f90 - contains the subroutine 'motion integrate'
! which integrates the equations of motion to update coordinates
! 9. neighbor.f90 - contains two subroutines,
! 'neighbor' - creates neighbor lists, and
! 'parallel' - finds separation for parallel fibers
! 10. sort.f90 - contains the subroutine 'sort' which sorts segments
! into contacting groups (called by delta twist)
! 11. static friction.f90 - Coulombic friction constraint is
! applied here (found within 'friction forces')
! 12. variables.f90 - declaration of all variables in the main body
! 13. x forces.f90 - contains the subroutine 'x forces' which
! calculates the constraint forces at the joints
#####
##### START PROGRAM #####
#####
program flexfric
implicit none
! All of the variables in the main body of the program
integer nobj,npcn,ngr
! nobj - number of fibers
! nos - number of segments
! npcn - number of potential contacts
! ngr - number of potential groups
parameter (nobj=400,nos=5,npcn=500,ngr=700)
real*8 :: p
parameter (p1=3.14159265359)
real*8,dimension(nobj) :: rcmx,rcmy,rcmz,ucmx,ucmy,ucmz,ucvx,ucvy,ucvz
real*8,dimension(nobj,nos) :: fx,fy,fz,qd,qd1,qd2,qd3,fxp,fyp
real*8,dimension(nobj,nos) :: ux,uy,uz,wx,wy,wz,uxf1,uyf1,uzf1
real*8,dimension(nobj,nos) :: qdotc,qdotc1,qdotc2,qdotc3,qe1,qe2,qe3
! rcmx,rcmy,rcmz - fiber center of mass
! fx,fy,fz - segment centers
! qd,qd1,qd2,qd3 - segment euler parameters
! qdotc,... - time derivatives of Euler Parameters
! qe1,... - time derivatives of Euler Parameters from previous time
! fxp,fyp,z - segment orientational vectors
! ucmx,ucmy,ucmz - fiber center of mass velocity
! ucov,ucovy,ucovz - fiber center of mass velocity from previous time
! ux,uy,uz - segment velocity
! uxfl,uyfl,uzfl - ambient flow field velocity
! wx,wy,wz - segment angular velocity
! real*8,dimension(nobj,nos) :: R11,R12,R13,R21,R22,R23
! real*8,dimension(nobj,nos) :: R11eq,R12eq,R13eq,R21eq,R22eq,R23eq
! real*8,dimension(nobj,nos) :: R31eq,R32eq,R33eq
! R11,R12,... - segment rotation matrix
! R11eq,... - equilibrium rotation matrix
! Xx,Xy,Xz - intrafiber constraint forces
! Yx,Yy,Yz - restoring bending/twisting torques
! real*8,dimension(nobj,nos) :: Fx,Fy,Fz,tbx,tby,tz
! real*8,dimension(nobj,nos) :: fbx,fby,fbz,tbx,tby,tbz
! real*8,dimension(nobj,nos) :: fbx,fby,fbz,tbx,tby,tbz
! fx,fy,fz - frictional forces on segment
! tbx,tby,tz - segment body force (i.e. gravity,etc.)
! fbx,fby,fbz - segment body force
! tbx,tby,tbz - segment body torque
! fcx,fcy,fcz - segment colloidal repulsive force
! tcx,tcy,tcz - segment colloidal repulsive torque
! real*8,dimension(nobj,nos) :: D1,D2,D3,A11,A12,A13,A23,A22,A33
! real*8,dimension(nobj,nos) :: C11,C12,C13,C23,C22,C33
! D1,D2,D3 - "Jeffery" term in hydrodynamic torque
! A11,... - A inverse term in notes
! C11,... - C inverse term in notes
! real*8,dimension(nobj,npcn) :: nx,ny,nz,si,sj,q
! real*8,dimension(nobj,npcn) :: ex1,ex2,ex3,ey1,ey2,ey3
! real*8,dimension(nobj,npcn) :: G1x,G1y,G1z,G2x,G2y,G2z
! nx,ny,nz - normals between contacting fibers
! si,sj - distance from center of segment to contact point
! g - gap between fiber centers at contact point
! ex1,...,ex3,ey1,...,ey3 - vector from i to contact point
! G1j,...,G2j - vector from j to contact point
! integer :: next(2,4,npcn,nobj),nclose(nobj,nos)
! integer :: ifiber(4,npcn,ngr),ngr(nobj,nos),ncnt(ngr),ncpfn(nobj,nos)
! next(i,h,m,i) - i-th neighbor of fiber m, segment i
! nclose(m,i) - number of neighbors of fiber m, segment i
! ifiber(1,ct,mg) - 1st fiber in contact ct, group mg
! ngr(m) - group # of fiber m
! ncnt(mg) - # of contacts in group mg
! ncpfn(m) - number of contacts with fiber m
! real*8 :: Omega_x,Omega_y,Omega_z,fp,kb,kt,dt,dtstrain
! side_x,side_y,side_z,E11,E12,E13,E22,E23,E33
! real*8 :: re,ec,ex,ey,ez,fc,fd,fr,fract,fp,thet,taeq,phi,eq
! Omega... - ambient flow field angular velocity
! rp - segment aspect ratio
! kb/kt - bending/twisting constants
! thetaeq/phi,eq - angles associated with the equil. configuration
! dt,dtstrain - time step, total time of run
! side_x,side_y,side_z - simulation box dimensions (x and y directions)
! E11,E12,sidey - rate of strain tensor
! rp - effective segment aspect ratio
! ec - eccentricity
! ex,ey,ez,fc,fd,fr - scalar resistance functions
! fract,fp - effective aspect ratio factor
! real*8 :: delta_x,mu_stat,mu_kin
! real*8 :: contact_cutoff,rep_cutoff,neighb_cutoff
! real*8 :: fstar,Fact,Actb,deact
! delta_x - shift variable for sliding periodic images
! mu_stat,mu_kin - static/kinetic coefficient of friction
! contact_cutoff - cutoff for contacts
! rep_cutoff - cutoff distances for calculating repulsive forces
! neighb_cutoff - cutoff for neighborlist
! fstar,fract - force prefactor, force exponential factor (decay length)
! Actar - Prefactor of the attractive force
! deact - decay length of the attractive force
! integer :: nfib,nseg,time_steps,num_groups,overs
! integer :: config_write,contact_write,check_neighbor,extra_write
! nfib,nseg - number of fiber, segments per fiber
! config_write - number of time steps between configuration writes
! check_neighbor - number of time steps between contact info writes
! extra_write - number of time steps between neighbor list checks
! time_steps - number of time steps
! num_groups - number of groups
! overs - number of overlapping contacts
! integer :: nrhs,lda,ldb,ldab,ldk,N_band,k1,ku
! nrhs - number of right hand sides for solving our linear systems
! lda - leading order dimension of the friction matrix
! ldb - leading order dimension of the right hand side
! ldab - leading order of the band storage matrix in solving for X

```

flexfric.f90

```

! ldx - leading order of rhs in solving for X
! Nband - dimension of matrix to solve for X (3*(nseq-1))
! kl/ku - number of lower/upper diagonal terms in banded matrix
real*8 :: nl3,volfrac,consistency,over_cut
! nl3 - dimensionless concentration ("n-I-cubed")
! volfrac = volume fraction
! consist - consistency = volfrac/2.6
! over_cut - limit to the overlapping of two fibers
real*8 :: duxdx,duydy,duzdz,duydz,duydy,duydz,duzdx,duzdy,duzdz
real*8 :: C0,C1,C2,C3,C4,rlimsq
! duxdx... - velocity gradient tensor
! C0,C1... - constant groupings
! rlimsq - initial squared cutoff distance for contacting fibers
! #####
! Various temporary variables
integer :: idum1,idum2,mth,k,step,m,i,n,j,gc,ic,totai,contacts
! #####
! Common statements
common /rpsqgs/ tx,rv,tz,q0,q1,q2,q3,px,py,pz
common /rcm/ rcmx,rcmy,rcmz
common /fric_forces/ fx,fy,fz,tx,ty,tz
common /rep_forces/ fcx,fcy,fcz,tcx,tcy,tcz,fbx,fbz,tbx,tby,tbz
common /velocities/ ux,uy,uz,wx,wy,wz,q0dot,q1dot,q2dot,q3dot
common /um/ ucmx,ucmy,ucmz
common /ambicnt/ uxf1,uyf1,uzf1,ufz1,ufz1,Omega_x,Omega_y,Omega_z
common /params/ rlimsq,rcmz,step,m,i,n,j,gc,ic,totai,delta_rx
common /contact1/ ifiber,nrpp,nrcnt,rcpf,num_groups
common /contact2/ nx,ny,nz,si,sj,g,ex1,ex2,ex3,ey1,ey2,ey3,e
common /G1jx,G1jy,G1jz,G1ix,G1iy,G1iz
common /rotation/ R11,R12,R13,R21,R22,R23
common /equilrot/ R1eq,R2eq,R3eq,R13eq,R22eq,R23eq,R31eq,R32eq,R33eq
common /constaets/ Ya,Yc,Yb,C0,C1,C3,C4
common /points/ Yx,Yy,Yz,Xx,Yy,Xz
common /apcband/ Yb,Yby,Ybz
common /laststep/ req,qe1,qe2,qe3,ucox,ucoy,ucoz
! Files that are read
open (10,file='Parameters.in',status='old')
open (11,file='Files_Parameters.in',status='old')
open (12,file='Files_Parameters.in',status='old')
open (13,file='Equilibrium_Angles.in',status='old')
open (14,file='Xforces.in',status='unknown') ! Needed if restarting
! Files that are written to
open (20,file='README',status='unknown')
open (21,file='center_mass.dat',status='unknown')
open (22,file='euler_param.dat',status='unknown')
open (23,file='resist_func.dat',status='unknown')
open (24,file='inextens_next_guess.dat',status='unknown')
open (31,file='Contact_Info.dat',status='unknown')
open (40,file='dgsqv_errors.dat',status='unknown')
open (41,file='dgsqv_errors.dat',status='unknown')
! Format statements
1013 format (i4,3(iX,1pD23.15))
1023 format (i4,1X,13,3(1X,1pD23.15))
1026 format (i4,1X,13,6(1X,1pD23.15))
1024 format (i4,1X,13,4(1X,1pD23.15))
1063 format (i11,6,1X,6(13,1X),3F)
1113 format (f10.5,2(zx,14),1(zx,1pD23.15))
! Read in parameters and initial configuration information
read (10,*) nfile
read (10,*) nseq
read (10,*) rp
read (10,*) Rb

```

```

read (10,*) mu_stat
read (10,*) mu_kin
read (10,*) contact_cutoff
read (10,*) rep_cutoff
read (10,*) neighb_cutoff
read (10,*) over_cut
read (10,*) dt
read (10,*) strain
read (10,*) sidex,sidey,sidez
read (10,*) fraction_rp
read (10,*) config_write
read (10,*) contact_write
read (10,*) extra_write
read (10,*) check_neighbor
read (10,*) fstar_neighbor
read (10,*) fact
read (10,*) Astar
read (10,*) decaat
read (10,*) delta_rx
read (10,*) duxdx ! Read in velocity gradient.
read (10,*) duydy
read (10,*) duzdz
read (10,*) duxdx
read (10,*) duydy
read (10,*) duzdy
read (10,*) duxdy
read (10,*) duzdy
read (10,*) duzdx
read (10,*) duzdy
! Fiber coordinates
do m = 1,nfile
  read (11,*) idum1,rcmx(m),rcmy(m),rcmz(m)
  do i = 1,nseq
    read (12,*) idum1,idum2,q0(m,i),q1(m,i),q2(m,i),q3(m,i)
    dum = dsqrt(q0(m,i)**2 + q1(m,i)**2 + q2(m,i)**2 + q3(m,i)**2)
    q0(m,i) = q0(m,i)/dum
    q1(m,i) = q1(m,i)/dum
    q2(m,i) = q2(m,i)/dum
    q3(m,i) = q3(m,i)/dum
    ! uncommment to read in X-forces
    ! read (14,*) idum1,idum2,Xx(m,i),Xy(m,i),Xz(m,i)
    ! Find the soact matrix
    R11(m,i) = 2.00*(q0(m,i)*q0(m,i)+q1(m,i)*q1(m,i)*d1(m,i)) - 1.00
    R12(m,i) = 2.00*(q1(m,i)*q2(m,i) + q0(m,i)*q3(m,i))
    R13(m,i) = 2.00*(q1(m,i)*q3(m,i) - q0(m,i)*q2(m,i))
    R21(m,i) = 2.00*(q1(m,i)*q2(m,i) - q0(m,i)*q3(m,i))
    R22(m,i) = 2.00*(q2(m,i)*q2(m,i)+q2(m,i)*q2(m,i)) - 1.00
    R23(m,i) = 2.00*(q3(m,i)*q2(m,i) + q0(m,i)*q2(m,i))
    R31(m,i) = 2.00*(q1(m,i)*q3(m,i) + q0(m,i)*q2(m,i))
    R32(m,i) = 2.00*(q2(m,i)*q3(m,i) - q0(m,i)*q1(m,i))
    R33(m,i) = 2.00*(q3(m,i)*q3(m,i) - q0(m,i)*q1(m,i))
    px(m,i) = 2.00*(q1(m,i)*q3(m,i) + q0(m,i)*q2(m,i))
    py(m,i) = 2.00*(q2(m,i)*q3(m,i) - q0(m,i)*q1(m,i))
    pz(m,i) = 2.00*(q0(m,i)*q3(m,i) - q0(m,i)*q1(m,i))
    dum = dsqrt(px(m,i)**2+py(m,i)**2+pz(m,i)**2)
    px(m,i) = px(m,i)/dum
    py(m,i) = py(m,i)/dum
    pz(m,i) = pz(m,i)/dum
    ! Assign body forces and torques.
    fbx(m,i) = 0.00
    fby(m,i) = 0.00
    fbz(m,i) = 0.00
    tbx(m,i) = 0.00
    tby(m,i) = 0.00
    tbz(m,i) = 0.00
    ! Make the equilibrium rotation matrix
    if (i > 1) then
      read (13,*) idum1,idum2,theaeg,phieq
      R1ieq(m,i) = dcos(theaeg)*dcsin(phieq)
      R2ieq(m,i) = dcos(theaeg)*dsin(phieq)
      R3ieq(m,i) = -dsin(theaeg)
      R2ieq(m,i) = -dsin(phieq)

```


flexfric.f90

```

      neighb_cutoff,rllmsq,dt*step,a_rp,b_rp)
! First calculate the friction forces based on the X-forces
! from the previous time step
call friction_forces(mu,stat,mu_kin,fstar,fact,nrhs,lda,lldb, &
  step*dt,C0,C1,nx,uy,uz,total_contacts,Astar,deccat)
! Now find the X-forces with the new friction forces
call x_forces(nrhs,N_band,ldab,ldx,ku,k1,C0,C1,C2,C3,C4,Ya,Yc, &
  step*dt)
! Integrate the equations of motion and update coordinates
call motion_integrate(dt,step,C0,dt*step)
! Shift top and bottom cells for Lees-Edwards modification
delta_rx = delta_rx + sidex*dt
delta_ry = delta_ry - drint(delta_rx/sidex)*sidex
! Find the separations for the next time step
call delta_twist(over_cut,contact_cutoff,rep_cutoff, &
  next,nclose,overs,fstar,fact,fb,kt,dt*step,Astar,deccat)
! Write our contacting fibers every extra_write steps
if(mod(step,extra_write) == 0)then
  do gc = 1, num_groups
    do ic = 1, ncont(gc)
      m=ifiber(1,ic,gc);i=ifiber(2,ic,gc)
      n=ifiber(3,ic,gc);j=ifiber(4,ic,gc)
      write(35,1063) dt*step,m,i,n,j,gc,ic, &
        si(gc,ic),sj(gc,ic),g(gc,ic)
    enddo
  enddo
endif
! Write contact evolution every contact_write steps
if(mod(step,contact_write) == 0)then
  write(37,1113) dt*step,num_groups,total_contacts,overs
endif
! Rewrite configurations every config_write steps
! Write out configurations at the prescribed time step
if(mod(step,config_write) == 0)then
  write(21,*) step*dt
  write(22,*) step*dt
  write(26,*) step*dt
  do m = 1, nfib
    write(21,1013) m,rcmx(m),rcmy(m),rcmz(m)
  do
    write(22,1024) m,i,q0(m,i),q1(m,i),q2(m,i),q3(m,i)
    write(26,1023) m,i,xx(m,i),xy(m,i),xz(m,i)
  enddo
enddo
endif
enddo Main
end Program flexfric

```


neighbor_list.f90

```

real*8 :: sx,sy,sz,px,py,piz,pjx,pjy,pjz,pdotp,rp,xmin,ymin
real*8 :: posneg,pn2,dist,sjip,sjim,sjip,sjim
integer :: m,i,n,j
! The different end point to fiber contact points
sjip = pi*x + pi*y + pi*z + rp*pdotp
sjim = pi*x + pi*y + pi*z - rp*pdotp
sjip = -(pj*x + pj*y + pj*z + pjz*sz) + rp*pdotp
sjim = -(pj*x + pj*y + pjz*sz) - rp*pdotp
! For fiber i
if (Abs(sjip) < Abs(sjim)) then
  xmin = sjip
  posneg = 1.D0
elseif (Abs(sjip) > Abs(sjim)) then
  xmin = sjim
  posneg = -1.D0
else
  xmin = 0.D0
  posneg = 0.D0
endif
! For fiber j
if (xmin >= rp) xmin = rp
if (xmin <= -rp) xmin = -rp
! For fiber i
if (Abs(sjip) < Abs(sjim)) then
  ymin = sjip
elseif (Abs(sjip) > Abs(sjim)) then
  ymin = sjim
else
  ymin = 0.D0
  posneg = 0.D0
endif
if (ymin >= rp) ymin = rp
if (ymin <= -rp) ymin = -rp
if (Abs(xmin) < rp .and. Abs(ymin) < rp) then
  if (pdotp > 0.D0) then
    pn2 = 1.D0
  else
    pn2 = -1.D0
  endif
endif
dist = (rp + posneg*xmin)/2.D0
xmin = xmin - posneg*dist
ymin = ymin + posneg*pn2*dist
endif
end subroutine parallel

```

delta_twist.f90

```

!*****
! Subroutine: delta_twist
! calculates the bending/twisting torques as well as
! interparticle separations
!*****
subroutine delta_twist(over_cut,contact_cutoff,rep_cutoff, &
next_nclose,overs,fsfar,fbt,kt,time,Astar,decat)
implicit none
integer nof,nos,npcn,npr
parameter (nof=400,nos=5,npcn=500,npr=700)
! Variables from the Main Body
real*8,dimension(nof,nos) :: rx,ry,tz,q1,q2,q3,px,py,pz
real*8,dimension(nof,nos) :: ux1,uy1,uz1,r11,r12,r13,r21,r22,r23
real*8,dimension(nof,nos) :: R11eq,R12eq,R13eq,R21eq,R22eq,R23eq
real*8,dimension(nof,nos) :: R31eq,R32eq,R33eq
real*8,dimension(nof,nos) :: fx,fy,fz,tx,ty,tz
real*8,dimension(nof,nos) :: fcx,fcy,fcz,tcx,tcy,tcz
real*8,dimension(nof,nos) :: fbx,fbz,fbt,tbx,tbz,tz
real*8,dimension(nof,nos) :: D1,D2,D3,A11,A12,A13,A23,A22,A33
real*8,dimension(nof,nos) :: C11,C12,C13,C23,C22,C33
real*8,dimension(nof,nos+1) :: Yx,Yy,Yz,XX,XY,Xz,Ybx,Yby,Ybz
real*8,dimension(npr,npcn) :: nx,ny,nz,si,sj,g
real*8,dimension(npr,npcn) :: ex1,ex2,ex3,ey1,ey2,ey3
real*8 :: IP,sidex,sidz,sides,delta_rx,kt,over_cut,Astar,decat
real*8 :: E11,E12,E13,E22,E23,E33,C0,C1,C3,C4,Ya,Yc,Yh,rep_cutoff
integer :: nfib,nseg,num_groups,overs
integer :: ifiber(4,npcn,npr),ngrp(nof*nos),ncnt(npnr)
integer :: ncpf(nof*nos),next(2,4*npcn,nof*nos),nclose(nof*nos)
! New Variables
real*8 :: dx,dy,svy,svz,cx,cy,cz,xmin,ymin,ang_theta,ang_phi
real*8 :: dx,dy,az,g1j,n1j,n2j,n3j,force
! sxx,svy,svz - segment center of mass separation vector
! cx,cy,cz - unit vector of (sxx,svy,svz)
! xmin,ymin - distance to contact along fiber from center
! ang_theta,ang_phi - amount the joint is deformed from equil.
! dby,dz - vector connecting contact point to contact point
! g1j,temp - vector to contact distance at contact point
! force - magnitude of normal force at contact
! The rest are dummy variables
real*8 :: xami,yami,zami,pdotp,ss,sm,ym,sep,tmp,xi(8),yj(8),sep
real*8 :: zexx,zexy,zexz,zdccc,d1x,d1y,d1z,dir,dum
real*8 :: y1cx,y1cy,y1tz,y1eqz,y1eqy,y1eqz,y1eqz
real*8 :: y2cx,y2cy,y2tz,y2eqz,y2eqy,y2eqz,y2eqz
integer :: m1,n1,j1,k1,corx,corz,corz1,ipos,ith
common /spsqs/ ix,iy,iz,q0,q1,q2,q3,px,py,pz
common /frc_forces/ fcx,fcy,fcz,tcx,tcy,tcz,fbx,fbz,tbx,tbz
common /ambnt/ ux1,uy1,uz1,omega_x,omega_y,omega_z
common /andcc/ D1,D2,D3,A11,A12,A13,A23,A22,A33, &
C11,C12,C13,C23,C22,C33
common /params/ nfib,nseg,ip,sidex,sidz,sides,delta_rx
common /contact/ ifiber,ngrp,ncnt,ncpf,num_groups
common /contact2/ nx,ny,nz,si,sj,g,ex1,ex2,ex3,ey1,ey2,ey3, &
G1jX,G1jY,G1jZ,G1jX,G1jY,G1jZ
common /rotation/ R11,R12,R13,R21,R22,R23
common /equilrot/ R11eq,R12eq,R13eq,R21eq,R22eq,R23eq, &
R31eq,R32eq,R33eq
common /constants/ Ya,Yc,Yh,C0,C1,C3,C4
common /joints/ Yx,Yy,Yz,XX,XY,Xz
common /specbend/ Ybx,Yby,Ybz
! Zero variables

```

```

do m = 1, num_groups
ncnt(m) = 0
enddo
num_groups = 0; overs = 0
do m = 1, nfib
do i = 1, nseg
fx(m,i) = 0.D0; fy(m,i) = 0.D0; fz(m,i) = 0.D0
tx(m,i) = 0.D0; ty(m,i) = 0.D0; tz(m,i) = 0.D0
fx(m,i) = 0.D0; fy(m,i) = 0.D0; fz(m,i) = 0.D0
tx(m,i) = 0.D0; ty(m,i) = 0.D0; tz(m,i) = 0.D0
ngrp(m-1)*nseg+i = 0
enddo
! Loop over all fiber segments
do m = 1, nfib
do i = 1, nseg
! The inner loop only looks for neighbors of segment (m,i)
do k = 1, nclose(m-1)*nseg+i
n = next(1,k,(m-1)*nseg+i)
j = next(2,k,(m-1)*nseg+i)
forc = 0.D0
! Find minimum image (for shear flow system).
sxx = rx(n,j) - rx(m,i)
syy = ry(n,j) - ry(m,i)
szz = rz(n,j) - rz(m,i)
corx = dnint(syy/sidex)
corz = dnint(szz/sidex)
sxx = sxx - corz*delta_rx
syy = sxx - corx*sidex
szz = sxx - corx*sidex
rxi = rx(n,j) - sxx
ryi = ry(n,j) - syy
rzi = rz(n,j) - szz
! Locate positions on rod segments from the center of
! masses that correlate to the closest separation
! point between the rod segments
pdotp = px(m,i)*rx(n,j) + py(m,i)*py(n,j) + pz(m,i)*pz(n,j)
! Check if segments are parallel
if (pdotp*pdotp /= 0.D0) then
call parallel(sxx,svy,szz,px(m,i),py(m,i),pz(m,i), &
px(n,j),py(n,j),pz(n,j),pdotp,rxami,yami)
sep = (sxx*yami*py(n,j)-xmini*px(m,i))*2 + &
(szy*yami*pz(n,j)-xmini*pz(m,i))*2 + &
(szz*yami*pz(n,j)-xmini*pz(m,i))*2
g1j = dsqrt(sep)
n1jx = (sxx-yami*px(n,j)-xmini*px(m,i))/g1j
n1jy = (syy-yami*py(n,j)-xmini*py(m,i))/g1j
n1jz = (szz-yami*pz(n,j)-xmini*pz(m,i))/g1j
if (g1j < 2.D0) overs = overs + 1
if (sep < over_cut) g1j = over_cut
forc = fstar*dexp(-decat*(g1j-2.D0)) * (g1j-2.D0)
! Sort segments if they are contacting
if (sep < contact_cutoff) call sort(nseg,m,i,n,j, &
xmin,ymin,g1j,n1jx,n1jy,n1jz,px,py,pz,time,rep)
! Not parallel, find closest distance between two lines
else
xmin = -(px(n,j)*sxx+py(n,j)*syy+pz(n,j)*szz)*pdotp + &
(px(m,i)*sxx+py(m,i)*syy+pz(m,i)*szz)/ &
(1.D0-pdotp*pdotp)
ymin = (px(m,i)*sxx+py(m,i)*syy+pz(m,i)*szz)*pdotp - &
(px(n,j)*sxx+py(n,j)*syy+pz(n,j)*szz)/ &
(1.D0-pdotp*pdotp)
dx = rx(n,j)*ymin*px(m,i) - rx(m,i)*xmin*px(n,i)
dy = ry(n,j)*ymin*py(m,i) - ry(m,i)*xmin*py(n,i)
dz = rz(n,j)*ymin*pz(m,i) - rz(m,i)*xmin*pz(n,i)

```


delta_twist.f90

```

dum = dsqrt(yitx*yitx+yity*yity+yitz*yitz)
yitx = yitx/dum
yity = yity/dum
yitz = yitz/dum
yieqx = zeqx - cx*(cx*zeqx+cy*zeqy+cz*zeqz)
yieqy = zeqy - cy*(cx*zeqx+cy*zeqy+cz*zeqz)
yieqz = zeqz - cz*(cx*zeqx+cy*zeqy+cz*zeqz)
dum = dsqrt(yieqx*yieqx+yieqy*yieqy+yieqz*yieqz)
yieqx = yieqx/dum
yieqy = yieqy/dum
yieqz = yieqz/dum
zdotz = yitx*yieqx + yity*yieqy + yitz*yieqz
dirx = yity*yieqz - yitz*yieqy
diry = yitz*yieqx - yitx*yieqz
dirz = yitx*yieqy - yity*yieqx
dum = DSQR(dirx*dirx + diry*diry + dirz*dirz)
if (zdotz.gt.1.D0-1.e-14) then
  Ytx = 0.D0
  Yty = 0.D0
  Ytz = 0.D0
else
  ang_phi = DACOS(zdotz)
  Ytx = -kt*ang_phi*(dirx/dum)
  Yty = -kt*ang_phi*(diry/dum)
  Ytz = -kt*ang_phi*(dirz/dum)
endif
! Add the bending and twisting torques together
Yx(m,i) = Ybex + Ytx
Yy(m,i) = Ybey + Yty
Yz(m,i) = Ybez + Ytz
endif
! Calculate some commonly used groupings
A11(m,i) = 1.D0/Ya + C3*Fz(m,i)*Fz(m,i)
A12(m,i) = C3*Fz(m,i)*Fy(m,i)
A13(m,i) = C3*Fz(m,i)*Fz(m,i)
A22(m,i) = 1.D0/Ya + C3*Fy(m,i)*Fy(m,i)
A23(m,i) = C3*Fy(m,i)*Fz(m,i)
A33(m,i) = 1.D0/Ya + C3*Fz(m,i)*Fz(m,i)
C11(m,i) = 1.D0/Yc + C4*Fz(m,i)*Fz(m,i)
C12(m,i) = C4*Fz(m,i)*Fy(m,i)
C13(m,i) = C4*Fz(m,i)*Fz(m,i)
C22(m,i) = 1.D0/Yc + C4*Fy(m,i)*Fy(m,i)
C23(m,i) = 1.D0/Yc + C4*Fz(m,i)*Fz(m,i)
D1(m,i) = -Yt*(E12*Fz(m,i)+E23*Fz(m,i)+E23*Fz(m,i))*Fz(m,i) - s
D2(m,i) = -Yt*(E13*Fz(m,i)+E23*Fz(m,i)+E23*Fz(m,i))*Fy(m,i) - s
D3(m,i) = -Yt*(E11*Fz(m,i)+E12*Fy(m,i)+E13*Fz(m,i))*Fz(m,i) - s
D3(m,i) = -Yt*(E11*Fz(m,i)+E12*Fy(m,i)+E13*Fz(m,i))*Fy(m,i) - s
! ambient velocity field
uxfl(m,i) = rz(m,i) - uyfl(m,i)
uzfl(m,i) = 0.D0
enddo
enddo
end subroutine delta_twist

```


sort.f90

```

ncont(itmp) = 0
ic = 0
do ii = nctmp+1, ncont(mgt)
  ic = ic + 1
  ifiber(1,ii,mgt) = ifiber(1,ic,itmp)
  ifiber(2,ii,mgt) = ifiber(2,ic,itmp)
  ifiber(3,ii,mgt) = ifiber(3,ic,itmp)
  ifiber(4,ii,mgt) = ifiber(4,ic,itmp)
  m_old = (ifiber(1,ic,itmp)-1)*nseg + ifiber(2,ic,itmp)
  n_old = (ifiber(3,ic,itmp)-1)*nseg + ifiber(4,ic,itmp)
  ngrp(m_old) = ngrp(m)
  ngrp(n_old) = ngrp(m)
  si(mgt,ii) = si(itmp,ic)
  sj(mgt,ii) = sj(itmp,ic)
  nx(mgt,ii) = nx(itmp,ic)
  ny(mgt,ii) = ny(itmp,ic)
  nz(mgt,ii) = nz(itmp,ic)
  G1jx(mgt,ii) = G1jx(itmp,ic)
  G1jy(mgt,ii) = G1jy(itmp,ic)
  G1jz(mgt,ii) = G1jz(itmp,ic)
  G2jx(mgt,ii) = G2jx(itmp,ic)
  G2jy(mgt,ii) = G2jy(itmp,ic)
  G2jz(mgt,ii) = G2jz(itmp,ic)
  G3jx(mgt,ii) = G3jx(itmp,ic)
  G3jy(mgt,ii) = G3jy(itmp,ic)
  G3jz(mgt,ii) = G3jz(itmp,ic)
  G4jx(mgt,ii) = G4jx(itmp,ic)
  G4jy(mgt,ii) = G4jy(itmp,ic)
  G4jz(mgt,ii) = G4jz(itmp,ic)
enddo

ncont(mgt) = ncont(mgt) + 1
ifiber(1,ncont(mgt),mgt) = m2; ifiber(2,ncont(mgt),mgt) = i
ifiber(3,ncont(mgt),mgt) = n2; ifiber(4,ncont(mgt),mgt) = j
si(mgt,ncont(mgt)) = si; sj(mgt,ncont(mgt)) = sj;
g(mgt,ncont(mgt)) = g;
nx(mgt,ncont(mgt)) = ni; ny(mgt,ncont(mgt)) = nj;
nz(mgt,ncont(mgt)) = ni;
G1jx(mgt,ncont(mgt)) = si; G1jy(mgt,ncont(mgt)) = sj;
G1jz(mgt,ncont(mgt)) = g;
G2jx(mgt,ncont(mgt)) = si; G2jy(mgt,ncont(mgt)) = sj;
G2jz(mgt,ncont(mgt)) = g;
G3jx(mgt,ncont(mgt)) = si; G3jy(mgt,ncont(mgt)) = sj;
G3jz(mgt,ncont(mgt)) = g;
G4jx(mgt,ncont(mgt)) = si; G4jy(mgt,ncont(mgt)) = sj;
G4jz(mgt,ncont(mgt)) = g;
endif
endif
return
end subroutine sort

```

friction_forces.f90

```

!*****
! Subroutine: friction_forces
! calculates static friction forces on groups of
! contacting fiber segments
!*****
subroutine friction_forces(mu_stat,mu_kin,fstar,fact,nrhs,lda,ldeb, &
    time,C0,C1,ux,uy,uz,total_contacts,Astar,deccat)
    implicit none
    integer nof,nos,npcn,npgr
    parameter (nof=400,nos=5,npcn=500,npgr=700)
    ! Old variables
    real*8,dimension(nof,nos) :: rx,ry,tz,q0,q1,q2,q3,px,py,pz
    real*8,dimension(nof,nos) :: fx,fy,fz,tx,ty,tz
    real*8,dimension(nof,nos) :: fcx,fcy,fcz,tcx,tcy,tcz
    real*8,dimension(nof,nos) :: D1,D2,D3,A11,A12,A13,A23,A22,A33
    real*8,dimension(nof,nos) :: C11,C12,C13,C23,C22,C33
    real*8,dimension(nof,nos) :: fbx,fbz,tbx,tbz
    real*8,dimension(nof,nos) :: uxfl,uyfl,uzfl,ux,uy,uz
    real*8,dimension(nof,nos+1) :: Yx,Yy,Yz,XX,XY,Xz
    real*8,dimension(npgr,npcn) :: nx,nv,nz,si,sj,g
    real*8,dimension(npgr,npcn) :: ex1,ex2,ex3,ey1,ey2,ey3
    real*8,dimension(npgr,npcn) :: G1jx,G1jy,G1jz,G1jx,G1jy,G1jz
    real*8 :: time,C0,C1,mu_stat,mu_kin,fstar,fact,Astar,deccat
    integer :: nfib,nseg,num_groups,ifiber(4,npcn,npgr)
    integer :: nprp(nof*nos),ncont(npgr),ncpf(nof*nos)
    ! New variables
    ! total_contacts,nrhs,ldeb,ldeb,N_size
    real*8 :: P(3*npcn),A(3*npcn,3*npcn)
    real*8 :: A_back(3*npcn,3*npcn),P_back(3*npcn)
    ! A_back - two copies of the matrix describing contacts
    ! P_back - two copies of right hand side vector with A
    ! Dummy variables
    real*8 :: det,fric_max,fric_sq
    real*8 :: fux,qv,qv_dum,Ok(3,3),posneg,C1x,G1y,G1z,G2x,G2y,G2z
    real*8 :: dirx,diry,dirz,ax,ay,az,ajx,ajy,ajz
    real*8 :: forc,bix,bjz,bjx,bjy,bjz
    integer :: gc,lc,nv,i,j,k1,k2,tz,m2,i2,n2,j2,r,r,s,info
    logical :: stat,ic
    common /rep_force/ rx,ry,tz,q0,q1,q2,q3,px,py,pz
    common /ambient/ fx,fy,fz,tx,ty,tz,fcx,fcy,fcz,tcx,tcy,tcz
    common /rep_forces/ fx,fy,fz,tx,ty,tz,fbx,fbz,tbx,tbz,tby,tbz
    common /params/ nfib,nseg,npgr,ncont,npgr,num_groups
    common /contacts1/ ifiber,npgr,ncont,npgr,num_groups
    common /contacts2/ nx,nv,nz,si,sj,g,ex1,ex2,ex3,ey1,ey2,ey3, &
        G1jx,G1jy,G1jz,G1jx,G1jy,G1jz
    common /Andec/ D1,D2,D3,A11,A12,A13,A23,A22,A33, &
        C11,C12,C13,C23,C22,C33
    common /joints/ Xx,Yy,Zz,XX,XY,Xz
    2001 format(i0.5,zx,14,1x,14,1x,INFO = ',13)
    total_contacts = 0
    ! Loop over all the groups to solve for contact forces
    do gc = 1, num_groups
        N_size = 3*ncont(gc)
        do l = 1, N_size
            do j = 1, N_size
                A(j,1) = 0.D0
            enddo
            P(l) = 0.D0
        enddo
        ! Loop over contacts in that group
        do lc = 1, ncont(gc)
            k1 = 3*lc - 2
            m = ifiber(l,lc,gc)
            n = ifiber(1,lc,gc)
            j = ifiber(4,lc,gc)

```

```

! Find the right hand side components
! These are all sub-calculations.
aix = uxfl(m,i) + &
A11(m,i)*(fcx(m,i)+fbx(m,i)+Kx(m,i+1))-Xx(m,i) + &
A12(m,i)*(fcy(m,i)+fby(m,i)+Ky(m,i+1))-Yy(m,i) + &
A13(m,i)*(fcz(m,i)+fbz(m,i)+Kz(m,i+1))-Xz(m,i)
aiy = uyfl(m,i) + &
A12(m,i)*(fcx(m,i)+fbx(m,i)+Kx(m,i+1))-Xx(m,i) + &
A22(m,i)*(fcy(m,i)+fby(m,i)+Ky(m,i+1))-Yy(m,i) + &
A23(m,i)*(fcz(m,i)+fbz(m,i)+Kz(m,i+1))-Xz(m,i)
aiz = uzfl(m,i) + &
A13(m,i)*(fcx(m,i)+fbx(m,i)+Kx(m,i+1))-Xx(m,i) + &
A23(m,i)*(fcy(m,i)+fby(m,i)+Ky(m,i+1))-Yy(m,i) + &
A33(m,i)*(fcz(m,i)+fbz(m,i)+Kz(m,i+1))-Xz(m,i)
dirx = D1(m,i) + Yx(m,i+1)-Yx(m,i) + C1*tcx(m,i) + tbx(m,i) + &
C0*(py(m,i)*Kz(m,i+1)+Xz(m,i)) - &
p2(m,i)*Xy(m,i+1)+Xy(m,i))
diry = D2(m,i) + Yy(m,i+1)-Yy(m,i) + C1*tcy(m,i) + tby(m,i) + &
C0*(pz(m,i)*Kx(m,i+1)+Xx(m,i)) - &
p2(m,i)*Xz(m,i+1)+Xz(m,i))
dirz = D3(m,i) + Yz(m,i+1)-Yz(m,i) + C1*tcz(m,i) + tbz(m,i) + &
C0*(px(m,i)*Ky(m,i+1)+Xy(m,i)) - &
p2(m,i)*Xx(m,i+1)+Xx(m,i))
bix = Omega_x + C11(m,i)*dircx + C12(m,i)*diry + C13(m,i)*dirz
biy = Omega_y + C12(m,i)*dircx + C22(m,i)*diry + C23(m,i)*dirz
biz = Omega_z + C13(m,i)*dircx + C23(m,i)*diry + C33(m,i)*dirz
ajx = uxfl(m,j) + &
A11(m,j)*(fcx(m,j)+fbx(m,j)+Kx(m,j+1))-Xx(m,j) + &
A12(m,j)*(fcy(m,j)+fby(m,j)+Ky(m,j+1))-Yy(m,j) + &
A13(m,j)*(fcz(m,j)+fbz(m,j)+Kz(m,j+1))-Xz(m,j)
ajy = uyfl(m,j) + &
A12(m,j)*(fcx(m,j)+fbx(m,j)+Kx(m,j+1))-Xx(m,j) + &
A22(m,j)*(fcy(m,j)+fby(m,j)+Ky(m,j+1))-Yy(m,j) + &
A23(m,j)*(fcz(m,j)+fbz(m,j)+Kz(m,j+1))-Xz(m,j)
ajz = uzfl(m,j) + &
A13(m,j)*(fcx(m,j)+fbx(m,j)+Kx(m,j+1))-Xx(m,j) + &
A23(m,j)*(fcy(m,j)+fby(m,j)+Ky(m,j+1))-Yy(m,j) + &
A33(m,j)*(fcz(m,j)+fbz(m,j)+Kz(m,j+1))-Xz(m,j)
dirx = D1(m,j) + Yx(m,j+1)-Xx(m,j) + C1*tcx(m,j) + tbx(m,j) + &
C0*(py(m,j)*Kz(m,j+1)+Xz(m,j)) - &
p2(m,j)*Xy(m,j+1)+Xy(m,j))
diry = D2(m,j) + Yy(m,j+1)-Yy(m,j) + C1*tcy(m,j) + tby(m,j) + &
C0*(pz(m,j)*Kx(m,j+1)+Xx(m,j)) - &
p2(m,j)*Xz(m,j+1)+Xz(m,j))
dirz = D3(m,j) + Yz(m,j+1)-Yz(m,j) + C1*tcz(m,j) + tbz(m,j) + &
C0*(px(m,j)*Ky(m,j+1)+Xy(m,j)) - &
p2(m,j)*Xx(m,j+1)+Xx(m,j))
bjx = Omega_x + C11(m,j)*dircx + C12(m,j)*diry + C13(m,j)*dirz
bjy = Omega_y + C12(m,j)*dircx + C22(m,j)*diry + C23(m,j)*dirz
bjz = Omega_z + C13(m,j)*dircx + C23(m,j)*diry + C33(m,j)*dirz
! Periodic boundaries correction term
fux = sidedx*dnint(uxfl(m,i)-uxfl(m,j))/sidedx
fy = -(tax - axk - fux + fby-g1jz(gc,lc)-b1z-g1jy(gc,lc)) - &
(fjy-g1iz(gc,lc)-bjz-g1jy(gc,lc))
qy = -(tay - ayj + fux-g1jx(gc,lc)-b1x-g1jz(gc,lc)) - &
(fjz-g1ix(gc,lc)-bjx-g1iz(gc,lc))
qz = -(taz - ajz + (bix-g1jy(gc,lc)-bjy-g1jx(gc,lc)) - &
(fjx-g1jy(gc,lc)-bjy-g1jx(gc,lc)))
! Define the plane of contact
ex1(gc,lc) = 1.D0 - nx(gc,lc)*nx(gc,lc)
ex2(gc,lc) = -ny(gc,lc)*nx(gc,lc)
ex3(gc,lc) = -nz(gc,lc)*nx(gc,lc)
dum = dsqrt(ex1(gc,lc)**2+ex2(gc,lc)**2+ex3(gc,lc)**2)
ex1(gc,lc) = ex1(gc,lc)/dum
ex2(gc,lc) = ex2(gc,lc)/dum
ex3(gc,lc) = ex3(gc,lc)/dum
ey1(gc,lc) = ny(gc,lc)*ex3(gc,lc) - nz(gc,lc)*ex2(gc,lc)
ey2(gc,lc) = nz(gc,lc)*ex1(gc,lc) - nx(gc,lc)*ex3(gc,lc)

```

friction_forces.f90

```

    ey3(gc,ic) = nx(gc,ic)*ex2(gc,ic) - ny(gc,ic)*ex1(gc,ic)
    dum = dsqrt(ey1(gc,ic)**2+ey2(gc,ic)**2+ey3(gc,ic)**2)
    ey1(gc,ic) = ey1(gc,ic)/dum
    ey2(gc,ic) = ey2(gc,ic)/dum
    ey3(gc,ic) = ey3(gc,ic)/dum
    ! Fall in the actual rhs vector
    P(kl+1) = qx*ex1(gc,ic) + qy*ex2(gc,ic) + qz*ex3(gc,ic)
    P(kl+2) = qx*ey1(gc,ic) + qy*ey2(gc,ic) + qz*ey3(gc,ic)
    ! Do the diagonal of the matrix A
    Qik(1,1) = A11(m,i) + A11(n,j) - 6
    Cl*(-G1z(gc,ic)*C22(m,i)*G1z(gc,ic) + G1z(gc,ic)*C22(m,i)*G1z(gc,ic) + G1z(gc,ic)*C23(m,i)*G1y(gc,ic) + G1y(gc,ic)*C23(m,i)*G1z(gc,ic) + G1y(gc,ic)*C33(m,i)*G1z(gc,ic) - 6
    G1y(gc,ic)*C23(m,i)*G1z(gc,ic) - 6
    Cl*(-G1z(gc,ic)*C22(n,j)*G1z(gc,ic) + G1z(gc,ic)*C22(n,j)*G1z(gc,ic) + G1z(gc,ic)*C23(n,j)*G1y(gc,ic) + G1y(gc,ic)*C23(n,j)*G1z(gc,ic) + G1y(gc,ic)*C33(n,j)*G1z(gc,ic) - 6
    G1y(gc,ic)*C23(n,j)*G1z(gc,ic) - 6
    Qik(1,2) = A12(m,i) + A12(n,j) - 6
    Cl*( G1z(gc,ic)*C12(m,i)*G1z(gc,ic) - 6
    G1z(gc,ic)*C23(m,i)*G1x(gc,ic) + 6
    G1y(gc,ic)*C13(m,i)*G1z(gc,ic) + 6
    G1y(gc,ic)*C33(m,i)*G1x(gc,ic) - 6
    Cl*( G1z(gc,ic)*C12(n,j)*G1z(gc,ic) - 6
    G1z(gc,ic)*C23(n,j)*G1x(gc,ic) + 6
    G1y(gc,ic)*C13(n,j)*G1z(gc,ic) + 6
    G1y(gc,ic)*C33(n,j)*G1x(gc,ic) - 6
    Qik(1,3) = A13(m,i) + A13(n,j) - 6
    Cl*(-G1z(gc,ic)*C12(m,i)*G1y(gc,ic) + 6
    G1z(gc,ic)*C22(m,i)*G1x(gc,ic) + 6
    G1y(gc,ic)*C13(m,i)*G1y(gc,ic) - 6
    G1x(gc,ic)*C33(m,i)*G1y(gc,ic) - 6
    Cl*(-G1z(gc,ic)*C12(n,j)*G1y(gc,ic) + 6
    G1z(gc,ic)*C22(n,j)*G1x(gc,ic) + 6
    G1y(gc,ic)*C13(n,j)*G1y(gc,ic) - 6
    G1x(gc,ic)*C33(n,j)*G1y(gc,ic) - 6
    Qik(2,2) = A22(m,i) + A22(n,j) - 6
    Cl*(-G1z(gc,ic)*C11(m,i)*G1z(gc,ic) + 6
    G1z(gc,ic)*C11(m,i)*G1z(gc,ic) + 6
    G1z(gc,ic)*C13(m,i)*G1x(gc,ic) - 6
    G1x(gc,ic)*C13(m,i)*G1z(gc,ic) - 6
    Cl*( G1z(gc,ic)*C11(n,j)*G1z(gc,ic) + 6
    G1z(gc,ic)*C12(n,j)*G1x(gc,ic) + 6
    G1y(gc,ic)*C13(n,j)*G1z(gc,ic) + 6
    G1x(gc,ic)*C13(n,j)*G1x(gc,ic) - 6
    Qik(2,3) = A23(m,i) + A23(n,j) - 6
    Cl*( G1z(gc,ic)*C11(m,i)*G1y(gc,ic) + 6
    G1y(gc,ic)*C11(m,i)*G1z(gc,ic) + 6
    G1z(gc,ic)*C12(m,i)*G1x(gc,ic) + 6
    G1x(gc,ic)*C12(m,i)*G1y(gc,ic) - 6
    Cl*( G1z(gc,ic)*C11(n,j)*G1y(gc,ic) + 6
    G1y(gc,ic)*C11(n,j)*G1z(gc,ic) + 6
    G1z(gc,ic)*C12(n,j)*G1x(gc,ic) + 6
    G1x(gc,ic)*C12(n,j)*G1y(gc,ic) - 6
    G1y(gc,ic)*C23(n,j)*G1x(gc,ic) + 6
    G1x(gc,ic)*C23(n,j)*G1y(gc,ic) - 6
    ! Constrain the motion to the plane of contact...to get A
    A(kl ,kl ) = Qik(1,1)*ex1(gc,ic) + Qik(1,2)*ex2(gc,ic) + &
    Qik(1,3)*ex3(gc,ic)
    A(kl ,kl+1) = Qik(1,2)*ex1(gc,ic) + Qik(2,2)*ex2(gc,ic) + &
    Qik(2,3)*ex3(gc,ic)
    A(kl ,kl+2) = Qik(1,3)*ex1(gc,ic) + Qik(2,3)*ex2(gc,ic) + &
    Qik(3,3)*ex3(gc,ic)
    A(kl+1,kl+1) = Qik(1,1)*ex1(gc,ic) + Qik(1,2)*ex2(gc,ic) + &
    Qik(1,3)*ex3(gc,ic)
    A(kl+1,kl+2) = Qik(1,2)*ex1(gc,ic) + Qik(2,2)*ex2(gc,ic) + &
    Qik(2,3)*ex3(gc,ic)
    A(kl+2,kl+1) = Qik(1,3)*ex1(gc,ic) + Qik(2,3)*ex2(gc,ic) + &
    Qik(3,3)*ex3(gc,ic)
    A(kl+2,kl+2) = Qik(1,3)*ex1(gc,ic) + Qik(2,3)*ex2(gc,ic) + &
    Qik(3,3)*ex3(gc,ic)
    ! Loop over contacts again to get contact dependency
    do ic2 = 1, ncnt(gc)
    ! already did the diagonal
    if(ic /= ic2) then
    k2 = 3*ic2 - 2
    m2 = ifiber(1,ic2,gc) ; i2 = ifiber(2,ic2,gc)
    n2 = ifiber(3,ic2,gc) ; j2 = ifiber(4,ic2,gc)
    if((m-1)*nseq+i) == (m2-1)*nseq+i2) then ! case 1
    r = m ; s = i ; posneg = 1,D0
    G1x = G1ix(gc,ic) ; G1y = G1iy(gc,ic) ; G1z = G1iz(gc,ic)
    G2x = G1ix(gc,ic2) ; G2y = G1iy(gc,ic2)
    G2z = G1iz(gc,ic2)
    elseif((m-1)*nseq+i) == ((n2-1)*nseq+j2)) then ! case 2
    r = m ; s = i ; posneg = -1,D0
    G1x = G1ix(gc,ic) ; G1y = G1iy(gc,ic) ; G1z = G1iz(gc,ic)
    G2x = G1ix(gc,ic2) ; G2y = G1iy(gc,ic2)
    G2z = G1iz(gc,ic2)
    elseif((n-1)*nseq+i) == ((m2-1)*nseq+i2)) then ! case 3
    r = n ; s = j ; posneg = -1,D0
    G1x = G1ix(gc,ic) ; G1y = G1iy(gc,ic) ; G1z = G1iz(gc,ic)
    G2x = G1ix(gc,ic2) ; G2y = G1iy(gc,ic2)
    G2z = G1iz(gc,ic2)
    elseif((n-1)*nseq+i) == ((n2-1)*nseq+j2)) then ! case 4
    r = n ; s = j ; posneg = 1,D0
    G1x = G1ix(gc,ic) ; G1y = G1iy(gc,ic) ; G1z = G1iz(gc,ic)
    G2x = G1ix(gc,ic2) ; G2y = G1iy(gc,ic2)
    G2z = G1iz(gc,ic2)
    else = 0
    endif
    ! If there are two dependent contacts...
    if (t > 0) then
    Qik(1,1) = posneg*(A11(r,s) - 6
    Cl*(-G1z*C23(tr,s)*G2z - G1y*C33(tr,s)*G2y) +
    G1y*C23(tr,s)*G2z - G1z*C33(tr,s)*G2y + &
    Qik(1,2) = posneg*(A12(tr,s) - 6
    Cl*( G1z*CL2(tr,s)*G2z - G1y*C23(tr,s)*G2x - 6
    G1y*C13(tr,s)*G2z + G1y*C33(tr,s)*G2x)
    Qik(1,3) = posneg*(A13(tr,s) - 6
    Cl*(-G1z*CL2(tr,s)*G2y + G1z*C22(tr,s)*G2x + 6
    G1y*C13(tr,s)*G2y - G1y*C23(tr,s)*G2x)
    Qik(2,1) = posneg*(A12(tr,s) - 6
    Cl*( G1z*CL2(tr,s)*G2z - G1z*CL3(tr,s)*G2y) - 6
    G1x*C23(tr,s)*G2z + G1x*C33(tr,s)*G2y)
    Qik(2,2) = posneg*(A22(tr,s) - 6
    Cl*(-G1y*CL1(tr,s)*G2z + G1z*CL3(tr,s)*G2x + 6
    G1x*CL13(tr,s)*G2z - G1x*C33(tr,s)*G2x)
    Qik(2,3) = posneg*(A23(tr,s) - 6
    G1x*CL13(tr,s)*G2y - G1z*CL2(tr,s)*G2x - 6
    G1x*CL12(tr,s)*G2y + G1x*C23(tr,s)*G2x)
    Qik(3,1) = posneg*(A13(tr,s) - 6
    Cl*(-G1y*CL2(tr,s)*G2z - G1y*CL3(tr,s)*G2y + 6
    G1x*C22(tr,s)*G2z - G1x*C23(tr,s)*G2y)
    Qik(3,2) = posneg*(A23(tr,s) - 6
    Cl*( G1y*CL1(tr,s)*G2z - G1y*CL3(tr,s)*G2x - 6
    G1x*CL2(tr,s)*G2z + G1x*C23(tr,s)*G2x)
    
```

friction_forces.f90

```

Oik(3,3) = posneg*(A33(r,s) - &
C1*(-Gly*C11(r,s)*G2y + Gly*C12(r,s)*G2x + &
G1x*C12(r,s)*G2y - G1x*C22(r,s)*G2x)
! Put into contact plane
A(k1 ,k2 ) = Oik(1,1)*ex1(gc,ic) + &
Oik(2,1)*ex2(gc,ic) + Oik(3,1)*ex3(gc,ic)
A(k1 ,k2+1) = Oik(1,2)*ex1(gc,ic) + &
Oik(2,2)*ex2(gc,ic) + Oik(3,2)*ex3(gc,ic)
A(k1 ,k2+2) = Oik(1,3)*ex1(gc,ic) + &
Oik(2,3)*ex2(gc,ic) + Oik(3,3)*ex3(gc,ic)
A(k1+1,k2 ) = Oik(1,1)*ey1(gc,ic) + &
Oik(2,1)*ey2(gc,ic) + Oik(3,1)*ey3(gc,ic)
A(k1+1,k2+1) = Oik(1,2)*ey1(gc,ic) + &
Oik(2,2)*ey2(gc,ic) + Oik(3,2)*ey3(gc,ic)
A(k1+1,k2+2) = Oik(1,3)*ey1(gc,ic) + &
Oik(2,3)*ey2(gc,ic) + Oik(3,3)*ey3(gc,ic)
A(k1+2,k2 ) = 0.00
A(k1+2,k2+1) = 0.00
A(k1+2,k2+2) = 0.00
else
A(k1,k2) = 0.00; A(k1,k2+1) = 0.00; A(k1,k2+2) = 0.00
A(k1+1,k2) = 0.00; A(k1+1,k2+1) = 0.00
A(k1+1,k2+2) = 0.00
A(k1+2,k2) = 0.00; A(k1+2,k2+1) = 0.00
A(k1+2,k2+2) = 0.00
endif
endif
enddo
! Apply the static friction constraint
! The static friction constraint searches for contacts that should
! be broken, if one must be broken, then we go back and resolve for
! all the other contact forces in the absence of the broken one.
static = true.
do while(static == true.)
! Save a copy of the system in case it needs to be redone
do i = 1, Nsize
do j = 1, Nsize
A_back(i,j) = A(i,j)
endif
P_back(i) = P(i)
enddo
! Solve the system with an IUD solver
! If there is only one contact, then we know the solution
if (N_size == 3) then
! Determinant of A
det = A_back(1,3)*A_back(2,2)*A_back(3,1) - &
A_back(1,2)*A_back(2,3)*A_back(3,1) - &
A_back(1,3)*A_back(2,1)*A_back(3,2) + &
A_back(1,1)*A_back(2,3)*A_back(3,2) + &
A_back(1,2)*A_back(2,1)*A_back(3,3) - &
A_back(1,1)*A_back(2,2)*A_back(3,3)
if (Abs(det) < 1.e-14) then
write(40,*) 'Singular 3-Man'
write(40,*) time,gc,ic ! Writes errors
stop
endif
! Calculate the friction force
P_back(1) = ((A_back(2,3)*A_back(3,2) - &
A_back(2,2)*A_back(3,3))*P(1) + &
(A_back(1,2)*A_back(3,3) - A_back(1,3)*A_back(3,2))*P(2) + &
(A_back(1,3)*A_back(3,3) - A_back(1,2)*A_back(3,2))*P(3)/det
P_back(2) = ((A_back(2,1)*A_back(3,3) - &
A_back(2,3)*A_back(3,1))*P(1) + &
(A_back(1,3)*A_back(3,1) - A_back(1,1)*A_back(3,3))*P(2) + &
(A_back(1,1)*A_back(3,3) - A_back(1,3)*A_back(3,1))*P(3)/det
P_back(3) = ((A_back(2,2)*A_back(3,1) + &
A_back(2,1)*A_back(3,2))*P(1) + &

```

```

(A_back(1,1)*A_back(3,2) - A_back(1,2)*A_back(3,1))*P(2) + &
(A_back(1,2)*A_back(2,1) - A_back(1,1)*A_back(2,2))*P(3)/det
else
P_back(1) = P(1); P_back(2) = P(2); P_back(3) = P(3)
! This is LAPACK IUD routine to solve the linear system
call DGSV(Nsize,nrhs,A_back,lda,ipiv,P_back,ldb,info)
if (info /= 0) then
write(40,2001) time,gc,ic,info
stop
endif
! Loop over all the contacts to calculate force magnitudes
fric_max = 0.00; imax = 0
do ic = 1, ncnt(gc)
kl = 3*ic - 2
! Square of the normal force
forc = fstar*dexp(-fact*(g(gc,ic)-2.00)) - &
Astar*dexp(-decat*(g(gc,ic)-2.00)*(g(gc,ic)-2.00))
! Square of the friction force
fric_sq = P_back(kl)**2 + P_back(kl+1)**2 + P_back(kl+2)**2
! Check to see if the magnitude is too great
if (fric_sq > (mu stat*forc)**2) then
if (fric_sq > fric_max) then
fric_max = fric_sq
imax = ic
endif
endif
enddo
! If too big, break that contact with the larges f value and
! recalculate the for the new friction forces
if (imax > 0) then
if (imax < ncnt(gc)) then
do ic = imax, ncnt(gc)-1
kl = 3*ic - 2
! Shift the contact info back one spot
ifiber(1,ic,gc) = ifiber(1,ic+1,gc)
ifiber(2,ic,gc) = ifiber(2,ic+1,gc)
ifiber(3,ic,gc) = ifiber(3,ic+1,gc)
ifiber(4,ic,gc) = ifiber(4,ic+1,gc)
nx(gc,ic) = nx(gc,ic+1)
ny(gc,ic) = ny(gc,ic+1)
nz(gc,ic) = nz(gc,ic+1)
sx(gc,ic) = sx(gc,ic+1)
sj(gc,ic) = sj(gc,ic+1)
g(gc,ic) = g(gc,ic+1)
Gjx(gc,ic) = Gjx(gc,ic+1); Gjy(gc,ic) = Gjy(gc,ic+1)
Gjz(gc,ic) = Gjz(gc,ic+1)
Glx(gc,ic) = Glx(gc,ic+1); Gly(gc,ic) = Gly(gc,ic+1)
Glz(gc,ic) = Glz(gc,ic+1)
F(k1) = P(k1+3)
F(k1+1) = P(k1+4)
F(k1+2) = P(k1+5)
! Erase the row and column of the contact
do j = 1, 3*ncnt(gc)
A(j,k1) = A(j,k1+3)
A(j,k1+1) = A(j,k1+4)
A(j,k1+2) = A(j,k1+5)
enddo
do j = 1, 3*ncnt(gc)
A(k1,j) = A(k1+3,j)
A(k1+1,j) = A(k1+4,j)
A(k1+2,j) = A(k1+5,j)
enddo
endif
ncnt(gc) = ncnt(gc) - 1; N_size = 3*ncnt(gc)
if (N_size <= 0) static = .false.
else

```

friction_forces.f90

```

    static = .false.
  endif
enddo
! Assign the final friction force to the appropriate fiber
do ic = 1, ncnt(gc)
  m = ifiber(1,ic,gc); i = ifiber(2,ic,gc)
  n = ifiber(3,ic,gc); j = ifiber(4,ic,gc)
  k1 = 3*ic - 2
  fx(m,i) = fx(m,i) + P_back(k1)
  fy(m,i) = fy(m,i) + P_back(k1+1)
  fz(m,i) = fz(m,i) + P_back(k1+2)
  fx(n,j) = fx(n,j) - P_back(k1)
  fy(n,j) = fy(n,j) - P_back(k1+1)
  fz(n,j) = fz(n,j) - P_back(k1+2)
  tx(m,i) = tx(m,i) +  $\delta$ 
  ty(m,i) = ty(m,i) +  $\delta$ 
  tz(m,i) = tz(m,i) +  $\delta$ 
  tx(n,j) = tx(n,j) -  $\delta$ 
  ty(n,j) = ty(n,j) -  $\delta$ 
  tz(n,j) = tz(n,j) -  $\delta$ 
  total_contacts = total_contacts + ncnt(gc)
enddo
end subroutine friction_forces

```

x_forces.f90

```

!*****
! Subroutine: x_forces
! keeps the fiber inextensible
!*****
subroutine x_forces(nrhs,N_band,ldab,ldx,ku,kl,C0,C1,C2,C3,C4, &
  Ya,Yc,time)
  implicit none
  integer nof,nos,npcm,npqr
  parameter (nof=400,nos=5,npcm=500,npqr=700)
  ! Old variables
  real*8,dimension(nof,nos) :: rx,ry,zz,q0,q1,q2,q3,px,py,pz
  real*8,dimension(nof,nos) :: fx,fy,fcz,tcz,tcy,tbz
  real*8,dimension(nof,nos) :: fbx,fbz,fbz,tbx,tby,tbz
  real*8,dimension(nof,nos) :: ux,uy,uz,wx,wy,wz,q0dot,q1dot,q2dot,q3dot
  real*8,dimension(nof,nos) :: uxf1,uyf1,uzf1,dl,D2,D3
  real*8,dimension(nof,nos) :: A11,A12,A13,A23,A22,A33
  real*8,dimension(nof,nos) :: C11,C12,C13,C23,C22,C33
  real*8,dimension(nof,nos) :: R11,R12,R13,R21,R22,R23
  real*8 :: Omega_x,Omega_y,Omega_z,rs,sidez,sidey,sidez,delta_rx
  integer :: nfbf,nsseg,nrhs,ldab,ldx,ku,kl,N_band
  ! New and dummy variables
  real*8 :: AB(16,3*(nos-1)),V(3*(nos-1))
  ! AB - the matrix for the banded linear system for X
  ! V - the right hand side for the banded linear system for X
  integer :: m_i,k1,k2,info,ipiv(3*(nos-1)),j
  common /rsps/ rx,ry,zz,q0,q1,q2,q3,px,py,pz
  common /fric/ fbx,fbz,fbz,tbx,tby,tbz
  common /rel/ fccx,fcy,fcz,tcz,tcy,tbz,fbz,fbz,tbx,tby,tbz
  common /vel/ uxf1,uyf1,uzf1,wx,wy,wz,q0dot,q1dot,q2dot,q3dot
  common /ambit/ dl,D2,D3,A11,A12,A13,A23,A22,A33, &
  C11,C12,C13,C23,C22,C33
  common /parans/ nfbf,nsseg,rs,sidez,sidey,sidez,delta_rx
  common /rotat/ rx,ry,zz,wx,wy,Yz
  common /rotat/ R11,R12,R13,R21,R22,R23
  ! Solve the system of each fiber
  do m_i = 1, nfbf
    do k1 = 3*(nos-1)
      ! Right hand side components
      ux(m_i) = uxf1(m_i) + A11(m_i)*(fex(m_i)+fbx(m_i)+fx(m_i)) + &
        A12(m_i)*(fcx(m_i)+fby(m_i)+fy(m_i)) + &
        A13(m_i)*(fcz(m_i)+fbz(m_i)+fz(m_i)) + &
      uy(m_i) = uyf1(m_i) + A12(m_i)*(fex(m_i)+fbx(m_i)+fx(m_i)) + &
        A22(m_i)*(fcx(m_i)+fby(m_i)+fy(m_i)) + &
        A23(m_i)*(fcz(m_i)+fbz(m_i)+fz(m_i)) + &
      uz(m_i) = uzf1(m_i) + A13(m_i)*(fex(m_i)+fbx(m_i)+fx(m_i)) + &
        A23(m_i)*(fcx(m_i)+fby(m_i)+fy(m_i)) + &
        A33(m_i)*(fcz(m_i)+fbz(m_i)+fz(m_i)) + &
      wx(m_i) = Omega_x + C11(m_i)*(&
        D1(m_i)+ix(m_i,i+1)-ix(m_i,i)+tbcx(m_i,i)+ &
        C12(m_i)*(D2(m_i,i)+iy(m_i,i+1)-iy(m_i,i)+tby(m_i,i)+ &
        C13(m_i)*(D3(m_i,i)+iz(m_i,i+1)-iz(m_i,i)+tbz(m_i,i)+ &
        C1*(tcz(m_i,i)+tz(m_i,i)))
      wy(m_i) = Omega_y + C12(m_i)*(&
        D1(m_i)+ix(m_i,i+1)-ix(m_i,i)+tbcx(m_i,i)+ &
        C1*(tcx(m_i,i)+tx(m_i,i))) + &
        C22(m_i)*(D2(m_i,i)+iy(m_i,i+1)-iy(m_i,i)+tby(m_i,i)+ &
        C1*(tcy(m_i,i)+ty(m_i,i))) + &
        C23(m_i)*(D3(m_i,i)+iz(m_i,i+1)-iz(m_i,i)+tbz(m_i,i)+ &
        C1*(tcz(m_i,i)+tz(m_i,i)))
      wz(m_i) = Omega_z + C13(m_i)*(&

```

```

D1(m_i)+Yx(m_i,i+1)-Yx(m_i,i)+tbcx(m_i,i) + &
C1*(tcx(m_i,i)+tx(m_i,i))) + &
C23(m_i)*(D2(m_i,i)+iy(m_i,i+1)-iy(m_i,i)+tby(m_i,i) + &
C1*(tcy(m_i,i)+ty(m_i,i))) + &
C33(m_i)*(D3(m_i,i)+iz(m_i,i+1)-iz(m_i,i)+tbz(m_i,i) + &
C1*(tcz(m_i,i)+tz(m_i,i)))
! Start calculate for 2nd joint (X_1 = 0)
if(i > 1)then
  ! Right hand side
  V(k1-3) = ux(m_i,i-1)-ux(m_i,i) + &
    rp*(wy(m_i,i)*pz(m_i,i)-wz(m_i,i)*py(m_i,i) + &
    wy(m_i,i-1)*pz(m_i,i-1)-wz(m_i,i-1)*py(m_i,i-1))
  V(k1-2) = uy(m_i,i-1)-uy(m_i,i) + &
    rp*(vz(m_i,i)*px(m_i,i)-wx(m_i,i)*pz(m_i,i) + &
    vz(m_i,i-1)*px(m_i,i-1)-wx(m_i,i-1)*pz(m_i,i-1))
  V(k1-1) = uz(m_i,i-1)-uz(m_i,i) + &
    rp*(vx(m_i,i)*py(m_i,i)-wy(m_i,i)*px(m_i,i) + &
    vx(m_i,i-1)*py(m_i,i-1)-wy(m_i,i-1)*px(m_i,i-1))
  if(i < nsseg) then
    ! S matrix grouping
    AB(k1+ku+1+(k1)-(k1-3),(k1-3)) = 1./Ya-C2 + &
      (C3+C2)*px(m_i,i)*px(m_i,i)
    AB(k1+ku+1+(k1)-(k1-2),(k1-2)) = (C3+C2)*py(m_i,i)*py(m_i,i)
    AB(k1+ku+1+(k1)-(k1-1),(k1-1)) = (C3+C2)*pz(m_i,i)*pz(m_i,i)
    AB(k1+ku+1+(k1)-(k1-3),(k1-3)) = &
      (C3+C2)*px(m_i,i)*px(m_i,i)
    AB(k1+ku+1+(k1)-(k1-2),(k1-2)) = &
      (C3+C2)*py(m_i,i)*py(m_i,i)
    AB(k1+ku+1+(k1)-(k1-1),(k1-1)) = &
      (C3+C2)*pz(m_i,i)*pz(m_i,i)
    ! U matrix grouping
    AB(k1+ku+1+(k1-3),(k1-3)) = 1./Ya-C2 + &
      (C3+C2)*px(m_i,i)*px(m_i,i)
    AB(k1+ku+1+(k1-2),(k1-2)) = (C3+C2)*py(m_i,i)*py(m_i,i)
    AB(k1+ku+1+(k1-1),(k1-1)) = (C3+C2)*pz(m_i,i)*pz(m_i,i)
    AB(k1+ku+1+(k1-3),(k1-3)) = &
      (C3+C2)*px(m_i,i)*px(m_i,i)
    AB(k1+ku+1+(k1-2),(k1-2)) = &
      (C3+C2)*py(m_i,i)*py(m_i,i)
    AB(k1+ku+1+(k1-1),(k1-1)) = &
      (C3+C2)*pz(m_i,i)*pz(m_i,i)
  ! U matrix grouping
  AB(k1+ku+1+(k1-3),(k1-3)) = 1./Ya-C2 + &
    (C3+C2)*px(m_i,i)*px(m_i,i)
  AB(k1+ku+1+(k1-2),(k1-2)) = (C3+C2)*py(m_i,i)*py(m_i,i)
  AB(k1+ku+1+(k1-1),(k1-1)) = (C3+C2)*pz(m_i,i)*pz(m_i,i)
  AB(k1+ku+1+(k1-3),(k1-3)) = &
    (C3+C2)*px(m_i,i)*px(m_i,i)
  AB(k1+ku+1+(k1-2),(k1-2)) = &
    (C3+C2)*py(m_i,i)*py(m_i,i)
  AB(k1+ku+1+(k1-1),(k1-1)) = &
    (C3+C2)*pz(m_i,i)*pz(m_i,i)
  ! U matrix grouping
  AB(k1+ku+1+(k1-3),(k1-3)) = 1./Ya-C2 + &
    (C3+C2)*px(m_i,i)*px(m_i,i)
  AB(k1+ku+1+(k1-2),(k1-2)) = (C3+C2)*py(m_i,i)*py(m_i,i)
  AB(k1+ku+1+(k1-1),(k1-1)) = (C3+C2)*pz(m_i,i)*pz(m_i,i)
  AB(k1+ku+1+(k1-3),(k1-3)) = &
    (C3+C2)*px(m_i,i)*px(m_i,i)
  AB(k1+ku+1+(k1-2),(k1-2)) = &
    (C3+C2)*py(m_i,i)*py(m_i,i)
  AB(k1+ku+1+(k1-1),(k1-1)) = &
    (C3+C2)*pz(m_i,i)*pz(m_i,i)
endif
endif
if(i < nsseg) then
  ! T matrix grouping
  AB(k1+ku+1+(k1)-(k1-3),(k1-3)) = -2.D0*(1./Ya+C2) + &
    (-C3+C2)*px(m_i,i)*px(m_i,i) + px(m_i,i+1)*px(m_i,i+1) + &
    px(m_i,i+1)*py(m_i,i+1)
  AB(k1+ku+1+(k1)-(k1-2),(k1-2)) = &
    (-C3+C2)*py(m_i,i)*py(m_i,i) + py(m_i,i+1)*py(m_i,i+1) + &
    py(m_i,i+1)*pz(m_i,i+1)
  AB(k1+ku+1+(k1)-(k1-1),(k1-1)) = &
    (-C3+C2)*pz(m_i,i)*pz(m_i,i) + pz(m_i,i+1)*pz(m_i,i+1) + &
    pz(m_i,i+1)*px(m_i,i+1)
  AB(k1+ku+1+(k1)-(k1-3),(k1-3)) = &
    (-C3+C2)*px(m_i,i)*px(m_i,i) + px(m_i,i+1)*px(m_i,i+1) + &
    px(m_i,i+1)*py(m_i,i+1)
  AB(k1+ku+1+(k1)-(k1-2),(k1-2)) = &
    (-C3+C2)*py(m_i,i)*py(m_i,i) + py(m_i,i+1)*py(m_i,i+1) + &
    py(m_i,i+1)*pz(m_i,i+1)
  AB(k1+ku+1+(k1)-(k1-1),(k1-1)) = &
    (-C3+C2)*pz(m_i,i)*pz(m_i,i) + pz(m_i,i+1)*pz(m_i,i+1) + &
    pz(m_i,i+1)*px(m_i,i+1)
endif
endif

```

x_forces.f90

```

      AB(kl+ku+1+(kl+2)-(kl+1),(kl+1),(kl+2))
      AB(kl+ku+1+(kl+2)-(kl+1),(kl+1),(kl+1)) = &
      AB(kl+ku+1+(kl+1)-(kl+2),(kl+2),(kl+2))
      AB(kl+ku+1+(kl+2)-(kl+2),(kl+2)) = -2.D0*(1./A+C2) + &
      (-C3+C2)*pz(mr,i) + pz(mr,i+1)*pz(mr,i+1)
    endif
  enddo
! Solve the system using a LAPACK banded solver
call DGBSV(N,Band,kl,ku,nrhs,AB,ldab,ipiv,V,ldx,info)
if(info /= 0)then
  write(41,*) time,m,info
  stop
endif
! Assign values to the constraint forces
do i = 1, nseg
  if(i < nseg)then
    kl = 3*(i) - 2
    Xx(m,i+1) = V(kl)
    Xy(m,i+1) = V(kl+1)
    Xz(m,i+1) = V(kl+2)
  endif
! Now we know everything, so we can calculate the
! velocities of the fiber segments
  ux(m,i) = ux(m,i) + A11(m,i)*(Xx(m,i+1)-Xx(m,i)) + &
  A12(m,i)*(Xy(m,i+1)-Xy(m,i)) + A13(m,i)*(Xz(m,i+1)-Xz(m,i))
  uy(m,i) = uy(m,i) + A12(m,i)*(Xx(m,i+1)-Xx(m,i)) + A22(m,i)*(Xy(m,i+1)-Xy(m,i)) + &
  A23(m,i)*(Xz(m,i+1)-Xz(m,i))
  uz(m,i) = uz(m,i) + A13(m,i)*(Xx(m,i+1)-Xx(m,i)) + A23(m,i)*(Xy(m,i+1)-Xy(m,i)) + &
  A23(m,i)*(Xz(m,i+1)-Xz(m,i))
  wx(m,i) = wx(m,i) + C0*( &
  C11(m,i)*(py(m,i)*(Xz(m,i+1)+Xz(m,i)) - &
  pz(m,i)*(xy(m,i)*(Xy(m,i+1)+Xy(m,i))) + &
  C12(m,i)*(pz(m,i)*(Xx(m,i+1)+Xx(m,i))) - &
  px(m,i)*(Xz(m,i+1)+Xz(m,i))) + &
  C13(m,i)*(px(m,i)*(Xy(m,i+1)+Xy(m,i))) - &
  py(m,i)*(Xx(m,i+1)+Xx(m,i)))
  wy(m,i) = wy(m,i) + C0*( &
  C12(m,i)*(py(m,i)*(Xz(m,i+1)+Xz(m,i))) - &
  C22(m,i)*(pz(m,i)*(Xy(m,i+1)+Xy(m,i))) + &
  C23(m,i)*(px(m,i)*(Xz(m,i+1)+Xz(m,i))) - &
  C23(m,i)*(px(m,i)*(Xy(m,i+1)+Xy(m,i))) + &
  C13(m,i)*(py(m,i)*(Xx(m,i+1)+Xx(m,i)))
  wz(m,i) = wz(m,i) + C0*( &
  C13(m,i)*(py(m,i)*(Xz(m,i+1)+Xz(m,i))) - &
  C23(m,i)*(pz(m,i)*(Xy(m,i+1)+Xy(m,i))) + &
  C23(m,i)*(pz(m,i)*(Xx(m,i+1)+Xx(m,i))) - &
  C33(m,i)*(px(m,i)*(Xz(m,i+1)+Xz(m,i))) + &
  C33(m,i)*(px(m,i)*(Xy(m,i+1)+Xy(m,i))) - &
  py(m,i)*(Xx(m,i+1)+Xx(m,i)))
  enddo
enddo
end subroutine x_forces

```

motion_integrate.f90

```

!*****
! Subroutine: motion_integrate
! Bashforth method.
!*****
subroutine motion_integrate(dt,step,C0,time)
implicit none
integer nof,nos,npcon,npgr
parameter (nof=400,nos=5,npcon=500,npgr=700)
! Old variables
real*8,dimension(nof,nos) :: rx,ry,zz,q0,q1,q2,q3,px,py,pz
real*8,dimension(nof,nos) :: ux,uy,wz,wx,wy,wz,q0dot,q1dot,q2dot,q3dot
real*8,dimension(nof,nos) :: D1,D2,D3,A11,A12,A13,A23,A22,A33
real*8,dimension(nof,nos) :: C11,C12,C13,C23,C22,C33
real*8,dimension(nof,nos) :: R11,R12,R13,R21,R22,R23
real*8,dimension(nof,nos+1) :: Yx,Yy,Yz,Xx,Xy,Xz
real*8 :: rP,sidez,sidey,delta_rx,dt,C0,time
integer :: nfib,nsegs,step
! New and dummy variables
real*8 :: wbx,wbx,wbz,wbz,dum,pjx,pjz,pxk,pyk,pzk
integer :: m,i,corx,corz,corz,mth,k,j
common /fsgs/ rx,ry,zz,q0,q1,q2,q3,px,py,pz
common /fcm/ rcmx,rcmy,rcz
common /velocities/ ux,uy,wz,wx,wy,wz,q0dot,q1dot,q2dot,q3dot
common /fcm/ ucmx,ucmy,ucmz
common /AandC/ D1,D2,D3,A11,A12,A13,A23,A22,A33, &
C11,C12,C13,C23,C22,C33
common /params/ rP,sidez,sidey,sidez,delta_rx
common /rotation/ R11,R12,R13,R21,R22,R23
common /joints/ Yx,Yy,Yz,Xx,Xy,Xz
! Integrate each fiber individually
Main: do m = 1, nfib
ucmx(m) = 0.0
ucmy(m) = 0.0
ucmz(m) = 0.0
do i = 1, nsegs
! Find the FIBER center of mass velocity
ucmx(m) = ucmx(m) + ux(m,i) / ucmz(m) + uy(m,i)
ucmy(m) = ucmy(m) + uz(m,i) / ucmz(m) + vx(m,i)
! Find the time derivative of the Euler parameters
wbx = R11(m,i)*wx(m,i) + R12(m,i)*wy(m,i) + R13(m,i)*wz(m,i)
wby = R21(m,i)*wx(m,i) + R22(m,i)*wy(m,i) + R23(m,i)*wz(m,i)
wbz = px(m,i)*wx(m,i) + py(m,i)*wy(m,i) + pz(m,i)*wz(m,i)
q0dot(m,i) = 0.5D0*(wbx-q1(m,i) - wby-q2(m,i) - wbz-q3(m,i))
q1dot(m,i) = 0.5D0*(wbx-q1(m,i) + wby-q2(m,i) - wby-q3(m,i))
q2dot(m,i) = 0.5D0*(wbx-q1(m,i) + wby-q2(m,i) + wbx-q3(m,i))
q3dot(m,i) = 0.5D0*(wbz-q0(m,i) + wby-q1(m,i) - wbx-q2(m,i))
! Integrate the Euler parameters (Adams-Bashforth)
if (istep == 1) then
q0(m,i) = q0(m,i) + q0dot(m,i)*dt
q1(m,i) = q1(m,i) + q1dot(m,i)*dt
q2(m,i) = q2(m,i) + q2dot(m,i)*dt
q3(m,i) = q3(m,i) + q3dot(m,i)*dt
else
q0(m,i) = q0(m,i) + (1.5*q0dot(m,i) - 0.5*q0dot(m,i))*dt
q1(m,i) = q1(m,i) + (1.5*q1dot(m,i) - 0.5*q1dot(m,i))*dt
q2(m,i) = q2(m,i) + (1.5*q2dot(m,i) - 0.5*q2dot(m,i))*dt
q3(m,i) = q3(m,i) + (1.5*q3dot(m,i) - 0.5*q3dot(m,i))*dt
end if
end do
end Main
! Integrate the fiber centers of mass
ucmx(m) = ucmx(m)/DBLE(nsegs)
ucmy(m) = ucmy(m)/DBLE(nsegs)
ucmz(m) = ucmz(m)/DBLE(nsegs)
if (step == 1) then
rcmx(m) = rcmx(m) + ucmx(m)*dt
rcmy(m) = rcmy(m) + ucmy(m)*dt
rcmz(m) = rcmz(m) + ucmz(m)*dt
ucox(m) = ucmx(m)
ucoy(m) = ucmy(m)
ucocz(m) = ucmz(m)
else
rcmx(m) = rcmx(m) + (1.5*ucmx(m) - 0.5*ucox(m))*dt
rcmy(m) = rcmy(m) + (1.5*ucmy(m) - 0.5*ucoy(m))*dt
rcmz(m) = rcmz(m) + (1.5*ucmz(m) - 0.5*ucocz(m))*dt
ucoy(m) = ucmy(m)
ucocz(m) = ucmz(m)
endif
! Check periodic boundaries for a fiber leaving the box
corx = dhint(rcmx(m)/sidez)
corz = dhint(rcmz(m)/sidez)
rcmx(m) = rcmx(m) - corx*delta_rx
rcmz(m) = rcmz(m) - corz*delta_rz
rcmx(m) = rcmx(m) - corx*sidez
rcmz(m) = rcmz(m) - corz*sidez
! Check if the time step was too big
if (rcmx(m)-rcmx(m) > sidez*sidez.or. &
rcmz(m)-rcmz(m) > sidez*sidez) then
write(500,*,14,3('P')) time,m,rcmx(m),rcmy(m),rcmz(m)
write(500,*,14,3('P')) time,m,rcmx(m),rcmy(m),rcmz(m)
stop
endif
! Regrow the fibers
do i = 1, nsegs
if (i == 1) then
pjx = 0.0D0; pjy = 0.0D0; pjz = 0.0D0
do j = 2, nsegs
pkx = 0.0D0; pky = 0.0D0; pkz = 0.0D0
do k = 2, j-1
pkx = pkx + px(m,k)
pky = pky + py(m,k)
pkz = pkz + pz(m,k)
end do
end if
end do

```

```

q2(m,i) = q2dot(m,i)
q3(m,i) = q3dot(m,i)
endif
dum = dsqrt(q0(m,i)**2 + q1(m,i)**2 + q2(m,i)**2 + q3(m,i)**2)
q0(m,i) = q0(m,i)/dum
q1(m,i) = q1(m,i)/dum
q2(m,i) = q2(m,i)/dum
q3(m,i) = q3(m,i)/dum
! Calculate the new rotation matrix and p-vectors
R11(m,i) = 2.D0*(g0(m,i)*g0(m,i) + q1(m,i)*q1(m,i)) - 1.D0
R12(m,i) = 2.D0*(g1(m,i)*g0(m,i) + q0(m,i)*q1(m,i))
R13(m,i) = 2.D0*(g1(m,i)*g3(m,i) - q0(m,i)*q2(m,i))
R21(m,i) = 2.D0*(g1(m,i)*g3(m,i) - q0(m,i)*q2(m,i))
R22(m,i) = 2.D0*(g0(m,i)*g0(m,i) + q2(m,i)*q2(m,i)) - 1.D0
R23(m,i) = 2.D0*(g3(m,i)*g0(m,i) + q0(m,i)*q2(m,i))
px(m,i) = 2.D0*(g1(m,i)*q3(m,i) + q0(m,i)*q2(m,i))
py(m,i) = 2.D0*(g3(m,i)*q2(m,i) - q0(m,i)*q1(m,i))
pz(m,i) = 2.D0*(g0(m,i)*q0(m,i) + g3(m,i)*q3(m,i)) - 1.D0
dum = dsqrt(px(m,i)**2 + py(m,i)**2 + pz(m,i)**2)
px(m,i) = px(m,i)/dum
py(m,i) = py(m,i)/dum
pz(m,i) = pz(m,i)/dum
endif
! Integrate the fiber centers of mass
ucmx(m) = ucmx(m)/DBLE(nsegs)
ucmy(m) = ucmy(m)/DBLE(nsegs)
ucmz(m) = ucmz(m)/DBLE(nsegs)
if (step == 1) then
rcmx(m) = rcmx(m) + ucmx(m)*dt
rcmy(m) = rcmy(m) + ucmy(m)*dt
rcmz(m) = rcmz(m) + ucmz(m)*dt
ucox(m) = ucmx(m)
ucoy(m) = ucmy(m)
ucocz(m) = ucmz(m)
else
rcmx(m) = rcmx(m) + (1.5*ucmx(m) - 0.5*ucox(m))*dt
rcmy(m) = rcmy(m) + (1.5*ucmy(m) - 0.5*ucoy(m))*dt
rcmz(m) = rcmz(m) + (1.5*ucmz(m) - 0.5*ucocz(m))*dt
ucoy(m) = ucmy(m)
ucocz(m) = ucmz(m)
endif
! Check periodic boundaries for a fiber leaving the box
corx = dhint(rcmx(m)/sidez)
corz = dhint(rcmz(m)/sidez)
rcmx(m) = rcmx(m) - corx*delta_rx
rcmz(m) = rcmz(m) - corz*delta_rz
rcmx(m) = rcmx(m) - corx*sidez
rcmz(m) = rcmz(m) - corz*sidez
! Check if the time step was too big
if (rcmx(m)-rcmx(m) > sidez*sidez.or. &
rcmz(m)-rcmz(m) > sidez*sidez) then
write(500,*,14,3('P')) time,m,rcmx(m),rcmy(m),rcmz(m)
write(500,*,14,3('P')) time,m,rcmx(m),rcmy(m),rcmz(m)
stop
endif
! Regrow the fibers
do i = 1, nsegs
if (i == 1) then
pjx = 0.0D0; pjy = 0.0D0; pjz = 0.0D0
do j = 2, nsegs
pkx = 0.0D0; pky = 0.0D0; pkz = 0.0D0
do k = 2, j-1
pkx = pkx + px(m,k)
pky = pky + py(m,k)
pkz = pkz + pz(m,k)
end do
end if
end do

```

```
motion_integrate.f90
```

```

    enddo
    p_jx = p_jx + (p_x(m,i) + p_x(m,j) + 2*p_kx)
    p_jy = p_jy + (p_y(m,i) + p_y(m,j) + 2*p_ky)
    p_jz = p_jz + (p_z(m,i) + p_z(m,j) + 2*p_kz)
  enddo
  rx(m,i) = rcmx(m) - (rp/dblE(nseg))*p_jx
  ry(m,i) = rcmy(m) - (rp/dblE(nseg))*p_jy
  rz(m,i) = rcz(m) - (rp/dblE(nseg))*p_jz
else
  p_jx = 0.D0; p_jy = 0.D0; p_jz = 0.D0
  do mth = 2, i-1
    p_jx = p_jx + p_x(m,mth)
    p_jy = p_jy + p_y(m,mth)
    p_jz = p_jz + p_z(m,mth)
  enddo
  rx(m,i) = rx(m,1) + rp*p_x(m,1) + 2.D0*rp*p_jx + rp*p_x(m,i)
  ry(m,i) = ry(m,1) + rp*p_y(m,1) + 2.D0*rp*p_jy + rp*p_y(m,i)
  rz(m,i) = rz(m,1) + rp*p_z(m,1) + 2.D0*rp*p_jz + rp*p_z(m,i)
endif
enddo
enddo Main_m
end subroutine motion_integrate

```

kinetic_friction_force.f90

```

!*****
! Subroutine: friction forces
! calculates static friction forces on groups of
! contacting fiber segments
!*****
subroutine friction_forces(mu_stat,mu_kin,fstar,fact,nrhs,lda,ldb, &
    time,C0,C1,ux,uy,uz,total_contacts,Astar,deccat)
    implicit none
    integer nof,nos,npcn,npgr
    parameter (nof=400,nos=7,npcn=500,npgr=700)
    ! Old variables
    real*8,dimension(nof,nos) :: rx,ry,tz,q0,q1,q2,q3,px,py,pz
    real*8,dimension(nof,nos) :: fx,fy,fz,tx,ty,tz
    real*8,dimension(nof,nos) :: fcx,fcy,fcz,tcx,tcy,tcz
    real*8,dimension(nof,nos) :: D1,D2,D3,A11,A12,A13,A23,A22,A33
    real*8,dimension(nof,nos) :: C11,C12,C13,C23,C22,C33
    real*8,dimension(nof,nos) :: fbx,fbz,tbx,tby,tbz
    real*8,dimension(nof,nos+1) :: uxf1,uyf1,uzf1,ux,uy,uz
    real*8,dimension(nof,nos) :: Yx,Yy,Yz,XX,XY,Xz
    real*8,dimension(npgr,npcn) :: nx,nv,nz,si,sj,g
    real*8,dimension(npgr,npcn) :: ex1,ex2,ex3,ey1,ey2,ey3
    real*8,dimension(npgr,npcn) :: G1jx,G1jy,G1jz,G1jx,G1jy,G1jz
    real*8 :: time,C0,C1,mu_stat,mu_kin,fstar,fact,Astar,deccat
    integer :: nfib,nseg,num_groups,ifiber(4,npcn,npgr)
    integer :: nprp(nof*nos),ncont(npgr),ncpf(nof*nos)
    ! New variables
    integer :: total_contacts,nrhs,lda,ldb,N_size
    real*8 :: P(3*npcn),A(3*npcn,3*npcn)
    ! A,A,back - two copies of the matrix describing contacts
    ! P,back - two copies of right hand side vector with A
    ! Dummy variables
    real*8 :: det,fric_max,fric_sq,r_cont(3,3),delta_uij(3)
    real*8 :: fux,qv,qz,dum,Oik(3,3),posneg,G1x,G1y,G1z,G2x,G2y,G2z
    real*8 :: dirx,bix,diry,biz,bjy,bjz,Du,bdy(3)
    integer :: gc,lc,nr,i,j,k1,k2,ic2,m2,12,n2,j2,r,r,s,info
    logical :: stat,ic
    common /rep_force/ rx,ry,tz,q0,q1,q2,q3,px,py,pz
    common /ambient/ fux,fy,fz,tx,ty,tz,fbx,fbz,tbx,tby,tbz
    common /fric_force/ fx,fy,fz,tcx,tcy,tcz,fbx,fbz,tbx,tby,tbz
    common /params/ nrb,nseg,rp,sidez,sidey,sidez,delta_rx
    common /contact2/ nx,nv,nz,si,sj,g,ex1,ex2,ex3,ey1,ey2,ey3, &
        G1jx,G1jy,G1jz,G1jx,G1jy,G1jz
    common /time/ D1,D2,D3,A11,A12,A13,A23,A22,A33, &
        C11,C12,C13,C23,C22,C33
    common /format/ i3,i4,i4,i4,i4,INFO = '13'
    ! Loop over all the groups to solve for contact forces
    do gc = 1, num_groups
        N_size = 3*ncont(gc)
        do l = 1, N_size
            do j = 1, N_size
                A(j,1) = 0.D0
            enddo
            P(l) = 0.D0
        enddo
        ! Loop over contacts in that group
        do lc = 1, ncont(gc)
            k1 = 3*lc - 2
            m = ifiber(l,lc,gc)
            n = ifiber(3,lc,gc)

```

```

! Find the right hand side components
! These are all sub-calculations.
aix = uxf1(m,i) + &
A11(m,i)*(fcx(m,i)+fbx(m,i)+kx(m,i+1))-kx(m,i) + &
A12(m,i)*(fcy(m,i)+fby(m,i)+ky(m,i+1))-ky(m,i) + &
A13(m,i)*(fcz(m,i)+fbz(m,i)+kz(m,i+1))-kz(m,i)
aiy = uyf1(m,i) + &
A12(m,i)*(fcx(m,i)+fbx(m,i)+kx(m,i+1))-kx(m,i) + &
A22(m,i)*(fcy(m,i)+fby(m,i)+ky(m,i+1))-ky(m,i) + &
A23(m,i)*(fcz(m,i)+fbz(m,i)+kz(m,i+1))-kz(m,i)
aiz = uzf1(m,i) + &
A13(m,i)*(fcx(m,i)+fbx(m,i)+kx(m,i+1))-kx(m,i) + &
A23(m,i)*(fcy(m,i)+fby(m,i)+ky(m,i+1))-ky(m,i) + &
A33(m,i)*(fcz(m,i)+fbz(m,i)+kz(m,i+1))-kz(m,i)
dirx = D1(m,i) + Yx(m,i+1)-Yx(m,i) + C1*tcx(m,i) + tbx(m,i) + &
C0*(py(m,i)*kz(m,i+1)+Xz(m,i)) - &
p2(m,i)*kx(m,i+1)+Xy(m,i))
diry = D2(m,i) + Yy(m,i+1)-Yy(m,i) + C1*tcy(m,i) + tby(m,i) + &
C0*(pz(m,i)*kx(m,i+1)+Xx(m,i)) - &
p2(m,i)*ky(m,i+1)+Xz(m,i))
dirz = D3(m,i) + Yz(m,i+1)-Yz(m,i) + C1*tcz(m,i) + tbz(m,i) + &
C0*(px(m,i)*kx(m,i+1)+Xy(m,i)) - &
p2(m,i)*kz(m,i+1)+Xx(m,i))
bix = Omega_x + C11(m,i)*dirx + C12(m,i)*diry + C13(m,i)*dirz
biy = Omega_y + C12(m,i)*dirx + C22(m,i)*diry + C23(m,i)*dirz
biz = Omega_z + C13(m,i)*dirx + C23(m,i)*diry + C33(m,i)*dirz
ajx = uxf1(n,j) + &
A11(n,j)*(fcx(n,j)+fbx(n,j)+kx(n,j+1))-kx(n,j) + &
A12(n,j)*(fcy(n,j)+fby(n,j)+ky(n,j+1))-ky(n,j) + &
A13(n,j)*(fcz(n,j)+fbz(n,j)+kz(n,j+1))-kz(n,j)
ajy = uyf1(n,j) + &
A12(n,j)*(fcx(n,j)+fbx(n,j)+kx(n,j+1))-kx(n,j) + &
A22(n,j)*(fcy(n,j)+fby(n,j)+ky(n,j+1))-ky(n,j) + &
A23(n,j)*(fcz(n,j)+fbz(n,j)+kz(n,j+1))-kz(n,j)
ajz = uzf1(n,j) + &
A13(n,j)*(fcx(n,j)+fbx(n,j)+kx(n,j+1))-kx(n,j) + &
A23(n,j)*(fcy(n,j)+fby(n,j)+ky(n,j+1))-ky(n,j) + &
A33(n,j)*(fcz(n,j)+fbz(n,j)+kz(n,j+1))-kz(n,j)
dirx = D1(n,j) + Yx(n,j+1)-Yx(n,j) + C1*tcx(n,j) + tbx(n,j) + &
C0*(py(n,j)*kz(n,j+1)+Xz(n,j)) - &
p2(n,j)*kx(n,j+1)+Xy(n,j))
diry = D2(n,j) + Yy(n,j+1)-Yy(n,j) + C1*tcy(n,j) + tby(n,j) + &
C0*(pz(n,j)*kx(n,j+1)+Xx(n,j)) - &
p2(n,j)*ky(n,j+1)+Xz(n,j))
dirz = D3(n,j) + Yz(n,j+1)-Yz(n,j) + C1*tcz(n,j) + tbz(n,j) + &
C0*(px(n,j)*kx(n,j+1)+Xy(n,j)) - &
p2(n,j)*kz(n,j+1)+Xx(n,j))
bjx = Omega_x + C11(n,j)*dirx + C12(n,j)*diry + C13(n,j)*dirz
bjy = Omega_y + C12(n,j)*dirx + C22(n,j)*diry + C23(n,j)*dirz
bjz = Omega_z + C13(n,j)*dirx + C23(n,j)*diry + C33(n,j)*dirz
! Periodic boundaries correction term
fux = sidedx*dnint((uxf1(m,i)-uxf1(n,j))/sidedx)
fy = -(tax - axk - fux + fuz + fby*G1z(gc,ic)-biz*G1y(gc,ic)) - &
(fy)*G1z(gc,ic)-bjz*G1y(gc,ic))
qy = -(tay - ayj + fux*G1x(gc,ic)-bix*G1jz(gc,ic)) - &
(fz)*G1x(gc,ic)-bjx*G1z(gc,ic))
qz = -(taiz - ajz + (bix*G1jy(gc,ic)-bjy*G1jx(gc,ic)) - &
(fjz)*G1y(gc,ic)-bjy*G1jx(gc,ic))
! Define the plane of contact
ex1(gc,ic) = 1.D0 - nx(gc,ic)*nx(gc,ic)
ex2(gc,ic) = -ny(gc,ic)*nx(gc,ic)
ex3(gc,ic) = -nz(gc,ic)*nx(gc,ic)
dum = dsqrt(ex1(gc,ic)**2+ex2(gc,ic)**2+ex3(gc,ic)**2)
ex1(gc,ic) = ex1(gc,ic)/dum
ex2(gc,ic) = ex2(gc,ic)/dum
ex3(gc,ic) = ex3(gc,ic)/dum
ey1(gc,ic) = ny(gc,ic)*ex3(gc,ic) - nz(gc,ic)*ex2(gc,ic)
ey2(gc,ic) = nz(gc,ic)*ex1(gc,ic) - nx(gc,ic)*ex3(gc,ic)

```

kinetic_friction_force.f90

```

    ey3(gc,ic) = nx(gc,ic)*ex2(gc,ic) - ny(gc,ic)*ex1(gc,ic)
    dum = dsqrt(ey1(gc,ic)**2+ey2(gc,ic)**2+ey3(gc,ic)**2)
    ey1(gc,ic) = ey1(gc,ic)/dum
    ey2(gc,ic) = ey2(gc,ic)/dum
    ey3(gc,ic) = ey3(gc,ic)/dum
    ! Fall in the actual rhs vector
    P(kl+1) = qx*ex1(gc,ic) + qy*ex2(gc,ic) + qz*ex3(gc,ic)
    P(kl+2) = qx*ey1(gc,ic) + qy*ey2(gc,ic) + qz*ey3(gc,ic)
    ! Do the diagonal of the matrix A
    Qik(1,1) = A11(m,i) + A11(n,j) - 6
    Cl*(-G1z(gc,ic)*C22(m,i)*G1z(gc,ic) + G1z(gc,ic)*C22(m,i)*G1z(gc,ic) + G1z(gc,ic)*C23(m,i)*G1y(gc,ic) + G1y(gc,ic)*C23(m,i)*G1z(gc,ic) + G1y(gc,ic)*C33(m,i)*G1z(gc,ic) - 6
    G1y(gc,ic)*C23(m,i)*G1z(gc,ic) - 6
    Cl*(-G1z(gc,ic)*C22(n,j)*G1z(gc,ic) + G1z(gc,ic)*C22(n,j)*G1z(gc,ic) + G1z(gc,ic)*C23(n,j)*G1y(gc,ic) + G1y(gc,ic)*C23(n,j)*G1z(gc,ic) + G1y(gc,ic)*C33(n,j)*G1z(gc,ic) - 6
    G1y(gc,ic)*C23(n,j)*G1z(gc,ic) - 6
    G1y(gc,ic)*C33(n,j)*G1z(gc,ic) - 6
    Qik(1,2) = A12(m,i) + A12(n,j) - 6
    Cl*( G1z(gc,ic)*C12(m,i)*G1z(gc,ic) - 6
    G1z(gc,ic)*C23(m,i)*G1x(gc,ic) + 6
    G1z(gc,ic)*C13(m,i)*G1z(gc,ic) + 6
    G1y(gc,ic)*C33(m,i)*G1z(gc,ic) - 6
    Cl*( G1z(gc,ic)*C12(n,j)*G1z(gc,ic) - 6
    G1z(gc,ic)*C23(n,j)*G1x(gc,ic) + 6
    G1z(gc,ic)*C13(n,j)*G1z(gc,ic) + 6
    G1y(gc,ic)*C33(n,j)*G1z(gc,ic) - 6
    Qik(1,3) = A13(m,i) + A13(n,j) - 6
    Cl*(-G1z(gc,ic)*C12(m,i)*G1y(gc,ic) + 6
    G1z(gc,ic)*C22(m,i)*G1x(gc,ic) + 6
    G1z(gc,ic)*C13(m,i)*G1x(gc,ic) - 6
    G1x(gc,ic)*C33(m,i)*G1z(gc,ic) - 6
    Cl*( G1z(gc,ic)*C12(n,j)*G1y(gc,ic) + 6
    G1z(gc,ic)*C22(n,j)*G1x(gc,ic) + 6
    G1z(gc,ic)*C13(n,j)*G1x(gc,ic) - 6
    G1x(gc,ic)*C33(n,j)*G1z(gc,ic) - 6
    Qik(2,2) = A22(m,i) + A22(n,j) - 6
    Cl*(-G1z(gc,ic)*C11(m,i)*G1z(gc,ic) + 6
    G1z(gc,ic)*C11(m,i)*G1y(gc,ic) + 6
    G1z(gc,ic)*C12(m,i)*G1x(gc,ic) + 6
    G1z(gc,ic)*C13(m,i)*G1y(gc,ic) - 6
    G1x(gc,ic)*C11(m,i)*G1z(gc,ic) - 6
    Cl*( G1z(gc,ic)*C11(n,j)*G1z(gc,ic) + 6
    G1z(gc,ic)*C11(n,j)*G1y(gc,ic) + 6
    G1z(gc,ic)*C12(n,j)*G1x(gc,ic) + 6
    G1z(gc,ic)*C13(n,j)*G1y(gc,ic) - 6
    G1x(gc,ic)*C11(n,j)*G1z(gc,ic) - 6
    G1x(gc,ic)*C12(n,j)*G1x(gc,ic) + 6
    G1x(gc,ic)*C13(n,j)*G1y(gc,ic) - 6
    Qik(2,3) = A23(m,i) + A23(n,j) - 6
    Cl*( G1z(gc,ic)*C11(m,i)*G1y(gc,ic) + 6
    G1z(gc,ic)*C12(m,i)*G1x(gc,ic) + 6
    G1z(gc,ic)*C13(m,i)*G1y(gc,ic) - 6
    G1x(gc,ic)*C11(m,i)*G1z(gc,ic) - 6
    Cl*( G1z(gc,ic)*C11(n,j)*G1y(gc,ic) + 6
    G1z(gc,ic)*C12(n,j)*G1x(gc,ic) + 6
    G1z(gc,ic)*C13(n,j)*G1y(gc,ic) - 6
    G1x(gc,ic)*C11(n,j)*G1z(gc,ic) - 6
    G1x(gc,ic)*C12(n,j)*G1x(gc,ic) + 6
    G1x(gc,ic)*C13(n,j)*G1y(gc,ic) - 6
    ! Constrain the motion to the plane of contact...to get A
    A(kl ,kl ) = Qik(1,1)*ex1(gc,ic) + Qik(1,2)*ex2(gc,ic) + &
    Qik(1,3)*ex3(gc,ic)
    A(kl ,kl+1) = Qik(1,2)*ex1(gc,ic) + Qik(2,2)*ex2(gc,ic) + &
    Qik(2,3)*ex3(gc,ic)

```

```

    Qik(2,3)*ex3(gc,ic)
    A(kl ,kl+2) = Qik(1,3)*ex1(gc,ic) + Qik(2,3)*ex2(gc,ic) + &
    Qik(3,3)*ex3(gc,ic)
    A(kl+1,kl ) = Qik(1,1)*ey1(gc,ic) + Qik(1,2)*ey2(gc,ic) + &
    Qik(1,3)*ey3(gc,ic)
    A(kl+1,kl+1) = Qik(1,2)*ey1(gc,ic) + Qik(2,2)*ey2(gc,ic) + &
    Qik(2,3)*ey3(gc,ic)
    A(kl+1,kl+2) = Qik(1,3)*ey1(gc,ic) + Qik(2,3)*ey2(gc,ic) + &
    Qik(3,3)*ey3(gc,ic)
    A(kl+2,kl ) = nx(gc,ic)
    A(kl+2,kl+1) = ny(gc,ic)
    A(kl+2,kl+2) = nz(gc,ic)
    ! Loop over contacts again to get contact dependency
    do ic2 = 1, ncnt(gc)
    ! already did the diagonal
    if(ic /= ic2) then
    k2 = 3*ic2 - 2
    m2 = ifiber(1,ic2,gc) ; i2 = ifiber(2,ic2,gc)
    n2 = ifiber(3,ic2,gc) ; j2 = ifiber(4,ic2,gc)
    if((m-1)*nseq+i) == (m2-1)*nseq+i2) then ! case 1
    r = m ; s = i ; posneg = 1,d0
    G1x = G1ix(gc,ic) ; G1y = G1iy(gc,ic) ; G1z = G1iz(gc,ic)
    G2x = G1ix(gc,ic2) ; G2y = G1iy(gc,ic2)
    G2z = G1iz(gc,ic2)
    elseif((m-1)*nseq+i) == ((n2-1)*nseq+j2)) then ! case 2
    r = m ; s = i ; posneg = -1,d0
    G1x = G1ix(gc,ic) ; G1y = G1iy(gc,ic) ; G1z = G1iz(gc,ic)
    G2x = G1ix(gc,ic2) ; G2y = G1iy(gc,ic2)
    G2z = G1iz(gc,ic2)
    elseif((n-1)*nseq+i) == ((m2-1)*nseq+i2)) then ! case 3
    r = n ; s = j ; posneg = -1,d0
    G1x = G1ix(gc,ic) ; G1y = G1iy(gc,ic) ; G1z = G1iz(gc,ic)
    G2x = G1ix(gc,ic2) ; G2y = G1iy(gc,ic2)
    G2z = G1iz(gc,ic2)
    elseif((n-1)*nseq+i) == ((n2-1)*nseq+j2)) then ! case 4
    r = n ; s = j ; posneg = 1,d0
    G1x = G1ix(gc,ic) ; G1y = G1iy(gc,ic) ; G1z = G1iz(gc,ic)
    G2x = G1ix(gc,ic2) ; G2y = G1iy(gc,ic2)
    G2z = G1iz(gc,ic2)
    else = 0
    endif
    ! If there are two dependent contacts...
    if (t > 0) then
    Qik(1,1) = posneg*(A11(r,s) - 6
    Cl*(-G1z*C23(tr,s)*G2z - G1y*C33(tr,s)*G2y) +
    G1y*C23(tr,s)*G2z - G1z*C33(tr,s)*G2y) + &
    Qik(1,2) = posneg*(A12(tr,s) - 6
    Cl*( G1z*CL2(tr,s)*G2z - G1y*C23(tr,s)*G2x - 6
    G1y*C13(tr,s)*G2z + G1y*C33(tr,s)*G2x)
    Qik(1,3) = posneg*(A13(tr,s) - 6
    Cl*(-G1z*CL2(tr,s)*G2y + G1z*C22(tr,s)*G2x + 6
    G1y*C13(tr,s)*G2y - G1y*C23(tr,s)*G2x)
    Qik(2,1) = posneg*(A12(tr,s) - 6
    Cl*( G1z*CL2(tr,s)*G2z - G1z*CL3(tr,s)*G2y) + &
    G1x*C23(tr,s)*G2z + G1x*C33(tr,s)*G2y)
    Qik(2,2) = posneg*(A22(tr,s) - 6
    Cl*(-G1y*CL1(tr,s)*G2z + G1z*CL3(tr,s)*G2x + 6
    G1x*C13(tr,s)*G2z - G1x*C33(tr,s)*G2x)
    Qik(2,3) = posneg*(A23(tr,s) - 6
    G1x*CL1(tr,s)*G2y - G1z*CL2(tr,s)*G2x - 6
    G1x*CL3(tr,s)*G2y + G1x*C23(tr,s)*G2x)
    Qik(3,1) = posneg*(A13(tr,s) - 6
    Cl*(-G1y*CL2(tr,s)*G2z - G1y*CL3(tr,s)*G2y + 6
    G1x*C22(tr,s)*G2z - G1x*C23(tr,s)*G2y)
    Qik(3,2) = posneg*(A23(tr,s) - 6
    Cl*( G1y*CL1(tr,s)*G2z - G1y*CL3(tr,s)*G2x - 6
    G1x*CL2(tr,s)*G2z + G1x*C23(tr,s)*G2x)

```

kinetic_friction_force.f90

```

      Qik(3,3) = posneg*(A33(tr,s) - &
      C1*(-Gly*C11(tr,s)*G2y + Gly*C12(tr,s)*G2x + &
      G1x*C12(tr,s)*G2y - G1x*C22(tr,s)*G2x)
      ! Put into contact plane
      A(k1,k2) = Qik(1,1)*ex1(gc,ic) + &
      Qik(2,1)*ex2(gc,ic) + Qik(3,1)*ex3(gc,ic)
      A(k1,k2+1) = Qik(1,2)*ex1(gc,ic) + &
      Qik(2,2)*ex2(gc,ic) + Qik(3,2)*ex3(gc,ic)
      A(k1,k2+2) = Qik(1,3)*ex1(gc,ic) + &
      Qik(2,3)*ex2(gc,ic) + Qik(3,3)*ex3(gc,ic)
      A(k1+1,k2) = Qik(1,1)*ey1(gc,ic) + &
      Qik(2,1)*ey2(gc,ic) + Qik(3,1)*ey3(gc,ic)
      A(k1+1,k2+1) = Qik(1,2)*ey1(gc,ic) + &
      Qik(2,2)*ey2(gc,ic) + Qik(3,2)*ey3(gc,ic)
      A(k1+1,k2+2) = Qik(1,3)*ey1(gc,ic) + &
      Qik(2,3)*ey2(gc,ic) + Qik(3,3)*ey3(gc,ic)
      A(k1+2,k2) = 0.00
      A(k1+2,k2+1) = 0.00
      A(k1+2,k2+2) = 0.00
      else
      A(k1,k2) = 0.00; A(k1,k2+1) = 0.00; A(k1,k2+2) = 0.00
      A(k1+1,k2) = 0.00; A(k1+1,k2+1) = 0.00
      A(k1+1,k2+2) = 0.00
      A(k1+2,k2) = 0.00; A(k1+2,k2+1) = 0.00
      A(k1+2,k2+2) = 0.00
      endif
    enddo
  enddo
  ! Apply the static friction constraint
  ! This keeps or breaks contacts based on static friction
  static = true
  do while(static == true.)
  ! Save a copy of the system in case it needs to be redone
  do i = 1, Nsize
    do j = 1, Nsize
      A_back(i,j) = A(i,j)
    enddo
    P_back(i) = P(i)
  enddo
  ! Solve the system with an IUD solver
  call DGSV(Nsize,nrhs,A_back,lda,ipiv,P_back,ldb,info)
  if (info /= 0) then
    write(40,2001) time,gc,ic,info
  stop
  endif
  ! Loop over all the contacts to calculate the force mags.
  fric_max = 0.00; lmax = 0
  do ic = 1, ncnt(gc)
    kl = 3-ic-2
    forc = fstar*depx/(-fact*(g(gc,ic)-2.00))
    fric_sq = P_back(kl)**2 + P_back(kl+1)**2 + P_back(kl+2)**2
    ! Check to see if the magnitude is too great
    if (fric_sq > (nm_stat*forc)**2) then
      if (fric_sq > fric_max) then
        fric_max = fric_sq; lmax = ic
      endif
    endif
  enddo
  ! If too big, break that contact, and recalculate
  if (lmax > 0) then ! must break a contact if true
    ! Assign kinetic friction force to that contact
    nkin = nkin + 1
    forc = fstar*depx/(-fact*(g(gc,lmax)-2.00))
    m = fiber(l,lmax,gc); i = fiber(2,lmax,gc)
    n = fiber(3,lmax,gc); j = fiber(4,lmax,gc)
    ! Need to define a direction. Use the relative
    ! velocities of the fibers from the previous time step

```

```

      Delta_uij(1) = ux(nr,j) - ux(mr,i)
      Delta_uij(2) = uy(nr,j) - uy(mr,i)
      Delta_uij(3) = uz(nr,j) - uz(mr,i)
      ! Reflect Delta_uij into the plane of the contact
      Du_body(1) = Delta_uij(1)*ex1(gc,imax) + &
      Delta_uij(2)*ex2(gc,imax) + Delta_uij(3)*ex3(gc,imax)
      Du_body(2) = Delta_uij(1)*ey1(gc,imax) + &
      Delta_uij(2)*ey2(gc,imax) + Delta_uij(3)*ey3(gc,imax)
      Du_body(3) = 0.00
      ! Transform back into space coordinates
      R_cont(1,1) = ex1(gc,imax); R_cont(1,2) = ex2(gc,imax)
      R_cont(1,3) = ex3(gc,imax)
      R_cont(2,1) = ey1(gc,imax); R_cont(2,2) = ey2(gc,imax)
      R_cont(2,3) = ey3(gc,imax)
      R_cont(3,1) = nx(gc,imax); R_cont(3,2) = ny(gc,imax)
      R_cont(3,3) = nz(gc,imax)
      Delta_uij(1) = R_cont(1,1)*Du_body(1) + &
      R_cont(2,1)*Du_body(2) + R_cont(3,1)*Du_body(3)
      Delta_uij(2) = R_cont(1,2)*Du_body(1) + &
      R_cont(2,2)*Du_body(2) + R_cont(3,2)*Du_body(3)
      Delta_uij(3) = R_cont(1,3)*Du_body(1) + &
      R_cont(2,3)*Du_body(2) + R_cont(3,3)*Du_body(3)
      dum = dsqrt(Delta_uij(1)*Delta_uij(1) + Delta_uij(2)**2 + &
      Delta_uij(3)**2)
      Delta_uij(1) = Delta_uij(1)/dum
      Delta_uij(2) = Delta_uij(2)/dum
      Delta_uij(3) = Delta_uij(3)/dum
      ! Assign friction forces to fibers
      fx(mr,i) = fx(nr,j) + mu_kin*forc*Delta_uij(1)
      fy(mr,i) = fy(nr,j) + mu_kin*forc*Delta_uij(2)
      fz(mr,i) = fz(nr,j) + mu_kin*forc*Delta_uij(3)
      fx(nr,j) = fx(nr,j) - mu_kin*forc*Delta_uij(1)
      fy(nr,j) = fy(nr,j) - mu_kin*forc*Delta_uij(2)
      fz(nr,j) = fz(nr,j) - mu_kin*forc*Delta_uij(3)
      tx(mr,i) = tx(nr,j) + mu_kin*forc*(Gijy(gc,imax)*Delta_uij(3) &
      ty(mr,i) = ty(nr,j) + mu_kin*forc*(Gijz(gc,imax)*Delta_uij(1) &
      tz(mr,i) = tz(nr,j) + mu_kin*forc*(Gijx(gc,imax)*Delta_uij(2) &
      tx(nr,j) = tx(nr,j) - mu_kin*forc*(Gijx(gc,imax)*Delta_uij(2) &
      ty(nr,j) = ty(nr,j) - mu_kin*forc*(Gijy(gc,imax)*Delta_uij(3) &
      tz(nr,j) = tz(nr,j) - mu_kin*forc*(Gijz(gc,imax)*Delta_uij(1) &
      if (lmax < ncnt(gc)) then
        do ic = lmax, ncnt(gc)-1
          kl = 3-ic-2
          fiber(1,ic,gc) = fiber(1,ic+1,gc)
          fiber(2,ic,gc) = fiber(2,ic+1,gc)
          fiber(3,ic,gc) = fiber(3,ic+1,gc)
          fiber(4,ic,gc) = fiber(4,ic+1,gc)
          nx(gc,ic) = nx(gc,ic+1); ny(gc,ic) = ny(gc,ic+1)
          ny(gc,ic) = nz(gc,ic+1)
          sz(gc,ic) = sz(gc,ic+1)
          sj(gc,ic) = sj(gc,ic+1)
          Gijx(gc,ic) = Gijx(gc,ic+1)
          Gijy(gc,ic) = Gijy(gc,ic+1)
          Gijz(gc,ic) = Gijz(gc,ic+1)
          Gijx(gc,ic) = Gijx(gc,ic+1)
          Gijy(gc,ic) = Gijy(gc,ic+1)
          Gijz(gc,ic) = Gijz(gc,ic+1)
          P(kl) = P(kl+3); P(kl+1) = P(kl+4); P(kl+2) = P(kl+5)
          do j = 1, 3*ncnt(gc)
            A(j,kl) = A(j,kl+3); A(j,kl+1) = A(j,kl+4)
            A(j,kl+2) = A(j,kl+5)
          enddo
        enddo

```

kinetic_friction_force.f90

```

do j = 1, 3*nnt(gc)
  A(kl,j) = A(kl+3,j); A(kl+1,j) = A(kl+4,j)
  A(kl+2,j) = A(kl+5,j)
enddo
enddo
endif
nnt(gc) = nnt(gc) - 1; N_size = 3*nnt(gc)
if (N_size <= 0) static = .false.
else
  static = .false.
endif
enddo
! Assign the final friction force to the appropriate fiber
do ic = 1, nnt(gc)
  n = ifiber(1,ic,gc); i = ifiber(2,ic,gc)
  m = ifiber(3,ic,gc); j = ifiber(4,ic,gc)
  kl = 3*ic - 2
  fx(m,i) = fx(m,i) + P_back(kl)
  fy(m,i) = fy(m,i) + P_back(kl+1)
  fz(m,i) = fz(m,i) + P_back(kl+2)
  fx(n,j) = fx(n,j) - P_back(kl)
  fy(n,j) = fy(n,j) - P_back(kl+1)
  fz(n,j) = fz(n,j) - P_back(kl+2)
  tx(m,i) = tx(m,i) + (Gijz(gc,ic) * P_back(kl+2) - G
  ty(m,i) = ty(m,i) + (Gijz(gc,ic) * P_back(kl) - G
  tz(m,i) = tz(m,i) + (Gijz(gc,ic) * P_back(kl+2) - G
  tx(n,j) = tx(n,j) - (Gijz(gc,ic) * P_back(kl+1) - G
  ty(n,j) = ty(n,j) - (Gijz(gc,ic) * P_back(kl+2) - G
  tz(n,j) = tz(n,j) - (Gijz(gc,ic) * P_back(kl) - G
  Gijz(gc,ic) * P_back(kl+2)
  Gijz(gc,ic) * P_back(kl)
  Gijz(gc,ic) * P_back(kl+2)
  Gijz(gc,ic) * P_back(kl+1)
  Gijz(gc,ic) * P_back(kl+2)
  Gijz(gc,ic) * P_back(kl)
  Gijz(gc,ic) * P_back(kl)
enddo
total_contacts = total_contacts + nnt(gc)
enddo
end subroutine friction_forces

```

D.2 Code to calculate the average particle stress

The particle contribution to the stress (σ^p) is calculated using the program `stress.f90`. The program reads the input parameter file (`Parameters.in`) and the configuration output files from a simulation code (`center_mass.dat`, `euler_param.dat`, and `inextens_next_guess.dat`). The code calculates the average stress for every configuration read, and outputs the six independent components of the suspension stress (σ^p/σ^* , where $\sigma^* = \pi n L^3 \eta_o \dot{\gamma} / 6 N_{\text{seg}}^3 \ln 2r_p$) into the file `stress_tensor.dat` at the given time intervals. The steady-state stress is found by averaging the stress components starting at a specified strain (γ_{ss}), and the final steady-state stress is found in the file `Results_stress.dat`.

The following pages contain the code `stress.f90`. The subroutines called, `delta_twist`, `sort`, `friction_forces`, and `x_forces`, and the variable definitions are the same as those used in `flexfric.f90`.

stress.f90

```

open(i3,file='EquilibriumAngles.in',status='old')
open(i4,file='inxtens_next_guess.dat',status='unknown')
! Files that are written to.
open(i20,file='Results stress.dat',status='unknown')
open(i21,file='floc_center_mass.dat',status='unknown')
open(i22,file='floc_euler_param.dat',status='unknown')
open(i23,file='group_fiber_info.dat',status='unknown')
open(i27,file='stress_tensor.dat',status='unknown')
open(i40,file='dgsrv_errors.dat',status='unknown')
open(i41,file='dgsrv_errors.dat',status='unknown')
! Read in parameters and initial configuration information
! Read in initial parameters
read(i0,*) nfib
read(i0,*) nseg
read(i0,*) rp
read(i0,*) kb
read(i0,*) mu_stat
read(i0,*) mu_kin
read(i0,*) contact_cutoff
read(i0,*) rep_cutoff
read(i0,*) neighb_cutoff
read(i0,*) dt_cut
read(i0,*) strain
read(i0,*) side_x, side_y, side_z
read(i0,*) fraction_rp
read(i0,*) contact_write
read(i0,*) extra_write
read(i0,*) check_neighbor
read(i0,*) factar
read(i0,*) factr
read(i0,*) beta_r
read(i0,*) decatt
read(i0,*) delta_rx
read(i0,*) duvdx
read(i0,*) duvdy
read(i0,*) duvdz
read(i0,*) duvdx
read(i0,*) duvdy
read(i0,*) duvdz
read(i0,*) duvdx
read(i0,*) duvdy
read(i0,*) duvdz
close(i0)
! Fiber coordinates
do m = 1, nfib
do i = 1, nseg
! Assign body forces and torques.
fxb(m,i) = 0.D0
fby(m,i) = 0.D0
fzb(m,i) = 0.D0
cxb(m,i) = 0.D0
cby(m,i) = 0.D0
cbz(m,i) = 0.D0
! Make the equilibrium rotation matrix
if (i > 1) then
read(i3,*) idum1, idum2, thetaeq, phi1eq
R11eq(m,i) = dcos(thetaeq)*dcos(phi1eq)
R12eq(m,i) = dcos(thetaeq)*dsin(phi1eq)
R13eq(m,i) = -dsin(thetaeq)
R21eq(m,i) = -dsin(phi1eq)
R22eq(m,i) = dcos(phi1eq)
R23eq(m,i) = 0.D0
R31eq(m,i) = dsin(thetaeq)*dcos(phi1eq)
R32eq(m,i) = dsin(thetaeq)*dsin(phi1eq)
R33eq(m,i) = dcos(thetaeq)
endif
enddo
enddo
! Calculate some commonly used constants in the program
! Rate of strain tensor for the flow field.
E11 = 0.5D0*(duvdx + duvdx)
E12 = 0.5D0*(duvdx + duvdy)
E13 = 0.5D0*(duvdx + duvdz)
E22 = 0.5D0*(duvdy + duvdy)
E23 = 0.5D0*(duvdy + duvdz)
E33 = 0.5D0*(duvdz + duvdz)
! Fluid angular velocity
Omega_x = 0.5D0*(duvdy - duvdx)
Omega_y = 0.5D0*(duvdx - duvdz)
Omega_z = 0.5D0*(duvdy - duvdx)
! Resistance functions
re = fraction_rp*rp
ecc = dsqrt(re*re - 1.D0)/re
Xa = (8.D0*ecc**3/3.D0)/(-2.0*ecc+(1.0+ecc*ecc) * &
dlog((1.D0+ecc)/(1.D0-ecc)))
Ya = (16.D0*ecc**3/3.D0)/(2.0*ecc+(3.0*ecc*ecc-1.0) * &
dlog((1.D0+ecc)/(1.D0-ecc)))
Xc = (4.D0*ecc**3/3.D0)*(1.0-ecc*ecc)/(2.0*ecc-(1.0-ecc*ecc) * &
dlog((1.D0+ecc)/(1.D0-ecc)))
Yc = (4.D0*ecc**3/3.D0)*(2.0-ecc*ecc)/(-2.0*ecc+(1.0+ecc*ecc) * &
dlog((1.D0+ecc)/(1.D0-ecc)))
Yh = (4.D0*ecc**5/3.D0)/(-2.0*ecc+(1.0+ecc*ecc) * &
dlog((1.D0+ecc)/(1.D0-ecc)))
! Other constants
kt = 0.67D0*kb ! twisting constant
C0 = 3.D0/(4.D0*rp)
C1 = 3.D0/(4.D0*rp*rp)
C2 = 3.D0/(4.D0*Yc)
C3 = 1.D0/Ya - 1.D0/Ya
C4 = 1.D0/Yc - 1.D0/Yc
! vectors to describe flow field
e1(1) = 0.D0; e1(2) = 0.D0; e1(3) = 1.D0
e2(1) = 1.D0; e2(2) = 0.D0; e2(3) = 0.D0
contact_cutoff = (contact_cutoff + 2.D0)**2
rep_cutoff = (rep_cutoff + 2.D0)**2
zero = 0.D0
k1 = 1; lda = 3*npcn; ldb = 3*npcn
k1 = isopr(k1)
ldab = 2*kl + ku + 1; ldx = 3*(nseg-1); Nband = 3*(nseg-1)
nL3 = nfib*(2*nseg*rp)**2/(side_x*side_y*side_z)
volfrac = nfib*nseg*pi*(2*rp)/(side_x*side_y*side_z)
consistency = volfrac/2.6D0
! Make the README file to explain which run this is:
write(i20,*) 'Stress Calculation Results'
write(i20,*) '*****'
write(i20,*) 'Number of fibers/segments:', nfib, nseg
write(i20,*) 'Aspect Ratio of fiber:', rp*nseg
write(i20,*) 'Box Side Lengths:', side_x, side_y, side_z
write(i20,*) 'Coefficients of Friction:', mu_stat, mu_kin
write(i20,*) 'Bending Constant:', kb
write(i20,*) 'concentration, nL3:', nL3
! Loop over all configurations in the input files
check = 0
N_avg = 0
print, 'At what strain do you want to start averaging?'
read*, start_strain
do while (check == 0)
read(i1,*, iostat=check) time
read(i2,*, iostat=check) time
read(i4,*, iostat=check) time
if (check == 0) then
do m = 1, nfib
read(i11,*) idum1, rcmx(m), rcmz(m), rcmz(m)

```


stress.f90

```

p2 = px(m,i)*e2(1,1)*py(m,i)*e2(2,2)+pz(m,i)*e2(3,3)
! Isotropic term
ITterm = p1*e2/6.D0 + (fh(1)*rx(m,i)+fh(2)*py(m,i)+ &
fh(3)*rz(m,i))/rp**2
! Extra particle stress
Stress(1,1) = Stress(1,1) + p1*(e2(1,1)*px(m,i) + &
px(m,i)*e2(1,1) - p1*p2*px(m,i)*px(m,i) - &
wy(m,i)*pz(m,i)-wz(m,i)*py(m,i))*px(m,i) - &
px(m,i)*wy(m,i)*pz(m,i)-wz(m,i)*py(m,i))*py(m,i) + &
(3.0/rp**2)*(fh(1)*rx(m,i) + rx(m,i)*fh(1)) - ITterm
Stress(1,2) = Stress(1,2) + p1*(e2(1,1)*py(m,i) + &
py(m,i)*e2(2,1) - p1*p2*px(m,i)*py(m,i) - &
wy(m,i)*pz(m,i)-wz(m,i)*py(m,i))*py(m,i) - &
px(m,i)*wy(m,i)*pz(m,i)-wz(m,i)*py(m,i))*pz(m,i) + &
(3.0/rp**2)*(fh(1)*ry(m,i) + ry(m,i)*fh(2))
Stress(1,3) = Stress(1,3) + p1*(e2(1,1)*pz(m,i) + &
pz(m,i)*e2(3,1) - p1*p2*px(m,i)*pz(m,i) - &
wy(m,i)*pz(m,i)-wz(m,i)*py(m,i))*pz(m,i) - &
px(m,i)*wy(m,i)*pz(m,i)-wz(m,i)*py(m,i))*px(m,i) + &
(3.0/rp**2)*(fh(1)*rz(m,i) + rz(m,i)*fh(3))
Stress(2,2) = Stress(2,2) + p1*(e2(2,1)*py(m,i) + &
py(m,i)*e2(2,2) - p1*p2*py(m,i)*py(m,i) - &
wy(m,i)*pz(m,i)-wz(m,i)*py(m,i))*py(m,i) - &
px(m,i)*wy(m,i)*pz(m,i)-wz(m,i)*py(m,i))*pz(m,i) + &
(3.0/rp**2)*(fh(2)*ry(m,i) + ry(m,i)*fh(2)) - ITterm
Stress(2,3) = Stress(2,3) + p1*(e2(2,1)*pz(m,i) + &
pz(m,i)*e2(3,2) - p1*p2*py(m,i)*pz(m,i) - &
wy(m,i)*pz(m,i)-wz(m,i)*py(m,i))*pz(m,i) - &
px(m,i)*wy(m,i)*pz(m,i)-wz(m,i)*py(m,i))*px(m,i) + &
(3.0/rp**2)*(fh(2)*rz(m,i) + rz(m,i)*fh(3)) - ITterm
enddo

enddo
enddo
! Find the variance/standard deviation
do m = 1, N_avg
Str_Dev(1,1) = Str_Dev(1,1) + (Str_sq11(m) - &
Str_sq11(N_avg))**2
Str_Dev(1,2) = Str_Dev(1,2) + (Str_sq12(m) - &
Str_sq12(N_avg))**2
Str_Dev(1,3) = Str_Dev(1,3) + (Str_sq13(m) - &
Str_sq13(N_avg))**2
Str_Dev(2,2) = Str_Dev(2,2) + (Str_sq22(m) - &
Str_sq22(N_avg))**2
Str_Dev(2,3) = Str_Dev(2,3) + (Str_sq23(m) - &
Str_sq23(N_avg))**2
Str_Dev(3,3) = Str_Dev(3,3) + (Str_sq33(m) - &
Str_sq33(N_avg))**2
enddo
! Average over all realizations
write(20,*) "Overall Particle Stress Tensor"
write(20,*,f,3x,f,3x,f") Stress_Avg(1,1)/dble(N_avg), &
Stress_Avg(1,2)/dble(N_avg), Stress_Avg(1,3)/dble(N_avg), &
Stress_Avg(2,2)/dble(N_avg), Stress_Avg(2,3)/dble(N_avg), &
Stress_Avg(2,3)/dble(N_avg), Stress_Avg(3,3)/dble(N_avg)
write(20,*,f,3x,f,3x,f") Stress_Avg(1,1), Stress_Avg(1,2), Stress_Avg(1,3), Stress_Avg(2,2), Stress_Avg(2,3), Stress_Avg(3,3)
! First and Second Normal Particle Stress Differences"
write(20,*,f,5x,f") (Stress_Avg(1,1)-Stress_Avg(3,3))/dble(N_avg), &
(Stress_Avg(3,3)-Stress_Avg(2,2))/dble(N_avg)
write(20,*) "Standard deviation of the Stress Tensor"
write(20,*,f,3x,f,3x,f") Str_Dev(1,1), Str_Dev(1,2), Str_Dev(1,3), Str_Dev(2,2), Str_Dev(2,3), Str_Dev(3,3)
! Write out the biggest file to a file
do m = 1, nfile
if(storfile(m) == .true.) then
write(21,"i5.1x,3f", m, rcmx(m), rcmy(m), rcnz(m)
do i = 1, nseg
write(22,"i5.1x,i3.1x,4f", m, i, q0(m,i), q1(m,i), q2(m,i), q3(m,i)
enddo
endif
enddo
end Program stress_calc

```

D.3 Planar network elongation code

The code used to find the tensile strength of a fiber network is in the file called `Tensile_approx.f90`. The code has the same basic structure as the `flexfric` program used for linear flows. The basic difference is in the boundary conditions, and the fact that the extra constraint force for pulling fibers must be calculated. For this system, the periodic boundary conditions are only applied in the y direction, and there are additional forces in the z direction for the fibers that interact with the top and bottom surfaces via repulsive forces only. Included below is the main body of the code, `Tensile_approx`, and two major subroutine revisions to `delta_twist` and `x_forces`. The other subroutines are the same as those above with the correction to the periodic boundary conditions as demonstrated in `delta_twist`.

Tensile_approx..f90

```

! Code 2: Approximate code for fibers with static being compressed between two plate
s
program Tensile_approx
implicit none
! nof - number of fibers
! ncn - number of segments
! npcn - number of potential contacts
! npr - number of potential groups
! npl - number of fibers being pulled
integer nof,nos,npcn,npr
parameter(nof=360,nos=5,npcn=1100,npr=800)
! All of the variables in the main body of the program
real*8 :: pi
parameter(pi=3.14159265359)
real*8,dimension(nof) :: rcmx,rcmy,rcmz,ucmx,ucmy,ucmz
real*8,dimension(nof) :: ucox,ucoy,ucoz
real*8,dimension(nof,nos) :: rx,ry,tz,q0,q1,q2,q3,px,py,pz,ux,uy,uz
real*8,dimension(nof,nos) :: wx,wy,wz,q0dot,q1dot,q2dot,q3dot
! rcmx,rcmy,rcmz - fiber center of mass
! rx,ry,tz - sement centers
! q0,q1,q2,q3 - segment euler parameters
! q0dot... - time derivatives of Euler Parameters
! px,py,pz - segment orientational vectors
! ucmx,ucmy,ucmz,ucmx - fiber center of mass velocity
! ux,uy,uz - segment velocity
! uxf1,uyf1,uzf1 - ambient flow field velocity
! wx,wy,wz - segment angular velocity
real*8,dimension(nof,nos) :: R11,R12,R13,R21,R22,R23
real*8,dimension(nof,nos) :: R11eq,R12eq,R13eq,R21eq,R22eq
real*8,dimension(nof,nos) :: R23eq,R31eq,R32eq,R33eq
! R11,R12,... - segment body rotation matrix
! R11eq,R12eq,... - equilibrium rotation matrix (arbitrary for each fiber)
! Xx,Xy,Xz - intrafiber constraint forces
! Yx,Yy,Yz - bending/twisting torques
real*8,dimension(nof,nos) :: Fx,Fy,Fz,tz,ty,tz,fcx,fcy,fcz
real*8,dimension(nof,nos) :: tcz,fcz,tcz,fbx,fbz,tbx,tby,tbz,fbx
! Fx,Fy,Fz - frictional forces on segment
! tx,ty,tz - frictional torques on segment
! fbx,fbz,fbz - segment body force (i.e. gravity, etc.)
! tbx,tby,tbz - segment body torque
! fcx,fcy,fcz - segment colloidal repulsive force
! tcz,fcz,tcz - segment colloidal repulsive torque
! Fx,Fy,Fz - pulling force
real*8,dimension(nof,nos) :: A11,A12,A13,A23,A22,A33
real*8,dimension(nof,nos) :: C11,C12,C13,C23,C22,C33
real*8,dimension(nof,nos) :: qe0,qe1,qe2,qe3,d1
! A11,... - A inverse term in notes
! qe0,... - qdot's at the last time step
! d1(m,1) - grab position on the m,1th pulled fiber
real*8,dimension(npr,npcn) :: nx,ny,nz,si,sj,g,exi,ex2,ex3
real*8,dimension(npr,npcn) :: eyi,ey2,ey3,g1jx,g1jy,g1jz
real*8,dimension(npr,npcn) :: g1jx,g1jy,g1jz
! nx,ny,nz - normals between contacting fibers
! si,sj - distance from center of segment to contact point
! g - gap between fiber centers at contact point
! ex1,...,ey1,... - defines plane that contains the friction force
! G1jx,...,G1jz... - vector s1j*p +/- g1j*n
integer :: next(2,2,npcn,nof,nos),nclose(nof,nos)
integer :: pull_check(nof,nos),Fiber(2,nof),ncpf(nof*nos)
integer :: lifber(4,npcn,npr),ngrp(nof,nos),ncnt(npr)
! next(nth,m,1) - 1th neighbor of fiber m, segment 1
! nclose(m,1) - number of neighbors of fiber m, segment 1
! lifber(1,ct,m) - 1st fiber in contact ct, group mg
! ngrp(m) - group # of fiber m
! ncnt(m) - # of contacts in group mg
! ncpf(m) - number of contacts with fiber m

```

```

real*8 :: ip,kb,kt,dt,strain,sidex,sidex,sidey,sidez,rc,ecc
real*8 :: Xa,Ya,Xc,Yc,Yh,fraction_ip
! Omega... - ambient flow field angular velocity
! ip - segment aspect ratio
! kb/kt - bending/twisting constants
! thetaeq/phiqeq - angles associated with the equil. configuration
! dt,strain - time step, total time of run
! side - simulation box size
! re - effective segment aspect ratio
! ecc - eccentricity
! Xa,Ya,Xc,Yc,Yh - scalar resistance functions
! fraction_ip - effective aspect ratio factor
real*8 :: tstar,mu_stat,mu_kin,contact_cutoff,rep_cutoff
real*8 :: neighb_cutoff,fstar,fact,dt_2,Astar,decat
! tstar - current strain
! delrx - shift variable for sliding periodic images
! mu_stat/mu_kin - static/kinetic coefficient of friction
! contact_cutoff - cutoff for contacts
! rep_cutoff - cutoff distance for calculating repulsive forces
! neighb_cutoff - cutoff for neighborlist
! fstar,fact - force prefactor, force exponential factor
! dt_2 - smaller time step if dt is too big
! Astar - Prefactor of the attractive force
! decatt - decay length of the attractive force
integer :: nfib,nseg,time_steps,config_write,contact_write
! nfib,nseg - number of fiber, segments per fiber
! config_write - number of time steps between configuration writes
! contact_write - number of time steps between contact info writes
! check_neighbor - number of time steps between neighbor list checks
! time_steps - number of time steps
! num_groups - number of groups
! overs - number of overlapping contacts
! substeps - number of steps at the smaller time step
integer :: nrhs,lhs,lhb,lhb,ldb,N,Nband,k1,ku,npull
! nrhs - number of right hand sides for solving our linear systems
! lhs - leading order dimension of the friction matrix
! lhb - leading order dimension of the right hand side
! ldb - leading order of the band storage matrix in solving for X
! ldx - leading order of rhs in solving for X (3*(nseg-1))
! Nband - dimension of matrix to solve for X
! N1/k1u - number of over/upper diagonal terms in banded matrix
real*8 :: n13,volfrac,viscosity,over_t
! n13 - wall_ep_cutoff,wall_conc_cutoff
! volfrac - volume fraction
! consist - consistency, volfrac/2.6
integer :: idum1,idum2,mth,K,step,m,r1,r1j,gc,ic
integer :: total_contacts,extra_writer,num_small_steps
real*8 :: dum,theataeq,phiqeq,pxj,pyj,pzj,pxk,pyk,pzk
real*8 :: fwz,upx,cof_tens,cof_writer,co_write,e_write
! fwz - force on the top plate
! upx - velocity that the mat is being pulled apart
! Common statements
! Common /rpsps/ rx,ry,rz,q0,q1,q2,q3,px,py,pz
! Common /rpic/ rcmx,rcmy,rcmz
! Common /rpic_forces/ fx,fy,fz,tbx,tby,tz,fbx,fbz,tbx,tby,tbz
! Common /velocities/ ux,uy,uz,wx,wy,wz,q0dot,q1dot,q2dot,q3dot
! Common /ucm/ ucmx,ucmy,ucmz
! Common /AandC/ A11,A12,A13,A23,A22,A33,C11,C12,C13,C23,C22,C33
! Common /Params/ nfib,nseg,rp,sidex,sidey,sidez
! Common /contact1/ lifber,ngrp,ncnt,ncpf,num_groups
! Common /contact2/ nx,ny,nz,si,sj,g,ex1,ex2,ex3,ey1,ey2,ey3, &
! G1jx,G1jy,G1jz,g1jx,g1jy,g1jz
! Common /rotation/ R11,R12,R13,R21,R22,R23
! Common /equilrot/ R11eq,R12eq,R13eq,R21eq,R22eq,R23eq, &

```

Tensile_approx..f90

```

R31eq,R32eq,R33eq
common /constants/ Ya,Yc,Yh,C0,C1,C3,C4
common /joints/ Xx,Yy,Xz,Xx,Xy,Xz
common /laststep/ q0,q1,q2,q3,ucox,ucoy,ucoz
! Files that are read
open (10,files='Parameters.in',status='old')
open (11,files='Centers of Mass.in',status='old')
open (12,files='Euler Parameters.in',status='old')
open (13,files='Equilibrium Angles.in',status='old')
! Files that are written to.
open (20,files='README',status='unknown')
open (21,files='center.mass.dat',status='unknown')
open (22,files='euler.param.dat',status='unknown')
open (23,files='resist_func.dat',status='unknown')
open (26,files='nextens_next_guess.dat',status='unknown')
open (35,files='Contact Info.dat',status='unknown')
open (37,files='Number of Contacts.dat',status='unknown')
open (38,files='tensile_strength.dat',status='unknown')
open (40,files='dgesv_Fric_errors.dat',status='unknown')
open (41,files='dgesv_X_errors.dat',status='unknown')
! Format statements
1013 format (i4,3(1x,1pD23.15))
1023 format (i4,1x,1x,3(1x,1pD23.15))
1026 format (i4,1x,1x,6(1x,1pD23.15))
1024 format (i4,1x,1x,4(1x,1pD23.15))
1063 format (f11,6,1x,6(1x,1x),3f)
1113 format (f12,7,4(2x,i4))
1123 format (f10,5,2(2x,i4),1(2x,1pD23.15))
! Read in parameters and initial configuration information
! Read in initial parameters
read (10,*) nfib
read (10,*) nseg
read (10,*) rp
read (10,*) kb
read (10,*) mu
read (10,*) mu_kin
read (10,*) contact_cutoff
read (10,*) rep_cutoff
read (10,*) neighb_cutoff
read (10,*) over_cut
read (10,*) dt
read (10,*) strain
read (10,*) sideX,sideY,sideZ
read (10,*) fraction_ip
read (10,*) cF_write
read (10,*) e_write
read (10,*) check_neighbor
read (10,*) fstar
read (10,*) fact
read (10,*) Astar
read (10,*) decatt
read (10,*) upx
! Fiber coordinates
do m = 1,nfib
  read (11,*) idum1,rcmx(m),rcmy(m),rcmz(m)
  do l = 1,nseg
    read (12,*) idum2,q0(m,i),q1(m,i),q2(m,i),q3(m,i)
    dum = dsqrt(q0(m,i)**2 + q1(m,i)**2 + q2(m,i)**2 + q3(m,i)**2)
    q1(m,i) = q0(m,i)/dum
    q2(m,i) = q1(m,i)/dum
    q3(m,i) = q3(m,i)/dum
    ! Find the roation matrix
    R11(m,i) = 2.00*(q0(m,i)*q0(m,i)+q1(m,i)*q1(m,i)) - 1.00
    R12(m,i) = 2.00*(q1(m,i)*q2(m,i) + q0(m,i)*q3(m,i))
    R13(m,i) = 2.00*(q1(m,i)*q3(m,i) - q0(m,i)*q2(m,i))
    R21(m,i) = 2.00*(q0(m,i)*q2(m,i) - q0(m,i)*q3(m,i))
    R22(m,i) = 2.00*(q1(m,i)*q2(m,i) + q0(m,i)*q1(m,i))
    R23(m,i) = 2.00*(q1(m,i)*q3(m,i) - q0(m,i)*q2(m,i)) - 1.00
    R31(m,i) = 2.00*(q0(m,i)*q3(m,i) + q0(m,i)*q2(m,i)) - 1.00
    R32(m,i) = 2.00*(q1(m,i)*q2(m,i) + q0(m,i)*q1(m,i))
    R33(m,i) = 2.00*(q1(m,i)*q3(m,i) - q0(m,i)*q2(m,i))
    ! Assign body forces and torques.
    fbx(m,i) = 0.00; fby(m,i) = 0.00; fbz(m,i) = 0.00
    tbx(m,i) = 0.00; tby(m,i) = 0.00; tbz(m,i) = 0.00
    ! Make the equilibrium rotation matrix
    if (i > 1) then
      read (13,*) idum1,idum2,theaeg,phieq
      R11eq(m,i) = dcos(theaeg)*dcos(phieq)
      R12eq(m,i) = dcos(theaeg)*dsin(phieq)
      R13eq(m,i) = -dsin(theaeg)
      R21eq(m,i) = -dsin(phieq)
      R22eq(m,i) = dcos(phieq)
      R23eq(m,i) = 0.00
      R31eq(m,i) = dsin(theaeg)*dcos(phieq)
      R32eq(m,i) = dsin(theaeg)*dsin(phieq)
      R33eq(m,i) = dcos(theaeg)
    endif
    ! Find initial position of each fiber segment
    do i = 1, nseg
      if (i == 1) then
        pxj = 0.00; pyj = 0.00; pjz = 0.00
        do j = 2, nseg
          rpx = 0.00; rpy = 0.00; rpz = 0.00
          do k = 2, i-1
            pxk = rpx + px(m,k); pyk = rpy + py(m,k)
            pkz = rpkz + pz(m,k)
          enddo
          pxj = rpx + (px(m,i) + px(m,j) + 2*pkx)
          pyj = rpy + (py(m,i) + py(m,j) + 2*pkj)
          pjz = rpkz + (pz(m,i) + pz(m,j) + 2*pkz)
        enddo
        rx(m,i) = rcmx(m) - (rp/DBLE(nseg))*pxj
        ry(m,i) = rcmy(m) - (rp/DBLE(nseg))*pyj
        rz(m,i) = rcmz(m) - (rp/DBLE(nseg))*pjz
      else
        pxj = 0.00; pyj = 0.00; pjz = 0.00
        do mch = 2, i-1
          pxj = rpx + px(m,mch); pyj = rpy + py(m,mch)
          pjz = rpkz + pz(m,mch)
        enddo
        rx(m,i) = rx(m,i) + rp*px(m,i) + 2.00*rp*px(m,i)
        ry(m,i) = ry(m,i) + rp*py(m,i) + 2.00*rp*py(m,i)
        rz(m,i) = rz(m,i) + rp*pz(m,i) + 2.00*rp*pz(m,i)
      endif
    enddo
  enddo
close (10); close (11); close (12); close (13)
! Calculate some commonly used constants in the program
ecc = fraction_ip*rp
re = fraction_ip*rp
Xa = (8.00*ecc**3/3.00)/(-2.0*ecc+(1.0+ecc*ecc))* &
dlog((1.00+ecc)/(1.00-ecc))
Ya = (16.00*ecc**3/3.00)/(2.0*ecc+(3.0*ecc*ecc-1.0))* &
dlog((1.00+ecc)/(1.00-ecc))
Xc = (4.00*ecc**3/3.00)*(1.0+ecc*ecc)/(2.0*ecc-(1.0+ecc*ecc))* &
dlog((1.00+ecc)/(1.00-ecc))
Yc = (4.00*ecc**3/3.00)*(2.0+ecc*ecc)/(-2.0*ecc+(1.0+ecc*ecc))* &
dlog((1.00+ecc)/(1.00-ecc))
enddo

```

Tensile_approx..f90

```

Yh = (4.D0*ecc**5/3.D0)/(-2.0*ecc*(1.0+ecc*ecc)) *
dlog((1.D0+ecc)/(1.D0-ecc))
write(25,*) 'Xa = ',Xa; write(25,*) 'Ya = ',Ya
write(25,*) 'Xc = ',Xc; write(25,*) 'Yc = ',Yc
write(25,*) 'Yh = ',Yh
! Other constants
time_steps = nint(strain*sidex/(dt*upx)) ! number of time steps
config_write = nint(cf_write*sidex/(dt*upx))
contact_write = nint(cn_write*sidex/(dt*upx))
extra_write = nint(e_write*sidex/(dt*upx))
kt = 0.67D0*kb ! twisting constant
C0 = 3.D0/(4.D0*rp); C1 = 3.D0/(4.D0*rp*rp)
C2 = 3.D0/(4.D0*Yc); C3 = 1.D0/Xa - 1.D0/Ya
C4 = 1.D0/Xc - 1.D0/Yc
rlmsq = (2.0*(rp+1)+1.5)*(2.0*(rp+1)+1.5)
neighb_cutoff = (2.D0 + neighb_cutoff) + 2.D0
wall_rep_cutoff = rep_cutoff + 2.D0
wall_rep_cutoff = (contact_cutoff + 2.D0)**2
zero = 0.D0
nrhs = 1; lda = 3*nrpcn; ldb = 3*nrpcn
kl = 5; ku = 5
ldab = 3*(nos-1)+nos; ldx = 3*(nos-1)+nos; Nband = 3*(nseg-1)
nl3 = nfib*(2*nseg*rp)**3/(sidex*sidex*sidex)
volfrac = nfib*nseg*rp*(2*rp)/(sidex*sidex*sidex)
consistency = volfrac/2.D0
! Make the README file to explain which run this is:
write(20,*) 'Fibers with kinetic friction'
write(20,*)
write(20,*) 'Number of Fibers:', nfib
write(20,*) 'Number of Segments:', nseg
write(20,*) 'Aspect Ratio of a Segment:', rp
write(20,*) 'Aspect Ratio of fiber:', rp*nseg
write(20,*) 'Time Step:', dt
write(20,*) 'Total Strain:', strain
write(20,*) 'a30 1x 3e" Box Initial Side Lengths:', sidex, sidey, sidez
write(20,*) 'Coefficients of Friction:', mu_stat, mu_kin
write(20,*) 'Bending Constant:', kb
write(20,*) 'Twisting Constant:', kt
write(20,*) 'Contact Volume:', nl3, nl3
write(20,*) 'Final Volume Fraction:', volfrac
write(20,*) 'Consistency:', consistency
! Call neighbor list subroutine and write initial configuration
call neighbor_list_subroutine and write initial configuration
write(21,*) step*dt
write(22,*) step*dt
write(26,*) step*dt
do m = 1, nfib
write(21,1013) m,rcmx(m),rcmy(m),rcmz(m)
do i = 1, nseg
write(22,1024) m,i,q0(m,i),q1(m,i),q2(m,i),q3(m,i)
write(26,1023) m,i,xx(m,i),xy(m,i),xz(m,i)
enddo
enddo
! Identify the fibers that are pulled at opposing x-faces
call Grab(npull,di,pull_check,pfiber)
! Get initial guesses for X-forces
call delta_twist(over_cut,contact_cutoff,rep_cutoff,next,&
nclose,overs,fstar,fact,kb,kt,zero,Astar,decat, &
wall_rep_cutoff,wall_cont_cutoff,fwz)
call x_forces(nrhs,Nband,ldab,ldx,ku,kl,C0,C1,C2,C3,Ya,Yc,zero, &
ngRP,di,pull_check,upx,tot_tens)
! zero the total tensile force
tot_tens = 0.D0
!#####
!##### MAIN TIME LOOP #####
!#####

```

```

do step = 1, time_steps
! Update the neighbor list
if(mod(step,check_neighbor) == 0) call neighbor(next,nclose, &
neighb_cutoff,rlmsq,dt*step)
! Calculate the friction forces at contacts
call friction_forces(mu_stat,mu_kin,fstar,fact,nrhs,lda,ldb, &
dt*step,C0,C1,C3,Ya,Yc,ux,uy,uz,tot_contacts,Astar, &
decat,di,pull_check,upx,tot_tens)
! Update inextensibility constraint forces
call x_forces(nrhs,Nband,ldab,ldx,ku,kl,C0,C1,C2,C3,Ya,Yc, &
dt*step,ngRP,di,pull_check,upx,tot_tens)
! Integrate the equations of motion
call motion_integrate(dt,step,C0,dt*step)
! Update the interparticle separations for next time step
call delta_twist(over_cut,contact_cutoff,rep_cutoff,next,&
nclose,overs,fstar,fact,kb,kt,dt*step,Astar,decat, &
wall_rep_cutoff,wall_cont_cutoff,fwz)
! Occasionally write contact information
if(mod(step,extra_write) == 0) then
do gc = 1, num_groups
do ic = 1, ncnt(gc)
m=ifiber(1,ic,gc);i=ifiber(2,ic,gc)
n=ifiber(3,ic,gc);j=ifiber(4,ic,gc)
write(35,1063) dt*step,m,i,n,j,gc,ic,si(gc,ic), &
s_j(gc,ic),g(gc,ic)
enddo
enddo
! Occasionally write the number of system contacts
if(mod(step,contact_write) == 0) then
total_contacts = 0
do gc = 1, num_groups
total_contacts = total_contacts + ncnt(gc)
enddo
write(37,1113) dt*step,num_groups,total_contacts,overs
write(38,*) dt*step*upx/sidex,tot_tens/(dble(contact_write))
tot_tens = 0.D0
num_small_steps = 0
endif
! Occasionally write system configurations
if(mod(step,conf_write) == 0) then
write(22,*) step*dt
write(26,*) step*dt
do m = 1, nfib
write(21,1013) m,rcmx(m),rcmy(m),rcmz(m)
do i = 1, nseg
write(22,1024) m,i,q0(m,i),q1(m,i),q2(m,i),q3(m,i)
write(26,1023) m,i,xx(m,i),xy(m,i),xz(m,i)
enddo
enddo
enddo
end Program Tensile_approx

```

delta_twist.f90

```

! This routine calculate the bending/twisting torques as well as
! interparticle separations
subroutine delta_twist(over_cut,contact_cutoff,rep_cutoff,next, &
  nclose,overs,fstar,fact,kb,kt,time,Astar,deccat,wall_rep_cutoff, &
  wall_cont_cutoff,fwz)
  implicit none
  integer nof,nos,npcn,npr
  parameter (nof=360,nos=5,npcn=1100,npr=800)
  real*8,dimension(nof,nos) :: rx,ry,tz,q0,q1,q2,q3,px,py,pz
  real*8,dimension(nof,nos) :: R11,R12,R13,R21,R22,R23
  real*8,dimension(nof,nos) :: R11eq,R12eq,R13eq,R21eq,R22eq,R23eq
  real*8,dimension(nof,nos) :: R31eq,R32eq,R33eq
  real*8,dimension(nof,nos) :: fx,fy,tz,tx,ty,tz,fcx,fcy,fcz
  real*8,dimension(nof,nos) :: tcz,tcy,tcz,fbx,fbz,tbx,tby,tbz,fbz,fbz
  real*8,dimension(nof,nos) :: C11,C12,C13,C23,C22,C33
  real*8,dimension(nof,nos+1) :: Yx,Yy,Yz,Xx,Xy,Xz
  real*8,dimension(npr,npnc) :: nx,nv,nz,si,sj,g,ex1,ex2,ex3
  real*8,dimension(npr,npnc) :: ey1,ey2,ey3,Gijx,Gijy,Gijz
  real*8,dimension(npr,npnc) :: G1ix,G1iy,G1iz
  real*8 :: rp,sidex,sidye,sidez,contact_cutoff,axx,svy,szz,time
  real*8 :: xmi,rzmi,rzmi,pdotp,xmin,ymn,ymn,sp,xm,ym,dx,dy,dz,gij
  real*8 :: nijx,nijy,nijz,forc_xi(8),Yj(8),sep,fstar,fact
  real*8 :: ang,vltx,vlty,vltz,vltx,vlty,vlty,vlty,vlty,vlty,vlty
  real*8 :: sep,tmp,over_cut,wsep1,wsep2
  real*8 :: yeq,veq,veqz,xeq,xeqz,xeqz,peqi(3),Astar,deccat
  real*8 :: ang,lheta,ang,phi,wall_rep_cutoff,wall_cont_cutoff,fwz
  integer :: nfib,nseg,m,i,n,j,num_groups,k,corr,cory,corz
  integer :: overs,ipos,ith
  integer :: ifiber(4,npnc,npr),npr(nof,nos),nnt(npnc)
  integer :: ncpf(nof,nos),next(2,2*npnc,nof,nos),nclose(nof,nos)
  common /rseg/ rx,ry,tz,q0,q1,q2,q3,px,py,pz
  common /rep_forces/ fcx,fcy,fcz,tx,ty,tz,fbx,fbz,tbx,tby,tbz
  common /fric_forces/ fx,fy,fcz,tz,ty,tz,fbx,fbz,tbx,tby,tbz
  common /hand/ A11,A12,A13,A23,A22,A33,C11,C12,C13,C23,C22,C33
  common /parms/ nfib,nseg,rp,sidex,sidye,sidez
  common /contacts/ ax,nv,nz,si,sj,g,ex1,ex2,ex3,ey1,ey2,ey3, &
  G1ix,G1iy,G1iz,G1ix,G1iy,G1iz
  common /rotation/ R11,R12,R13,R21,R22,R23
  common /Jseg/ R11eq,R12eq,R13eq,R21eq,R22eq,R23eq, &
  common /Jconstants/ Ya,Yc,Yb,C0,C1,C3,C4
  common /Joints/ Yx,Yz,Xx,Xy,Xz
  ! Zero variables
  do m = 1, num_groups
    ncnt(m) = 0
  enddo
  num_groups = 0; overs = 0; fwz = 0.00
  do i = 1, nseg
    do j = 1, nseg
      ! Zero forces
      fx(m,i) = 0.00; fy(m,i) = 0.00; fz(m,i) = 0.00
      tx(m,i) = 0.00; ty(m,i) = 0.00; tz(m,i) = 0.00
      fcx(m,i) = 0.00; fcy(m,i) = 0.00; fcx(m,i) = 0.00
      tcz(m,i) = 0.00; tcy(m,i) = 0.00; tcz(m,i) = 0.00
      npr(m-1)*nseg+1 = 0
    enddo
  enddo
  ! Loop over all pairs in the neighbor list
  do m = 1, nfib
    do i = 1, nseg
      do k = 1, nclose(m-1)*nseg+1
        n = next(1,k,(m-1)*nseg+1)
        j = next(2,k,(m-1)*nseg+1)
        force = 0.00
      enddo
    enddo
  enddo

```

```

! Find minimum image in the y-direction only.
sxx = rx(n,j) - rx(m,i)
syy = ry(n,j) - ry(m,i)
szz = rz(n,j) - rz(m,i)
cory = dnint(syy/sidye)
syy = syy - cory*sidye
rxmi = rx(n,j) - sxx
rymi = ry(n,j) - syy
rzmi = rz(n,j) - szz
! Locate positions on rod segments from the center
! that correlate to the closest
! separation point between the rod segments.
pdotp = px(m,i)*px(n,j) + py(m,i)*py(n,j) + pz(m,i)*pz(n,j)
if (pdotp*pdotp == 1.00) then
  call parallel(sxx,syy,szz,px(m,i),py(m,i),pz(m,i), &
    px(n,j),py(n,j),pz(n,j),pdotp,rx,xmin,ymn)
  sep = (sxx*ymn*px(n,j)-xmin*py(m,i))*2 + &
    (syy*ymn*py(n,j)-xmin*py(m,i))*2 + &
    (szz*ymn*pz(n,j)-xmin*pz(m,i))*2
  gjj = dsqrt(sep)
  nijx = (sxx*ymn*px(n,j)-xmin*px(m,i))/gj
  nijy = (syy*ymn*py(n,j)-xmin*py(m,i))/gj
  nijz = (szz*ymn*pz(n,j)-xmin*pz(m,i))/gj
  if (gj < 2.00) overs = overs + 1
  if (gj < over_cut) gj = over_cut
  include 'forc.f90'
  if (sep < contact_cutoff) call sort(nseg,m,i,n,j, &
    xmin,ymn,gij,nijx,nijy,nijz,px,py,pz,time,rep)
else
  xmin = -(px(n,j)*sxx+py(n,j)*syy+pz(n,j)*szz)*pdotp + &
    (px(m,i)*sxx+py(m,i)*syy+pz(m,i)*szz)/ &
    (1.00-pdotp*pdotp)
  ymn = ((px(m,i)*sxx+py(m,i)*syy+pz(m,i)*szz)*pdotp - &
    (px(n,j)*sxx+py(n,j)*syy+pz(n,j)*szz))/ &
    (1.00-pdotp*pdotp)
  dx = rx(n,j)+ymn*px(n,j)-rxmi-xmin*px(m,i)
  dy = ry(n,j)+ymn*py(n,j)-rymi-xmin*py(m,i)
  dz = rz(n,j)+ymn*pz(n,j)-rzmi-xmin*pz(m,i)
  sep = dx**2 + dy**2 + dz**2
  ! Only proceed if the separation is small enough.
  if (sep < rep_cutoff) then
    xm = dabs(xmin)
    ym = dabs(ymn)
    ! Middle of the two bodies contact
    if (xm < rp) .and. (ym < rp) then
      gjj = dsqrt(sep)
      nijx = dx/gjj; nijy = dy/gjj; nijz = dz/gjj
      ! Check for overlaps and find the magnitude
      ! of the repulsive force.
      if (gj < 2.00) then
        overs = overs + 1
      endif
      if (gj < over_cut) gjj = over_cut
    endif
    force = fstar*dexp(-fact*(gj-2.00))
    if (sep < contact_cutoff) call sort(nseg,m,i,n,j, &
      xmin,ymn,gij,nijx,nijy,nijz,px,py,pz,time,rep)
  ! Check for end interactions (8 possibilities)
  else
    Yj(1) = rp; xi(1) = px(m,i)*sxx + py(m,i)*syy &
      + pz(m,i)*szz + Yj(1)*pdotp
    Yj(2) = -rp; xi(2) = px(m,i)*sxx + py(m,i)*syy + &
      pz(m,i)*szz + Yj(2)*pdotp
    xi(3) = rp; Yj(3) = -(px(n,j)*sxx + py(n,j)*syy + &
      pz(n,j)*szz) + xi(3)*pdotp
    xi(4) = -rp; Yj(4) = -(px(n,j)*sxx + py(n,j)*syy + &
      pz(n,j)*szz) + xi(4)*pdotp
    xi(5) = rp; Yj(5) = rp
    xi(6) = rp; Yj(6) = -rp
  endif
endif

```

delta_twist.f90

```

      xi(7) = -rp; yj(7) = rp
      xi(8) = -rp; yj(8) = -rp
      sep = 1000.D0; ipos = 1
      do ith = 1, 8
        sep_tmp = (sx+vj(ith)*px(n,j)-xi(ith))* &
          py(m,i))**2 + (sy+vj(ith)*py(n,j)-xi(ith))* &
          pz(m,i))**2
        if (sep_tmp < sep .and. Abs(xi(ith)) < rp .and. Abs(vj(ith)) <= rp) then
          sep = sep_tmp; ipos = ith
        endif
      enddo
      ! Check if an end interaction is the one
      if (sep < rep_cutoff) then
        nij = dsqrt(sep)
        nijx = (sx+vj(ipos)*px(n,j) - xi(ith))/gij
        nijy = (sy+vj(ipos)*py(n,j) - yj(ith))/gij
        nijz = (sz+vj(ipos)*pz(n,j) - zj(ith))/gij
        xmin = xi(ipos); ymin = yj(ipos)
        if (gij < 2.D0) then
          overs = overs + 1
          if (gij < over_cut) gjj = over_cut
        endif
        forc = fstar*dexp(-fact*(gij-2.D0))
        if (sep < contact_cutoff) call sort(nsep,m,i,&
          n,j,xmin,ymin,gij,nijx,nijy,nijz,px,py,pz,&
          time,rp)
      endif
    endif
  endif
endif
if (sep < rep_cutoff) then
  forc = fstar*dexp(-fact*(gij-2.D0))
  if (sep < contact_cutoff) call sort(nsep,m,i,&
    n,j,xmin,ymin,gij,nijx,nijy,nijz,px,py,pz,&
    time,rp)
endif
endif
if (sep < rep_cutoff) then
  forc = fstar*dexp(-fact*(gij-2.D0))
  if (sep < contact_cutoff) call sort(nsep,m,i,&
    n,j,xmin,ymin,gij,nijx,nijy,nijz,px,py,pz,&
    time,rp)
endif
endif
! Calculate forces if the contact is close
if (gij < wall_rep_cutoff) then
  nijx = 0.D0; nijy = 0.D0; nijz = -1.D0
  if (gij < 2.D0) then
    overs = overs + 1
    if (gij < over_cut) gjj = over_cut
  endif
  forc = fstar*dexp(-fact*(gij-2.D0))
  fcy(m,i) = fcy(m,i) - nijy*forc
  fcy(n,i) = fcy(n,i) + nijy*forc
  fcz(m,i) = fcz(m,i) - nijz*forc
  fcz(n,i) = fcz(n,i) + nijz*forc
  tcx(m,i) = tcx(m,i) - forc*xmin*(py(m,i)*nijz- &
    pz(m,i)*nijy)
  tcx(n,i) = tcx(n,i) + forc*xmin*(py(m,i)*nijz- &
    pz(m,i)*nijy)
  tcy(m,i) = tcy(m,i) - forc*xmin*(pz(m,i)*nijx- &
    px(m,i)*nijz)
  tcy(n,i) = tcy(n,i) + forc*xmin*(pz(m,i)*nijx- &
    px(m,i)*nijz)
  tcz(m,i) = tcz(m,i) - forc*xmin*(px(m,i)*nijy- &
    py(m,i)*nijx)
  tcz(n,i) = tcz(n,i) + forc*xmin*(px(m,i)*nijy- &
    py(m,i)*nijx)
  ! Force on the top wall
  fwz = iwz + nijz*forc
endif
! Calculate joint torques
! Calculate bending and twisting torques, both isotropic
if (i > 1) then ! no torque in "first" joint
  ! Find the bending component first
  zeqz = R11(m,i-1)*R33eq(m,i) + R21(m,i-1)*R32eq(m,i) + &
    px(m,i-1)*R33eq(m,i)
  zeqy = R12(m,i-1)*R33eq(m,i) + R22(m,i-1)*R32eq(m,i) + &
    py(m,i-1)*R33eq(m,i)
  zeqz = R13(m,i-1)*R33eq(m,i) + R23(m,i-1)*R32eq(m,i) + &
    pz(m,i-1)*R33eq(m,i)
  zdotz = px(m,i)*zeqz + py(m,i)*zeqy + pz(m,i)*zeqz
  dirxz = py(m,i)*zeqz - pz(m,i)*zeqy
  dirzy = px(m,i)*zeqz - pz(m,i)*zeqy
  dirz = px(m,i)*zeqz + py(m,i)*zeqy
  dum = DSGRT(dirz*dirz + diry*diry + dirx*dirx)
  if (zdotz > 1.D0-1.e-14) then
    Ybx = 0.D0; Yby = 0.D0; Ybz = 0.D0
  endif
endif
! Check for contacts with the bottom plate
wsep1 = rz(m,i) + rp*pz(m,i) + 1.D0
wsep2 = rz(m,i) - rp*pz(m,i) + 1.D0
! If one of the ends is close to the wall...
if (Abs(wsep1) < wall_cont_cutoff .and. &
  Abs(wsep2) < wall_cont_cutoff) then
  gjj = rz(m,i) + 1.D0; xmin = 0.D0
  elseif(wsep1 < wsep2) then
    gjj = wsep1; xmin = rp
  else
    gjj = wsep2; xmin = -rp
  endif

```

```
delta_twist.f90
```

```

else
  ang_theta = DACOS(zdotz)
  ybx = -kb*ang_theta*(dirx/dum)
  yby = -kb*ang_theta*(diry/dum)
  ybz = -kb*ang_theta*(dirz/dum)
endif
! Find the twisting component
cx = rx(m,i) - rx(m,i-1)
cy = ry(m,i) - ry(m,i-1)
cz = rz(m,i) - rz(m,i-1)
dum = DSQRT(cx*cx + cy*cy + cz*cz)
cx = cx/dum; cy = cy/dum; cz = cz/dum
! Y equilibrium
zeqx = R11(m,i-1)*R21eq(m,i) + R21(m,i-1)*R22eq(m,i) + &
px(m,i-1)*R23eq(m,i)
zeyy = R12(m,i-1)*R21eq(m,i) + R22(m,i-1)*R22eq(m,i) + &
py(m,i-1)*R23eq(m,i)
zezz = R13(m,i-1)*R21eq(m,i) + R23(m,i-1)*R22eq(m,i) + &
pz(m,i-1)*R23eq(m,i)
! Y in body frame perp. to c
vtx = R21(m,i) - cx*(cx*R21(m,i)+cy*R22(m,i)+cz*R23(m,i))
vty = R22(m,i) - cy*(cx*R21(m,i)+cy*R22(m,i)+cz*R23(m,i))
vtz = R23(m,i) - cz*(cx*R21(m,i)+cy*R22(m,i)+cz*R23(m,i))
dum = dsqrt(vtx*vtx+vty*vty+vtz*vtz)
vtx = vtx/dum; vty = vty/dum; vtz = vtz/dum
! Y equilibrium perp. to c
vleqx = zeqx - cx*(cx*zeqx+cy*zeyy+cz*zezz)
vleqy = zeyy - cy*(cx*zeqx+cy*zeyy+cz*zezz)
vleqz = zezz - cz*(cx*zeqx+cy*zeyy+cz*zezz)
dum = dsqrt(vleqx*vleqx+vleqy*vleqy+vleqz*vleqz)
vleqx = vleqx/dum; vleqy = vleqy/dum; vleqz = vleqz/dum
zdotz = vity*vleqx - vitx*vleqy + vitz*vleqz
dirx = vity*vleqx - vitx*vleqy
diry = vitx*vleqx - vity*vleqy
dirz = vitz*vleqx - vitz*vleqy
dum = DSQRT(dirx*dirx + diry*diry + dirz*dirz)
if(zdotz.gt.1.D0-1.e-14) then
  Ytx = 0.D0; Yty = 0.D0; Ytz = 0.D0
else
  ang_phi = DACOS(zdotz)
  Ytx = -kt*ang_phi*(dirx/dum)
  Yty = -kt*ang_phi*(diry/dum)
  Ytz = -kt*ang_phi*(dirz/dum)
endif
Yx(m,i) = Ybx + Ytx
Yy(m,i) = Yby + Yty
Yz(m,i) = Ybz + Ytz
endif
! Calculate some commonly used groupings
A11(m,i) = 1.D0/ta + C3*px(m,i)*px(m,i)
A12(m,i) = C3*px(m,i)*py(m,i)
A13(m,i) = C3*px(m,i)*pz(m,i)
A22(m,i) = 1.D0/ta + C3*py(m,i)*py(m,i)
A23(m,i) = C3*py(m,i)*pz(m,i)
A33(m,i) = 1.D0/ta + C3*pz(m,i)*pz(m,i)
C11(m,i) = 1.D0/yc + C4*px(m,i)*px(m,i)
C12(m,i) = C4*px(m,i)*py(m,i)
C13(m,i) = C4*px(m,i)*pz(m,i)
C22(m,i) = 1.D0/yc + C4*py(m,i)*py(m,i)
C23(m,i) = C4*py(m,i)*pz(m,i)
C33(m,i) = 1.D0/yc + C4*pz(m,i)*pz(m,i)
enddo
enddo
1023 Format(14,1x,i3,3(1x,1PD23.15))
end subroutine delta_twist

```


x_forces2.f90

```

V(k2) = upx*pull_check(m,i) - ux(m,i) + &
di(m,i)*(py(m,i)*wz(m,i) - pz(m,i)*wy(m,i))
endif
enddo
! Use the LAPACK routine to do the LUD
call DGEYS(N,band+npff,nrhs,AB,ldab,ipiv,v,idx,info)
if(info /= 0)then
write(41,'f,1x,i5,1x','INFO_X = ',i4*) time,m,info
stop
endif
! Assign forces and calculate velocities
npff = 0
do i = 1, nseg
if(i < nseg)then
k1 = 3*(i) - 2
Xx(m,i+1) = V(k1)
Xy(m,i+1) = V(k1+1)
Xz(m,i+1) = V(k1+2)
endif
if(pull_check(m,i) /= 0)then
npff = npff + 1
fpx(m,i) = V(3*(nseg-1)+npff)
tot_tens = tot_tens + pull_check(m,i)*fpx(m,i)
endif
ux(m,i) = ux(m,i) + A11(m,i)*(Xx(m,i+1)-Xx(m,i))+fpx(m,i) + &
A12(m,i)*(Xy(m,i+1)-Xy(m,i)) + A13(m,i)*(Xz(m,i+1)-Xz(m,i))
uy(m,i) = uy(m,i) + A12(m,i)*(Xx(m,i+1)-Xx(m,i))+fpx(m,i) + &
A22(m,i)*(Xy(m,i+1)-Xy(m,i)) + A23(m,i)*(Xz(m,i+1)-Xz(m,i))
uz(m,i) = uz(m,i) + A13(m,i)*(Xx(m,i+1)-Xx(m,i))+fpx(m,i) + &
A23(m,i)*(Xy(m,i+1)-Xy(m,i)) + A33(m,i)*(Xz(m,i+1)-Xz(m,i))
wx(m,i) = wx(m,i) + C11(m,i)*C0*(py(m,i)+Xz(m,i+1)-Xz(m,i))-&
pz(m,i)*(Xy(m,i+1)+Xy(m,i)) + &
C12(m,i)*(C0*(pz(m,i)+Xx(m,i+1)+Xx(m,i))-px(m,i)*&
(Xz(m,i+1)+Xz(m,i)))+C1*di(m,i)*pz(m,i)+fpx(m,i) + &
C13(m,i)*(C0*(px(m,i)+Xy(m,i+1)+Xy(m,i))-py(m,i)*&
(Xx(m,i+1)+Xx(m,i)))-C1*di(m,i)*py(m,i)+fpx(m,i)
wy(m,i) = wy(m,i) + C12(m,i)*C0*(py(m,i)+Xz(m,i+1)-Xz(m,i))-&
pz(m,i)*(Xy(m,i+1)+Xy(m,i)) + &
C22(m,i)*(C0*(pz(m,i)+Xx(m,i+1)+Xx(m,i))-px(m,i)*&
(Xz(m,i+1)+Xz(m,i)))+C1*di(m,i)*pz(m,i)+fpx(m,i) + &
C23(m,i)*(C0*(px(m,i)+Xy(m,i+1)+Xy(m,i))-py(m,i)*&
(Xx(m,i+1)+Xx(m,i)))-C1*di(m,i)*py(m,i)+fpx(m,i)
wz(m,i) = wz(m,i) + C13(m,i)*C0*(py(m,i)+Xz(m,i+1)-Xz(m,i))-&
pz(m,i)*(Xy(m,i+1)+Xy(m,i)) + &
C23(m,i)*(C0*(pz(m,i)+Xx(m,i+1)+Xx(m,i))-px(m,i)*&
(Xz(m,i+1)+Xz(m,i)))+C1*di(m,i)*pz(m,i)+fpx(m,i) + &
C33(m,i)*(C0*(px(m,i)+Xy(m,i+1)+Xy(m,i))-py(m,i)*&
(Xx(m,i+1)+Xx(m,i)))-C1*di(m,i)*py(m,i)+fpx(m,i)
endif
enddo
return
end subroutine x_forces

```

D.4 Example simulation: The star test flocculation

To demonstrate the typical input and output files of the simulations, we will present data for two time steps of the “star” test flocculation (illustrated in Fig. D.1). The parameter

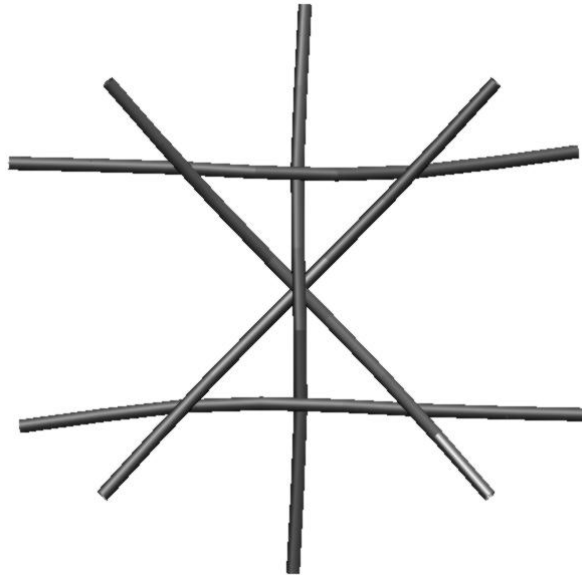


Figure D.1: Star configuration used in example files.

file, `Parameters.in` appears as

```

5           :nfib
7           :nseg
8.0        :rp
38.0       :kb
20.000     :mu_stat
20.00      :mu_kin
0.33       :contact_cutoff
0.66       :rep_cutoff
5.0        :neighb_cutoff
1.85       :overlap
0.0001     :dt
0.0002     :strain
200.0 200.0 200.0 :sidex,sidey,sidez

```

```

0.7          :fraction_rp
1            :config_write
1            :contact_write
1            :extra_write
50           :check_neighbor
150.0        :fstar
20.0         :fact
0.0          :Astar
35.0         :decatt
0.0          :delta_rx
0.0          :duxdx
0.0          :duydx
0.0          :duzdx
0.0          :duxdy
0.0          :duydy
0.0          :duzdy
1.0          :duxdz
0.0          :duydz
0.0          :duzdz

```

The centers of mass of the fibers $[rcmx(m), rcmy(m), rcmz(m)]$ are

1	-0.0000000244	3.4926345144	-0.0000000147
2	10.4451728846	2.4899385274	21.3245014739
3	-10.4451728628	2.4899385247	-21.3245014771
4	-0.0000000142	-1.6756001142	0.0000000023
5	0.0000000223	2.1520755077	0.0000000172

The fiber segment Euler parameters $[q0(m,i), q1(m,i), q2(m,i), q3(m,i)]$ are

1	1	0.9610773292	0.0723833950	0.2663893755	-0.0113009753
1	2	0.9627437545	0.0731900752	0.2600415982	-0.0120848351
1	3	0.9682988971	0.0761133800	0.2374601445	-0.0147200236
1	4	0.9730774843	0.0000000028	0.2304782192	0.0000000109
1	5	0.9682988968	-0.0761133746	0.2374601461	0.0147200454
1	6	0.9627437543	-0.0731900692	0.2600415998	0.0120848568
1	7	0.9610773290	-0.0723833889	0.2663893771	0.0113009969
2	1	0.5001700275	-0.1155868662	0.8553925322	-0.0690886079
2	2	0.4968494821	-0.1159362444	0.8573500048	-0.0681934646
2	3	0.4875819928	-0.1171688056	0.8626996957	-0.0654561407
2	4	0.5024695172	-0.1367899625	0.8532857070	-0.0267655115
2	5	0.5341660565	-0.1521875211	0.8314165266	0.0158789720
2	6	0.5657786419	-0.1470189806	0.8112236482	0.0140050119
2	7	0.5742575118	-0.1456192163	0.8055076317	0.0134465282
3	1	0.5742575113	0.1456191995	0.8055076350	-0.0134465402
3	2	0.5657786413	0.1470189637	0.8112236514	-0.0140050237
3	3	0.5341660558	0.1521875038	0.8314165300	-0.0158789831
3	4	0.5024695176	0.1367899446	0.8532857100	0.0267655012
3	5	0.4875819943	0.1171687876	0.8626996981	0.0654561305
3	6	0.4968494837	0.1159362265	0.8573500071	0.0681934543
3	7	0.5001700291	0.1155868483	0.8553925345	0.0690885976
4	1	0.1145106768	-0.0241004144	0.9864162955	0.1152795161
4	2	0.1240927777	-0.0229203624	0.9853874091	0.1143997090
4	3	0.1368841123	-0.0149014062	0.9868213790	0.0849956112
4	4	0.1405195473	0.0000000160	0.9900779044	0.0000000022
4	5	0.1368841149	0.0149014382	0.9868213785	-0.0849956068
4	6	0.1240927811	0.0229203943	0.9853874084	-0.1143997050
4	7	0.1145106803	0.0241004462	0.9864162948	-0.1152795124
5	1	0.8152475853	-0.0495575408	0.5753332270	0.0436703871
5	2	0.8105313587	-0.0501339450	0.5819215516	0.0435064572
5	3	0.8059105681	-0.0376640415	0.5900371645	0.0307525729
5	4	0.8056981498	0.0000000000	0.5923263386	-0.0000000003
5	5	0.8059105681	0.0376640413	0.5900371645	-0.0307525734
5	6	0.8105313588	0.0501339447	0.5819215515	-0.0435064576
5	7	0.8152475854	0.0495575405	0.5753332269	-0.0436703876

The equilibrium angles in the joints (θ_{eq} and ϕ_{eq}) are

1	2	0.0	0.0
1	3	0.0	0.0
1	4	0.0	0.0
1	5	0.0	0.0
1	6	0.0	0.0
1	7	0.0	0.0
2	2	0.0	0.0
2	3	0.0	0.0
2	4	0.0	0.0
2	5	0.0	0.0
2	6	0.0	0.0
2	7	0.0	0.0
3	2	0.0	0.0
3	3	0.0	0.0
3	4	0.0	0.0
3	5	0.0	0.0
3	6	0.0	0.0
3	7	0.0	0.0
4	2	0.0	0.0
4	3	0.0	0.0
4	4	0.0	0.0
4	5	0.0	0.0
4	6	0.0	0.0
4	7	0.0	0.0
5	2	0.0	0.0
5	3	0.0	0.0
5	4	0.0	0.0
5	5	0.0	0.0
5	6	0.0	0.0
5	7	0.0	0.0

The output files include the fiber centers of mass at the designated strain intervals, in the file `center_mass.dat`:

```

0.000000
1  0.000000  3.492635  0.000000
2  10.445173  2.489939  21.324501
3 -10.445173  2.489939 -21.324501
4  0.000000 -1.675600  0.000000
5  0.000000  2.152076  0.000000
0.000100
1  0.000000  3.492488  0.000000
2  10.447668  2.490019  21.324870
3 -10.447668  2.490019 -21.324870
4  0.000000 -1.675699  0.000000
5  0.000000  2.152169  0.000000
0.000200
1  0.000000  3.492501  0.000000
2  10.449886  2.490152  21.324918
3 -10.449886  2.490152 -21.324918
4  0.000000 -1.676082  0.000000
5  0.000000  2.152273  0.000000

```

The output fiber segment Euler parameters at the designated strain intervals are
(euler_param.dat):

```

0.000000
1  1  0.961077  0.072383  0.266389 -0.011301
1  2  0.962744  0.073190  0.260042 -0.012085
1  3  0.968299  0.076113  0.237460 -0.014720
1  4  0.973077  0.000000  0.230478  0.000000
1  5  0.968299 -0.076113  0.237460  0.014720
1  6  0.962744 -0.073190  0.260042  0.012085
1  7  0.961077 -0.072383  0.266389  0.011301
2  1  0.500170 -0.115587  0.855393 -0.069089
2  2  0.496849 -0.115936  0.857350 -0.068193
2  3  0.487582 -0.117169  0.862700 -0.065456
2  4  0.502470 -0.136790  0.853286 -0.026766
2  5  0.534166 -0.152188  0.831417  0.015879
2  6  0.565779 -0.147019  0.811224  0.014005

```

2	7	0.574258	-0.145619	0.805508	0.013447
3	1	0.574258	0.145619	0.805508	-0.013447
3	2	0.565779	0.147019	0.811224	-0.014005
3	3	0.534166	0.152188	0.831417	-0.015879
3	4	0.502470	0.136790	0.853286	0.026766
3	5	0.487582	0.117169	0.862700	0.065456
3	6	0.496849	0.115936	0.857350	0.068193
3	7	0.500170	0.115587	0.855393	0.069089
4	1	0.114511	-0.024100	0.986416	0.115280
4	2	0.124093	-0.022920	0.985387	0.114400
4	3	0.136884	-0.014901	0.986821	0.084996
4	4	0.140520	0.000000	0.990078	0.000000
4	5	0.136884	0.014901	0.986821	-0.084996
4	6	0.124093	0.022920	0.985387	-0.114400
4	7	0.114511	0.024100	0.986416	-0.115280
5	1	0.815248	-0.049558	0.575333	0.043670
5	2	0.810531	-0.050134	0.581922	0.043506
5	3	0.805911	-0.037664	0.590037	0.030753
5	4	0.805698	0.000000	0.592326	0.000000
5	5	0.805911	0.037664	0.590037	-0.030753
5	6	0.810531	0.050134	0.581922	-0.043506
5	7	0.815248	0.049558	0.575333	-0.043670
0.000100					
1	1	0.961065	0.072406	0.266428	-0.011315
1	2	0.962769	0.073054	0.259986	-0.012056
1	3	0.968254	0.076268	0.237577	-0.015008
1	4	0.973074	0.000000	0.230493	0.000000
1	5	0.968254	-0.076268	0.237577	0.015008
1	6	0.962769	-0.073053	0.259986	0.012056
1	7	0.961065	-0.072406	0.266428	0.011315
2	1	0.500144	-0.115567	0.855410	-0.069090
2	2	0.496835	-0.115966	0.857361	-0.068109
2	3	0.487597	-0.117057	0.862701	-0.065519
2	4	0.502469	-0.136509	0.853336	-0.026599
2	5	0.534240	-0.152621	0.831294	0.015654
2	6	0.565618	-0.147026	0.811334	0.014018
2	7	0.574272	-0.145603	0.805500	0.013462
3	1	0.574272	0.145603	0.805500	-0.013462
3	2	0.565618	0.147026	0.811334	-0.014018
3	3	0.534240	0.152621	0.831294	-0.015654
3	4	0.502469	0.136509	0.853336	0.026599
3	5	0.487597	0.117057	0.862701	0.065519

3	6	0.496835	0.115966	0.857361	0.068109
3	7	0.500144	0.115567	0.855410	0.069090
4	1	0.114511	-0.024097	0.986421	0.115237
4	2	0.124038	-0.022717	0.985398	0.114412
4	3	0.136831	-0.014917	0.986819	0.085107
4	4	0.140498	0.000000	0.990081	0.000000
4	5	0.136831	0.014917	0.986819	-0.085107
4	6	0.124038	0.022717	0.985398	-0.114412
4	7	0.114511	0.024097	0.986421	-0.115237
5	1	0.815203	-0.049546	0.575397	0.043669
5	2	0.810548	-0.050285	0.581910	0.043184
5	3	0.805915	-0.037780	0.590019	0.030842
5	4	0.805678	0.000000	0.592354	0.000000
5	5	0.805915	0.037780	0.590019	-0.030842
5	6	0.810548	0.050285	0.581910	-0.043184
5	7	0.815203	0.049546	0.575397	-0.043669
0.000200					
1	1	0.961057	0.072406	0.266456	-0.011323
1	2	0.962779	0.072990	0.259968	-0.012088
1	3	0.968230	0.076329	0.237649	-0.015092
1	4	0.973067	0.000000	0.230521	0.000000
1	5	0.968230	-0.076329	0.237649	0.015092
1	6	0.962779	-0.072990	0.259968	0.012089
1	7	0.961057	-0.072406	0.266456	0.011323
2	1	0.500117	-0.115553	0.855429	-0.069082
2	2	0.496833	-0.115967	0.857366	-0.068059
2	3	0.487578	-0.117002	0.862718	-0.065543
2	4	0.502460	-0.136532	0.853338	-0.026615
2	5	0.534280	-0.152698	0.831254	0.015638
2	6	0.565519	-0.147094	0.811391	0.013979
2	7	0.574268	-0.145589	0.805505	0.013477
3	1	0.574268	0.145589	0.805505	-0.013477
3	2	0.565519	0.147094	0.811391	-0.013979
3	3	0.534280	0.152698	0.831254	-0.015638
3	4	0.502460	0.136532	0.853338	0.026615
3	5	0.487578	0.117002	0.862718	0.065543
3	6	0.496833	0.115967	0.857366	0.068059
3	7	0.500117	0.115553	0.855429	0.069082
4	1	0.114494	-0.024062	0.986427	0.115214
4	2	0.123998	-0.022663	0.985403	0.114420
4	3	0.136788	-0.014886	0.986822	0.085141
4	4	0.140472	0.000000	0.990085	0.000000

4	5	0.136788	0.014886	0.986822	-0.085141
4	6	0.123998	0.022663	0.985403	-0.114420
4	7	0.114494	0.024062	0.986427	-0.115214
5	1	0.815165	-0.049565	0.575453	0.043614
5	2	0.810552	-0.050372	0.581911	0.042988
5	3	0.805924	-0.037906	0.589998	0.030863
5	4	0.805659	0.000000	0.592380	0.000000
5	5	0.805924	0.037906	0.589998	-0.030863
5	6	0.810552	0.050372	0.581911	-0.042988
5	7	0.815165	0.049565	0.575453	-0.043614

The inextensibility constraint forces $[X_x(m,i), X_y(m,i), X_z(m,i)]$ are output at the designated strain intervals in the file `inextens_next_guess.dat`:

```
0.000100
1 1 0.000000 0.000000 0.000000
1 2 8.945158 -1.414426 4.199382
1 3 11.356708 5.275594 10.915071
1 4 1.732342 -44.052780 18.875272
1 5 1.732342 44.052780 18.875272
1 6 11.356708 -5.275593 10.915071
1 7 8.945158 1.414426 4.199382
2 1 0.000000 0.000000 0.000000
2 2 -4.312483 -0.912840 5.402027
2 3 -7.854282 3.209117 7.433969
2 4 -18.066637 -24.074243 -1.083512
2 5 -23.720952 20.758888 5.399209
2 6 -8.790727 -2.867540 10.197740
2 7 -3.057214 -1.287083 11.027709
3 1 0.000000 0.000000 0.000000
3 2 -3.057214 1.287083 11.027709
3 3 -8.790727 2.867540 10.197740
3 4 -23.720952 -20.758888 5.399209
3 5 -18.066637 24.074244 -1.083512
3 6 -7.854282 -3.209117 7.433969
3 7 -4.312483 0.912840 5.402027
```

4	1	0.000000	0.000000	0.000000
4	2	-6.638623	-1.597692	1.127467
4	3	1.076507	22.487677	11.859292
4	4	-0.280106	23.840557	11.912845
4	5	-0.280106	-23.840557	11.912845
4	6	1.076507	-22.487676	11.859292
4	7	-6.638623	1.597692	1.127467
5	1	0.000000	0.000000	0.000000
5	2	3.694651	0.041156	5.504406
5	3	15.996154	16.716110	2.122702
5	4	18.024515	17.354588	3.369749
5	5	18.024515	-17.354588	3.369749
5	6	15.996154	-16.716110	2.122702
5	7	3.694651	-0.041156	5.504405
0.000200				
1	1	0.000000	0.000000	0.000000
1	2	8.447680	-0.864983	3.743926
1	3	11.283273	3.351111	8.945914
1	4	2.833793	-42.196053	20.882831
1	5	2.833793	42.196053	20.882831
1	6	11.283273	-3.351111	8.945914
1	7	8.447680	0.864983	3.743926
2	1	0.000000	0.000000	0.000000
2	2	-4.492539	-0.695563	5.383355
2	3	-7.833429	2.183719	8.065427
2	4	-19.931681	-23.448566	-1.125947
2	5	-26.626911	19.708077	8.320957
2	6	-7.410398	-2.745143	11.569918
2	7	-2.828959	-1.228660	10.554379
3	1	0.000000	0.000000	0.000000
3	2	-2.828959	1.228660	10.554379
3	3	-7.410397	2.745143	11.569918
3	4	-26.626911	-19.708078	8.320957
3	5	-19.931681	23.448566	-1.125947
3	6	-7.833429	-2.183719	8.065427
3	7	-4.492539	0.695563	5.383355
4	1	0.000000	0.000000	0.000000
4	2	-7.067618	-1.397758	1.710206
4	3	0.941304	22.079896	13.488825
4	4	-0.884040	21.675987	13.878221
4	5	-0.884040	-21.675987	13.878221
4	6	0.941304	-22.079896	13.488825

4	7	-7.067618	1.397758	1.710206
5	1	0.000000	0.000000	0.000000
5	2	3.629950	-0.051289	5.581923
5	3	22.134237	17.008785	4.268916
5	4	24.126759	17.838575	5.252596
5	5	24.126759	-17.838575	5.252596
5	6	22.134237	-17.008785	4.268916
5	7	3.629950	0.051289	5.581923

The number of groups, contacts, and overlapping fiber segments in the suspension at the given strain interval are output in the file `Number_of_Contacts.dat`:

0.0001000	7	8	0
0.0002000	7	8	0

The contact specifics are output in the file `Contact_info.dat`, which include (in order) the strain interval, the first fiber segment in the contact (m, i) , the second fiber segment in the contact (n, j) , the group containing the contact (`gc`), the contact number in that group [`nc`], the contact position on fiber segment m, i [`si(gc,nc)`], the contact position on fiber segment n, j [`sj(gc,nc)`], and the centerline-to-centerline separation [`g(gc,nc)`]:

0.00010	1	3	3	4	1	1	-6.396966	-0.487807	2.058803
0.00010	1	4	4	4	2	1	0.000000	0.000000	2.024084
0.00010	4	4	5	4	2	2	0.000000	0.000000	2.059454
0.00010	1	5	2	4	3	1	6.396966	0.487807	2.058803
0.00010	2	3	4	2	4	1	-5.100570	0.079312	2.078914

0.00010	2	5	5	6	5	1	5.977024	-1.032985	2.099180
0.00010	3	3	5	2	6	1	-5.977024	1.032985	2.099180
0.00010	3	5	4	6	7	1	5.100570	-0.079312	2.078914
0.00020	1	3	3	4	1	1	-6.397766	-0.488535	2.060636
0.00020	1	4	4	4	2	1	0.000000	0.000000	2.025303
0.00020	4	4	5	4	2	2	0.000000	0.000000	2.061344
0.00020	1	5	2	4	3	1	6.397766	0.488535	2.060636
0.00020	2	3	4	2	4	1	-5.100121	0.079906	2.080573
0.00020	2	5	5	6	5	1	5.976297	-1.030541	2.100895
0.00020	3	3	5	2	6	1	-5.976297	1.030541	2.100895
0.00020	3	5	4	6	7	1	5.100121	-0.079906	2.080573

Bibliography

- [1] M.P. Allen and D.J. Tildesley. *Computer Simulation of Liquids*. Oxford Science Publications, 1991.
- [2] K.E. Almin, P. Biel, and D. Wahren. An experimental investigation of the shear modulus of model fibre networks. *Svensk Papperstidning*, 67:772–774, 1967.
- [3] E.A. Amelina, E.D. Shchukin, A.M. Parfenova, A.I. Bessonov, and I.V. Viden-skii. Adhesion of the Cellulose Fibers in Liquid Media: 1. Measurement of the Contact Friction Force. *Colloid Journal*, 60(5):537–540, 1998.
- [4] O. Andersson. Some Observations of Fibre Suspensions in Turbulent Motion. *Svensk Papperstidning*, 69(2):23–31, 1966.
- [5] D.F. Arola, R.L. Powell, and M.J. McCarthy. NMR imaging of pulp suspensions flowing through an abrupt pipe expansion. *AIChE J.*, 44(12):2597–2606, 1998.
- [6] G.K. Batchelor. Slender-body theory for particles of arbitrary cross-section in Stokes flow. *J. Fluid Mech.*, 44:419–440, 1970.
- [7] G.K. Batchelor. The stress system in a suspension of force-free particles. *J. Fluid Mech.*, 41:545–570, 1970.
- [8] G.K. Batchelor. The stress generated in a non-dilute suspension of elongated particles by pure straining motion. *J. Fluid Mech.*, 46:813–829, 1971.
- [9] J. Baumgarte. Stabilization of Constraints and Integrals of Motion in Dynamical Systems. *Computer Methods in Applied Mechanics and Engineering*, 1:1–16, 1972.
- [10] M.L. Becraft and A.B. Metzner. The rheology, fiber orientation, and processing behavior of fiber-filled fluids. *J. Rheol.*, 36(1):143–174, 1992.
- [11] L. Beghella. *The Tendency of Fibers to Build Flocs*. PhD thesis, Åbo Akademi University, Turku, Finland, 1998.

- [12] C.P.J. Bennington, R.J. Kerekes, and J.R. Grace. The Yield Stress of Fibre Suspensions. *Can. J. Chem. Eng.*, 68:748–757, 1990.
- [13] R.B. Bird, W.E. Stewart, and E.N. Lightfoot. *Transport Phenomena*. John Wiley and Sons, New York, 1st edition, 1960.
- [14] G. Bossis and J.F. Brady. Self-diffusion of Brownian particles in concentrated suspensions under shear. *J. Chem. Phys.*, 9:5437–5448, 1987.
- [15] K.E. Brenan, S.L. Campbell, and L.R. Petzold. *Numerical solution of initial-value problems in differential- algebraic equations*. North-Holland, New York, 1989.
- [16] F.P. Bretherton. The motion of rigid particles in a shear flow at low reynolds number. *J. Fluid Mech.*, 14:284–304, 1962.
- [17] W.F. Busse. Mechanical Structures in Polymer Melts. I. Measurements of Melt Strength and Elasticity. *J. Polym. Sci. A2: Polymer Physics*, 5:1249–1259, 1967.
- [18] M. Chaouche and D.L. Koch. Rheology of non-Brownian rigid fiber suspensions with adhesive contacts. *J. Rheol.*, 45(2):369–382, 2001.
- [19] B. Chen, D. Tatsumi, and T. Matsumoto. Floc Structure and Flow Properties of Pulp Fiber Suspensions. *J. Soc. Rheol., Japan*, 30(1):19–25, 2002.
- [20] I.L. Claeys and J.F. Brady. Suspensions of prolate spheroids in Stokes flow. Part 1. Dynamics of a finite number of particles in an unbounded fluid. *J. Fluid Mech.*, 251:411–442, 1993.
- [21] I.L. Claeys and J.F. Brady. Suspensions of prolate spheroids in Stokes flow. Part 2. Statistically homogeneous dispersions. *J. Fluid Mech.*, 251:443–477, 1993.
- [22] I.L. Claeys and J.F. Brady. Suspensions of prolate spheroids in Stokes flow. Part 3. Hydrodynamic transport properties of crystalline dispersions. *J. Fluid Mech.*, 251:479–500, 1993.
- [23] R.G. Cox. The motion of long slender bodies in a viscous fluid. Part 1. General Theory. *J. Fluid Mech.*, 44:791–810, 1970.
- [24] R.W. Davison. The Weak Link in Paper Dry Strength. *Tappi*, 55(4):567–573, 1972.

- [25] S.M. Dinh and R.C. Armstrong. A Rheological Equation of State for Semiconcentrated Fiber Suspensions. *J. Rheol.*, 28(3):207–227, 1984.
- [26] L. Durflofsky, J.F. Brady, and B. Bossis. Dynamic simulation of hydrodynamically interacting particles. *J. Fluid Mech.*, 180:21–49, 1987.
- [27] X.-J. Fan, N. Phan-Thien, and R. Zheng. Simulation of fibre suspension flows by the Brownian configuration field method. *J. Non-Newtonian Fluid Mech.*, 84:257–274, 1999.
- [28] X.J. Fan, N. Phan-Thien, and R. Zheng. A direct simulation of fibre suspensions. *J. Non-Newtonian Fluid Mech.*, 74:113–135, 1998.
- [29] R.R. Farnood, S.R. Loewen, and C.T.J. Dodson. Estimation of intra-floc forces. *Appita*, 47(5):391–396, 1994.
- [30] F. Folgar and C.L. Tucker III. Orientation Behavior of Fibers in Concentrated Suspensions. *J. Reinforced Plastics and Composites*, 3:98–119, 1984.
- [31] O.L. Forgacs and S.G. Mason. The Flexibility of Wood-Pulp Fibers. *Tappi*, 41(11):695, 1958.
- [32] O.L. Forgacs and S.G. Mason. Particle Motions in Sheared Suspensions IX. Spin and Deformation of Threadlike Particles. *J. Colloid Science*, 14:457–472, 1959.
- [33] O.L. Forgacs, A.A. Robertson, and S.G. Mason. The Hydrodynamic Behaviour of Paper-Making Fibres. *Pulp Pap. Mag. Can.*, 59(5):117–128, 1958.
- [34] S. Goto, H. Nagazono, and H. Kato. The flow behavior of fiber suspensions in Newtonian fluids and polymer solutions. I. Mechanical properties. *Rheol. Acta*, 25:119–129, 1986.
- [35] O.G. Harlen, R.R. Sundararajakumar, and D.L. Koch. Numerical simulations of a sphere settling through a suspension of neutrally buoyant fibres. *J. Fluid Mech.*, 388:355–388, 1999.
- [36] E.J. Haug. *Computer Aided Kinematics and Dynamics of Mechanical Systems. Volume I: Basic Methods*. Allyn and Bacon, Needham Heights, MA, 1989.
- [37] R.C. Hibbeler. *Mechanics of Materials*. Prentice Hall, Upper Saddle River, NJ, 2nd edition, 1994.

- [38] F.B. Hildebrand. *Introduction to Numerical Analysis*. Dover Publications, Inc., New York, second edition, 1974.
- [39] M.J. Hourani. Fiber flocculation in pulp suspension flow, Part 2: Experimental Results. *Tappi J.*, 71:186–189, 1988.
- [40] Y. Iso, D.L. Koch, and C. Cohen. Orientation in simple shear flow of semi-dilute fiber suspensions. 1. Weakly elastic fluids. *J. Non-Newtonian Fluid Mech.*, 62:115–134, 1996.
- [41] G.B. Jeffery. The Motion of Ellipsoidal Particles Immersed in a Viscous Fluid. *Proc. Roy. Soc. London Ser. A*, 102:161–179, 1922.
- [42] C.G. Joung, N. Phan-Thien, and X.J. Fan. Direct simulation of flexible fibers. *J. Non-Newtonian Fluid Mech.*, 99:1–36, 2001.
- [43] R.J. Kerekes. Pulp floc behavior in entry flow to constrictions. *Tappi J.*, 66(1):88, 1983.
- [44] R.J. Kerekes. Perspectives on Fibre Flocculation in Papermaking. In *1995 International Paper Physics Conference*, page 23. CPPA, Montreal, 1995.
- [45] R.J. Kerekes and C.J. Schell. Characterization of Fibre Flocculation Regimes by a Crowding Factor. *J. Pulp Pap. Sci.*, 18:J32–J38, 1992.
- [46] R.J. Kerekes and C.J. Schell. Effects of fiber length and coarseness on pulp flocculation. *Tappi J.*, 78(2):133–139, 1995.
- [47] R.J. Kerekes, R.M. Soszynski, and P.A. Tam Doo. The Flocculation of Pulp Fibres. In V. Punton, editor, *Papermaking Raw Materials*, Transactions of the Eighth Fundamental Research Symposium Held at Oxford, pages 265–310. Mechanical Engineering Publications Limited, 1985.
- [48] J.K. Kim and S.H. Park. Fiber orientation and rheological properties of short fiber-reinforced plastics at higher shear rates. *J. Mater. Sci.*, 35(5):1069–1078, 2000.
- [49] S. Kim and S.J. Karrila. *Microhydrodynamics: Principles and Selected Applications*. Butterworth-Heinemann, Stoneham, MA, 1991.
- [50] T. Kitano and T. Kataoka. The rheology of suspensions of vinylon fibers in polymer liquids. I. Suspensions in silicone oil. *Rheol. Acta*, 20:390–402, 1981.

- [51] T. Kitano and T. Kataoka. The rheology of suspensions of vinylon fibers in polymer liquids. II. Suspensions in polymer solutions. *Rheol. Acta*, 20:403–415, 1981.
- [52] C.W. Lee and R.S. Brodkey. A Visual Study of Pulp Floc Dispersion Mechanisms. *AIChE J.*, 33(2):297, 1987.
- [53] J. Lumiainen. *Papermaking Part 1, Stock Preparation and Wet End*. Finnish Paper Engineers' Association and TAPPI, Finland, 2000.
- [54] M.B. Mackaplow and E.S.G. Shaqfeh. A numerical study of the rheological properties of suspensions of rigid, non-Brownian fibres. *J. Fluid Mech.*, 329:155–186, 1996.
- [55] S.G. Mason. The Flocculation of Cellulose Fibre Suspensions. *Pulp and Paper Magazine of Canada*, 49:99–104, 1948.
- [56] S.G. Mason. The Flocculation of Pulp Suspensions and the Formation of Paper. *Tappi*, 33:440–444, 1950.
- [57] J. Mewis and A.B. Metzner. The rheological properties of suspensions of fibres in newtonian fluids subjected to extensional deformations. *J. Fluid Mech.*, 62:593–600, 1974.
- [58] R. Meyer and D. Wahren. On the Elastic Properties of Three-Dimensional Fibre Networks. *Svensk Papperstidning*, 67(10):432–436, 1964.
- [59] W.J. Milliken, M. Gottlieb, A.L. Graham, L.A. Mondy, and R.L. Powell. The viscosity volume fraction relation for suspensions of rod-like particles by falling ball rheometry. *J. Fluid Mech.*, 202:217–232, 1989.
- [60] U. Mohlin, J. Dahlbom, and J. Hornatowska. Fiber deformation and sheet strength. *Tappi J.*, 79(6):105–111, 1996.
- [61] M.A. Nawab and S.G. Mason. The Viscosity of Dilute Suspensions of Thread-like Particles. *J. Phys. Chem.*, 62:1248–1253, 1958.
- [62] K. Niskanen. *Paper Physics*. Papermaking Science and Technology, Book 16. Finnish Paper Engineers' Association and TAPPI, Finland, 1998.
- [63] D.H. Page, R.S. Seth, B.D. Jordan, and M.C. Barbe. Curl, crimps, kinks and microcompressions in pulp fibres—their origin, measurement and significance. In V. Punton, editor, *Papermaking Raw Materials*, Transactions of the Eighth

Fundamental Research Symposium Held at Oxford, pages 183–227. Mechanical Engineering Publications Limited, 1985.

- [64] M.P. Petrich, D.L. Koch, and C. Cohen. An experimental determination of the stress-microstructure relationship in semi-concentrated fiber suspensions. *J. of Non-Newtonian Fluid Mech.*, 95:101–133, 2000.
- [65] W.H. Press, S.A. Teukolsky, W.T. Vetterling, and B.P. Flannery. *Numerical Recipes in FORTRAN*. Cambridge University Press, New York, 2nd edition, 1992.
- [66] M. Rahnema, D.L. Koch, Y. Iso, and C. Cohen. Hydrodynamic, translational diffusion in fiber suspensions subject to simple shear flow. *Phys. Fluids A*, 5(3):849–862, 1995.
- [67] M. Rahnema, D.L. Koch, and E.S.G. Shaqfeh. The effect of hydrodynamic interactions on the orientation distribution in a fiber suspension subject to simple shear flow. *Phys. Fluids A*, 7(3):487–506, 1995.
- [68] S. Ranganathan and S.G. Advani. Fiber-fiber interactions in homogeneous flows of nondilute suspensions. *J. Rheol.*, 35(8):1499–1522, 1991.
- [69] B.N. Rao, L. Tang, and M.C. Altan. Rheological Properties of non-Brownian spheroidal particle suspensions. *J. Rheol.*, 38(5):1335–1351, 1994.
- [70] A.A. Robertson and S.G. Mason. Flocculation in Flowing Pulp Suspensions. *Pulp Pap. Mag. Can. (Convention Issue)*, pages 263–269, 1954.
- [71] R.F. Ross and D.J. Klingenberg. Dynamic simulation of flexible fibers composed of linked rigid bodies. *J. Chem. Phys.*, 106:2949–2960, 1997.
- [72] W.B. Russel, D.A. Saville, and W.R. Schowalter. *Colloidal Dispersions*. Cambridge University Press, Cambridge, 1989.
- [73] C.F. Schmid. *Simulations of Flocculation in Flowing Fiber Suspensions*. PhD thesis, University of Wisconsin-Madison, 1999.
- [74] C.F. Schmid and D.J. Klingenberg. Mechanical flocculation of flowing fiber suspensions. *Physical Review Letters*, 84(2):290–293, 2000.
- [75] C.F. Schmid, L.H. Switzer, and D.J. Klingenberg. Simulations of Fiber Flocculation: Effects of Fiber Properties and Interfiber Friction. *J. Rheol.*, 44:781–809, 2000.

- [76] C.T. Scott, L.H. Switzer III, and D.J. Klingenberg. Network rupture in small, planar fiber networks. to be published.
- [77] R.S. Seth. The effect of fiber length and coarseness on the tensile strength of wet webs: a statistical geometry explanation. *Tappi J.*, 78(3):99–102, 1995.
- [78] E.S.G. Shaqfeh and G.H. Fredrickson. The hydrodynamic stress in a suspension of rods. *Phys. Fluids A*, 2:7–24, 1990.
- [79] E.D. Shchukin, I.V. Videnskii, E.A. Amelina, A.I. Bessonov, A.M. Parfenova, G. Aranovich, and M. Donokhi. Adhesion of Cellulose Fibers in Liquid Media: 2. Measurement of Contact Force of Attraction. *Colloid Journal*, 60(5):541–543, 1998.
- [80] P. Skjetne, R.F. Ross, and D.J. Klingenberg. Simulation of single fiber dynamics. *J. Chem. Phys.*, 107(6):2108–2121, 1997.
- [81] R.M. Soszynski and R.J. Kerekes. Elastic interlocking of nylon fibers suspended in liquid. Part 2. Process of interlocking. *Nordic Pulp Pap. Res. J.*, (4):180–184, 1988.
- [82] title = Elastic interlocking of nylon fibers suspended in liquid. Part 1. Nature of Cohesion among fibers Soszynski, R.M. and R.J. Kerekes. *Nordic Pulp Pap. Res. J.*, (4):172–179, 1988.
- [83] B. Steenberg, N. Thalen, and D. Wahren. Formation and properties of fibre networks. In F. Bolam, editor, *Transactions of the third fundamental research symposium 1965*, pages 177–186, Cambridge, England, 1966.
- [84] R.R. Sundararajakumar and D.L. Koch. Structure and properties of sheared fiber suspensions with mechanical contacts. *J. Non-Newtonian Fluid Mech.*, 73:205–239, 1997.
- [85] N. Takeuchi, S. Senda, K. Namba, and G. Kuwabara. Formation and destruction of fibre flocs in a flowing pulp suspension. *Appita*, 37(3):223–230, 1983.
- [86] P.A. Tam Doo and R.J. Kerekes. A method to measure wet fiber flexibility. *Tappi*, 64(3):113–116, 1981.
- [87] N. Thalén and D. Wahren. Shear Modulus and Ultimate Shear Strength of Some Paper Pulp Fibre Networks. *Svensk Papperstidning*, 67(7):259–264, 1964.
- [88] J.P.K. Tillet. Axial and transverse Stokes flow past slender axisymmetric bodies. *J. Fluid Mech.*, 44:401–417, 1970.

- [89] B.J. Trevelyan and S.G. Mason. Particle Motions in Sheared Suspensions. I. Rotations. *J. Colloid Science*, 6:354–367, 1951.
- [90] C.L. Tucker III. Flow regimes for fiber suspensions in narrow gaps. *J. Non-Newtonian Fluid Mech.*, 39:239–268, 1991.
- [91] D. Wahren. On the Visco-Elastic Properties of Fibre Networks. *Svensk Papperstidning*, 67(9):378–384, 1964.
- [92] J. Wittenburg. *Dynamics of Systems of Rigid Bodies*. Number Stuttgart. B.G. Teubner, 1977.
- [93] S. Yamamoto and T. Matsuoka. A method for dynamic simulation of rigid and flexible fibers in a flow field. *J. Chem. Phys.*, 98:644–650, 1993.
- [94] S. Yamamoto and T. Matsuoka. Viscosity of dilute suspensions of rodlike particles: A numerical simulation method. *J. Chem. Phys.*, 100:3317–3324, 1994.
- [95] S. Yamamoto and T. Matsuoka. Dynamic Simulation of Flow-Induced Fiber Fracture. *Polymer Engineering and Science*, 35:1022–1030, 1995.
- [96] S. Yamamoto and T. Matsuoka. Dynamic Simulation of Microstructure and Rheology of Fiber Suspensions. *J. Chem. Phys.*, 102:2254–2260, 1995.
- [97] S. Yamamoto and T. Matsuoka. Dynamic Simulation of Microstructure and Rheology of Fiber Suspensions. *Polymer Engineering and Science*, 36:2396–2402, 1996.
- [98] Y. Yamane, Y. Kaneda, and M. Doi. Numerical simulation of semi-dilute suspensions of rodlike particles in shear flow. *J. Non-Newtonian Fluid Mech.*, 54:405–421, 1994.
- [99] S. Zauscher and D.J. Klingenberg. Friction between cellulose surfaces measured with colloidal probe microscopy. *Colloids and Surfaces A: Physicochemical and Engineering Aspects*, 178:213–229, 2001.
- [100] S. Zauscher, C.T. Scott, and J.L. Willet. Pulp extrusion for recycling wastepapers and paper mill sludges. *Tappi J.*, 83(6):62, 2000.
- [101] R.H. Zhao and R.J. Kerekes. The effect of suspending liquid viscosity on fiber flocculation. *Tappi J.*, 76:183–188, 1993.